Microscopie à fluorescence sélective et volumétrique pour la localisation de molécules uniques dans des environnements encombrés

Tommaso Galgani

PSL UNIVERSITÉ PARIS

THÈSE DE DOCTORAT
DE L'UNIVERSITÉ PSL

Selective and volumetric fluorescence microscopy for single-molecule localization in crowded environments

Microscopie à fluorescence sélective et volumétrique pour la localisation de molécules uniques dans des environnements encombrés

Soutenue par
Tommaso Galgani
Le 29-10-2021

Ecole doctorale n° 564
Physique en Ile-de-France

Spécialité
Physique

Composition du jury :

Sandrine, LÉVÊQUE-FORT DR, ISMO, Université Paris-Saclay, France	*Président*
Aleksandra, RADENOVIC PR, LBEN, EPFL, Suisse	*Rapporteur*
Ricardo, HENRIQUES PR, UCL, IGC, Portugal	*Rapporteur*
Antoine, COULON CR, Institut Curie, PSL, France	*Examinateur*
Jean-Baptiste, SIBARITA IR, IINS, Université de Bordeaux, France	*Examinateur*
Maxime, Dahan† DR, Institut Curie, PSL, France	*Directeur de thèse*
Bassam, HAJJ CR, Institut Curie, PSL, France	*Directeur de thèse*

institut Curie | PSL

Acknowledgments

There are times during a PhD in which you feel alone, but in reality, this project has been possible thanks to the precious contribution of many people, that, now, I would like to thank.

The first person that I want to truly thank is Bassam Hajj, my mentor and supervisor. It has been a long run, but your leadership guided me until the end of it. Thank you for everything I learnt with you. Thanks for teaching me the importance of being meticulous and rigorous. Thank you for being always available for constructive discussions. Thank you for having learnt so quickly how to be a good director, for conducting my first steps as a scientist and then let me free to explore. Thanks for sharing my enthusiasm when I had good results or found solutions for the project, but also for supporting me in front of the failures.

It has been a great honor to be a PhD candidate under the supervision of Maxime Dahan and I want to thank him for giving me this opportunity. In the short time during which I worked with him, I learnt what being a great scientist and leader means. He will always be an inspiration to follow.

I would like to thank all the members of the jury for accepting to evaluate my work. A special thank goes to the two reviewers Aleksandra Radenovic and Ricardo Henriques for their precious feedback.

I must thank Jean-Baptiste Sibarita and Rémi Galland for their fruitful collaboration on the project. Thank you for hosting me in your lab for a week of training that has been fundamental for the success of my thesis. Thanks to Hisham Forrière for sharing his incredible enthusiasm during my visit.

I am thankful to the members of the TAC: Sandrine Lévêque-Fort for the multiple and constructive exchanges about microscopy that we had during these years and Stéphanie Descroix for the support and guidelines that she always gave me.

I want to thank Mathieu Coppey for the guidance that he provided to the whole team in the last years, for his inspiring curiosity and scientific creativity (and also for the great winter retreat at his house in the Alps).

Many thanks to Graça Raposo, Mélanie Herrbach and the whole training unit of Institut Curie. Thank you for making the Ic3i international PhD program being such

a good environment.

Je tiens à remercier Rémi Fert et Eric Nicolau pour leur aide dans la fabrication de composants mécaniques personnalisés du microscope.

My PhD journey would not have been so exciting without all the members of the LOCCO team that I met during these years. Thanks to Thomas, Brieuc, Koyomi, Mirna and Louise. Thanks Maud for the positive vibes that you bring every day to the lab. Thank you, Jean for your spirit of curiosity, thank you Alicia for being always ready to laugh and have fun. A very special thank you to Lorena, for helping me with the cell culture mysteries, but most of all for your friendship and support during all these years. And for the best *torta al semolino* of my life. A big thanks goes to Yasmina for helping me with the analysis of my experiments. A Homero un enorme agradecimiento por el increíble trabajo que has hecho y por tu perseverancia ante las cosas tan difíciles que te he pedido. Thanks also to all the ex-members of the team for all the great moments that we shared: Momo, Koceila, Aleria, Laurence, Veer, Laura Z., Elie, and Kotryna.

A Laura C. devo molto più di un grazie. Per aver condiviso con me le tue conoscenze di biologia e la tua passione per la scienza. Però molto di più per essere stata la prima ad accogliermi a Parigi, per essere stata un riferimento durante questi anni e per avermi fatto sentire davvero tuo frate'.

I want to thank many members and ex-members of the PCC/UMR168 for having created such magic environment: John, Remy, Maj, Antoine, Camille, Achille, Thanh, Julien, Mathieu D., Vincent, Louis, Manuela, Joanna and many more.

I have been very lucky to find so many good friends during these years in Paris, and I want to thank them all. Thank you Maciej for your independent spirit. I owe you at least four *tiramisù*. A very big thanks to Raquel, Sam, Ozge and Anne. You girls have always brought great laughs and fun everywhere we have gone. I learnt a lot from each of you. Many thanks to Deep, for all the fun, the adventures and the stories that we had together, but also your support during these years in Paris. And for being an adopted Italy supporter. A special thank you to "the wisdom club": Theb, thank you for the brilliant discussions that we had on many different topics and for your very fine sense of humor, and Ram, thank you for being my good friend and having such a great heart.

In Paris, I also found a family: Sandra, gracias por ser tan atenta con los demás, por tu sonrisa contagiosa y tu alegría. Daniel for being such a character, for being so kind, so sincere and so secretly romantic. Darine, thank you very much for being always there when I needed you, for listening and advising me as a real friend does. And thank you for being my partner-in-crime in so many occasions of fun. You guys have made Paris home during all these years. The experiences that we shared will be always part of me.

Devo un grazie enorme ai miei amici in Italia. Grazie a Gugli e a l'Ammy per aver

portato un po' di casa a Parigi. Pippo, Giac e Livio, grazie per essere sempre i più folli di tutti. Livio, grazie anche per il tuo aiuto con le simulazioni del DMD. Grazie al Poli e a Edo per aver fatto insieme un vero viaggio d'*artistes.* Tommi Matte, grazie per essere il più *artiste* fra gli *artistes.* Ale, grazie perché per me sei un esempio. Diddi, Paci, Pelli, Papo e Boncia, grazie per il vostro supporto anche da 1000 km di distanza. Bando, un grande grazie per essere sempre accanto a me, sia in salita che in discesa. Cava, un grazie speciale per essere il grande amico che c'è sempre, non importa dove, quando e come. Gli amici di sempre restano per sempre.

Gracias a Marina, José Manuel y Javi por acogerme.

A Silvia, gracias por tu enorme cariño, por tu apoyo incondicional y por ser mi compañera de viaje en cada momento. Gracias por todo lo que aprendo contigo. Gracias por ser la mejor parte de esta historia.

E infine voglio ringraziare Giova, la Marta, il mio babbo Riccardo e la mia mamma Tiziana. Grazie per la famiglia che siamo, grazie per tutti i vostri insegnamenti, per l'amore che sempre mi avete dato, per aver accettato e supportato ogni giorno la mia partenza perché so che non è facile. Grazie per essere un porto sicuro che mi accoglie ogni volta che torno. Questa tesi la dedico a voi.

Résumé scientifique

La microscopie de fluorescence à molécule unique (SMFM pour *single molecule fluorescence microscopy*) est un outil puissant capable de détecter et de localiser des molécules fluorescentes individuelles (chromophores) dans un échantillon biologique avec spécificité et une grande précision. La détection et la localisation de chromophores spécifiques dans l'échantillon peuvent être utilisées pour effectuer le suivi de biomolécules uniques et ainsi étudier la dynamique des processus moléculaires dans des cellules vivantes. En outre, la grande précision avec laquelle il est possible de localiser des chromophores uniques a ouvert la voie au développement de la microscopie à super-résolution, grâce à laquelle nous pouvons aujourd'hui dépasser la limite de diffraction standard (~ 230 nm pour la lumière visible) et atteindre une imagerie à résolution nanométrique.

Cependant, la SMFM nécessite un rapport signal sur bruit (SNR) élevé pour détecter le faible signal émis par chaque chromophore. Les défis pour une imagerie efficace de la molécule unique proviennent directement de l'échantillon. En effet, un microscope standard peut acquérir l'image 2D du plan focal, alors que, le plus souvent, les échantillons sont intrinsèquement 3D. C'est le cas par exemple du noyau cellulaire. Dans des échantillons volumétriques, et avec une excitation non spécifique, l'émission des molécules fluorescentes hors foyer génère un bruit de fond élevé qui dégrade le rapport signal sur bruit. De plus, l'approche la plus directe pour réaliser une imagerie 3D consiste à scanner le plan focal pour imager différents plans de l'échantillon. Mais cette procédure n'offre pas une haute résolution temporelle et limite ainsi la gamme des processus moléculaires observables.

L'élimination du bruit de fond est fondamentale pour obtenir un rapport signal sur bruit élevé, tandis que l'augmentation de la résolution temporelle est essentielle pour étudier un large éventail de dynamiques volumétriques des biomolécules. Dans mon projet de thèse, nous avons développé une méthode SMFM innovante pour l'imagerie volumétrique instantanée avec une excitation confinée. Notre technique consiste en un système modulaire capable de produire une excitation volumétrique sélective et une imagerie 3D instantanée.

Dans notre méthode, l'excitation est confinée à une feuille de lumière pour réduire le bruit de fond des émetteurs hors foyer et augmenter le SNR. En

particulier, nous avons adopté la microscopie à illumination sélective en feuille de lumière et à objectif unique (soSPIM). Dans la soSPIM, grâce à des porte-échantillons microfabriqués avec un miroir à 45° situé à côté de l'échantillon, un seul objectif à forte ouverture numérique permet d'exciter l'échantillon et collecter la fluorescence. En plus, pour pouvoir imager le volume du noyau avec une haute résolution temporelle, nous avons implémenté la Microscopie MultiFocus (MFM). Grâce à des réseaux diffractifs (MFG) placés sur le trajet d'émission d'un microscope à fluorescence, le MFM permet d'imager simultanément jusqu'à 9 plans de l'échantillon sans balayage mécanique et en utilisant une seule caméra EMCCD. Le MFM est compatible avec l'imagerie de molécules uniques et étend considérablement la gamme observable de la dynamique moléculaire.

Pour optimiser notre système modulaire, nous avons développé plusieurs MFG pour régler le volume d'observation. Pour adapter l'excitation, nous avons développé deux autres modules. Tout d'abord, un télescope accordable automatisé permet d'ajuster l'étendu de l'excitation pour correspondre au volume d'observation du MFM. En plus, nous avons implémenté un module optique pour produire une excitation homogène sur le volume d'intérêt. Ce module est basé sur la mise en forme du faisceau d'excitation grâce à une matrice de micro-miroirs (ou DMD pour *digital micromirror device*). Le module a été conçu et optimisé pour fonctionner avec plusieurs longueurs d'onde.

Grâce à notre méthode, nous avons pu réaliser une imagerie efficace de molécules uniques dans le noyau cellulaire, avec une haute résolution temporelle et spatiale. En particulier, nous avons observé la dynamique des histones H2B dans le noyau de cellules vivantes de mammifères. Nous avons également observé la dynamique des protéines nucléaires CTCF et Cohesin dans le noyau de cellules souche de souris. Grâce à notre méthode, nous avons pu observer des volumes de $35 \times 35 \times 4\ \mu m^3$ chaque 20 ms. Enfin, nous avons reconstruit des images super-résolution de la membrane nucléaire, que nous avons imagée par la technique DNA-PAINT appliquée à la protéine Lamin-b. Notre méthode ouvre la voie vers des études biologiques plus poussées à l'échelle nanométrique en 3D et en profondeur.

Abstract

Single-molecule fluorescence microscopy (SMFM) is a powerful tool capable of detecting and localizing individual fluorescent molecules (chromophores) in a biological sample with specificity and high precision. The detection and localization of specific chromophores in the sample can be used to track single biomolecules and, thus, study the dynamics of molecular processes in living cells. Furthermore, the high precision with which it is possible to localize single chromophores has paved the way for the application of SMFM to super-resolution microscopy. Thanks to super-resolution microscopy we can now go beyond the standard diffraction limit (~ 230 nm for visible light) and achieve nanometer resolution imaging.

However, SMFM requires a high signal-to-noise ratio (SNR) to detect the weak signal emitted by each chromophore. The challenges for efficient single-molecule imaging come directly from the sample. Indeed, a standard microscope can acquire the 2D image of the focal plane, whereas, samples are inherently 3D extended. This is the case, for example, of the cell nucleus. With a non-specific excitation, in volumetric samples, the fluorescence of out-of-focus emitters generates a high background noise which degrades the SNR. Moreover, the most direct approach to perform 3D imaging is to scan the focal plane to image different planes of the sample. This procedure does not offer high temporal resolution and thus limits the range of observable molecular processes.

Reducing as much as possible the background noise is fundamental to obtain a high SNR, while increasing temporal resolution is essential to study a wide range of volumetric dynamics of biomolecules. In my thesis project, we have developed an innovative SMFM method for instantaneous volumetric imaging with confined excitation, based on a modular system capable of tuning independently the acquisition and excitation volumes in order to produce the perfect match of the two.

In our method, the excitation is confined to a light-sheet to reduce the background of out-of-focus emitters and increase the SNR. In particular, we adopted single-objective selective plane illumination microscopy (soSPIM). In soSPIM, using microfabricated sample holders with a 45° mirror located next to the sample, a single high-numerical aperture (NA) objective can excite the sample and collect

fluorescence. In addition, in order to image the volume of the nucleus with high temporal resolution, we have implemented MultiFocus Microscopy (MFM). Thanks to diffractive gratings (MFG) placed on the emission path of a fluorescence microscope, MFM allows to image simultaneously up to 9 planes of the sample without mechanical scanning and using a single EMCCD camera. MFM is compatible with single molecule imaging and greatly extends the observable range of molecular dynamics.

To optimize our modular system, we developed several $MFGs$ to adjust the observation volume. To adapt the excitation, we developed two other modules. First, an automated tunable beam expander is used to adjust the size of the excitation beam to match the observation volume. In addition, we have implemented an optical module to produce a homogeneous excitation over the volume of interest. This module is based on the shaping of the excitation beam by a digital micromirrors device (DMD). The module has been designed and optimized to work with several wavelengths.

Thanks to our method, we were able to perform efficient imaging of individual molecules in the cell nucleus, with high temporal and spatial resolution. In particular, we observed the dynamics of individual H2B histones in the nucleus of living mammalian cells. We also observed the dynamics of CTCF and Cohesin nuclear factors in the nucleus of mouse embryonic stem cells. Using our method, we were able to observe volumes of $35 \times 35 \times 4\ \mu m^3$ every 20 ms. Finally, we reconstructed super-resolution images of the nuclear membrane, which we imaged using the DNA-PAINT technique applied to the Lamin B1 protein. Our method paves the way for further biological studies at the nanoscale in 3D and in depth.

Table of contents

Preface

Fluorescence microscopy is a fundamental tool in many biological and biophysical quantitative investigations. This technique permits to directly observe cells and sub-cellular components with high specificity.

For centuries, the diffraction of light sets an intrinsic limit to the imaging capabilities of any optical device. Developed at the beginning of 19th century by Joseph von Fraunhofer, the diffraction theory has been exploited by George Biddell Airy to introduce the notion of point spread function, which describes how the light emitted by a point-like source distributes after going through an optical system. The point spread function of a point-like source of visible light is ~230 nm wide. Thereafter, Ernst Abbe and Lord Rayleigh exploited the definition of point spread function to describe the resolution limit of a microscope. Two fluorescence emitters at a distance below this limit are impossible to distinguish. Many advanced optical microscopy techniques developed in the last decades have overcome the diffraction limit, achieving nanometric resolution.

The evolution of fluorescence microscopy brought to the development of single-molecule fluorescence microscopy, a powerful tool that is capable of detecting and imaging single biomolecules. The challenge of imaging single fluorescent molecules resides in detecting the weak signal emitted by such small emitters. For that, the imaging technique must be optimized to minimize the background noise and achieve high signal-to-noise ratio (SNR). Thanks to high SNR in combination with optimized detection algorithms, the position of each fluorescent molecule is determined with high precision. In fixed samples, this information can be used to reconstruct super-resolution images with nanometric precision. In living samples, single-molecule localization and tracking is used to study dynamical processes at the molecular scale.

Single-molecule fluorescence microscopy capabilities of detecting and localizing single emitter is well adapted for the functional study of various cell environments, including the nucleus. In fact, the dynamic interaction and organization at diverse spatial and temporal scales of the chromatin and other nuclear proteins, play a crucial role in orchestrating several cellular functions. The study of various fundamental processes that take place in the nucleus, such as DNA transcription,

RNA replication, and DNA repair, could greatly benefit from intranuclear single-molecule imaging, even though efficient imaging tools for the direct *in vivo* observation of such processes at the single-molecule scale are still lacking.

Indeed, the density and the inherent 3D organization of the nucleus constitute an obstacle to detect single nuclear biomolecules. With non-specific widefield excitation of the sample, the emission of abundant out-of-focus fluorescent molecules creates high background noise that degrades the signal-to-noise ratio and limits the single-molecule detection. It is common to bleach the majority of the molecules to reach an adequate density for single-molecule imaging. Moreover, molecules are free to move in the volumetric extent of the nucleus. Standard imaging systems are capable of acquiring only a 2D image of the focal plane. Most common 3D imaging techniques rely on the sequential scanning of the focal plane to reconstruct a volume. These methods do not provide sufficient temporal resolution and limit the observable range of molecular dynamic processes.

Knocking down the background noise to enhance the signal-to-noise ratio and increasing the time resolution are essential to perform efficient volumetric single-molecule imaging in the nucleus. The gold strategy for the reduction of the background noise is selective plane illumination microscopy (SPIM). Nowadays, several different techniques for light-sheet microscopy at the single-molecule level have been developed. For efficient single-molecule imaging, it is crucial to maximize the photon collection efficiency by using high numerical aperture (NA) objectives.

The aim of this thesis is to develop an innovative method for fast and sensitive volumetric single-molecule fluorescence microscopy in dense environments. Our method is based on the combination of two advanced fluorescence microscopy techniques for high-NA light-sheet microscopy and fast volumetric 3D imaging: single-objective selective plane illumination microscopy (soSPIM) and multifocus microscopy (MFM). In soSPIM, a single a high-NA objective creates a thin light sheet and collect the fluorescence emission thanks to micro-fabricated sample holders which have a 45° mirror located beside the sample. The high-NA objective provides high photon collection capability, sensitivity to single-molecule and high signal-to-noise ratio. In MFM, several diffractive elements are inserted on the emission path of a fluorescence microscope to acquire up to 9 different focal planes simultaneously with no mechanical scan and using a single EMCCD camera. MFM dramatically extends the observable range of molecular dynamics and is compatible with single-molecule imaging.

To optimally combine these two methods, we developed a system that is able to produce selective, volumetric and homogenous excitation that match exactly the dimension of the observation volume. For that, we developed a modular system that allow to tune independently the excitation and observation volumes. Combining the benefits of light-sheet microscopy with instantaneous volumetric imaging, our

method provides single-molecule sensitivity over an extended volume, high spatial and temporal resolution. In fact, with our method we were able to detect single emitters in 3D samples over a volume up to $22 \times 22 \times 4$ μm with a temporal resolution up to 50 volumes/s. Thanks to our method we were able to perform fast volumetric single-molecule tracking in the nucleus of living cells. We observed the 3D dynamics of single H2B histones, CTCF and Cohesin nuclear factors. These three biomolecules play crucial roles in the structural organization of the chromatin at different length scales. We also performed super-resolution imaging of the nuclear membrane by targeting Lamin B1 protein with a DNA-PAINT approach.

After introducing the main challenges for performing single-molecule imaging in volumetric and dense environments, this manuscript describes in details the development of our innovative method for fast, 3D imaging with homogeneous excitation at the molecular scale. Finally, it shows the results that we obtained in 3D single-particle tracking experiments and volumetric super-resolution imaging.

This manuscript is organized in 5 chapters:

- Chapter 1 is dedicated to introducing the challenges of performing volumetric single-molecule fluorescence microscopy and discussing its applications. Initially, the principles of fluorescence microscopy are introduced, followed by the description of a standard fluorescence microscope. After, the concepts of point spread function (PSF) and diffraction limit are described starting from elements of diffraction theory. Then, the chapter contains a description of several techniques that overcame the diffraction limit. Next, the principles and challenges of single-molecule detection and localization are provided, followed by the presentation of the two main applications of single-molecule fluorescence microscopy: single-particle tracking and super-resolution imaging. Finally, this chapter elucidates the various strategies that have been developed for performing 3D imaging at the single-molecule level.
- Chapter 2 emphasizes the importance of selective excitation in single-molecule fluorescence microscopy. The chapter contains the description of the methods that have been specifically developed to allow the use of high-NA objectives. The chapter shows how the multiple challenges of performing light-sheet microscopy with high-NA objectives can be overcome by moving the excitation beam over the back pupil of the illumination lens. Finally, it contains a focus on techniques that use a single objective for both illuminating the sample and collecting the fluorescence.
- Chapter 3 presents the innovative method for fast 3D single-molecule imaging with selective, volumetric and homogeneous excitation that we developed in this project. Our system is based on the combination of two cutting-edge techniques: multifocus microscopy (MFM) and single-objective selective plane illumination microscopy (soSPIM). The first two parts of this chapter contains

the detailed description of the two techniques. To combine optimally the two methods, we developed several modules, each one dedicated at performing a specific task. The third part of this chapter contains the description and characterization of the module that we developed and automatized to tune the dimension of the excitation beam. The last part of this chapter provides the details about the development of the module dedicated to produce volumetric and homogenous selective excitation by beam shaping.

- Chapter 4 contains the results that we obtained using our newly developed method for single-particle tracking and super-resolution imaging. Initially, it is shown the importance of performing selective excitation with the comparison of several samples excited through light-sheet illumination and non-specific widefield excitation. After, a complete characterization of the capabilities of the imaging system performed using fluorescent beads of different size and velocity is provided. Following, it is shown how our system permits to explore various ranges of dynamics of different biomolecules, that participate to the regulation of chromatin structural organization. In particular, the third part of this chapter shows the experiments conducted for the 3D tracking of H2B histones, while the fourth part describes the observation of volumetric dynamics of two nuclear factors: CTCF and Cohesin. Finally, the chapter shows the results of super-resolution imaging of the nuclear membrane conducted by targeting the Lamin B1 protein through DNA-PAINT method.
- Chapter 5 includes the discussions and the future perspectives of this project.
- Annex 1 contains the detailed procedures for the alignment of the modules that we developed for tailoring the illumination.
- Annex 2 illustrates the programs that we wrote for simulating the volumetric excitation produced by beam shaping and for controlling the beam shaping module.
- Annex 3 includes the simulation that we performed to explore a possible strategy for the beam shaping module development based on the use of a custom-made prism.
- Annex 4 is dedicated to the protocols for cell culture and the preparation of the samples that have been used in the experiments illustrated in this manuscript.

Chapter 1

En route to single-molecule fluorescence microscopy

Fluorescence microscopy has become an essential tool in bioscience investigation and nowadays is used to study a wide range of different samples. In the last decades, many methods have been developed to introduce fluorescent molecules into biological samples. The specimen can be genetically transfected to express fluorescent proteins or it can be specifically labeled with organic fluorescent molecules.

The imaging capabilities of any optical system are inherently limited by the physical phenomenon of diffraction. Diffraction sets the resolution limit of an optical setup, and had constituted an impassable barrier to the observable details. In the last decades advanced microscopy techniques based on the detection of single fluorescent molecules in the biological environment have overcome the diffraction limit of optical system.

This chapter contains an overview of the fundamental concepts of fluorescence microscopy, with particular attention to its applications at the single-molecule level. First, an introduction to the photophysics of the fluorescence effect is provided, followed by a description of a standard fluorescence microscope. After, some elements of diffraction theory expose the concept of resolution limit. Later, several super-resolution techniques are presented. Then, single-molecule fluorescence microscopy is introduced, with a detailed focus on the parameters that regulate the detection and localization of single fluorescence molecules. Afterwards, it is explained how single-molecule fluorescence microscopy finds application in single-particle tracking experiments and super-resolution imaging. This part includes also a detail description of the super-resolution techniques based on single-molecule detection and localization. Finally, methods for the detection of single-molecule in 3D are showed.

1.1 Fluorescence microscopy

In fluorescence microscopy the interest is focused towards objects that emit fluorescence light. Fluorescence is a well-established physical phenomenon that consists in the emission of light by a molecule as a consequence of the absorption of light radiation.

Fluorescent molecules used in fluorescence microscopy are called chromophores. When a chromophore in the ground state absorbs enough energy from interaction with photons, its electronic, vibrational and rotational configuration changes, bringing the molecule to an excited state. Each absorbed photon transfers to the chromophore all its energy $E = hc/\lambda$, where h is Planck's constant, c the speed of light and λ the wavelength of the excitation photon. Most commonly, in fluorescence microscopy the energy carried by a photon brings the molecule in the first-excited singlet state. The chromophore tends naturally to relax from the singlet state back to the ground state by losing the exceeding energy. This relaxation happens with non-radiative or radiative mechanisms. In good chromophores, the energy gap between the singlet state (at the lowest vibrational level) and the ground state (at any vibrational level) is so deep that the molecule can return to the non-excited state only through the emission of a fluorescence photon with the same energy of the gap [1]. The excitation/emission cycle of the chromophores can be iterated until the molecule undergoes some conformational changes or intersystem crossing that drive the molecule into a dark state or a triplet state, respectively. The triplet state is an excited state with lower energy than the singlet state. A molecule in the triplet state has an electronic conformation in which the total electronic spin is 1. It differs from the first-excited singlet state, in which the molecule total electronic spin is equal 0. Irreversible photobleaching can occur to a molecule in the dark state that photochemically reacts with oxygen molecules or other organic molecules present in the samples. A photobleached chromophores cannot be excited to the fluorescent state anymore. A molecule in the triplet state can relax to the ground state by phosphorescence transition on a much slower time scale than fluorescence or through non-radiative mechanisms (**FIG. 1A**). During this time, a chromophore in the triplet state can transfer its energy to molecular oxygen present in the sample, leading to the formation of energetically excited singlet oxygen or superoxide radical. These two molecular species are called reactive oxygen species (ROS) that are phototoxic for the sample. Moreover, singlet oxygen is a direct participant in the photobleaching pathway [2].

For standard fluorescence transition, the emitted photon carries energy equal to the gap between the lowest vibrational level of the singlet state and the ground state. Therefore, the energy of the emitted photon is typically lower than the energy of the photon absorbed by the molecule i.e. higher emission wavelength. This effect

is called Stokes shift and it is exploited in fluorescence microscopy to optically separate the excitation and emission light (FIG. 1B).

In fluorescence microscopy, the number of emitted photons by each chromophore defines the imaging quality. The emitted photon flux is defined by the quantum yield and the extinction coefficient of the chromophore. The extinction coefficient measures the light absorption probability of the molecule. Having high extinction coefficient is useful mainly when the excitation intensity needs to be kept minimum, such as for imaging living samples. The number of emitted photons is regulated by the quantum yield of the chromophore. This property defines the ratio of the number of emitted photons to the number of absorbed photons. Normally, a quantum yield approaching 1 is desirable.

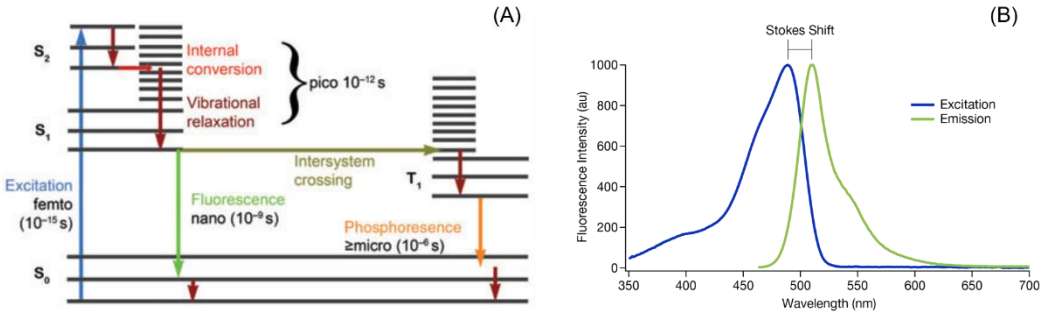

FIG. 1 – Fluorescence principle. *(A) Jablonski diagram represents the excitation of a fluorophore and the consequent fluorescence through the exchange of photons. For simplicity we consider a molecule having an electron pair. The spin orientation of each electron can be* $\pm 1/2$*. The electron pair can assume two different configurations. In the singlet state (S) the two electrons have antiparallel spins. With much lower probability, the two spins can have parallel orientation and in this case the molecule is said to be in the triplet state (T). When a chromophore absorbed goes from the ground state* S_0 *to an excited state* S_n*. Considering the first two excited singlet state* S_1 *and* S_2*, non-radiative mechanisms such as internal conversion or vibrational relaxation brings the molecule to the lowest vibrational level of* S_1 *state. Fluorescence brings the molecule back to the ground state* S_0 *through the emission of a photon. After several excitation/emission cycles, photobleaching of the chromophore can happen with several different mechanisms. Conformational changes can bring the molecule in a non-radiative dark state. Also, intersystem crossing can bring the molecule to the triplet state. The interaction of the chromophore in the triplet state with the oxygen in the sample results in photobleaching, producing phototoxic reactive oxygen species. Adapted from* [1]*. (B) The Stokes shift describes the difference between the energy thus the wavelength of the absorbed photon during the excitation of the molecule and the emitted photon during fluorescence.*

1.2 A standard fluorescence microscope

A fluorescence microscope uses fluorescence as a contrast mechanism. A combination of several optical elements allows to separate the excitation and emission and produce a magnified image of the sample. In modern fluorescence microscopy, the standard approach is widefield epi-illumination. In this configuration, the same objective lens (OBJ) illuminates the sample and collects the

fluorescence. Thanks to the Stokes shift, it is possible to illuminate the specimen with a given wavelength and filter the returning light to observe only the fluorescence at a longer shifted wavelength. Dedicated optics such as dichroic mirrors, emission and excitation filters are placed along the optical path to separate the illumination and the emission pathways. The dichroic mirror is conceived to reflect shorter excitation wavelengths and transmits longer fluorescence wavelengths. Coupling the dichroic mirrors with narrow excitation and emission filters, the illumination and emission pathways can be separated and independently manipulated. An objective lens is coupled with a tube lens (TL) to produce the magnified image of the sample plane on a conjugated image plane.

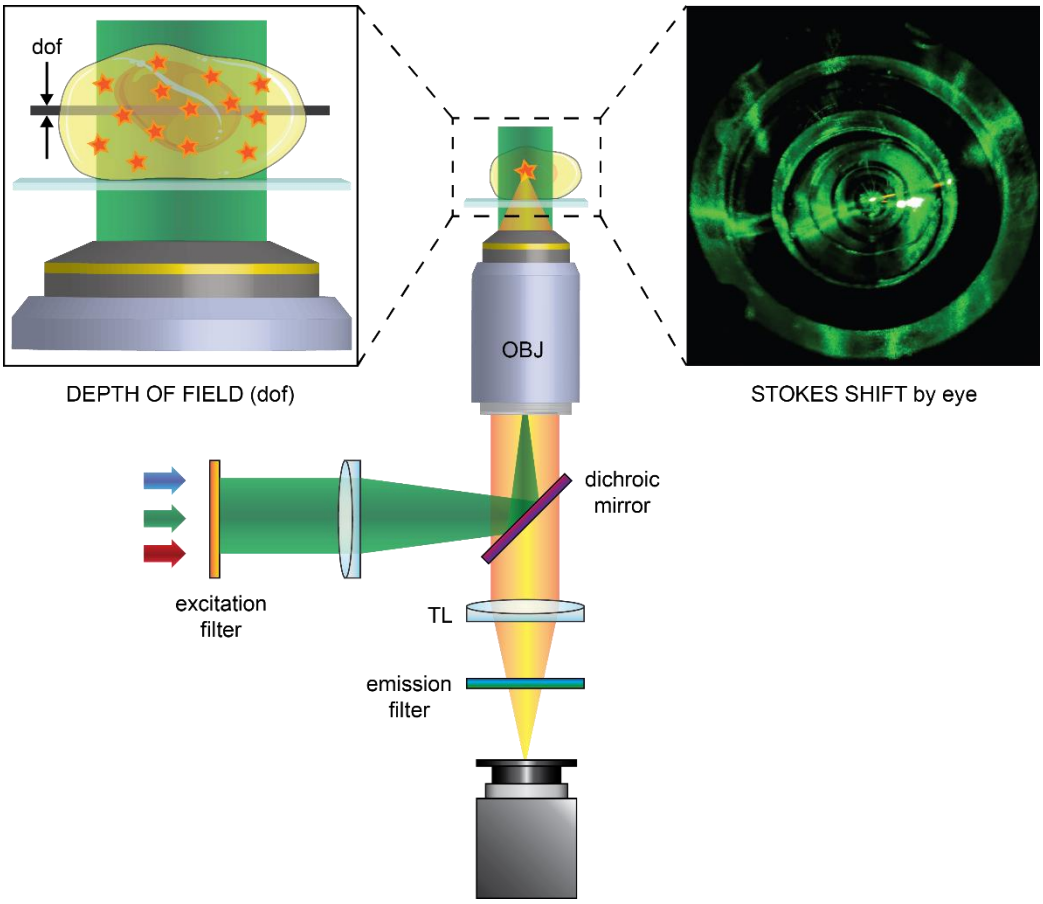

FIG. 2 – Optical scheme of a standard fluorescence microscope. *A dichroic mirror, coupled with narrow excitation and emission filters, separate the pathways of excitation and fluorescence. The objective and the tube lens, reproduce the image of the sample plane on the image plane, where a detector is placed. The top-left panel shows the depth of field of a standard fluorescence microscope, that is 600 nm extent along the optical axis. In the top-right picture, the Stokes shift can be observed by eye. The picture shows a tilted 561 nm laser beam exciting the sample made of a solution of Cy3 dyes. Fluorescence is observable in red. The difference in the excitation and fluorescence wavelengths is defined as Stokes shift and exploited to separate the excitation and emission pathways.*

Although one could expect to reproduce an infinitely thin section of the sample at the image plane using a standard epi-fluorescence microscope, the image of each

point is spread as an inherent consequence of diffraction. Paragraph 1.3 contains elements of diffraction theory and the detailed illustration of the concept of point spread function (PSF). For that, the region of the sample that appears in focus matches the PSF extent along z. The depth of field is defined as the distance between the nearest and the farthest thin planes from the objective lens that appear simultaneously in focus. At high numerical apertures of the microscope the depth of field is mainly defined by wave optics, while, for low numerical aperture, it is determined by the circle of confusion of geometrical optics. The depth of field is described as

$$dof = \frac{\lambda n}{NA^2} + \frac{n}{NA} e \,, \tag{1.1}$$

where λ is the wavelength, n is the refractive index of the immersion medium, NA is the numerical aperture. For visible light and high numerical aperture $dof = 600$ nm approximately (**FIG. 2**).

1.3 Diffraction theory and resolution limit of a microscope

The phenomenon of diffraction constitutes an intrinsic barrier to the capability of any optical system to produce distinguishable images of nearby light sources. This capability is defined as resolution. The diffraction phenomenon is due to the wave nature of light and to the finite dimensions of the optics in the imaging setup.

In 1835, George Biddely Airy defined theoretically the resolution of an optical device [3], elaborating the Fraunhofer diffraction theory and the Huygens-Fresnel theorem. The Huygens-Fresnel theorem states that any unobstructed point of a plane wavefront can be considered, at a given time, as a source of spherical secondary wavelets, all at the same wavelength. The interference of these wavelets generates overlapping plane waves, propagating in different directions, each one associated to a specific spatial frequency or diffraction order (**FIG. 3**).

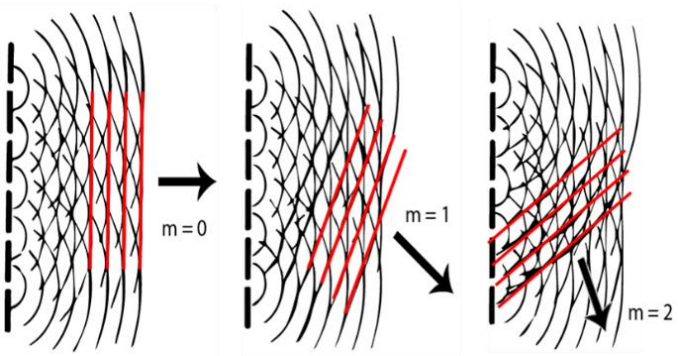

FIG. 3 – Principle of wavefront propagation. *The dashed line represents a series of points of the plane wavefront of an unobstructed radiation. Each point originates wavelets, that interfere. The interference creates the different diffraction orders of the far electromagnetic field. Adapted from [5].*

Let us now consider a plane wave that is incident on a lens. For the Fraunhofer diffraction theory this is equivalent to consider a plane wave through a circular aperture. It is possible to demonstrate that the electromagnetic field of wavelength λ, in a point $P = (p, q)$ of a plane at a certain distance from the objective, is

$$E(p,q) = \iint G(x,y) e^{\frac{-2\pi i}{\lambda}(px+qy)} dxdy\,, \tag{1.2}$$

where the integration area is the surface of the lens, described by the coordinates (x, y), and $G(x, y)$ is its transmission function, related to the shape of the lens [4]. According to (1.2), the electromagnetic field at the image plane of the lens is the Fourier transform of the transmission function G, and it depends on the spatial frequencies p/λ and q/λ.

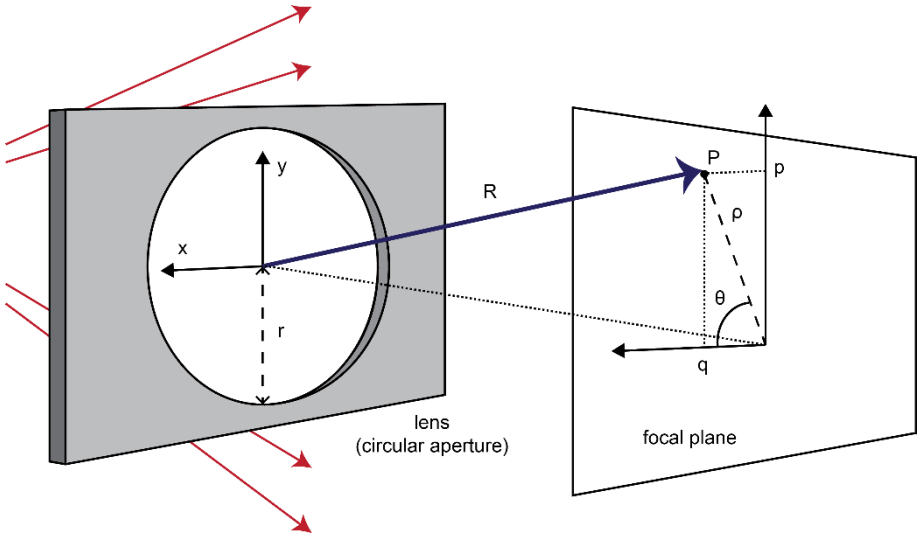

FIG. 4 – Fraunhofer diffraction of a circular aperture. *The scheme represents the involved parameters and coordinates in the lens and image plane. Acting as a circular aperture, the objective, as any other lens, diffracts the incoming light. This is illustrated by the spatial frequencies in red that are not collected by the objective*

For the symmetry of a circular aperture, let us move to a polar coordinates reference system. Now, $P = (p, q) = (\rho \cos\theta, \rho \sin\theta)$. The finite dimensions of the back pupil of the objective (more generally, of the lens) limit the number of spatial frequencies that will be collected by the lens and that will contribute to (1.2). Consequently, it is possible to demonstrate that the intensity of the radiation in the point P is

$$I(P) = |E(P)|^2 = I_0 \left(\frac{2J_1(kr\rho/R)}{kr\rho/R} \right)^2, \tag{1.3}$$

J_1being the first order Bessel function, $k = 2\pi/\lambda$, r the lens radius, R the distance

between P and the center of the lens, I_0 the intensity peak calculated for $(\rho, \theta) = (0,0)$ [5] (**FIG. 4**)**.** Therefore, the intensity in the image plane is described by the Airy function

$$I = I_0 \left(\frac{2J_1(u)}{u} \right)^2 . \tag{1.4}$$

The intensity distribution consists in several disks and the central one, called Airy disk, contains 84% of the total intensity of light. In conclusion, any lens can be considered as a circular aperture which distributes the light intensity of a point-like source according to the diffraction pattern. In a similar way, the objective lens of standard microscope (see paragraph 1.1) can collect only a limited number of spatial frequencies of the light emitted by each chromophore. Considering each emitter as a point-like source, the point spread functions (PSF) has been introduced to define the light intensity distribution in the image of a point-like source. The lateral $(x - y)$ PSF is well described by the Airy function (1.4) (**FIG. 5A**). The axial (z) PSF is non-stationary along the optical axis and more complicated to model. Among others, Richards-Wolf [6] and Gibson-Lanni [7] have proposed high precision models of the 3D PSF of a point-like source (**FIG. 5B**). In reality, the PSF of any optical system is degraded by several kind of aberrations. In thin samples, the dominant source of aberrations is the mismatch between the refractive indexes of the sample and the coverslip (and the immersion medium)[1].

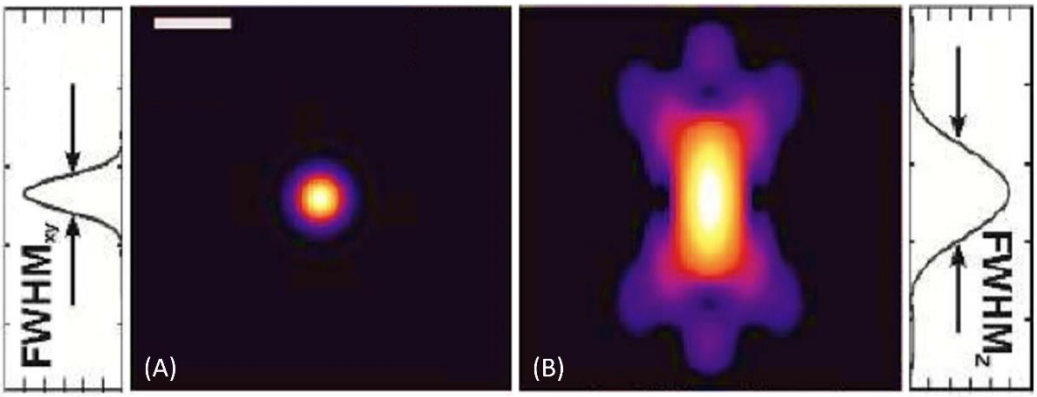

FIG. 5 – Point spread function $x - y$ and $x - z$ projections. *The point spread function describes the intensity distribution of light when an imaging system produces the image of a point-like source. (A) The Airy function represents well the lateral projection of the point spread function of a point-like source at the focal plane. (B) Axial projection of the point spread function of a point-like emitters at the focal plane. The frames show that the axial PSF is wider than the lateral PSF. Scale bar 1 μm.*

Resolution is the capabilities of an optical system to resolve two close point-like

[1] With reference to **FIG. 6** in fluorescence microscopy an imaging medium is used to match either the refractive index of the coverslip (in the case of high-NA objective) or the sample (to reduce aberration).

sources of light. In 1873, for the first time, Abbe derived empirically the resolution limit of a microscope [8]. With the concept of PSF in mind, he observed that the resolving power of a microscope decreases with the wavelength of the light. Also, he observed that the resolution increases with the objective numerical aperture $NA = n \sin\theta$, this describing the solid angle in which the photons are collected by the lens. Let us consider an objective working with an immersion medium of refractive index n and let λ be the excitation wavelength. Let P and Q be two points separated by a distance d, P being on the optical axis of the objective. Let θ be the angle formed by the most marginal rays that are captured by the objective lens with respect to the optical axis (**FIG. 6**).

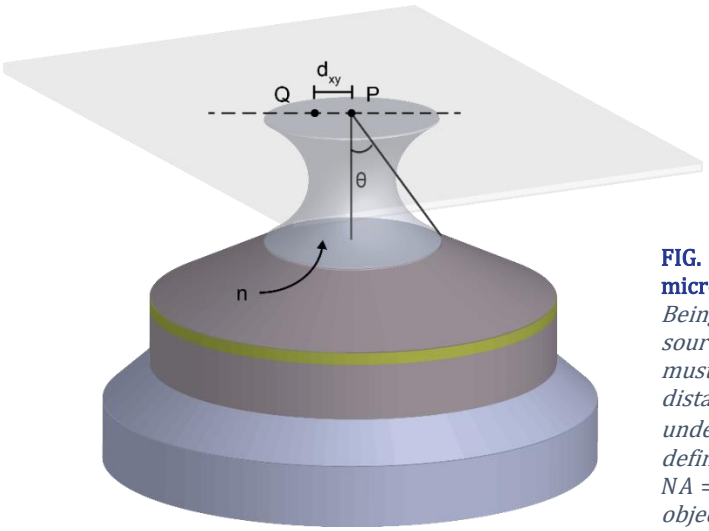

FIG. 6 – The resolving power of a microscope is limited by diffraction. *Being P and Q, two point-like sources of light at wavelength λ, they must be separated by a minimum distance d_{xy} to be distinguishable under a microscope. This distance is defined by the numerical aperture $NA = n \sin\theta$ of the microscope objective.*

Abbe's observations can be mathematically expressed saying that the minimum distance at which the points P and Q must be to be resolved by a microscope is

$$d_{x,y} = \frac{\lambda}{2NA}. \tag{1.5}$$

In 1879, Lord Rayleigh established a criterion for the resolution of two point-like sources of light [9]. Considering the images of two sources P and Q produced by a microscope, Rayleigh criterion states that the images of the two points will be resolved if the center of the Airy profile of one coincides with the first minimum of the diffraction pattern of the other or if the distance between these points is greater (**FIG. 7**). Therefore, the radius of the first Airy disk sets the Rayleigh's axial resolution limit at

$$d_{x,y} = 0.610\frac{\lambda}{NA}. \tag{1.6}$$

As observed by both Abbe and Rayleigh, the diffraction effect that establishes

the PSF plays a crucial role in the definition of the resolving power of a microscope. As seen in paragraph 1.1, the PSF is more extent in the axial direction then in the lateral direction, and we can expect that this affects negatively the axial resolving power of the imaging system. A formula that is generally accepted in literature for the axial resolution of a microscope is here reported:

$$d_z = \frac{2\lambda}{NA^2}. \tag{1.7}$$

To summarize the lateral resolution of a microscope corresponds to the is roughly 230 nm in the regime of visible light and for high NA objectives. The elongation of the PSF along the optical axis leads to an axial resolution that is roughly 600 nm for visible light and high NA objectives.

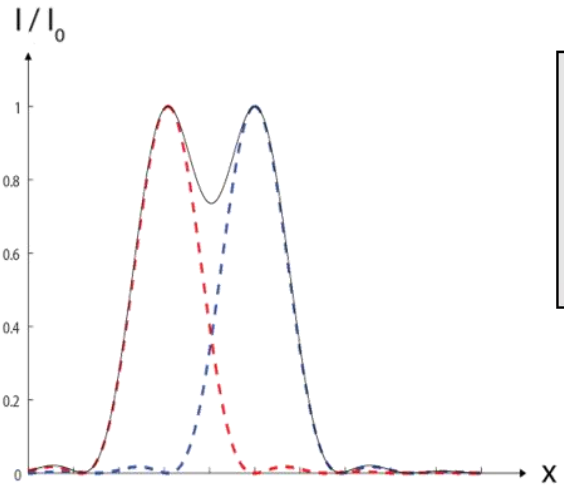

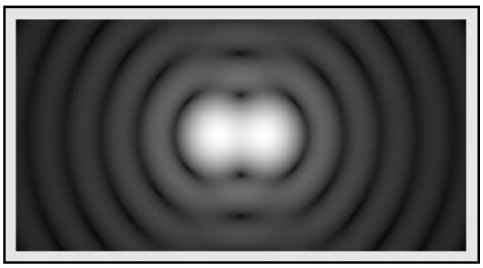

FIG. 7 – Rayleigh criterion. *The Rayleigh criterion sets the minimum distance between two resolvable points. In the frame, the projection of two 2D Airy functions at the limit condition*

1.4 Super-resolution fluorescence microscopy

The diffraction limit imposed for long time a limit on the resolution achievable by a microscope. In general, in fact, if an object is imaged using a microscope, the image produced is the result of the convolution of the object real structure and the PSF of the microscope. Therefore, the size of the PSF (see paragraph 1.3) sets the upper limit of a standard microscope. However, in the last decades, several methods have been developed to overcome this limitation and produce so-called super-resolution images. The key to overcoming the diffraction limit lies in the ability to distinguish objects that reside within the same diffraction-limited volume. Super-resolution techniques overcome the diffraction limit in many different ways: (i) by analyzing the fluctuation of the fluorescence, (ii) by collecting information from high spatial frequency, (iii) by bringing to the dark state chromophores that are in the outer region of the diffraction-limited excitation focus, (iv) by separating

the emission of individual molecules in space and time, (v) by combining some of the previous approach. This paragraph contains the explanation of the principles of the techniques in the first three groups. Techniques in the fourth and fifth groups will be explained in paragraph 1.7.

1.4.1 Overcoming the diffraction barrier by fluorescence fluctuation analysis

Super-resolution optical fluctuation imaging (SOFI) exploits the stochastic fluorescence variations of single dyes in time. Such variations originate from changes in photoblinking, polarization or brightness [10]. The key to resolution enhancement by SOFI is that fluorescent molecules fluctuate stochastically and independently of each other if they are separated by an average distance > 10 nm. To quantitatively measure the temporal fluorescence fluctuations, SOFI uses correlation analysis on the acquired videos. Considering the fluorescence from close by emitters, the recorded signal of each pixel of the camera is the sum of emission of several nearby single emitters. As shown by the authors in the original work, second-order autocorrelation function

$$G_2(\vec{r},\tau) = \langle \delta F(\vec{r}, t+\tau) \cdot \delta F(\vec{r}, t) \rangle_t \,, \tag{1.8}$$

calculated from the intensity fluctuations $\delta F(\vec{r})$ recorded by each pixel, is proportional to the squared PSF, thus increasing the resolution of the imaging system by a $\sqrt{2}$ factor. In principle, higher orders analysis can be performed transforming the nth-order correlation function into the nth-order cumulant functions (to eliminate lower orders cross-terms). It is possible to demonstrate that this provides a $\sqrt{n}$ factor enhancement of the resolution at the cost of very large dynamic intensity range, that reduces the apparent information contained in the final SOFI image. SOFI has been combined with PALM (see paragraph 1.7.1) to increase the achievable resolution [11].

Inspired by SOFI, super-resolution radial fluctuation (SRRF) microscopy, exploits the radiality of the fluorescence emission of each molecule in combination with temporal analysis in order to improve the lateral resolution [12].

The main advantage of SOFI and SRRF techniques is that they do not require complicated optical solution, high illumination intensity or specific optimization of the photophysics of the chromophore. To generate an image with resolution over the diffraction limit, techniques based on fluctuation analysis require the acquisition of relatively short sequence (< 1000 s) of standard fluorescence images. Working with low excitation intensity, these techniques are compatible with imaging of living samples. Thus, SOFI and SRRF represent optimal tools for *in vivo* super-resolution.

1.4.2 Accessing high spatial frequencies to increase the resolution

In paragraph 1.3 it has been explained how the inherent filtering of high spatial frequencies operated by any imaging system limits the achievable resolution.

In structured illumination microscopy (SIM), the sample is excited by a series of standing spatially modulated intensity profiles with different orientations or phases to increase the spatial frequencies detectable by the microscope [13]. The diffraction limit set a maximum spatial frequency that can be collected by a standard microscope. This order is $k_0 = 2\mathrm{NA}/\lambda_{em}$, where NA is the numerical aperture of the microscope and λ_{em} the wavelength of the emission. SIM extends the microscope resolution by moving higher spatial frequencies to the observable region in the form of moiré fringes. Moiré fringes are produced by frequency mixing whenever two signals are multiplied. If the illumination contains a spatial frequency $\overrightarrow{k_1}$, then each sample frequency $\vec{k}$ will produce moiré fringes at $\vec{k} - \overrightarrow{k_1}$. These frequencies will be observable if $\left|\vec{k} - \overrightarrow{k_1}\right| < k_0$. For linear structured illumination microscopy, diffraction also limits the spatial frequency that can be introduced. This means that $\left|\overrightarrow{k_1}\right| \leq 2NA/\lambda_{exc} \sim k_0$, where λ_{exc} is the excitation wavelength, and that the new resolution limit can at most be doubled to $2k_0$ (**FIG. 8**). To reconstruct the final super-resolution image, SIM requires to post-process multiple images, each one acquired at a different position of the structured illumination pattern, to discern the different harmonic components. Specifically, for a 2D SIM image 9 raw acquisitions (3 translations × 3 rotations) are required, while for a volumetric reconstruction 15 raw images (5 translations × 3 rotations) are needed. In principle, it is possible to increase indefinitely the resolution limit using non-linear structured illumination to shift higher spatial frequencies in the collection cone of the objective [14].

Since SIM does not require high intensity of light, another benefit of this method is photobleaching and low phototoxicity, representing an optimal technique for imaging of living samples [15].

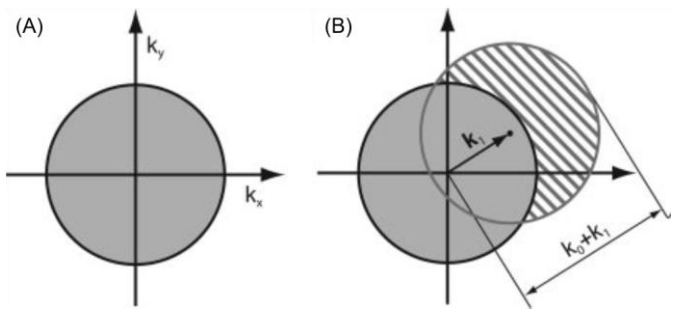

FIG. 8 – Super-resolution imaging by structured illumination microscopy. *(A) A standard microscope can only observe the spatial frequencies inside the grey circle with radius k_0. (B) If the sample is illuminated with a structured pattern that contains the spatial frequency k_1, the maximum observable harmonics shift to $k_0 + k_1$. Adapted from* [14].

1.4.3 Super-resolution imaging through stimulated emission depletion

The increase of resolution provided by methods like SOFI, SRRF and linear SIM allow to overcome the diffraction barrier, but the resolution that they provide is still limited. A different approach that permits to achieve nanometric resolution is first stimulation emission depletion (STED) fluorescence microscopy [16].

STED has been the first far-field super-resolution technique to be developed in 1994 by Stefan Hell, who was co-awarded the Nobel Prize in 2014 for his invention. In this method, a standard Gaussian beam for the excitation of the sample (OFF state to ON state) is aligned with a so-called STED beam. This beam is engineered in phase or polarization to create a doughnut-shaped focal intensity distribution. The STED beam produce the stimulated emission of excited chromophores (ON state to OFF state) and depletes the fluorescence everywhere but at its central region. Chromophores in the zero-intensity region produce spontaneous fluorescence. Fluorescence and stimulated emission can be spectrally separated. The central region of the STED beam has sub-diffraction size; therefore, super-resolved images are created by scanning the beam across the sample (**FIG. 9**). The spatial resolution is given by the size of the depleted central area of the STED beam, determined by the intensity threshold needed for the depletion. The equivalent of (1.5) for resolution limit in STED microscopy is

$$|d|_{x,y}^{STED} = d_{x,y} \frac{1}{\sqrt{1 + I_{STED}/I}} \tag{1.9}$$

where I_{STED} is the intensity of the STED beam and I is the saturation intensity of the chromophores.

According to (1.9), to get the best results in terms of resolution, depletion through stimulated emission requires the intensity of the STED beam to be high, leading to photobleaching and phototoxicity. For this, STED was thought to be incompatible with live imaging. Recent developments have demonstrated STED imaging of living samples using a pulsed excitation beam together with time-gating detection to allow a ~2–3-fold reduction of STED beam intensity [17]. Since STED is a scanning technique, the achievable temporal resolution is limited by the mechanical movement of the STED beam. Three-dimensional STED has been performed by generating a depletion illumination pattern surrounding the emitter at the focal point in all the directions, by using two opposing objectives [18] or two spatial light modulators [19].

Following the same principle of STED, reversible saturable optical fluorescence

transitions (RESOLFT) microscopy is part of the same category of super-resolution techniques [20]. The main difference with STED is that RESOLFT uses photoswitchable dyes. Photoswitchable dyes can cycle between the ON-state and OFF-state through the interaction with light at different wavelengths. Thanks to this feature, RESOLFT can overcome the diffraction barrier using a patterned illumination to modulate the fluorescence emission of molecules within the same diffraction-limited volume by cycling them between their ON and OFF states. The photoswitching cycle does not require a high intensity for the patterned beam. The use of low intensity represents a great benefit that RESOLFT technique brings over STED in the imaging of living sample and long-time acquisitions. It has been demonstrated that RESOLFT can guarantee isotropic 3D resolution of ~ 30 nm.

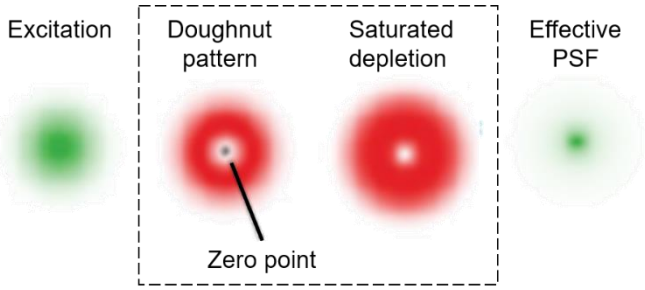

FIG. 9 - STED super-resolution microscopy. *A doughnut shaped beam stimulates the emission of chromophores outside of the zero-intensity area. This has sub-diffraction size; therefore, the effective PSF is smaller than the standard diffraction limit. Adapted from* [16].

1.5 Principles of single-molecule optical microscopy

As seen in paragraph 1.3, diffraction sets the resolution limit in conventional light microscopy. An infinitely small object is imaged as a finite size PSF. According to the Rayleigh criterion (1.6), it is possible to discriminate two simultaneously fluorescent particles if the distance between them is higher than the resolution limit. While the image of a single fluorescent particle is spread over the microscope PSF, the position of the emitter can be determined with high precision and accuracy.

Single-molecule localization microscopy (SMLM) field was born in the 1990s, when we started to localize individual fluorescence emitters, first in solution [21], and later in living cells [22]. SMLM is based on determining the position of individual chromophores in the sample with high precision by fitting the recorded PSF to a theoretical model. SMLM was first introduced for single-particle tracking (SPT) experiments. In SPT experiments, a time series of images of particles well separated in space, is recorded. The trajectories are reconstructed by localizing and identifying each individual particle throughout the sequence of images. The generated trajectories are used for investigating the molecular dynamics. Single-molecule tracking in living cells has been performed for the first time in 2000 [23], [24]. Later, the diffraction limit could be overcome by SMLM, when super-resolution

microscopy methods based on the localization of individual chromophores were introduced. In these methods, each fluorescent molecule is detected and localized with nanometric precision, and the image of the sample is reconstructed as a collection of individual localizations.

This paragraph is dedicated to explain the challenges of single-molecule detection and localization and it contains the description of the concepts of localization precision and accuracy. The next paragraphs illustrate the two main SMLM application: SPT and super-resolution imaging,

Single-molecule detection. Localization precision and accuracy

The PSF describes the image of a point-like light source obtained in a microscope (see paragraph 1.3). For most applications a chromophore can be considered as an isotropic emission source. Besides the several high precision model of 3D PSF that have been proposed, a precise comparison of localization algorithms [25] has demonstrated that a 2D Gaussian curve

$$I(x,y) = I_0 \exp\left\{-\frac{(x-x_0)^2+(y-y_0)^2}{2s^2}\right\} + b\,, \tag{1.10}$$

is a good approximation of the lateral PSF of an in-focus, isotropic, static chromophore. Here, (x_0, y_0) is the center of the curve, $I_0 = I(x_0, y_0)$ is the curve peak amplitude, s is the standard deviation of the 2D Gaussian and b is the background noise. Notably, determining the centroid of the molecule PSF by a least-squares fit on a Gaussian curve (1.10) represents a robust estimation of single chromophores lateral position [26] (**FIG. 10**).

Considering the lateral position (x_0, y_0) of an isolated fluorescent molecule, the localization precision of the x coordinate is defined as

$$\sigma_x = \sqrt{\frac{1}{n-1}\sum_{i=1}^{n}\left(x_{0,i} - \overline{x_0}\right)^2}\,, \tag{1.11}$$

where $\overline{x_0}$ is the average value of the n estimations $x_{0,i}$ of the x coordinate. Equation (1.11) can be easily adapted to describe the localization precision of the y-coordinate. Localization precision describes the spread of the position measurements around the mean value.

The single-molecule localization precision is affected by two main kinds of noise. The first one is the photon shot noise, a Poisson noise associated to the finite number of photons emitted by the emitter being localized. The second kind is the background noise, which occurs when detected photons reads do not necessarily originate from the chromophore. For the limited depth of field of a standard

microscope, the background noise is mainly due to the fluorescence coming from out-of-focus emitters. This depletes the signal-to-noise ratio (SNR). The background noise is also affected by the readout noise and the dark current of the camera.

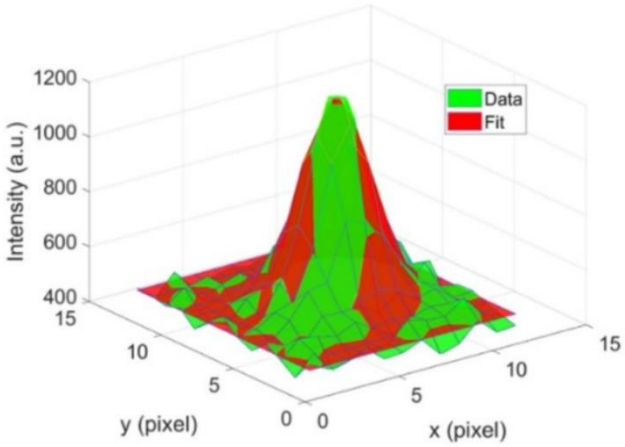

FIG. 10 - $x-y$ localization of a single chromophore. *By fitting the recorded fluorescence (green) with a 2-D Gaussian curve (red), the lateral position of the molecule is estimated as the centroid of the curve. Adapted from* [144].

Considering that the sensors used in fluorescence microscopy are single-photon sensitive, each photon collected in the image gives a measure of the position of the chromophore. For each coordinate, following (1.11), the best estimate of the single-molecule position is the average of the positions of each detected photons, with a statistical error

$$\langle \sigma_x^2 \rangle = \frac{s^2}{N}, \tag{1.12}$$

where s is the PSF standard deviation and N is the number of collected photons.

The pixelization noise comes from the finite physical pixel size a, and describes the uncertainty of the position of a single photon with respect to the pixel. Assuming $s > a$, the pixilation noise contributes to the single-molecule localization precision and (1.12) becomes

$$\langle \sigma_x^2 \rangle = \frac{s^2}{N} + \frac{a^2/12}{N}, \tag{1.13}$$

where $a^2/12$ is the variance of a top-hat distribution of size a.

To describe the single-molecule 2D localization precision while taking in account also the background noise, (1.13) must be extended to

$$\langle \sigma^2 \rangle = \frac{s^2 + a^2/12}{N} + \frac{8\pi s^4 b^2}{a^2 N^2}, \tag{1.14}$$

where b is the standard deviation of the distribution of the background noise. As stated by (1.14), the contribution of the photon shot noise to the single-molecule 2D

localization precision is inversely proportional to the number of collected photons, while the background noise contribution inversely scales with the square number of the collected photons.

A more recent and accurate model [27] sets the precision to

$$\langle \sigma^2 \rangle = \frac{16}{9}\frac{s^2 + a^2/12}{N} + \frac{8\pi b^2 (s^2 + a^2/12)}{a^2 N^2}. \qquad (1.15)$$

This general model applies assuming the isotropic emission of static chromophores at the focal plane. To take in account for more general assumptions, more rigorous methods have been developed to localize single-molecule with nanometric localization precision. Broader reviews about SMLM can be found in [28], [29].

Efficient single-molecule imaging is technically challenging, as shown by both (1.14) and (1.15). As a matter of fact, to reach high single-molecule detection capability and localization precision the number of collected photons N needs to be maximized. The photon collection efficiency is maximized using high-NA objectives. Furthermore, to optimize the detection and localization of single, fluorescent molecules, it is fundamental to minimize the background noise b. With non-specific illumination of the sample, such in widefield epi-illumination (see paragraph 1.2), the main source of background noise is the fluorescence coming from out-of-focus emitters. In this sense, light-sheet microscopy has been developed to confine the excitation of the sample in the area around the observable focal plane and consequently reduce the out-of-focus fluorescence. In Chapter 2 the different strategies specifically developed for single-molecule light-sheet microscopy will be introduced and described in details.

In [30], the authors reported that the achievable lateral localization precision through Gaussian fitting reaches ~1 nm in TIRF microscopy. In this technique, a dedicated high-NA objective illuminates the sample only around the coverslip surface using an evanescent wave. This illumination scheme reduces the background noise coming from out-of-focus emitters (see paragraph 2.2.2).

Another parameter that describes the performances of the single-molecule localization algorithm is the accuracy. An algorithm with high localization accuracy determines the position of single molecules without any bias in respect to the real location x_0. The localization accuracy is defined as

$$\Delta_x = \overline{x_0} - x_0, \qquad (1.16)$$

and it does not depend on the individual position measurements $x_{0,i}$. Therefore, the photon shot noise does not affect the localization accuracy. However, pixelization noise and background noise also limit the localization accuracy (**FIG. 11**).

As seen in paragraph 1.3, the axial PSF is difficult to model. For these reasons,

specific and optimized methods have been developed for the determination of the axial position of single chromophores in the sample, which will be illustrated in paragraph 1.8.

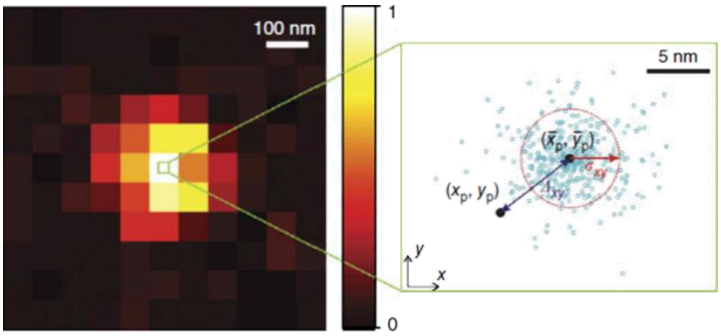

FIG. 11 – 2D Localization precision and accuracy. *From the image of a single emitters it is possible to estimate the localization precision* $\sigma_{xy} = \sqrt{\sigma_x^2 + \sigma_y^2}$ *and localization accuracy* $\Delta_{xy} = \sqrt{\Delta_x^2 + \Delta_y^2}$. *Adapted from [27].*

1.6 Single-particle tracking in biological living samples

Microscopy studies on living cells revealed a highly dynamic cellular environment in which molecular organization and interaction plays a major role. The development of SMLM offered a tool for quantitative investigation of the motion of biomolecules in living samples. Single-particle imaging and tracking (SPT) overcomes the limitation of ensemble measurement techniques (such as FRAP or FCS) and reveals the contribution and distribution of different subpopulation.

In SPT, individual molecules are imaged and localized in time. Localizations belonging to the same molecule and detected on consecutive frames are grouped into a single trajectory. The recorded trajectories are analyzed in order to extract information related to the diffusion behavior.

The most straightforward approach to analyze single-particle trajectories is to calculate the mean square displacement (MSD) over a lag time τ

$$MSD(\tau) = \langle |\vec{r}(t) - \vec{r}(t+\tau)|^2 \rangle_t \,, \tag{1.17}$$

where $\vec{r}(t) = (x(t), y(t), z(t))$ is the molecule position at time t. For a molecule diffusing with a pure random diffusion also known as Brownian motion, the means square displacement is

$$MSD(\tau) = 2nD\tau \,, \tag{1.18}$$

where n is the dimension of the localizations (2D or 3D) and D is the diffusion coefficient.

Other possible diffusion behaviors can be observed especially when molecules are confined physically, interacting with other molecules or in a flow. A more

complete characterization of different diffusion behavior based on the recorded trajectory is made by introducing the exponent α for anomalous diffusion

$$MSD(\tau) = 2nD\tau^{\alpha} . \qquad (1.19)$$

The molecule is found to be in sub-diffusion or in a super-diffusion regime for $\alpha < 1$ and $\alpha > 1$, respectively [31]. To generate the MSD curve (1.17), the trajectory of a particle is divided in sequential displacements, each one that happens after a certain lag time τ (i.e. a multiple of the exposure time of the camera that recorded the motion of the particle) (FIG. 12). However, for simplicity an apparent diffusion coefficient can be estimated by linear fitting the first points of an MSD curve, according to (1.18).

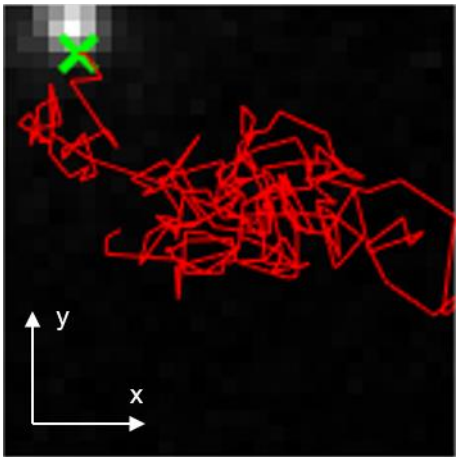

FIG. 12 – 2D trajectory of an isolated emitter. *For efficient analysis of individual biomolecules dynamics, it is crucial to reconstruct long trajectory. The picture shows the 2D Brownian motion of a fluorescent bead.*

To give a rigorous description of the motion of a molecular species, an abundant number of long trajectories needs to be recorded. The first requirement is to perform single-molecule localization with high spatial and temporal resolution. For that, a crucial step is to minimize the background noise in order to localize single molecules with high precision. The volumetric extent of the cellular environment represents the main obstacle due to the background contribution of out-of-focus emitters. Also, the limited depth of focus (1.1) and axial resolution (1.7) of a standard fluorescence microscope result in a 2D projection of the recorded trajectories. Diffusing molecules also tend to appear on a limited number of frames before moving out of focus. In the next paragraph, methods specifically developed for the 3D single-molecule localization will be presented.

The second key aspect to perform efficient imaging in the living sample is the ability to preserve cell viability throughout the acquisition. Here, photobleaching and phototoxicity are the two most critical problems that require adapted illumination strategies.

Another aspect resides in the efficient fluorescence labeling of biomolecules.

The labeling approach determines the degree of perturbation of the biological system, while the label sets the imaging wavelengths and the photon budget of the experiment. The discovery of genetically encoded fluorophores such as green fluorescent protein (GFP) and related proteins (e.g., YFP, mEOS, Dendra2) revolutionized intracellular labeling for live-cell imaging [32]. However, photon emission of fluorescent proteins is limited and they are poorly photostable. Over the past two decades a number of labeling strategies have been developed to attach chemical fluorophores to biomolecules inside cells with minimal intrusiveness. Recent development of self-labeling protein tags, such as HaloTag [33] and SnapTag [34], which can be genetically encoded in the cell and that can be targeted by organic dyes, offer a great alternative for single-molecule localization and tracking experiments in live samples. Here, organic dyes offer a brighter and more photostable fluorescence signal compared to fluorescent proteins, in addition to a wide range of emission wavelengths.

1.7 Super-resolution imaging based on the localization of individual chromophores

The high specificity of single-molecule fluorescence microscopy allows to target the structure of the sample with fluorescent biomolecules that can be individually detect and localized. Several different methods have been developed to separate the fluorescent chromophores in space and time. In this way, it is possible to localize all the molecules attached to structures of interest with high precision, and reconstruct a pointillistic map that provides a super-resolution image. For that, the density of labeling plays a crucial role. A high labeling density make impossible to find isolated fluorescent molecules and can be toxic for the sample. A low labeling density do not provide sufficient information for reconstructing the structure of the sample.

This paragraph illustrates the principle methods for super-resolution microscopy based on single-molecule localization.

1.7.1 Fluorescence photoactivation localization microscopy and stochastic optical reconstruction microscopy

A widely used approach for braking the diffraction barrier is based on single-molecule localization microscopy. The two main techniques are (direct) stochastic optical reconstruction microscopy [(d)STORM] [35], [36] and (fluorescence) photoactivated localization microscopy [(F)PALM] [37], [38]. The inventor of PALM technique, Eric Betzig, has been co-awarded Nobel Prize in 2014, with W.E. Moerner and Stefan Hell, for his contribution to the super-resolution

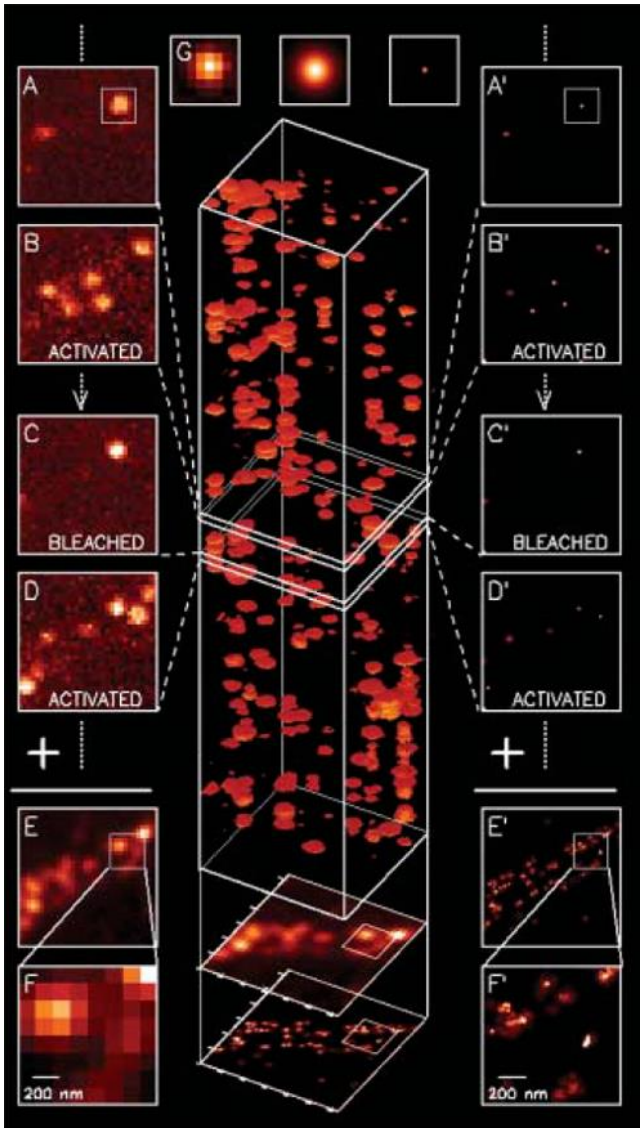

FIG. 13 – (F)PALM and (d)STORM. principle. *The panel describe the procedure for super-resolution imaging through single-molecule localization. (A) Before activation, only few molecules are in the bright ON state. (B) After activation and excitation, a stochastic group of molecules are brought to the ON state. After photobleaching (C), the activation/excitation cycle is repeated (D). The sum of all the diffracted images of isolated molecules is still a diffraction-limited image (E, F). However, an isolated molecule can be localized with nanometric precision by fitting the PSF to a Gaussian profile (G). The localization of each chromophore across all frames (A' through D') are combined to form a super-resolution image. The achievable resolution is influenced by the single-molecule localization precision. Adapted from [36].*

microscopy field. The common principle of (d)STORM and (F)PALM is to separate the emission of single molecules in space and time in order to localize their centers with high precision (see paragraph 1.5). For that, photoswitchable organic dyes or photoactivable fluorescent proteins are used in (d)STORM and (F)PALM, respectively. These kinds of chromophores can recover from the dark state after specific illumination for a certain number of times. The two terms can be used interchangeably to refer to SMLM-based super-resolution microscopy.

For both methods a high intensity illumination is required initially to drive most of the dyes to the dark state. Then, by exploiting the photophysical properties of the dyes, (d)STORM and (F)PALM stochastically switches or activates a subpopulation of chromophores that are isolated in space, driving them from the dark state to the ON state. The emitting chromophores will emit fluorescence before photobleaching or returning to the OFF state. The activation-imaging cycle is then repeated on

another subset of molecules. Thanks to sparse imaging and non-overlapping PSFs, the center of each molecule is determined with nanometric precision. This cyclic operation permits to discriminate molecules that otherwise would appear in the same diffraction-limited region. The final super-resolution pointillist image consists in the collection of all the localizations accumulated over time (**FIG. 13**), typically few tens of thousands of frames.

In SMLM-based super-resolution microscopy, high excitation intensity is used to maximize the number of photons emitted by each single dye. The use of high illumination intensities increases the probability of irreversible photobleaching the dyes. For this reason, the optimization of the imaging conditions is a crucial step in (d)STORM-(F)PALM super-resolution imaging. Indeed, a fine tune of the excitation intensity or the use of specific oxygen scavenger imaging buffer is required. SMLM-based super-resolution microscopy was later extended to the third dimension thanks to a large panel of imaging techniques that are summarized in paragraph 1.8.

1.7.2 Point Accumulation for Imaging in Nanoscale Topography and DNA-PAINT

An alternative strategy that permits to detect isolated fluorescent molecules in SMLM is point accumulation for imaging in nanoscale topography (PAINT). In PAINT, the imaging medium contains fluorescent dyes in solution that continuously and transiently bind to the sample [39]. Although all the chromophores are excited and emit light, their fast diffusion blurs their emissions. During a camera exposure, only the photons from bound dyes accumulate on the sensor producing clear PSFs. This permits to isolate single-molecules in space and time. The binding rate depends on the diffusion coefficient. When a molecule dissociates it goes back in the solution.

This method has been further developed to introduce binding specificity to labeled biological structures. For that, DNA nanotechnology has been used to develop DNA-PAINT [40], establishing a programmable target-probe interaction system. A DNA-PAINT system is composed by a docking strand, which binds the sample structure thanks to antibody (AB) labeling, and the complementary DNA-conjugated imager strand, which carries the chromophore (**FIG. 14A**). The DNA sequence determines the binding time between the docking and the imager strands. By combining immunofluorescence labeling strategies with AB-conjugated docking strands, DNA-PAINT provides high labeling specificity of (**FIG. 14B**).

Thanks to the short duration of the binding, apparent blinking of the dyes is decoupled from their photophysics, maximizing the photon budget. Also, photobleaching does not constitute a limitation in DNA-PAINT imaging thanks to the enormous number of chromophores in the solution. As such, DNA-PAINT methods

can be used for very long acquisitions. The optimized photon budget of DNA-PAINT allows to achieve nanometric localization precision and resolution. On the other side, the continuous diffusion of emitting dyes in the solution results in a high background noise if the illumination during the acquisition is not adapted.

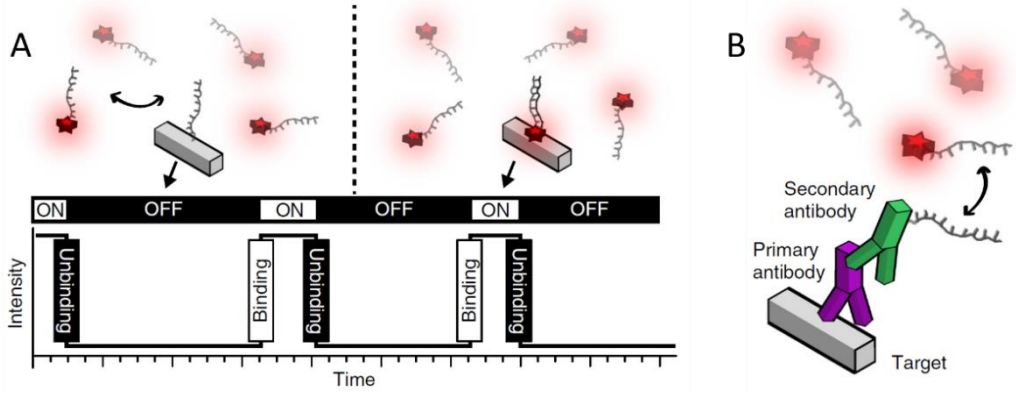

FIG. 14 - DNA-PAINT. (*A) DNA-PAINT concept. Transient binding of dye-labeled DNA strands (imagers) to their complementary target sequence (docking site) attached to a molecule of interest. The transient binding of imager strands is detected as 'blinking', illustrated by the intensity versus time trace. (B) protein-labeling strategy for DNA-PAINT using primary and DNA-conjugated secondary antibodies. Adapted from* [40].

1.7.3 Single-molecule localization by minimizing fluorescence flux

The most recent development for super-resolution microscopy is MINFLUX [41]. As shown before the emission of a single photon is sufficient to detect and localize a single fluorescent molecule. If the excitation beam presents a doughnut shape with a central (ideally) zero-intensity region, the detection of a single photon would be sufficient to know that the molecule position is not at the center of the doughnut excitation. In other words, the location of the molecule can be determined with high precision if the excitation donut is exactly centered on the molecule such as no photon is detected. performed with no photons needed if the center of the doughnut overlaps precisely the molecule. This is the basic principle of MINFLUX,

This technique combines the strengths of patterned illumination-based and single-molecule localization-based methods to reach molecular resolution. Similar to (d)STORM-(F)PALM, the stochastic photoswitching of dyes in MINFLUX is used to isolate individual chromophores. As in STED, MINFLUX uses a patterned beam with a (ideal) zero-intensity central region to excite the chromophores. While in STED the doughnut-shaped beam is intended to stimulate the emission depletion of the fluorescent dyes, in MINFLUX it is used to modulate the fluorescence excitation intensity. In practice three different positions of the doughnut intensity profile are

necessary to localize a chromophore (FIG. 15). To validate the predicted localization, a fourth measurement in which the excitation beam is centered on the predicted position of the molecule is performed.

MINFLUX allows nanometric localization of one molecule at a time. Thanks to a fast scan of the excitation patterned, the frequency of single-molecule localization can go up to 8 kHz. In contrast to other super-resolution methods, chromophores are localized in MINFLUX with high precision when no fluorescence is detected, thus MINFLUX does not require high excitation intensities. This represents a clear benefit in reducing photobleaching and phototoxicity. Thanks to its high resolution in space and time and the reduction of photobleaching, MINFLUX can be used for particle tracking in living samples [42]. By using a 3D doughnut patterned-illumination, MINFLUX has been used for volumetric and multicolor imaging [43].

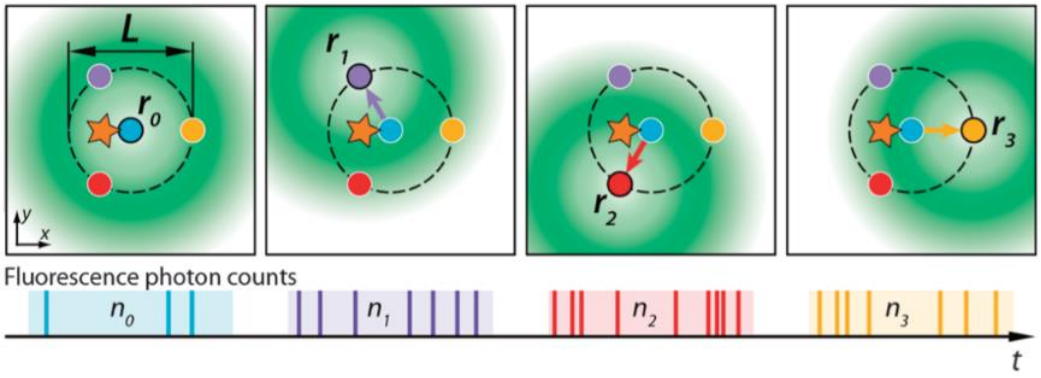

FIG. 15 - Localization of single emitter through MINFLUX. *The intensity-shaped excitation beam (in green) is modulated and deflected such that the zero-intensity region is sequentially placed at* r_0, r_1, r_2, r_3. *The respective fluorescence fluxes* n_0, n_1, n_2, n_3 *are registered and used to extract the molecular location. Adapted from* [41].

1.8 Single-molecule 3D localization

As seen in paragraph 1.3, the resolution along the optical axis of a standard fluorescence microscope is roughly two-fold worse than in the lateral dimension [44]. In fact, as seen in the $x - z$ projection, the PSF lateral width changes slowly near the focal plane (FIG. 5B). Moreover, in the absence of aberrations, the PSF is symmetric around the focal plane. The standard 2D PSF size is thus not sufficient to determine the z position of the emitter. The most direct approach to perform volumetric imaging is to acquire sequential 2D images of different object planes. This method does not provide high temporal resolution, restricting the observable range of molecular dynamics (see paragraph 1.6). Also, the photophysics of chromophore emission is much faster than the mechanical scan and the emitters can bleach during the z stack acquisition.

Several methods have been developed for 3D imaging at the single-molecule level to provide precise axial localization. These methods can be classified in different categories, according to the optical principle that they exploit. In multiplane methods the 3D PSF is sampled on multiple focal planes simultaneously while in PSF engineering methods the PSF of the microscope is precisely altered to encode the axial position in the recorded shape. Other methods determine the position of the molecule by exploiting different properties of the light such as intensity gradient of the excitation and emission, refraction of the fluorescence at the interface with the coverglass, or the self-interference of the emitted signal. For exhaustive reviews on 3D single-molecule localization methods, see [45], [46].

1.8.1 Multiplane methods

In multiplane methods, a standard fluorescence microscope is modified to image simultaneously multiple planes without mechanical movement. It provides high temporal resolution, limited only by the brightness of the chromophores and the acquisition rate of the camera. In multiplane methods the PSF of each chromophore is sampled simultaneously at several focal planes. In the first implementation of multiplane imaging, the fluorescence was split in different channels using beam splitters and sent simultaneously on different cameras at different distances from the tube lens, thus conjugated to a different focal plane[47]. Another approach allows the images of the different planes to be refocused on same camera by using refocusing lenses of different focal length [48], custom-made multi-plane prism [49], or dichroic mirrors to form separated detection paths of different length that conjugate the camera with two distinct planes of the sample[50].

In single-molecule applications high-NA objectives are typically used to maximize the number of emitted photons. However, the use of high-NA objectives would introduce significant spherical aberration in the refocused fluorescence light. For the method that we developed during this PhD project, we adopted MultiFocus Microscopy (MFM) [51]. MFM uses a high-NA objective and corrects for the spherical aberration. It will be described in details in paragraph 3.1.

1.8.2 PSF engineering methods

The shape of a standard PSF makes it difficult to determine the z coordinate of the chromophore from a single image (see paragraph 1.3). In PSF engineering methods, a precise axial localization is produced by encoding the distance of the chromophore from the focal plane in the shape of the microscope PSF. To minimize

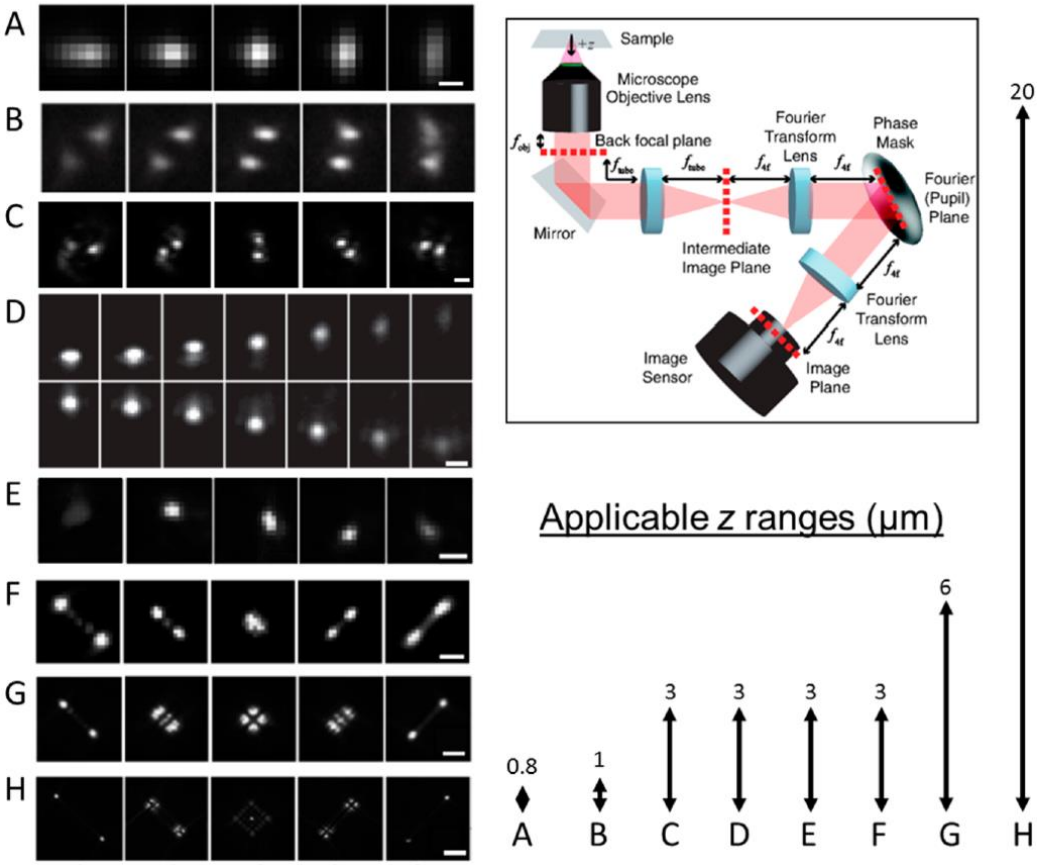

FIG. 16 – Comparison of PSF engineering methods. *In the top-right frame it is the optical scheme of a PSF engineering by phase modulation setup. A relay system originates a Fourier plane, on which it is placed the optical phase modulator. (A) Astigmatism, scale bar* ~0.5 *μm. (B) Phase ramp. (C)* Double helix, scale bar 2 *μm. (D) Self-bending PSF (split onto two camera regions), scale bar* 1 *μm. (E) Corkscrew, scale bar* 1 *μm. (F) A 3 μm range tetrapod, also known as saddle-point, scale bar* 1 *μm. (G) A 6 μm range tetrapod, scale bar* 2 *μm. (H) A 20 μm range tetrapod, scale bar* 5 *μm. The bottom-right corner shows the range of application of the different methods. Adapted from [44].*

the photon loss, in single-molecule fluorescence microscopy, the encoding of the chromophore z position is produced mainly by phase-only modulation of the PSF. The first implementation of PSF phase modulation has been performed by introducing a cylindrical lens on the emission path of a microscope to induce astigmatism. As a consequence, the lateral PSF becomes elliptical and the observed ellipticity changes as a function of the emitter axial position [52], [53]. Astigmatism has been used for 3D (d)STORM super-resolution imaging [54].

For more precise applications, PSF engineering can be performed by placing an optical phase modulator in the microscope Fourier plane, conjugated to the objective back focal plane (BFP). Such optical conjugation guarantees that the same modulation is produced over the whole field of view. The intensity of the electromagnetic field at the image plane is

$$I(u,v;x,y,z) \propto |F\{E(x',y';x,y,z)\cdot P(x',y')\}|^2 , \qquad (1.20)$$

where $E(x', y')$ is the electric field at the objective BFP generated by a point-like source at (x, y, z) relative to the focal plane and optical axis, $P(x', y')$ is a phase pattern imposed by the optical phase modulator and F represents the 2D Fourier transform. According to (1.20), an axial (z) displacement of the emitter from the focal plane is equivalent to the curvature in the phase of $E(x', y')$, and the phase pattern $P(x', y')$ modulates $E(x', y')$ in the image $I(u, v)$. The goal of PSF engineering is to choose a pattern $P(x', y')$ such as the amount of phase curvature, and thus z, is easily and precisely determined.

This approach has been exploited in many works, introducing various phase patterns to explore different z ranges. Together with the already mentioned astigmatic pattern, engineered PSF shape include rotating double-helix PSF [55], [56], corkscrew PSF [57], phase ramp PSF [58], self-bending PSF [59], and saddle-point/tetrapods PSF [60], [61] (**FIG. 16**).

Normally, in these methods, the phase pattern is optically introduced by a programmable liquid crystal spatial light modulator (SLM). SLM have a big number of pixels and can introduce complex phase pattern, but their functioning depends on the light polarization. To avoid this limitation, alternative method relies on a deformable mirror (DM) conjugated to the BFP of the objective that introduce simpler phase pattern with no photon loss. The efficiency of DM for astigmatic PSF engineering has been demonstrated in single-particle tracking and super-resolution experiments [62].

Methods based on PSF engineering determines the z position of each emitter from a specific feature appearing in the recorded image. The most common procedure is to identify such feature and generate precise calibration curves relating it to the z coordinate. Another approach relies on determining 3D model functions of the observed PSF [63]. This procedure can improve the localization precision but it is more complicated to perform due to the multiple 3D model functions that can be used.

1.8.3 Intensity-sensing methods

This class of methods uses the intensity profile of the excitation light to determine the z coordinate of the fluorescent molecules in the sample.

Assuming that all the chromophores have constant quantum yield and extinction coefficient, the fluorescence from each single-molecule depends only on the excitation. In this case, the relative axial position of each chromophore can be extracted from the fluorescence intensity if it shows a well characterized axial profile.

The first example of this approach made use of the evanescent field at the coverslip surface produced in total internal reflection fluorescence microscopy

(TIRF) [64] (see paragraph 2.2.2). The intensity of the TIR evanescent field decrease exponentially with the distance z from the coverslip surface as

$$I = I_0 \exp\left[-\frac{4\pi n z}{\lambda}\sqrt{\left(\frac{\sin\theta_i}{\sin\theta_c}\right)^2 - 1}\right], \tag{1.21}$$

where I_o is the excitation intensity at the coverslip surface, n is the refractive index of the coverslip, λ is the excitation wavelength (in vacuum), θ_i and θ_c the incident and critical angles, respectively. As a consequence, the emitters fluorescence intensity decreases with their distance from the coverslip. Therefore, it is possible to determine the relative z coordinate of each emitter from the expected excitation intensity (1.21) over a volume 250 nm axial range.

To extend the observable range, the same principle has been used to develop a confocal-based design for observing individual quantum dots (QDs) and gold nanoparticles, over a 10 μm axial range [65], [66]. In fact, the intensity of confocal illumination

$$I \propto \exp\left[-2r^2\,\frac{1 + z^2/z_R^2}{w_0^2}\right], \tag{1.22}$$

has a strong axial gradient, being r and z the in-plane and axial distances from the focus, w_0 the waist and z_R the Rayleigh distance of the beam. This method is designed for tracking a single particle at a time.

Recently, an innovative widefield method based on axial modulation of the excitation beam intensity has been developed for the axial localization of single chromophores (MODLOC) [67]. In MODLOC, the excitation light at the wavelength λ and angular frequency ω is modulated by interfering two tilted laser beams. The angle α between the two beams determines the fringe periodicity Λ and the angle θ between the fringes and the optical axis. The fringes are displaced with known steps while recording the emitted intensity of the same molecule. A lock-in amplifier measures the phase shift ϕ between the local oscillator and the detected signal. In the MODLOC configuration, an additional phase shift that depends on the lateral position x of the emitter is introduced as a consequence of the tilted interference pattern. The definitive axial position of the emitters can be determined as

$$z = \frac{\lambda\phi}{4\pi n \sin(\alpha/2)\sin(\theta)} - \frac{x}{\tan(\theta)}. \tag{1.23}$$

This method was used for in deep (up to 30 μm) super-resolution imaging of microtubules, clathrin and mithocondria, allowing to record the axial position of the chromophores over 700 nm.

A gradient excitation, in the shape of a 3D doughnut, has been used for performing 3D MINFLUX (see paragraph 1.7.3) [43]. With this technique, isotropic, 3D localization precision of ~3 nm has been reached.

1.8.4 Interface-sensing methods

In contrast to previous methods, this class of localization method relies on the coupling of the single molecule fluorescence emission to the coverslip.

A first example in this class of methods is given by supercritical angle fluorescence (SAF) microscopy [68]. This method relies on the coupling of the near field fluorescence emission to the interface of the coverslip when single emitters are at distances bellow the emission wavelength. In fact, fluorophores emit both a far-field and a near field fluorescence. The first one is propagative and the second one is evanescent that decays rapidly away from the molecule and thus does not reach the camera if the molecule is far from the coverslip. However, if the molecule is positioned at a distance bellow the emission wavelength from the coverslip, and thanks to the higher refractive index of the coverslip compared to the biological sample, a part of the emitted evanescent field can be coupled to a propagating wave. It propagates above the critical angle and can be collected with high-NA objectives (NA>1.4). As the evanescent wave exhibits an exponential decay, the amount of coupled and thus measured emission intensity depends on the axial position of the molecule from the coverslip. As such measuring the amount of light that propagate above the super-critical angle allow to determine the axial position of the molecule in the vicinity of the coverslip. In practice, the ratio of SAF to undercritical angle fluorescence (UAF) determines the axial localization of the emitters (FIG. 17). To

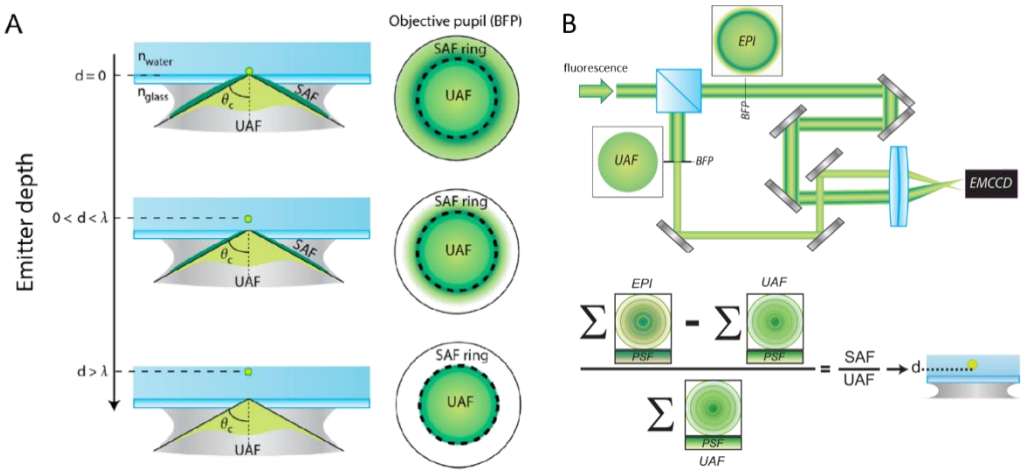

FIG. 17 – SAF microscopy. *(A) According to the emitter depth d in the sample, it is possible to collect the supercritical flurescence by using high-NA objective if $d < \lambda$. (B) The SAF signal can be determined as the difference between the total emitted fluorescence (EPI) and the UAF signal. The ratio of SAF to UAF presents a strong axial gradient. Adapted from* [68]

discriminate between the two contributions, the light is divided into two paths. In one of the paths an annular filter is placed on a plane conjugated to the back focal plane of the objective to block the supercritical component [69]. The two images are later compared to retrieve the axial position of each molecule. This method allowed nanometric imaging of living sample and it has been further developed for super-resolution imaging [70], [71].

1.8.5 Interference-sensing methods

A different approach uses the phase of single-molecule emitted fluorescence wavefront to determine the axial position through interferometry. The light emitted from a chromophore is self-coherent, thus it can be interfered with itself to sense the relative phase delay between different optical paths. The first realization of chromophores axial localization through fluorescence self-interference was performed by using two opposed objectives collecting the forward and backward emission. The fluorescence was self-interfered in a 4-channel [72] or 3-channel (iPALM) [73] configuration using specific beam-splitters. In such kind of configurations, a displacement δ of the emitters along z in a sample of refractive index n will produce a total phase shift $\Delta\phi = 4\pi n\delta/\lambda$ between the forward and backward optical path. The interference of the two optical paths generates a PSF with standard $x - y$ shape but with intensity that varies sinusoidally compared to the z position of the emitter. This method allows axial localization of a chromophore with extremely high precision of few nanometers, but over a restricted $\lambda/2n$ axial range.

A different method for axial localization based on self-interference of fluorescence is called SELFI [74]. This method uses a phase-only diffraction grating to generate the self-interference of fluorescence. The fluorescence of each chromophore is split in multiple diffraction orders (first four orders contain the 66% of the total energy) that interfere reciprocally in the image plane. In SELFI, the interference pattern and the total intensity of self-interference fluorescence are collected simultaneously to provide isotropic nanometric localization precision over a volume extended 600 nm around the focal plane (**FIG. 18**).

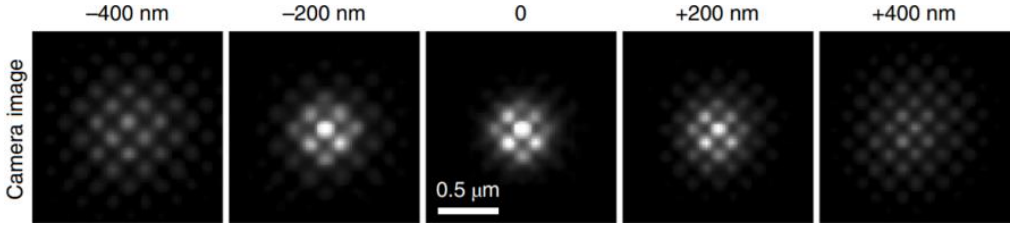

FIG. 18 – SELFI method discerns the axial position of a chromophore from the self-interfered fluorescence. *In SELFI, the interferograms are generated using a phase-only diffraction grating. Adapted from* [74].

Efficient imaging of individual molecules in the volume of the sample must provide high spatial and temporal resolution. In this chapter the challenges of performing single-molecule imaging in volumetric biological sample have been presented. Single-molecule fluorescence microscopy applications such SPT and super-resolution imaging are based on determining with high precision the position of isolated chromophore in the sample. Achieving high signal-to-noise ratio is crucial to be able to detect and precisely localize single biomolecules. For this reason, it is crucial to excite selectively the sample to reduce the background noise from out-of-focus emitters. In Chapter 2 methods for producing selective excitation for single-molecule applications are described in details.

Chapter 2

Selective illumination methods for fluorescence microscopy at the single-molecule level

The development of single-molecule fluorescence microscopy, in combination with optimized strategies for specific labeling of biomolecules, represented an enormous breakthrough for the investigation of molecular mechanisms in biological systems. A pressing issue resides in extending such investigations into multicellular organisms, which in turn raises additional challenges.

When imaging thick samples, such as cell colonies or tissue, their inherent volumetric extension represents the first obstacle for performing efficient SMLM. The fluorescence arising from out-of-focus emitters originates a high background noise that limits the single-molecule sensitivity of the imaging system and reduces the localization precision. This is especially true when imaging samples in all three dimensions through standard epi-illumination. Reducing the number of chromophores in the sample does not represent a definitive solution. Sufficient labeling density is in fact required to extract high-resolution spatial information from the sample, according to Nyquist criterion [75].

A second issue with 3D imaging is photobleaching. Using conventional widefield microscope can result in a premature photobleaching of fluorophores in sections of the sample that have not yet been imaged. This can impact the reconstruction quality and in the worst case completely hinder imaging the rest of the 3D structure.

As seen in paragraph 1.1, phototoxicity represents a third problem, especially when performing imaging of living samples. In fact, the use of high intensity excitation increases the risk of photodamage, thus perturbing the physiological condition of the specimen.

Tailoring the illumination represents the gold standard to reducing the background noise that originates from out-of-focus emitters. The specific excitation

of the sample also permits to use lower excitation intensity.

In the first part of this chapter, the main characteristics of the propagation and focusing of a coherent Gaussian laser beam are described. This introduction helps to fully understand the following parts of the chapter, in which different approaches for selective excitation are presented, with an emphasis on single-molecule imaging applications.

2.1 Characteristics of a focused Gaussian beam

Single-molecule fluorescence microscopy requires intense, near monochromatic illumination, such provided by a laser. The output of most lasers is described by the fundamental transverse Gaussian mode TEM00. The light of a laser is coherent and its propagation and collimation are well described by Gaussian beam optics. Such a Gaussian beam can be focused into the most concentrated spot.

The irradiance intensity of a Gaussian beam distributes according to

$$I(r) = I_0[w_0/w(z)]^2 \exp[-2r^2/w(z)^2]\,, \tag{2.1}$$

where r and z are the radial and axial distance from the propagation axis of the beam respectively, w_0 is the minimum radius size of the beam, known as waist, and $w(z)$ is the radius of the beam after propagating z distance along the optical axis. The radius of the beam is measured from the center of the Gaussian profile to I_0/e^2 intensity. Due to diffraction, the intensity profile diverges as the beam propagates. In the paraxial approximation the beam divergence θ is small and, λ being the wavelength of the radiation, the radius of the beam is given by

$$w(z) = w_0\sqrt{1+\left(\frac{\lambda z}{\pi w_0}\right)^2}\,, \tag{2.2}$$

in which the beam waist is

$$w_0 = \frac{\lambda}{\pi\theta}\,. \tag{2.3}$$

We define the Rayleigh length

$$z_R = \frac{\pi w_0^2}{\lambda} \tag{2.4}$$

such as $w(z_R) = \sqrt{2}w_0$, the distance over which the beam can propagate without diverging significantly (**FIG. 19**).

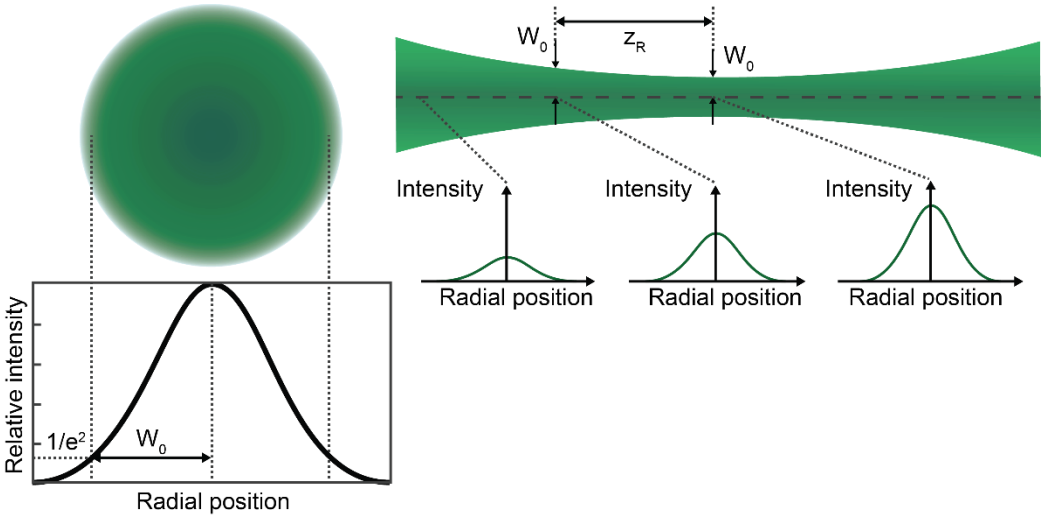

FIG. 19 – Propagation of a Gaussian beam. *The waist w_0 of the beam is defined as the position at which the maximum intensity is multiplied by $1/e^2$. The Rayleigh distance z_R defines the length over which the beam does not diverge significantly. The beam intensity decreases with the distance from the waist*

Following the thin lens approximation of linear optics, it is possible to describe the behavior of a Gaussian beam when a lens is placed on its optical path. Let us consider a lens with focal length f and a Gaussian beam with waist w_0 and Rayleigh distance z_R. If s is the distance between the lens and w_0, it is possible to demonstrate that the waist of the beam after the lens is

$$w_0' = w_0 \frac{f}{\sqrt{(s-f)^2 + z_R^2}}. \tag{2.5}$$

Equation (2.5) says that the focused beam waist can be minimized by reducing the f and $f - s$. In most of the case, the lens is placed so that the beam waist is very close ($s \ll z_R$) or very far ($s \gg z_R$) from it. In both these cases, for a collimated beam the focused spot is at a distance f from the lens. Although it is not possible to perfectly collimate a Gaussian beam with a certain waist, it is possible to minimize its divergence. For that, the lens has to be placed at a distance $s = f$ from the waist of the beam.

As stated by equation (1.2) in paragraph 1.3, a lens performs a Fourier transformation of the incoming electromagnetic field. This means that focusing a Gaussian beam at the BFP of a lens produces a collimated beam. Moreover, if the Gaussian beam is focused on the lens BFP at a certain distance from the optical axis, the collimated beam is tilted at the output of the lens. In a symmetric way, a collimated beam is focused by the lens in a point of the front focal plane (FFP), at a distance equal to the focal length of the lens, and if the collimated beam is incident on the lens with a certain angle then the focus point is translated with respect to the optical axis (**FIG. 20**).

This principle has been exploited to developed techniques for producing selective excitation as shown in the next paragraphs.

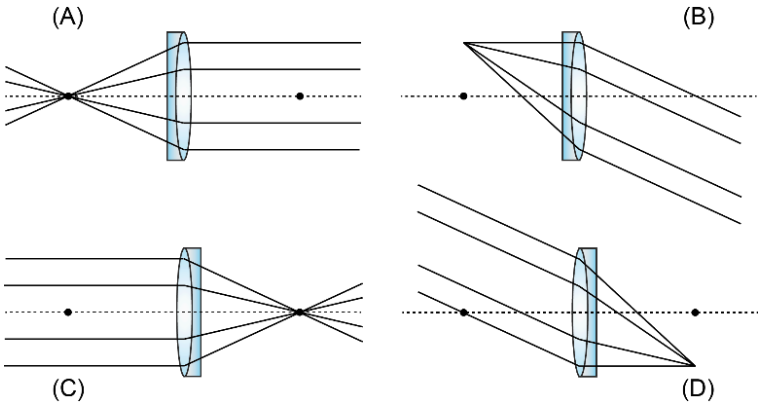

FIG. 20 – Fourier transformation by a lens. *For simplicity, the picture uses geometrical optics representation. (A) and (B) the different angles at the BFP result in different positions at the FFP. (C) and (D) the different positions at the BFP result in different angles at the FFP.*

2.2 Selective widefield excitation strategies

The most straightforward excitation scheme in fluorescence microscopy is epi-illumination. When a Gaussian beam is focused at the center of the back focal plane of the illumination objective, wide-field excitation of the sample is produced. In this way the whole volume of the specimen is excited, leading to a high background noise from out-of-focus emitters (FIG. 21A)

However, by using a single high-NA objective, it is possible to tailor the illumination so that the excitation volume is limited and the out-of-focus fluorescence is reduced. To tailor the illumination, the excitation beam has to be focused at different position on the back focal plane of the objective.

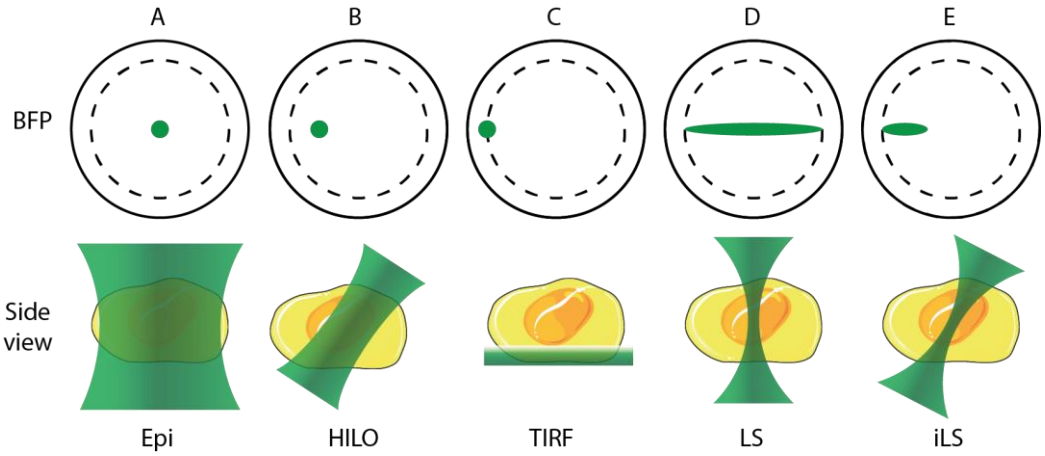

FIG. 21 - Selective excitation by focusing a Gaussian beam at different position on the back focal plane of the illumination objective. *Taking advantage of the Fourier transformation produced by the objective, the picture show how selective excitation is produced when the illumination beam is focused at different position on the BFP of the objective.*

2.2.1 Highly inclined and laminated optical sheet microscopy

Highly inclined and laminated optical sheet (HILO) microscopy [76] represented a primitive optical sectioning strategy with a single high-NA objective. In HILO, the excitation Gaussian beam is focused on a spot on the back focal plane of the illumination objective at a certain distance from the optical axis of the lens. As a consequence, the excitation beam exits the objective inclined compare to the optical axis (**FIG. 21B**). If the Gaussian beam is focused on the back focal plane of the objective at a distance d from its optical axis, it gets tilted compared to the optical axis of the objective by

$$\theta_i = \arcsin\left[\frac{d}{nf_{obj}}\right], \tag{2.6}$$

where n and f_{obj} are the refractive index of the objective immersion medium and the focal length of the lens respectively.

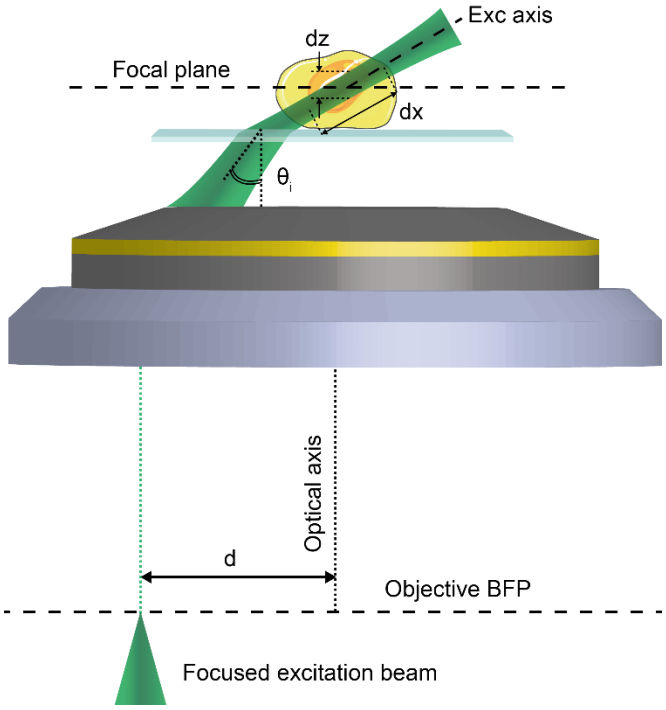

FIG. 22 – HILO selective illumination. *In HILO, a highly inclined and laminated optical sheet of light is used to confine the excitation to a smaller portion of the sample volume. However, the optical sectioning is limited by the physical properties of the objective.*

With reference to (**FIG. 22**), if the waist of the Gaussian beam after the objective is w_0 and m is the refractive index of the sample (aqueous medium) it is possible to demonstrate [77] that the thickness of the inclined illumination and the confocal parameter defining the length over which the divergence of the beam is limited, are

$$dz = 2w_0 \sqrt{\frac{1-\left(\frac{d^2}{m^2 f_{obj}}\right)^2}{1-\left(\frac{d^2}{n^2 f_{obj}}\right)^2}}, \tag{2.7}$$

$$dx = \frac{2\pi}{\lambda} w_0^2 \frac{1-\left(\frac{d^2}{m^2 f_{obj}}\right)^2}{1-\left(\frac{d^2}{n^2 f_{obj}}\right)^2}. \tag{2.8}$$

Equations (2.7) and (2.8) demonstrate that, for certain physical characteristics of the objective, the distance d from the optical axis of the focused spot on the back focal plane of the illumination objective sets the optical sectioning size. The intensity can be considered constant over the limited length set by the confocal parameter. Moreover, the intensity of the inclined excitation beam decreases with the incident angle, and thus with d. In practice, this limits the optical sectioning power to be several microns thick. Another limitation of HILO microscopy is due to the angle mismatch between the inclined beam and the detection plane, which critically reduces the observable field of view.

2.2.2 Confining the excitation through total internal reflection

In the previous paragraph we have seen that focusing the excitation beam on the back focal plane of the objective at a certain distance from the optical axis of the lens produces an inclined illumination. In total internal reflection fluorescence (TIRF) microscopy [78], the beam is focused near the edge of the objective back focal plane (**FIG. 21C**). The objective tilts the Gaussian beam that is incident on the coverslip surface with an angle θ_i defined compared to the optical axis of the objective. According to the Snell's law, when the beam crosses an interface to a smaller index of refraction medium (the interface between the coverglass and water) the refraction angle becomes larger. Therefore, it is possible to define a critical angle $\theta_c = \arcsin(n/n_G)$, above which the beam is totally reflected and only an evanescent wave exists at the interface. Here, n and n_G are the refractive indices of the sample medium and the coverglass respectively. In this case, a transvers evanescent field that can excite the sample at the interface is generated. Recalling equation (1.21) in paragraph 1.8.3, the intensity of the evanescent field is

$$I = I_0 \exp\left[-\frac{4\pi n z}{\lambda}\sqrt{\left(\frac{\sin\theta_i}{\sin\theta_c}\right)^2 - 1}\right],$$

where λ is the excitation wavelength. The penetration depth of the evanescent field is

$$z = \frac{\lambda}{4\pi} \frac{1}{\sqrt{n_G^2 \sin^2 \theta_i - n^2}}, \tag{2.9}$$

which typically is < 300 nm (**FIG. 23**).

By exploiting the evanescent field at the coverslip-sample interface, TIRF microscopy confines the illumination to a limited basal section of the sample, knocking down the background fluorescence. The excitation is more efficiently confined in TIRF than in HILO. Thus, typically, the achievable signal-to-noise is higher using TIRF microscopy. As a drawback, the low penetration power of the evanescent field limits the depth imaging capabilities of TIRF microscopy. This technique is limited to the observation of samples close to the coverslip surface.

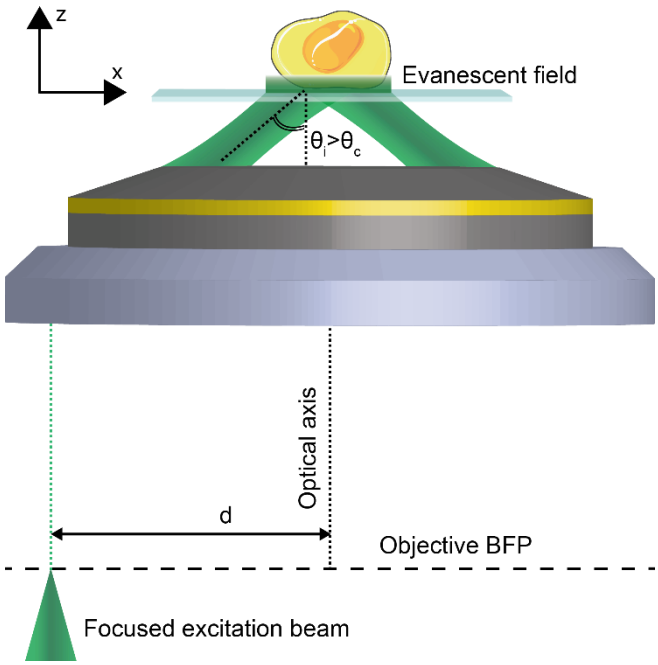

***FIG. 23* - Selective excitation through evanescent field in TIRF microscopy.** *Due to the refractive index mismatch between the immersion medium of the objective and the coverslip, an evanescent electromagnetic field originates at the separation surface in the case of total internal reflection. The evanescent field decays quickly in z, the excitation is then confined to the region close to the coverslip surface.*

2.3 Selective illumination through light-sheet microscopy using two objectives

In the previous paragraph we have seen how shifting the focused spot over the back focal plane of a high-NA objective produces confined excitation of the sample.

However, the edge of the back pupil represents the physical limit of this approach, and, in this case, the selective excitation reaches only a portion of the sample in the close proximity of the coverslip. Therefore, to improve optical sectioning away from the coverslip it is necessary to add a second lens. This is the fundamental idea of selective plane illumination microscopy (SPIM) [79]. Thanks to two lenses arranged with orthogonal optical axes, the excitation beam can be confined to a thin sheet of light, positioned at the focal plane of the second lens. The second lens is dedicated to collecting the fluorescence (**FIG. 24**). This design minimizes the background fluorescence from out-of-focus emitters. Also, it eliminates the angle mismatch between the illumination and the focal plane of the collection objective that limits the efficiency of HILO technique. Originally, SPIM, was designed for low-magnification imaging of large samples such *Drosophila* embryos and the illumination lens was a simple cylindrical lens. Nowadays, a common strategy for confining the excitation is represented by digital scanned laser light-sheet [80], in which a focused Gaussian beam is laterally scanned over the back pupil of the illumination objective (**FIG. 21D**).

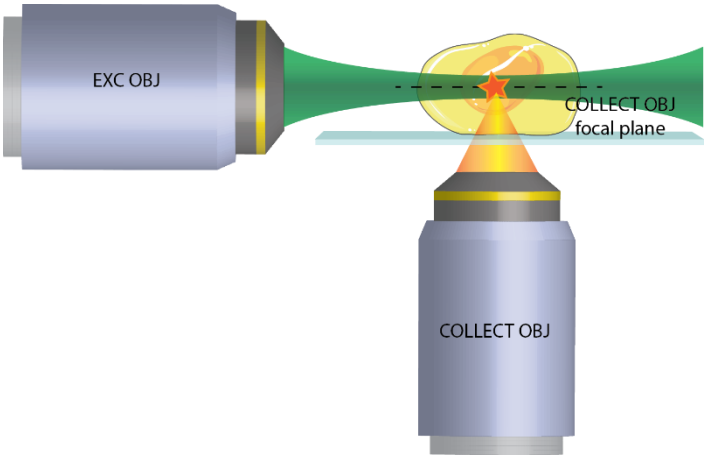

FIG. 24 – Selective Plane Illumination Microscopy (SPIM) with two perpendicular objectives. *The EXC OBJ confines the illumination in a thin light-sheet placed at the focal plane of the COLLECT OBJ that collects the fluorescence.*

To exploit light-sheet excitation for single-molecule fluorescence microscopy, it is fundamental to use high-NA objectives. In fact, the photon collection efficiency of a high-NA objective is crucial to detect the weak emission of individual chromophores. On the excitation side, high-NA objectives improve the optical sectioning of the sample. When the light-sheet is originated by scanning a Gaussian beam focused by a high-NA objective, the waist of the light-sheet defines the excitation thickness. In this case, equation (2.3) becomes

$$w_0 = \frac{\lambda}{\pi \mathrm{NA}}. \qquad (2.10)$$

However, a highly focused Gaussian beam with a small waist has a limited Rayleigh length, as stated by equation (2.4). This limits the distance over which the excitation is efficiently confined.

The standard design for light-sheet microscopy with two orthogonal objectives impose geometrical constraints that prevent the use of high-NA objectives. To overcome this limitation, several methods have been specifically developed for applying light-sheet microscopy to single-molecule imaging. In the following paragraphs these methods will be presented. References [81] and [82] provide a detailed review about light-sheet microscopy for single-molecule imaging.

2.3.1 Individual molecule localization with SPIM

The addition of a second objective has been fundamental to perform efficient single-molecule imaging in thick samples. The two orthogonal objectives configuration was first used to perform individual molecule localization through SPIM(IML-SPIM) [83]. In this work, two different illumination objectives can be alternatively used, in combination with a cylindrical lens to tune the excitation confinement. Specifically, a low-NA (0.8) has been used to produce a 4 μm thick light-sheet, while, using a high-NA (1.1) objective, a thinner 1.8 μm light-sheet has been realized. In this work, 3D PALM super-resolution imaging of thick spheroids of cells, embedded in agarose gel and mounted in a dedicated sample holder has been performed. An astigmatic lens was introduced on the detection path in order to infer the axial localization of single chromophore (see paragraph 1.8.2). The authors achieved < 35 nm and $65 - 140$ nm lateral and axial localization accuracy respectively, imaging up to 100 μm deep inside the sample.

With a similar method, light-sheet fluorescence microscopy has been exploited to perform single-particle tracking to study the 2D dynamics of individual mRNAs molecules in the nucleus of living cells [84]. In fact, as already mentioned, low excitation doses are sufficient in light-sheet microscopy, reducing photobleaching and photoxicity. In this work, the combination of a cylindrical lens with a long working distance 0.28 NA illumination objective produces a 3 μm thick light sheet. An orthogonal 1.2 NA objective collects the fluorescence from the sample, that is inserted in a dedicated holder.

The main limitation of this technique comes from the geometrical constraints imposed by the use of two orthogonal objectives, that consequently limit the NA of the excitation and collection objective. Moreover, dedicated sample holders must be used to fit the restricted space between the two lenses. To mitigate these problems, alternative methods use dedicated optics to reflect the light-sheet towards the sample. The different techniques that follow this approach will be described in the following paragraphs.

2.3.2 Reflected light-sheet microscopy

The main limitation of IML-SPIM is represented by the difficulties of placing two orthogonal objectives close to the specimen. To circumvent this problem, in reflected light-sheet microscopy (RLSM) [85] the illumination and imaging objectives are placed far from each side of the sample. A coated-tip is mounted on an atomic force microscopy (AFM) cantilever is used to reflect the light-sheet into the sample (**FIG. 25**). In RLSM, an efficient optical sectioning is produced by coupling a cylindrical lens and a 0.8 NA objective. A ~1 μm thick light-sheet is generated with a Rayleigh length of ~11 μm. This particular geometry is compatible with high-NA objectives (1.35 or 1.4) for the detection of the fluorescence, but induces a 2 μm gap from the coverslip which cannot be illuminated with the light-sheet

Since it allows the use of high-NA detection objective, RLSM offers a great potential for efficient imaging at the single-molecule level. In fact, 2D tracking of individual DNA transcription factors in living mammalian cells has been performed with RLSM.

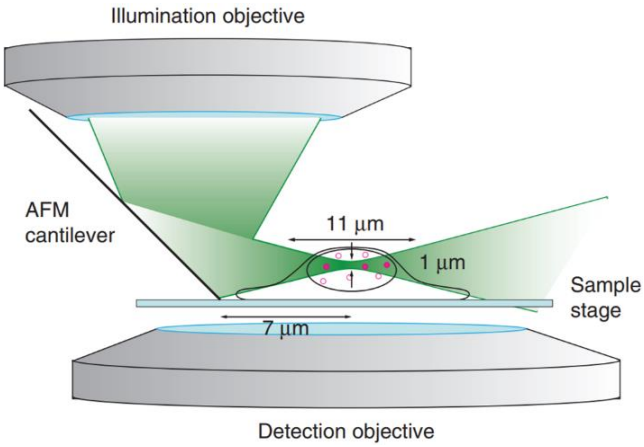

FIG. 25 – Reflected light-sheet microscopy (RLSM). *In RSLM, a mirror mounted on an AFM cantilever deflects the excitation beam toward the sample. This geometry permits to overcome the geometrical limitation of standard SPIM and use a high-NA objective to detect the fluorescence. Adapted from* [85].

2.3.3 Light-sheet Bayesian microscopy coupled with prism

A similar optical scheme for light-sheet microscopy is represented by prism-coupled light-sheet Bayesian microscopy (LSBM) [86]. In this technique, a cylindrical lens is coupled with a 0.55 NA condenser objective to form a ~2 μm thick light-sheet. A Pellin-Broca prism refracts the excitation beam horizontally to form the light sheet. With this design, the illumination and acquisition optical paths are at 120° angle. This permits to use high (>1) NA objective for collecting the fluorescence because. In LSBM, the sample is placed on a custom-made plate, slightly inclined to match the orientation of the prism surface (**FIG. 26**).

Thanks to high-NA objective and the reduction of out-of-focus background noise, LSBM was shown to be compatible with single-molecule imaging. In particular, (d)STORM/(F)PALM techniques have been performed in combination with Bayesian analysis of fluorescence fluctuation [87] to produce 2D super-resolution imaging of microtubules and heterochromatin in fixed cells, achieving a lateral resolution of ~30 nm. The Bayesian method applies a statistical model to infer the best possible distribution of molecules analyzing blinking and bleaching events across different frames. The method is able to resolve spatially overlapping fluorophores in densely labeled sample. In comparison with standard (d)STORM/(F)PALM techniques, the Bayesan analysis can, thus, extract considerably more single-molecule localizations from a single frame, achieving comparable resolution with the acquisition of only few hundred frames. Reducing the number of necessary acquisitions, live-cell super-resolution imaging of heterochromatin has been performed with LSBM.

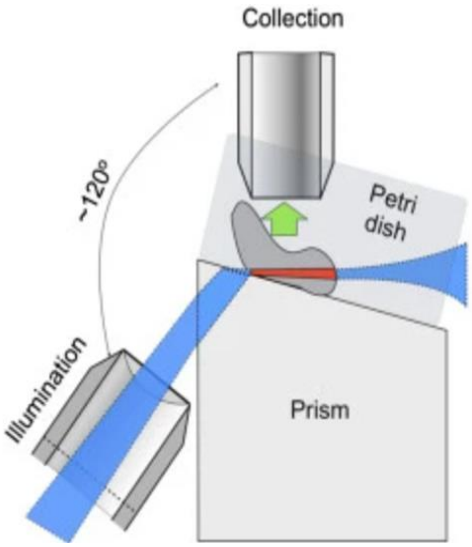

FIG. 26 – Optical scheme of prism-coupled light-sheet Bayesian microscopy. *The excitation light-sheet is tilted towards the sample by a prism. This geometry permits to reduce the geometrical constraints that typically afflict a two-objective light-sheet microscope. In fact, a second, high-NA objective, oriented at 120° respect to the illumination lens, can be used to collect the fluorescence. Adapted from* [86].

2.3.4 Prism-coupled tilted light-sheet microscopy

The main limitation of RLSM and LSBM is represented by the unobservable gap above the coverslip that cannot be illuminated with the light-sheet. Using a slightly tilted beam constitutes a solution to this problem, as demonstrated by tilted light sheet microscopy in combination with PSF engineering (3DTILT) [88]. Generally, when using a tilted excitation, the angle mismatch between the inclined beam and the detection plane reduces the observable field of view. In 3DTILT, PSF engineering is used to extend the observable axial range over the thickness of the light-sheet such that all the molecules within the illuminated section can be imaged by the

camera. Moreover, PSF engineering is used for the 3D localization of each chromophore (see paragraph 1.8.2) (FIG. 27).

In 3DTILT a cylindrical lens and a low-NA objective produce a ~2 μm thick light-sheet, which is reflected towards the sample with a ~10° angle compare to focal plane. The beam can be displaced with a motorized mirror conjugated to the back focal plane of the illumination objective in order to scan the sample volume. On the detection path, a high-NA (>1.4) objective collect the fluorescence, while a lens pair in 4f configuration allows to insert a dielectric phase mask that produces double-helix PSF shaped.

Single-molecule localization-based super-resolution imaging has been performed using 3DTILT to observe the mitochondria and the nuclear membrane of fixed cells. The combination of light-sheet microscopy with PSF engineering provided respectively 16 nm and 24 nm lateral and axial localization precision.

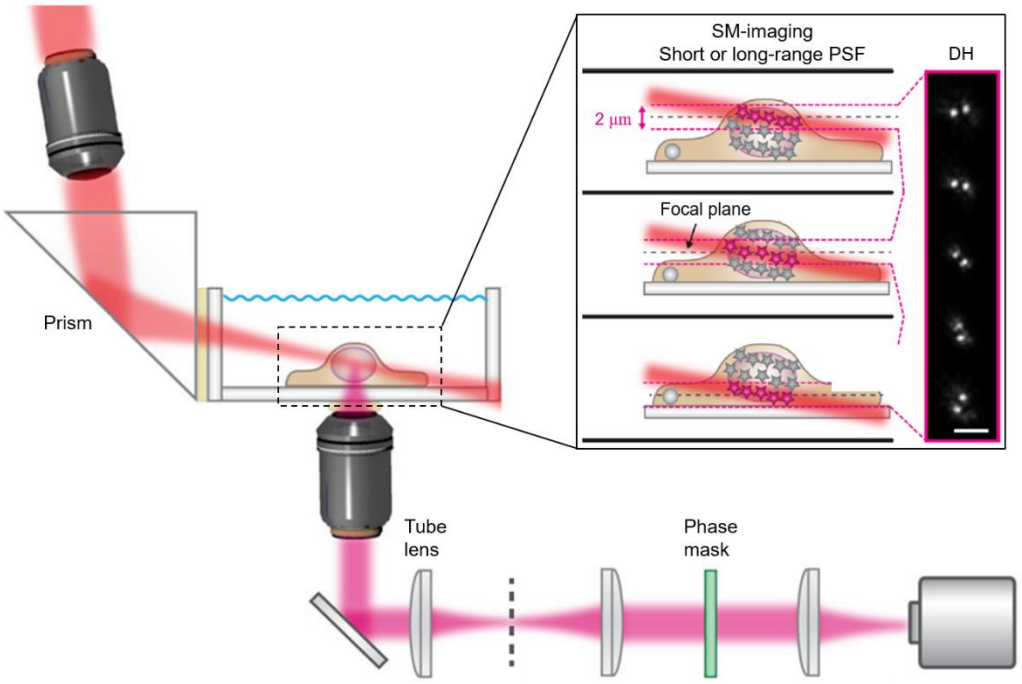

FIG. 27 – 3DTILT technique for volumetric imaging using a prism-coupled tilted light-sheet and PSF engineering. *A tilted excitation beam in scanned through the sample volume. On the acquisition path, a phase mask for double-helix PSF shaping allows the 3D localization of individual chromophore. In the frame it is represented how the PSF shape changes while scanning the ~2 μm thick light-sheet through the sample volume without any unobservable gap. Scale bar* 3 μm. *Adapted from* [88].

2.3.5 Light-sheet microscopy with Bessel beams

All the single-molecule light-sheet techniques examined in the previous paragraphs employ Gaussian beams. However, Gaussian beams limit the optical sectioning efficiency. As seen in paragraph 2.1, the intensity distribution (2.1) and

the propagation of a Gaussian beam are mainly defined by two connected parameters: the waist w_0 (2.3) and the Rayleigh length z_R (2.4). The excitation intensity of Gaussian light-sheet can be considered confined with a thickness given by w_0 and over a length given by $2z_R \propto w_0^2$. This means that the excitation confinement of a thin light sheet is preserved over a short range only. Thus, there is a compromise between the thickness and the achievable extension of a Gaussian light-sheet.

To improve the illumination selectivity, light-sheet microscopy based on Bessel beams has been developed [89], [90]. To form the Bessel beam, a Gaussian beam is masked to produce a ring. For that, an annular mask with inner radius r and outer radius R is placed on a plane conjugated with two galvo-mirrors (for the scan of the excitation beam) and the back focal plane of the illumination objective. Adjusting the thickness of the ring by changing r and R controls the Bessel beam characteristics. With reference to (**FIG. 28A**), the parameters that define the Bessel beam are

$$NA_{min}^{Bessel} = n \sin\alpha \,, \tag{2.11a}$$

$$NA_{MAX}^{Bessel} = n \sin A \,, \tag{2.12b}$$

$$\epsilon^{Bessel} = NA_{min}^{Bessel} / NA_{MAX}^{Bessel} \,, \tag{2.13c}$$

where n is the refraction index of the medium in which the Bessel beam propagates.

Considering the Bessel parameter ϵ, for $\epsilon^{Bessel} = 0$ the result is a Gaussian beam while for $\epsilon^{Bessel} \to 1$ the result is a long Bessel beam with small waist. However, a common issue of Bessel beams is the light intensity distribution in the side lobes, that originate as a consequence of diffraction of light going through the annular mask (**FIG. 28B**). Substantial energy resides in the side lobes and, for that, the cross-sectional profile of the excitation light-sheet, created by sweeping the Bessel beam, shows broad tails (**FIG. 28C**). To mitigate this effect, the annular mask can be made thicker ($\epsilon^{Bessel} \to 0$), at the cost of the length of the Bessel beam.

Bessel beam light-sheet excitation can be used in combination with many other methods to perform living-sample imaging and super-resolution imaging. As demonstrated in [79], super-resolution imaging of microtubules and mitochondria in fixed cells has been performed using Bessel beams to create different illumination patterns and perform 3D SIM. The combination of Bessel beams and SIM achieved isotropic imaging resolution. 3D SIM with Bessel beam excitation has been performed also in a two-photon excitation configuration. SIM and light-sheet microscopy are both non-invasive techniques, the combination of the two has been exploited to image in time the mitosis of chromosomes in the nucleus of living cells [91].

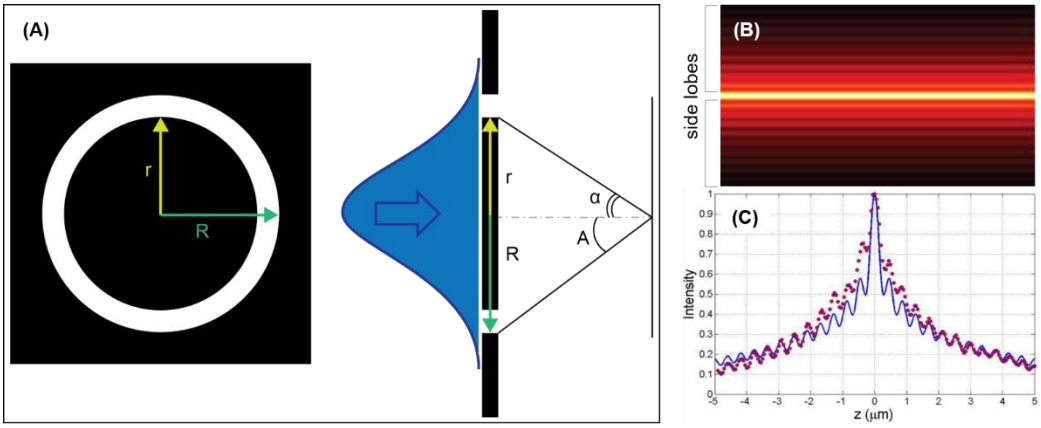

FIG. 28 - Bessel beam properties. *(A) A Bessel beam is produced by focusing the radiation obtained from a Gaussian beam incident on an annular mask. The size and thickness of the mask define the Bessel beam shape. (B) Simulated Bessel beam shows the light intensity distributed in the side lobes. (C) Sweeping a Bessel beam generate a light-sheet with prominent tails due to the energy in the side lobes. Adapted from [80].*

2.3.6 Lattice light-sheet microscopy with Bessel beams

Probably the most advanced light-sheet microscopy method, lattice light-sheet (LLS) addresses the critical side lobe issue of standard Bessel beams [92]. The LLS solves this problem by spacing a linear array of Bessel beams with the correct periodicity, such that the beams can be made to interfere constructively in the main lobes and destructively elsewhere. This greatly reduces the background contribution of the side lobes of conventional Bessel beams. To create the LLS, a fast SLM for binary phase patterning is placed on the illumination path, conjugated to the sample plane. As well as for Bessel beam light-sheet microscopy (see paragraph 2.3.5), two galvo-mirrors for the scan of the LLS and an annular mask are placed on the illumination path, optically conjugated to the back focal plane of the illumination 0.65 NA objective. The fluorescence is detected by a 1.1 NA objective, placed orthogonally to the illumination one. By modulating the phase patterning introduced by the SLM it is possible to produce multiple kinds of LLS with different light distribution while dithering the lattice (**FIG. 29**).

This system offers multiple operation modes. First, the authors show the combination of Bessel beam LLS and SIM that produce 3D super-resolution imaging of living cells. In this configuration the LLS is displaced in x and z directions using the galvo-mirrors to create a structured illumination. At every z plane, images are recorded while the lattice light-sheet is stepped in x direction the to form the structured illumination. The final 3D super-resolution image is reconstructed by spectral analysis (see SIM technique in paragraph 1.4.2). The combination of LLS and SIM was shown to be non-invasive by imaging the 3D dynamics of chromosomes during mitosis with a resolution below the diffraction limit. Taking advantage of the

non-invasiveness of LLS, the authors show the second operation mode performing single-molecule tracking in mouse embryonic stem cells (see Chapter 4). In this operation mode the LLS is dithered in x to produce 1.1 μm thin, homogeneous excitation. The dithering operation mode has been exploited to combine Bessel beam LLS and PALM. By scanning in z the dithered LLS, 3D super-resolution imaging of the nuclear membrane of fixed cells has been performed. The axial position of the chromophores was encoded by astigmatic PSF (see paragraph 1.8.2). Finally, the dynamics of DNA transcription factors were investigated, demonstrating the improvement in signal-to-noise ratio of LLS compare to standard Bessel beam light-sheet microscopy.

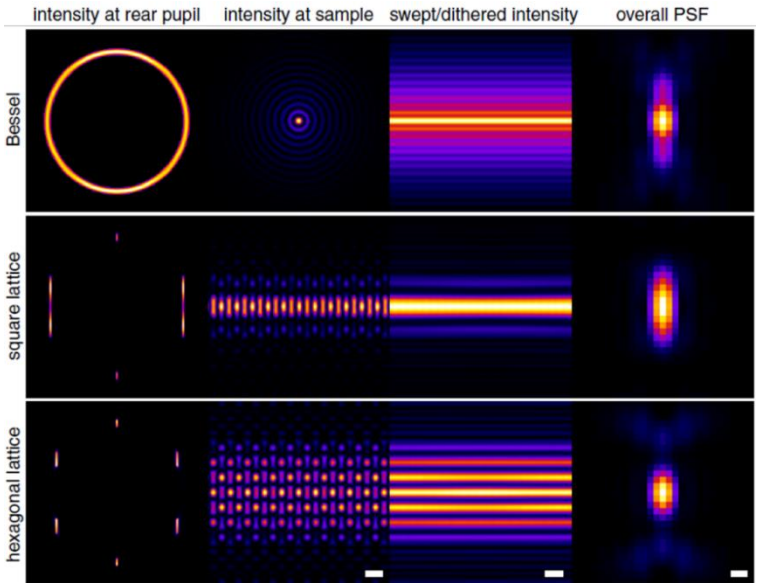

FIG. 29 - Comparison of light-sheets obtained with Bessel beam and different kinds of lattices. *The first column shows the intensity distribution at the rear pupil of the illumination objective. The second column shows the xz section of the intensity of Bessel beam and lattice. The third column shows the light-sheet xz profile after dithering. The fourth column shows respectively the xz PSF of Bessel light-sheet and lattices. Scale bar* 1 μm. *Adapted from* [92].

Despite the advantage of engineering the excitation sheet profile, mechanical constraint limits the range of NA that can be used when two separated objectives for the excitation and the fluorescence collection are used. Also, this solution imposes constraints on the sample size and mounting. Methods that tries to overcome these limitations are presented in the next paragraph.

2.4 Light-sheet microscopy with a single objective

To overcome the geometrical constraints of conventional methods, innovative strategies for light-sheet microscopy with a single and high-NA objective have been

developed in the last years. These methods can be divided in two main categories.

The first category of methods relies on remote imaging. In these methods, the task of matching the illuminated area to the observed one is translocated to a remote location. A virtual image conjugated to the sample is obtained thanks to a second objective placed on the emission path. The new virtual image can be observed with a third objective at the desired observation angle matching the tilt of the selective beam excitation.

The second category of methods is based on the alteration of the excitation optical path. In these techniques, the biological sample is placed in custom-made micro-fabricated holders, which present mirrored surface at specific distance from the biological sample. For the geometry of the holders, the sample is placed at the focal plane of the illumination objective and the mirrored surface reflects the excitation light-sheet outcoming from the objective to match the focal plane of the same lens.

The following paragraphs contain the details of the techniques that perform single-molecule light-sheet microscopy with a single high-NA objective.

2.4.1 Single-objective oblique light-sheet microscopy with remote focusing

When using inclined excitation light-sheet, the angle mismatch between the illumination axis and the detection plane constitutes a limitation of the effective NA of the imaging system. A common strategy for correcting this effect is represented by remote imaging. The first techniques based on this idea were oblique plane microscopy (OPM) [93], swept confocally-aligned planar excitation (SCAPE) microscopy [94] and axial plane optical microscopy (APOM) [95].

In OPM, three objectives are placed on the detection path. The first objective lens produces the light-sheet and collects the fluorescence. The second objective form a remote, virtual image of the sample in which the illuminated fluorescing area is inclined compared to the optical axis. The third objective is oriented with respect to the second objective in order to correctly reproduce the tilted virtual image on the camera. In conclusion, the remote focusing arrangement creates the in-focus image of an oblique plane of the sample but also shifts part of the light outside of the collectable cone of the third objective. The geometrical constraints limit the total effective collection NA of the microscope to 0.45 (**FIG. 30A**).

In SCAPE, a unique mechanism of scanning excitation and descanning detection corrects the angle mismatch. A polygonal mirror mounted on a galvanometer is optically conjugated to the back focal plane of the illumination/detection objective. By rotating the mirror, the incident angle of the excitation beam changes and, consequentially, the inclination of the light-sheet. With such an optical

configuration, the fluorescence is reflected on an adjacent facet of the polygonal mirror. The descanned fluorescence forms a stationary oblique image plane that is always aligned with the light-sheet. A rotated remote imaging system is then used to project this oblique image, as seen for OPM. The fast scanning-descannig mechanism of SCAPE is compatible with fast volumetric imaging. However, in SCAPE the illumination/detection objective has low NA (<1) and the total NA of the microscope is even lower, as seen for OPM.

Another technique for fast volumetric imaging with axial optical sectioning is APOM. In APOM a single 1.4 NA objective produces the vertical light sheet and collects the fluorescence. A second 1.4 NA objective forms a conjugated image. A mirror is placed exactly in this plane at 45° to reflect the virtual image back into the second objective, which forms a real axial image on a conjugated axial image plane. This mechanism is the same of SCAPE for a fixed 45° inclination, however the authors suggest that a tilting mirror can be used instead in order to achieve arbitrary plane imaging (**FIG. 30B**).

The general feature of all these techniques is that the excitation is confined around an oblique plane on the sample. This means that, compared to standard methods with horizontal light-sheet excitation, here $x - z$ planes of the sample are excited and imaged after being tilted back in-focus. None of these techniques have been used for single-molecule imaging, but they inspired the development of methods for super-resolution imaging and single-particle tracking, that are described in the following paragraphs.

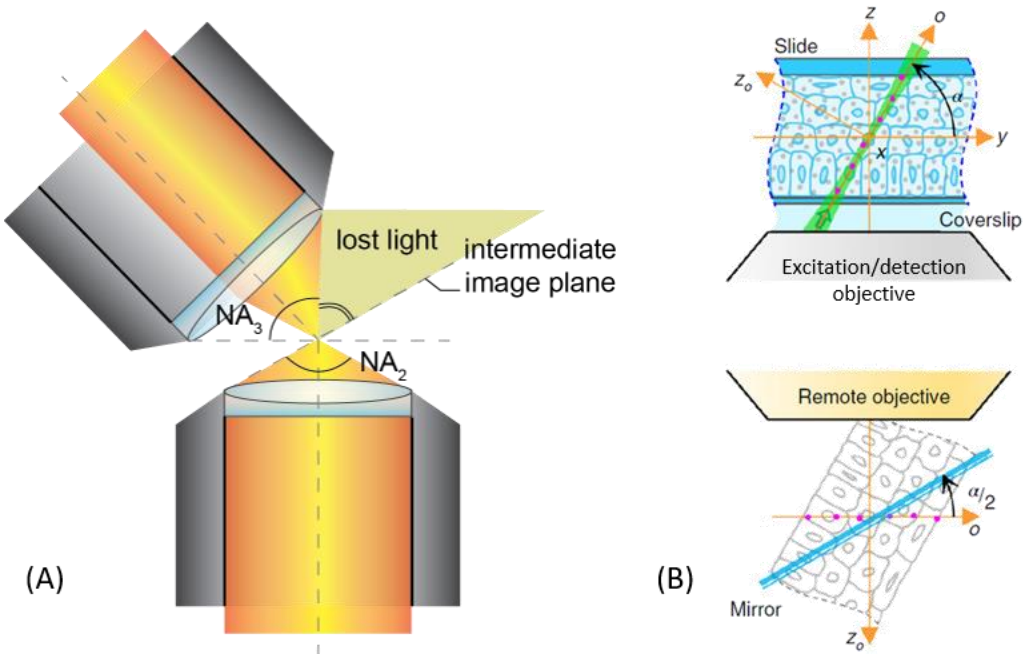

FIG. 30 – Remote focusing for inclined light-sheet microscopy. *(A) In OPM, a secondary objective (NA_2) and a tertiary objective (NA_3) produce an inclined intermediate image plane that compensate the angle of the excitation. (B) Mirror-based remote focusing of SCAPE and APOM.*

2.4.2 Epi-illumination SPIM for single-molecule imaging

Epi-illumination SPIM (eSPIM) [96] derives from standard oblique light-sheet microscopy methods such as OPM and SCAPE, described in the previous paragraph. In these techniques, the remote imaging module reduces the total NA of the microscope, which is a limiting factor for single-molecule imaging.

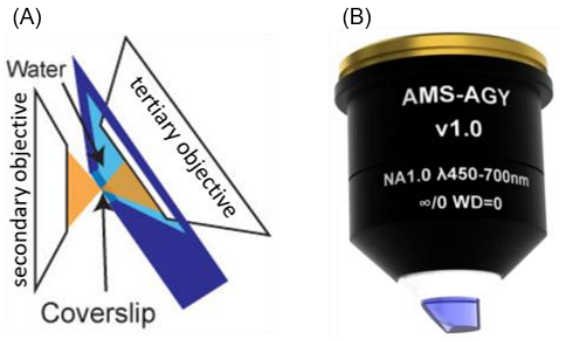

FIG. 31 – Solutions for high total NA remote imaging systems. *(A) The NA loss can be reduce using a water chamber that creates a refractive index mismatch and compress the cone of light of the secondary objective. Adapted from* [97]. *(B) Another optimization strategy of the remote imaging system to reduce the NA loss involves the use of glass-tipped tertiary objective. Adapted from* [98].

In eSPIM, a single 1.27 NA, water-immersion objective (O_1) is used for both exciting the sample and detecting the fluorescence, and a galvo-mirror conjugated to the back focal plane of the objective is used to scan the light-sheet laterally through the sample. The remote imaging system is composed by two objectives, respectively an air-immersion, 0.9 NA objective (O_2), and a water-immersion 1 NA objective (O_3), arranged at the same angle as the oblique illumination light-sheet. To reduce the total NA loss due to the remote imaging system, a 3D-printed chamber placed at the intermediate image plane matches the refractive indexes of the two lenses. A coverglass divides the chamber in two parts, one filled with water and the other with air. The refractive index air-water mismatch compresses the light-cone of O_2 into the light-cone of O_3, minimizing the collection NA loss (**FIG. 31A**). The total NA of the microscope is ~1.17.

The excitation optical path can be configured to produce Gaussian or Bessel beam light-sheet illumination. The authors demonstrated eSPIM performances in fast volumetric imaging of living sample, observing multiple kinds of structures with an acquisition rate up to 14.7 volumes/s. Moreover, single-molecule imaging capability of eSPIM has been demonstrated by performing super-resolution (d)STORM imaging of microtubules in fixed cells.

A comparable method for oblique plane microscopy at the single-molecule level has been developed with a different solution for the mitigation of total NA loss [97]. Here, a single, silicon-immersion, 1.35 NA objective produces the oblique light-sheet and collects the fluorescence. The remote imaging system is constituted by an air-immersion 0.95 NA objective and a custom-made glass-tipped tertiary objective [98] (**FIG. 31B**). The theoretical final NA of the microscope is ~1.28. In

comparison with other fluorescence microscopy techniques, such a value is sufficient for single-molecule imaging, however the authors did show such acquisitions. The authors demonstrated the high spatial and temporal resolution provided by this method by performing volumetric imaging of different kinds of living sample. The imaging speed reaches ~14 volumes/s and a resolution comparable to other standard fluorescence microscopy techniques.

2.4.3 Oblique-plane microscopy for super-resolution imaging

The two-objectives remote imaging system of OPM and SCAPE is not the unique way for producing the in-focus image of an oblique section of the sample. Recently, oblique-plane microscopy for single-molecule super-resolution imaging (obSTORM) [99] has been performed using just a secondary remote objective with an inclined mirror placed at its focal plane, following the same optical design of APOM (see paragraph 2.4.1).

The optical design of obSTORM is based on a 1.2 NA objective that produces the oblique light-sheet and collects the fluorescence. This is optically conjugated to a second, high-NA objective. An inclined mirror is placed after the second objective to form a virtual in-focus image at the focal plane of the lens. A quarter-wavelength plate and a polarized beam splitter reflects the in-focus virtual image of the oblique sample plane towards the camera. By scanning the oblique light-sheet through the sample, the authors performed multicolor (d)STORM to produce super-resolution images of microtubules and mitochondria of fixed cells achieving ~30 nm lateral resolution and ~60 nm axial resolution. The authors also performed super-resolution volumetric (d)STORM imaging of complex proteins in *C. elegans*, *Drosophila* and mouse retina.

In a recent, similar work [100], oblique plane microscopy was used for super-resolution imaging of microtubules and nucleoporins of fixed cells, achieving a lateral resolution < 70 nm. Also, the authors performed multiplexed and multi-color DNA-PAINT on tubulin structures and mitochondria of whole fixed cells, with lateral and axial resolution of ~90 nm and ~110 nm, respectively.

2.4.4 Single-objective light-sheet microscopy with microfabricated sample holders

Single-objective light-sheet microscopy (SO-LSM) refers to a method designed for fluorescence microscopy with optical sectioning of the sample using a single high-NA objective. The system is based on a micro-fabricated sample mounting chip with integrated reflective walls [101]. More specifically, the reflective wall of the

chip is inclined at 45° and constitute a micro-mirror that reflects horizontally the light-sheet into the sample. The specimen is positioned inside the micro-fabricated channel (**FIG. 32**). The chip provides a sealed environment where the imaging conditions can be adjusted rapidly and in an automated fashion. To generate the light-sheet, two different cylindrical lenses can be inserted on the optical path. The first one creates a thick and long illumination. The second one creates a thinner, but shorter light-sheet. In the latter configuration, the cylindrical lens is displaceable to adjust the position of the light-sheet waist compared to the sample in the chip. A galvo-mirror conjugated with the back focal plane of the unique objective sweeps the illumination to form the light sheet. In both configurations, the light-sheet is aligned with the focal plane. The 1.2 NA objective also collects the fluorescence from the sample after excitation. The geometry of the chip creates a gap of few microns height above the bottom surface in which the reflection of the light is not optimal. To image an entire cell the bottom surface must be covered with an agarose layer. The authors demonstrated SO-LSM method for volumetric (d)STORM super-resolution imaging of mitochondria, in combination with astigmatic PSF for the axial localization (see paragraph 1.8.2).

A similar approach known by single-objective SPIM (soSPIM) [102] relies on micro-fabricated wells for seeding the cells in the proximity of 45° inclined micromirrors that are used to reflect the light sheet. The method performs light-sheet microscopy and single-molecule imaging using a single high-NA objective for the excitation and the fluorescence detection. During this PhD project, we developed a modular system that provide selective volumetric excitation of the sample and instantaneous 3D imaging. We decided to adopt and adjust soSPIM to tailor the excitation beam and produce selective volumetric illumination. In the next chapter, all the details about the design and implementation of this innovative method will be provided and, in this context, soSPIM method will be described in paragraph 3.2.

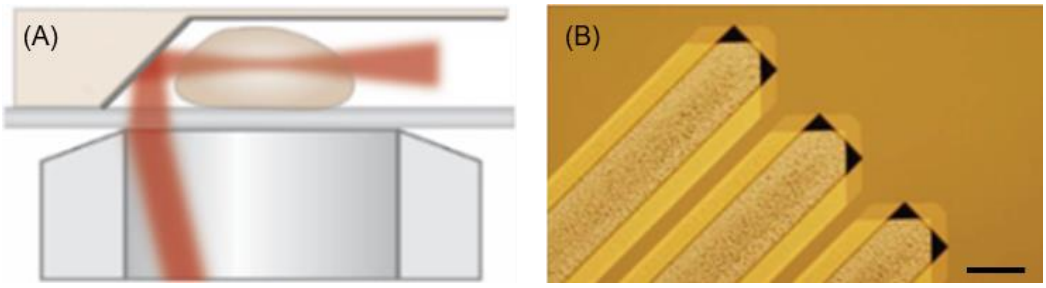

FIG. 32 – Custom-made microchannel for single-objective light-sheet microscopy. *(A) In single-objective light-sheet microscopy (SOLSM), the sample is placed is a microfluidic channel with reflective walls. The beam is horizontally reflected into the sample, perfectly aligned with the focal plane. The same high-NA objective that focus the beam in the sample also collects the fluorescence. Adapted from [71]. (B) Optical microscope image of four channels of the chip. Adapted from [83]. Scale bar* 100 μm.

Chapter 3

A novel method for instantaneous, volumetric, single-molecule imaging with selective excitation

A major trend in modern biological research is to move from 2D cell cultures into multicellular systems where 3D cell-cell and cell-extracellular matrix interactions provide a more realistic representation of the *in vivo* microenvironment. Beside stem cells, that tend to grow in 3D colonies (see paragraph 4.4), cells spheroids, 3D printed cells and organoids represent examples of such systems. Morphology and physiology of cells in 3D cultures are different from cells in 2D cultures, showing responses that in some ways resemble *in vivo* behavior [103]. Exploring the single-molecule organization and dynamics in such systems represents a first step in bridging the gap between single-cell investigations and the study of more complicated systems such as animals. As a consequence, a pressing challenge in modern single-molecule fluorescence microscopy is to image individual molecules in 3D samples, moving farther away from the coverslip. Single-molecule imaging deep in 3D samples raises specific requirements for efficient and sensitive imaging.

In this PhD thesis, we developed a new microscopy system for single-molecule imaging, able to perform both dynamics analysis and super-resolution imaging in volumetric samples. The challenges here can be summarized in (i) optimizing the signal-to-noise ratio for single-molecule acquisitions, (ii) reducing the phototoxicity when performing tracking experiments in living samples, (iii) performing fast 3D acquisition with single-molecule sensitivity to cope with fast dynamics of biomolecules, and (iv) the ability to detect single molecules in a dense environment.

Combining Multifocus microscopy and single-objective SPIM, our method offers an optimized selective volumetric excitation and instantaneous 3D detection. The efficient coupling of the two methods requires the perfect match of excitation and

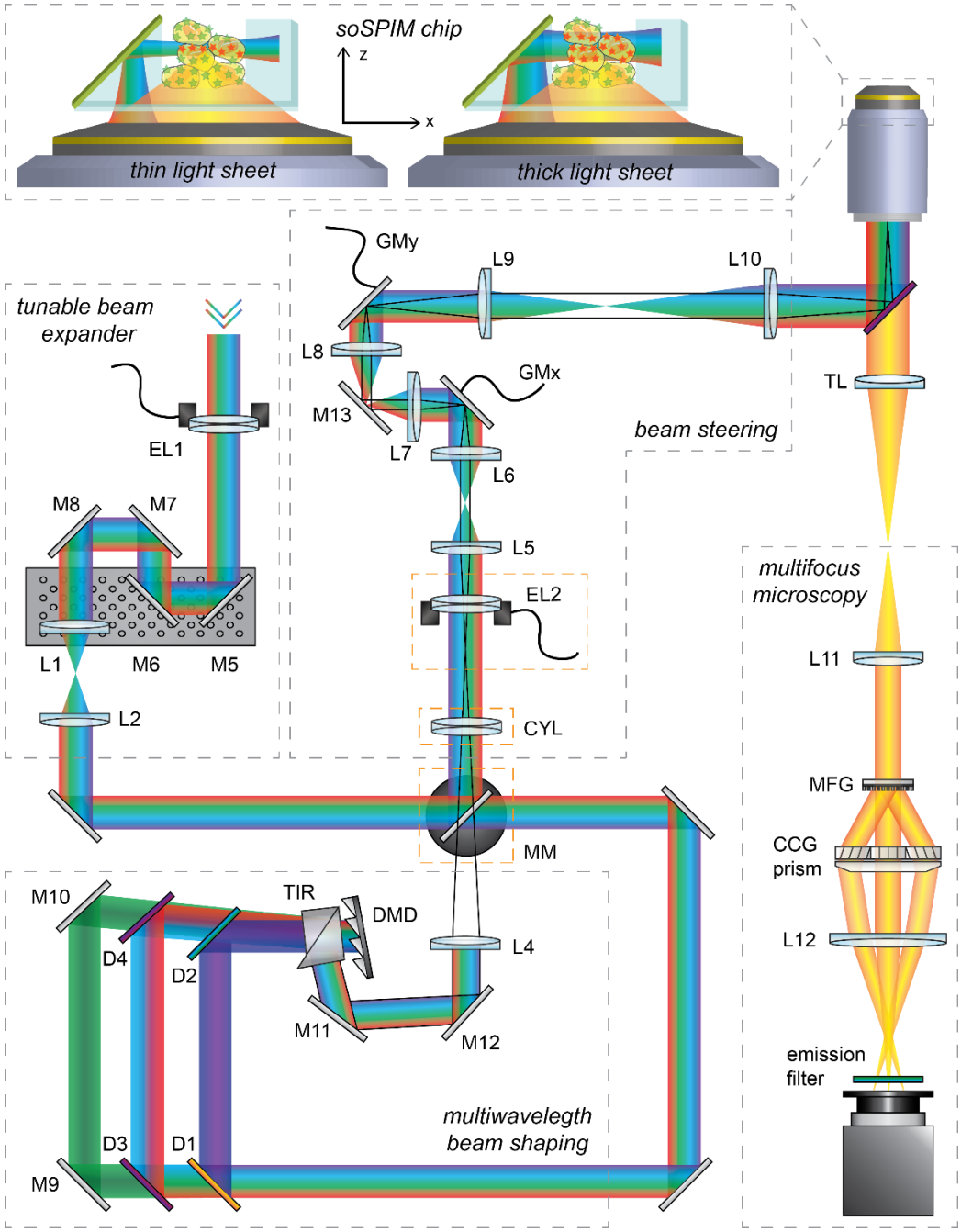

FIG. 33 – Modular system for instantaneous volumetric imaging at the single-molecule level through selective excitation. *A first module consists of an automated tunable beam expander that regulates the excitation beam size. Using a digital micromirror device (DMD), a second module shapes the beam to achieve homogeneous excitation. The shaped illumination follows the optical path represented by the black lines in the figure. A removable mirror (MM) can reflect the illumination directly towards a beam steering module. Volumetric imaging is performed by multifocus microscopy module placed on the emission path.*

acquisition volumes. To satisfy this requirement, we developed a modular system in which each unit fulfills specific purposes. First, an automatized tunable beam expander finely tunes the size of the excitation Gaussian beam. Second, a beam shaping module based on a digital micromirror device (DMD), modulates the

illumination beam and produces homogeneous excitation of a volume. Third, a beam steering module controls the selective volumetric excitation on the sample. Fourth, the sample is placed in a custom-made sample holder specially designed for soSPIM imaging. Finally, MFM is implemented on the detection path to produce instantaneous 3D imaging. We optimized this module to be able to tune the extension of the acquired volume. All the units are independent, but they have been designed to optimally perform together (**FIG. 33**).

This chapter is dedicated to the detailed description of the different modules. First, the two techniques at the core of the system, MFM and soSPIM, will be presented in details. Then, a precise description of the design and implementation of the tunable beam expander and beam shaping modules will be provided.

3.1 Instantaneous volumetric imaging through multifocus microscopy

The big challenge in biological fluorescence microscopy comes from the volumetric extension of the samples. As seen in paragraph 1.2, the depth of field of a standard fluorescence microscope is limited around the focal plane and the axial shape of the PSF reduces the microscope resolution in z, creating an obstacle for the 3D localization of single molecules. Conventional methods for acquiring 3D data sets require a mechanical z displacement of the objective or the sample to acquire multiple focal planes sequentially. A stack of 2D images is used to assemble a 3D image. The mechanical movement reduces the achievable temporal resolution and limits the observable range of dynamic biological processes. Also, ambiguous spatio-temporal information can be generated since the focal planes are not recorded simultaneously. To overcome these limitations, multiplane methods (see paragraph 1.8.1) use separate cameras to image simultaneously different planes in the sample. Nevertheless, refocusing by translating the camera away from the nominal focal plane induces some spherical aberration.

Alternatively, MFM [51] uses a single camera to acquire simultaneously the focal stack of multiple high-resolution (limited by the NA of the objective) 2D images. MFM is based on the use of several gratings to form multiple focus-shifted and aberration-free images on the same camera. Thus, MFM records a sample volume in a single exposure, and since no mechanical movements are involved, the achievable temporal resolution is limited only by the fluorescence brightness and the camera frame rate. Therefore, MFM can extend dramatically the observable range of biomolecules dynamics. MFM technology was developed in the lab before the beginning of my PhD project.

3.1.1 The optical setup for multifocus microscopy

With reference to **FIG. 33**, the multifocus microscope is essentially composed by three custom-designed optical elements that are installed on the detection path of a standard fluorescence microscope (Ti eclipse, by Nikon). The tube lens of the microscope TL ($f_{TL} = 200$ mm) and an achromatic relay lens $L11$ ($f_{11} = 150$ mm, AC254-150-A, by Thorlabs;) produce a secondary pupil plane, or Fourier plane. The multifocus grating (MFG), that is the first element of the multifocus microscope, is placed at this plane. The MFG (custom-made by Creative Microsystems,) performs two distinct functions. First, it splits the fluorescence signal into separate paths, each one associated with a diffraction order (m_x, m_y). The central grating motif of the MFG maximizes the diffraction efficiency, ensuring a uniform distribution of the fluorescence light in the desired diffraction orders. Second, it adds a specific defocusing power to each diffraction order. A final lens $L12$ ($f_{12} = 200$ mm, ACT508-200-A, by Thorlabs) refocuses the several diffraction orders on different parts of the imaging camera (iXon Ultra897, 512 × 512 active pixels, physical pixel size 16 μm × 16 μm, by Andor). As such, an array of images of various focal planes with constant focal step Δz are tiled side by side and imaged instantaneously on the same camera.

In [51], the authors report the details for a MFG that produce a 3 × 3 matrix of images associated with the diffraction orders $m_{x,y} = 0, \pm 1, \pm 2$. Initial design of the MFG was optimized to work with water-immersion objectives 1.3 NA at 520nm imaging wavelength. It was shown to be compatible with a 100X, oil-immersion, 1.4 NA (PLAN Apo 100XC Oil, by Nikon) at the fluorescence wavelength $\lambda = 620$. In this configuration, it produces the images of 9 distinct focal planes separated by an axial distance of ~450 nm. Different gratings however can be engineered to acquire a various number of plane and work with different objectives and wavelengths. Following, I detail the principle of wavefront correction and imaging by MFM.

The principle of MFM is to simultaneously focus the fluorescence originating from different focal planes on the same camera. While objective lenses are conceived such to produce a high-resolution image of point-like emitters placed at the focal plane, the wavefront of out-of-focus emitters is distorted mainly by depth-dependent spherical aberrations. For emission wavelength λ, the wavefront that they emit is shifted from a plane wave by a defocus error

$$\delta\phi(z) = \frac{2\pi}{\lambda} nz\sqrt{1 - \sin^2\theta}\,, \tag{3.1}$$

where z is the distance of the emitter from the focal plane, n is the refractive index of the objective immersion medium, and θ is the angle of incidence of light such as $n \sin\theta < n \sin\alpha =$ NA of the objective. Let $r_p = (x_p, y_p)$ be the radial coordinate in

the pupil plane (back focal plane of the objective). If f_{obj} is the objective focal length it was shown that

$$\delta\phi(z) = \frac{2\pi}{\lambda} nz \sqrt{1 - \frac{x_p^2 + y_p^2}{n^2 (f_{obj})^2}}. \tag{3.2}$$

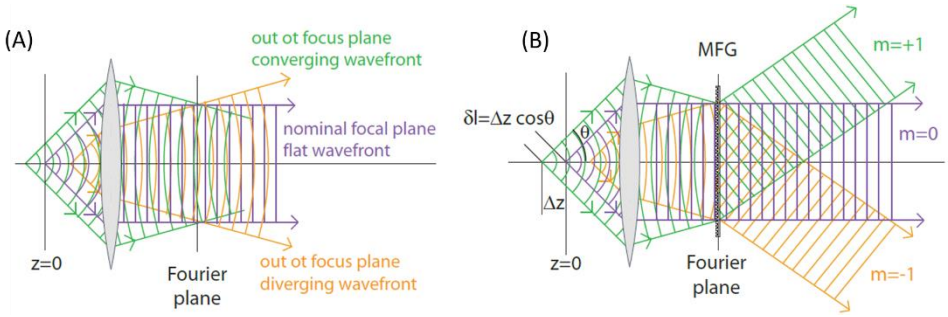

FIG. 34 – Aberration-corrected refocus with a multifocus grating (MFG). *(A) In a standard microscope, the light from the nominal focal plane (purple) exits the objective with a flat wavefront. Out-of-focus light exits the objective with a curved wavefront, either convergent (green) or divergent (yellow). (B) The MFG splits the fluorescence into a set of diffractive orders. A geometrical distortion in the grating pattern introduces a phase shift that is dependent on diffractive order, and that reverse the out-of-focus wavefront curvature of each focal plane in the multi-focus image. Therefore, also the out-of-focus planes exit the MFG with a flat wavefront. Adapted from* [51]

To create aberrations-free images, the MFG must compensate for this error (FIG. 34). This is obtained by introducing a specific distortion of the periodic pattern of the MFG. For simplicity, let us consider a distortion along x. A geometrical distortion δx of the periodic grating pattern, placed at the secondary pupil plane, produces a phase shift in the diffracted wavefront order m_x equal to

$$d\phi_{m_x}(\delta x) = \frac{2\pi m_x \delta x}{d}, \tag{3.3}$$

where d is the central periodicity of the pattern.

From (3.2) and (3.3), the geometrical distortion that must be introduced on the MFG pattern to compensates for the defocus error results

$$\delta x(r_p) = \frac{dnz}{\lambda} \sqrt{1 - \frac{x_p^2 + y_p^2}{n^2 (f_{obj})^2}}. \tag{3.4}$$

Equation (3.4) suggests that the design of the MFG must be optimized according to the objective lens and the wavelength of the fluorescence. If the distortion in the y direction is set such as $\delta y = N\delta x$, the MFG produces an $N \times N$ matrix of aberration-free images of different focal planes separated by a constant Δz step. The axial separation between the central order (nominal focal plane) and the diffractive

order (m_x, m_y) is $\Delta z(m_x + Nm_y)$. A nominal sampling of the emission PSF imposes an inter-plane distance Δz of half the axial PSF extent at most.

As any other diffractive optical element, the MFG is affected by chromatic dispersion, which would severely deteriorate the image quality if not corrected for, even across the relatively narrow wavelength spectrum of a single fluorophore (~30 nm). For that, the second core element of MFM microscope is a chromatic correction grating module (CCG), inserted on the detection optical path after the MFG at a distance where the diffraction orders are physically separated in space. The CCG (custom-made by Tessera Inc) consists in a panel of blazed diffractive gratings with different blazing orientation, each one optimized for the respective diffraction order generated by the MFG. The combination of CCG and a multi-faceted prism compensates the dispersion produced by the MFG, and tilts the beam such to precisely control the position of each diffraction order image on the imaging camera. Both the CCG and the prism have $> 95\%$ light transmittance, guaranteeing the light efficiency of the chromatic correction module (**FIG. 35**).

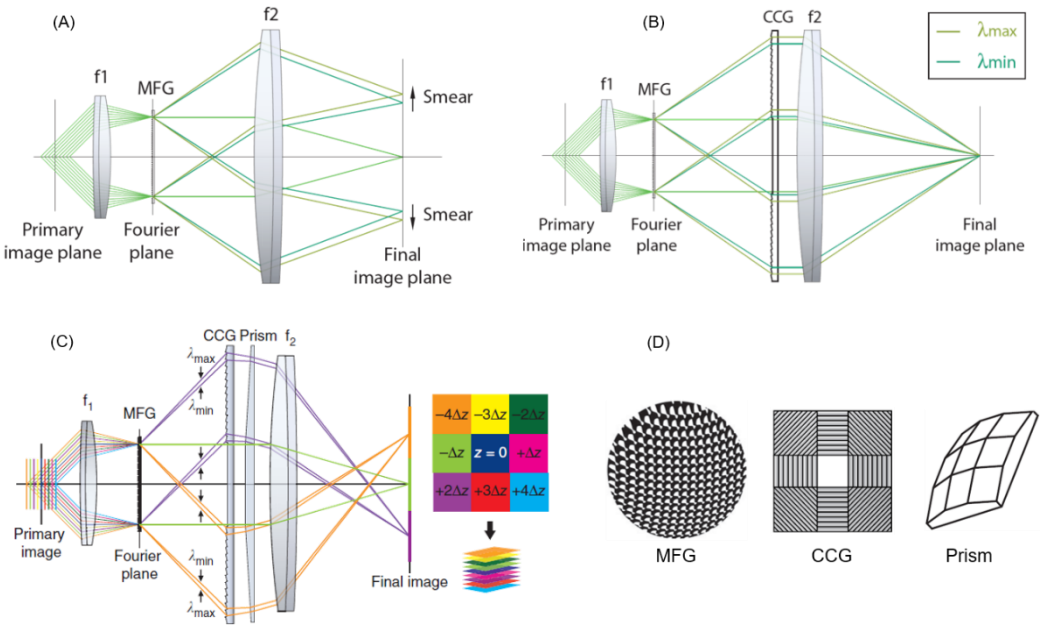

FIG. 35 – Instantaneous volumetric imaging through aberration-free, chromatic-corrected multifocus microscopy (MFM). *(A) The multifocus grating (MFG) refocuses the light coming from the nominal focal plane of the objective and a set of out-of-focus planes. However, as any other diffractive optics, it is affected by chromatic dispersion. With no chromatic correction, the different diffraction orders would appear smeared when refocused on the image plane. (B) A chromatic correction grating (CCG) is placed after the MFG to compensate the chromatic dispersion. Nevertheless, the CCG alone would refocus all the diffraction orders in the same point on the image plane. (C) For that a faceted prism is placed after the CCG to keep separated the optical path of the different diffraction orders. In this way, a $N \times N$ matrix is formed at the image plane, containing the collection of 2D images of different sections of the sample. (D) Schematic drawings of MFG, CCG and faceted prism. Adapted from* [51].

To provide a precise alignment, the MFG is placed in a rotational mount (RM25A, by Newport), attached to a holder with micrometric controls for the lateral

and axial position adjustment (LP-1A by Newport). As will be shown in paragraph 3.1.3, we produced multiple $MFGs$ to tune the acquisition volume. Each grating is installed and pre-aligned to the optical axis of the microscope in a dedicated mount holder equipped with a magnetic base. As such, gratings can be easily exchanged without any realignment procedure. These solutions result in an easily tunable and stable MFM microscope. In this thesis MFM imaging has been performed using different objectives, specifically a 100X, oil-immersion, 1.4 NA (CFI Plan Apo VC 100X Oil, by Nikon) lens and a 60X, water-immersion, 1.27 NA (CFI SR Plan Apo IR 60XC WI, by Nikon) lenses the final pixel size is 120 nm and 200 nm respectively. Considering that the sensor of the camera is divided in multiple areas to acquire different focal planes, the achievable field of view is ~ 20 μm × 20 μm for the 100X objective and ~ 34 μm × 34 μm for the 60X objective.

3.1.2 Volumetric image reconstruction in multifocus microscopy

Each frame acquired in MFM is a set of a z-stack images that are tiled side by side. In order to reconstruct the real 3D stack from the raw data, the different subsections of the images need to be carefully aligned and corrected for residual orientation mismatches. The $N \times N$ focal planes are aligned one on top of each other using a calibration matrix, generated at every imaging session. Using 200 nm fluorescent beads mounted on a coverslip, a focal series is generated by scanning the slides along z in steps of 60 nm or 100 nm with a piezoelectric stage. During the scan, the same beads appear successively in focus in each MFM sub-image. The beads are localized by fitting the fluorescence intensity in each sub-image to a 2D Gaussian profile. A transformation matrix is generated to superimpose the 2D localizations in the different focal planes. The same transformation is used on the experimental data to reconstruct the 3D volume for each time frame. The calibration procedure returns also the exact experimental interplane distance. The axial position of each focal plane is computed by a Gaussian fitting of the axial intensity profile of each bead on the plane of interest. The slope of the linear curve that relates each plane to its focal position returns the interplane distance. This is constant within an axial chromatic dispersion error that the CCG cannot correct. It is important to note that (3.3) and (3.4) show the wavelength-dependent MFG behavior. As a consequence, imaging at a different wavelength results in a slight modification of the corrected phase-shift profile that corresponds to a different axial position. Specifically, the effective Δz scales linearly with the wavelength.

In [51], authors demonstrated MFM imaging of the dynamics of Cse4 yeast centrosomes using a 100X, oil-immersion, 1.4 NA Nikon objective combined with 3×3 MFG. In this configuration, the volume depth acquired at every camera

exposure was ~4 μm. Single-molecule tracking has also been performed with the same objective and MFG to investigate the dynamics of RNA polymerase. MFM has been demonstrated to be compatible with multicolor whole-cell (d)STORM-(F)PALM super-resolution imaging. Examples include mitochondria in Hela cells and tubulin in *S. cerevisiae* yeast cells [104].

3.1.3 Engineering multiple multifocus gratings to tune the acquisition volume

The MFG is a phase-only, distorted grating, etched in fused silica. The main motif is designed to efficiently splitting the emission evenly between the diffraction orders of interest. In a phase-only diffraction grating, the shape of the grating pattern and its etching depth determines the energy distribution between the orders. We have developed our method with the idea of providing a completely tunable system. For that reason, we designed multiple kinds of gratings, each one engineered to work with a specific objective and a spectrum of wavelengths.

In a standard microscope, the PSF is calculated as the square of the Fourier transform of the pupil function (see equations (1.2) and (1.3)). In MFM, the phase grating modifies the pupil function. Calling G the matrix that describes the phase shift introduced by the MFG, the light distribution after diffraction of a multifocus microscope is given by the square of the Fourier transform of G (assuming an incoming plane wave). This principle is used to design the MFG.

The algorithm for the generation and optimization of MFG is described in [51]. The best motif design is computed by numeric iterations. For 9 planes MFG, the optimum diffraction performance consists of 3×3 diffraction orders of maximum brightness and evenness. Introducing the target matrix T to represent the desired diffraction orders distribution, a starting guess for G is created as a matrix of randomly distributed black (-1) and white (+1) pixels, representing respectively a phase shift $\phi_{pix} = 0, \pi$. The fast, 2D Fourier transform of G, $FFT2(G)$, is calculated and then squared to find the associated diffraction order distribution. Then, the algorithm calculates the cost function $[FFT2(G)]^2 - T$. In a following step, the phase of a random pixel of G is flipped, and the cost function associated with the new matrix is computed. The flipping is accepted if the new cost function was lower than the previous one. In a minimization process the algorithm loops this procedure over all the pixels of G to reduce the cost function. The result of the minimization process is a matrix G that describes the optimal grating pattern to produce 3×3 diffraction orders with optimized light distribution. The same algorithm can be used to design phase gratings for specific number of imaging planes.

In the optimization algorithm, it is also possible to modulate the phase of each pixel ϕ_{pix} to be 0 or a fraction of 2π. By modulating ϕ_{pix}, phase-tuned binary grating

[105] and multi-phase grating [106] were produced. The later have been reported to have a theoretical efficiency of 90%, against the 67% efficiency of binary phase grating such as the one reported in [51]. The phased tuned binary gratings show a multiwavelength compatible behavior and an efficiency of 75% that is comparable to the measured performance of multiphase gratings.

In practical terms, this phase shift corresponds to a physical etching depth of

$$\epsilon = \frac{\phi_{pix}\lambda}{2\pi(n-1)}, \tag{3.5}$$

where λ is the design working wavelength of the grating and n is the refractive index of the substrate at this wavelength.

Following this routine, we designed two different $MFGs$ in order to regulate the acquisition volume, specifically MFG_9 and MFG_4 that acquire simultaneously 9 and 4 planes, respectively. MFG_9 is equivalent to the MFG reported in. MFG_9 is designed to work with a 100X, oil-immersion, 1.4 NA, at the wavelength $\lambda = 620$. In this configuration, the spacing between planes being $\Delta_z \sim 450$ nm, MFM produces the simultaneous acquisition of a volume ~4 μm height. For such a grating, the authors of [51] reported a measured 65% efficiency with evenness between focal planes for a 9 plane, $\pi -$ phase, MFG.

In addition to MFG_9, we designed a MFG_4 that acquires simultaneously 4 focal planes. The optimization process results in a periodic pattern that distributes the fluorescence with high efficiency and uniformity over carefully chosen 4 of the 3×3 planes of the standard MFM acquisition matrix. For MFG_4, as suggested by the simulation, the phase shift from each pixel that provides the best efficiency and uniformity is $\phi = \pi$. By design, the space between planes is ~ 500 nm when used in combination with the 60X, water-immersion, 1.27 NA objective (FIG. 36).

From the fluorescent beads $z -$ stack calibration acquisition described in paragraph 3.1.2, it is possible to measure the real spacing between planes by

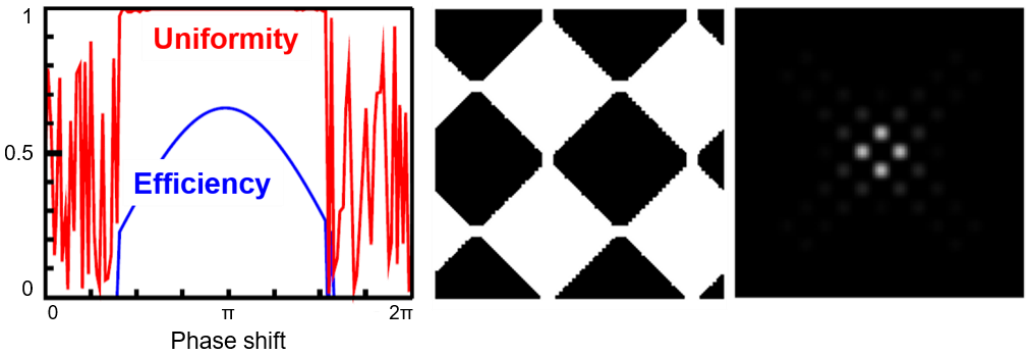

FIG. 36 – 4-planes diffraction grating. *The first box shows the efficiency and uniformity of the best grating performance designed for a phase difference of ϕ_{pix}. The second box shows the periodic pattern (before distortion) of the 4-planes diffraction grating. The third box shows the diffraction order distribution over the four diffraction orders* $(\pm 1,0)$ *and* $(0,\pm 1)$. *Adapted from* [105].

determining the axial position of each plane at which the beads intensity is maximal. For MFG_4, these measurements have suggested a real spacing of ~ 560 nm. Therefore, MFG_4 permits the instantaneous acquisition of a ~ 2 µm. However, for single-molecule localization, we can add the 1.5X built-in microscope additional magnification to obtain a spacing of ~ 250 nm. In this way the axial PSF is better sampled. Switching between MFG_9 and MFG_4 permits to easily tune the observation volume according to the sample of interest (**FIG. 37**).

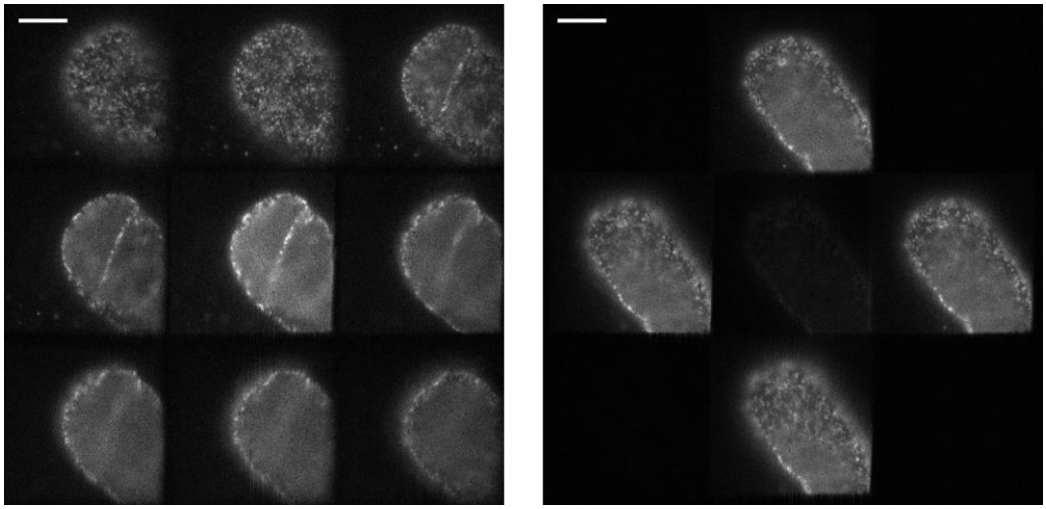

FIG. 37 – Tuning the acquisition volume by switching between 9-planes and 4-plane diffraction gratings. *The raw images of GFP-labeled nucleopores NUP96 in U2OS cells show a comparison of the volumes that can be acquired with the two different gratings that we developed. With the 9-planes grating it is possible to acquire the entire volume of the nucleus, while with the 4-planes only a thinner portion is acquired (bottom part of the nucleus). Scale bar 10 µm*

3.2 Single-objective selective plane illumination microscopy

Since its development, selective plane illumination microscopy (see paragraph 2.3) has become the gold standard for the reduction of the out-of-focus fluorescent background noise. Single-objective SPIM (soSPIM) [102] is an innovative method for single-molecule application of light-sheet microscopy that uses a unique, high-NA objective to produce the optical sectioning of the sample and to collect the fluorescence, increasing the photon collection efficiency and signal-to-noise ratio. The soSPIM technology has been fully developed by the "quantitative imaging of the cell" team, directed by Jean-Baptiste Sibarita, located at the Interdisciplinary Institute for Neuroscience, in Bordeaux. The development of our method has benefited from a collaboration with the team.

3.2.1 Dedicated sample holders for soSPIM

To perform light-sheet microscopy using a single high-NA objective, soSPIM relies on micro-fabricated custom-made sample holders for mounting the sample. The chip presents several arrays of aligned microwells, in the close proximity of a 45° inclined micro-mirror. Cells are placed in the microcavities before imaging. The excitation beam is obtained by focusing a collimated beam using the microscope objective. The beam is reflected on the mirror and directed towards the well to form a horizontal light sheet by fast beam scanning. The chip geometry guarantees the alignment of the microwell with the microscope optical axis. As such, the same objective is able to collect the resulting fluorescence signal. The chip is designed in a way that the bottom of the cavity is ~5 µm higher than the bottom of the mirror (FIG. 38). Therefore, the light-sheet can illuminate any portion of the sample without any unobservable region such in RSLM (see paragraph 2.3.2) and LSBM (see paragraph 2.3.3).

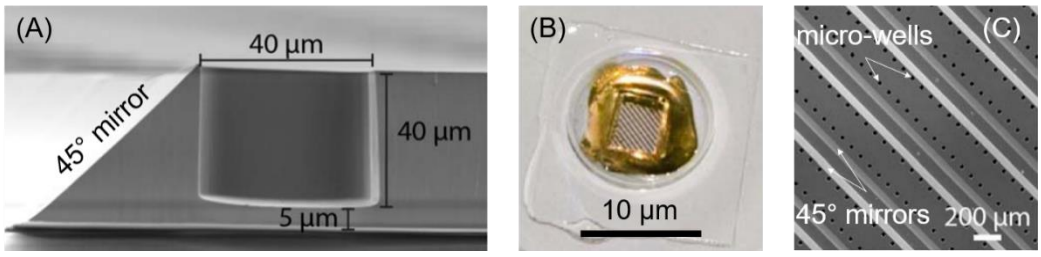

FIG. 38 – Microfabricated custom-made sample holder for soSPIM. *(A) SEM image of the section of a silicon wafer displaying a 45° surface created by anisotropic etching and a microwell created by dry etching. (B) final micro-fabricated device displaying 45° mirroring surfaces and microwells. (C) SEM images of a silicon wafer displaying 45° mirrors and an array of facing* 22 µm × 22 µm *microwells. Adapted from* [102].

The fabrication process of the chip is described in details in [102]. Here we recall the main fabrication steps. The primary mold for soSPIM chips fabrication is produced in silicon wafers by anisotropic etching in an alkaline solution (tetra-methyl ammonium hydroxide). A primary mold for cavities flanked by exactly 45° inclined surfaces is obtained by tuning the etching condition, i.e. alkaline solution, surfactant concentration or etching-bath temperature. Microwells 45 µm height and with different sizes (22 µm × 22 µm, 24 µm × 24 µm, 40µm × 40 µm and 60 µm × 300µm), aligned with the 45° inclined surfaces can be created with this procedure. The silicon wafer is replicated into a secondary mold made of polydimethylsiloxane (PDMS). With a capillary process, the secondary PDMS mold can be reproduced on standard coverslip using a UV-curable and glass index-matched polymer. The chips are then coated with a thin layer of gold by plasma sputtering in a vacuum chamber to make the 45° surfaces reflective. After metallization, the mirrors are protected with a layer of UV-curable polymer (NOA

73, Norland Products), applied by capillary flow while covering the microwell with a flat piece of PDMS. After UV exposure, PDMS is peeled off and the unprotected metal coating is removed by wet etching. Bigger soSPIM chips for the observation of embryos can be fabricated with a similar process.

3.2.2 The soSPIM excitation architecture

In soSPIM, the light-sheet is obtained by fast scanning a focused Gaussian beam. This section describes the required optical scheme to precisely control the position of the light-sheet at the sample (**FIG. 39**).

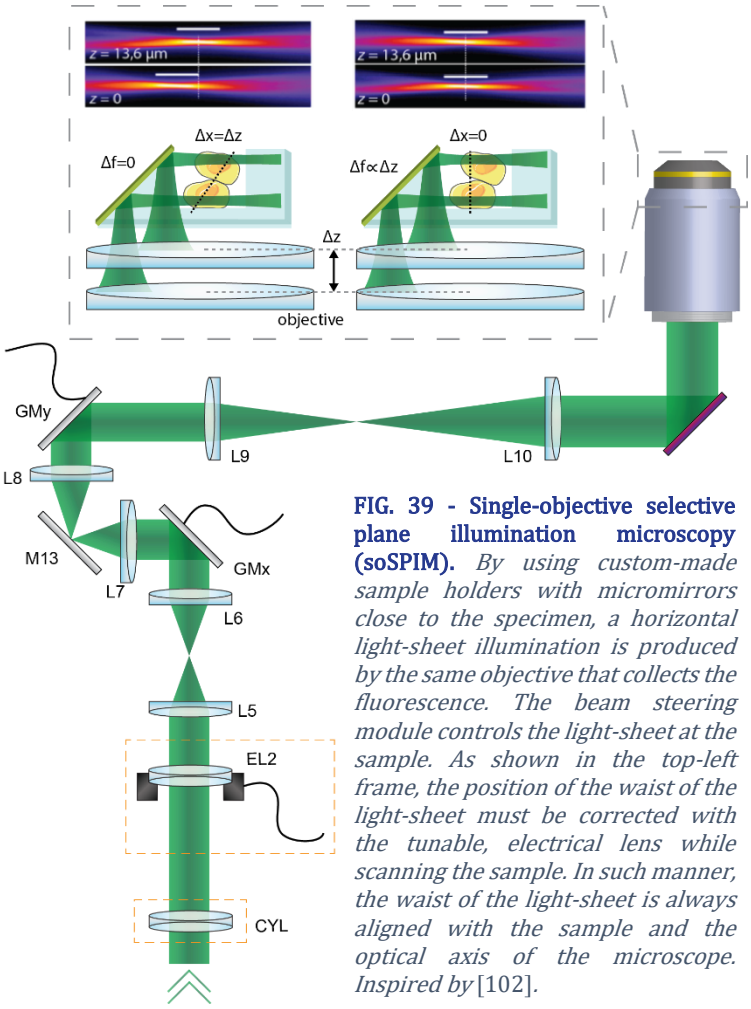

FIG. 39 - Single-objective selective plane illumination microscopy (soSPIM). *By using custom-made sample holders with micromirrors close to the specimen, a horizontal light-sheet illumination is produced by the same objective that collects the fluorescence. The beam steering module controls the light-sheet at the sample. As shown in the top-left frame, the position of the waist of the light-sheet must be corrected with the tunable, electrical lens while scanning the sample. In such manner, the waist of the light-sheet is always aligned with the sample and the optical axis of the microscope. Inspired by* [102].

To fully control the illumination, it is necessary to regulate (i) the lateral position of the excitation beam, (ii) the tip-tilt of the light-sheet compare to the mirror and the microwell, (iii) the position of the waist compare to the sample, which in soSPIM does not coincide with the nominal focal plane of the objective.

Since it is not possible to control all these parameters after the objective, it is necessary to access them remotely or at a plane conjugated to the Fourier plane of the objective. In fact, considering that a Fourier transformation relates the back focal plane of the objective to the sample plane, we can regulate the three parameters respectively (i) by changing the tip-tilt angle of the Gaussian beam compare to the back pupil of the objective, (ii) by displacing the excitation beam over the back focal plane of the objective, (iii) by introducing a defocusing of the excitation at the back pupil of the objective.

To do that, three relay systems composed by achromatic lenses originate three planes that are optically conjugated to the back focal plane of the objective. The systems are composed by lenses $L5$ and $L6$, $L7$ and $L8$ ($f_5 = f_6 = f_7 = f_8 = 50$ mm, AC254-050-A, by Thorlabs), $L9$ and $L10$ ($f_9 = 150$ mm, AC254-150-A, by Thorlabs, $f_{10} = 200$ mm, AC254-200-A, by Thorlabs) respectively. A tunable, electrical lens $EL2$ (Custom EL-10-30, by Optotune; focal lengths from -80 mm to +1000 mm) is placed on the first Fourier plane. This lens introduces a defocusing of the excitation Gaussian beam that adjusts the position of the waist of the light-sheet compared to the sample. The displacement of the waist varies linearly with the current i applied to $EL2$, i being dependent on the inverse of the focal length of $EL2$. The two galvo-mirrors GM_x and GM_y (ScannerMAX 506 actuators, by Pangolin, with dielectric mirrors, by Chroma) are placed respectively on the second and third planes conjugated to the Fourier plane of the objective. In this way, they control the tip-tilt angle of the excitation beam at the back focal plane of the objective, and thus regulate the position of the light-sheet at the sample plane. GM_x is responsible of the z positioning of the light-sheet, while GM_y produces the fast steering of the beam in the y direction. Finally, a mirror M_{13}, placed at a conjugated plane to the sample plane, controls the tip-tilt of the excitation beam at the sample plane. This is equivalent to displacing the beam in the BFP of the objective. The $M13$ mirror is placed at equal distance $f_7 = f_8 = 50$ mm between $L7$ and $L8$.

In [102], the authors demonstrated soSPIM single-molecule imaging capabilities performing 2D and 3D STORM super-resolution on the nuclear membrane of fixed cells, using a 60X, 1.2 NA, water-immersion objective (CFI Plan Apochromat VC 60×/1.2-NA water-immersion objective, Nikon). In such configuration, the light-sheet has strong optical sectioning power since its thickness is < 2 µm. The 3D localization of chromophore has been performed by introducing a cylindrical lens on the emission path in order to encode the axial position by the ellipticity of the recorded PSF. 3D volume imaging was obtained by scanning the thin light-sheet through the sample. The single-molecule 3D localization precision reached 22 nm × 74 nm ($xy \times z$) when imaging close to the bottom of the well. To demonstrate the flexibility of soSPIM, the authors also used lower NA objective to produce thicker light-sheet. With a 20X, 0.5 NA (CFI Plan Fluor 20×/0.5-NA) they

produced a ~ 4.3 µm thick light-sheet to observe embryos of *Drosophila*, imaging in 2D the histones and the membrane of the embryo. Thicker light-sheet can be obtained using a 10X, 0.3 NA (CFI Plan Fluor 10×/0.3-NA, Nikon).

3.2.3 Illumination software control

During the imaging process, the soSPIM architecture is completely controlled by a plugin in MetaMorph [107], developed by the authors of [102].

The software switches between different illumination modes to perform specific tasks with well controlled parameters. The main two modes are the soSPIM imaging mode and the widefield mode. In the latter, the excitation beam can be scanned over the area occupied by the sample without any reflecting on the side micro-mirror to simulate an epi-illumination. The parameters that control the beam displacement are organized in different tabs. The first step for using soSPIM is to calibrate the movement of the galvo-mirrors in the architecture according to the field of view. The procedure is controlled by the "Calibration" tab, which allows to draw standard excitation patterns by binding the simultaneous movement of two galvo-mirrors. A rectangular excitation profile is visualized thanks to a uniform fluorescent layer deposited on a covergalss. The dimensions of the rectangle are adjusted to cover the full area of the field of view. During the following calibration step, the software displaces a focused beam by discrete steps within the borders of the rectangle, generating a fluorescent spot. At each step, the center of the spot is localized with high precision. A calibration table is created in order to relate the galvo-mirror angle to the position of the excitation spot at the sample (**FIG. 40**).

The light sheet is produced by scanning the focused beam along the desired direction. This direction is defined manually by drawing a line along the edge of the reflecting mirror observed in transmission light. Once the system is calibrated and the light-sheet axis defined, the "Control" tab regulates the parameters associated with the dimension and position of the light-sheet during imaging. The parameters in this tab include the width of the light-sheet, its lateral and axial position compared to the well. The same tab regulates the focus of the electrical lens to displace the waist of the light-sheet. The software can correlate the axial position of the light-sheet, the position of the waist and the displacement of the objective. In fact, displacing the objective lens changes the plane of focus on the sample but the light-sheet remains at its previous position. The waist position will be shifted away from the optical axis. When the three parameters are locked together, the light-sheet always coincides with the focal plane of the objective and the waist is maintained aligned with the optical axis. Any shift in the light sheet position and waist due to the displacement of the focus of the objective is automatically compensated by the corresponding focal power of the electric lens and a displacement on the beam on

the reflecting micro-mirror (see **FIG. 39**).

The beam steering parameters are controlled in the "Setup" tab, which allows the user to regulate the properties of the scanning of the galvo-mirrors. The line along which the beam is scanned to produce the light-sheet is sampled by a defined number of points. The timespan of the light-sheet is defined by controlling the number of points and the scanning rate of the distance between two consecutive points. The width of the light-sheet, the sampling and the rate must be optimized such that the exposure time of the camera is a multiple of the timespan.

In MetaMorph, the soSPIM plugin can be interfaced with the laser sources and the dichroic mirrors of the microscope (see paragraph 1.2). The selection of the excitation wavelength and the respective filters is thus automated. Also, the software can control the intensity of the laser light.

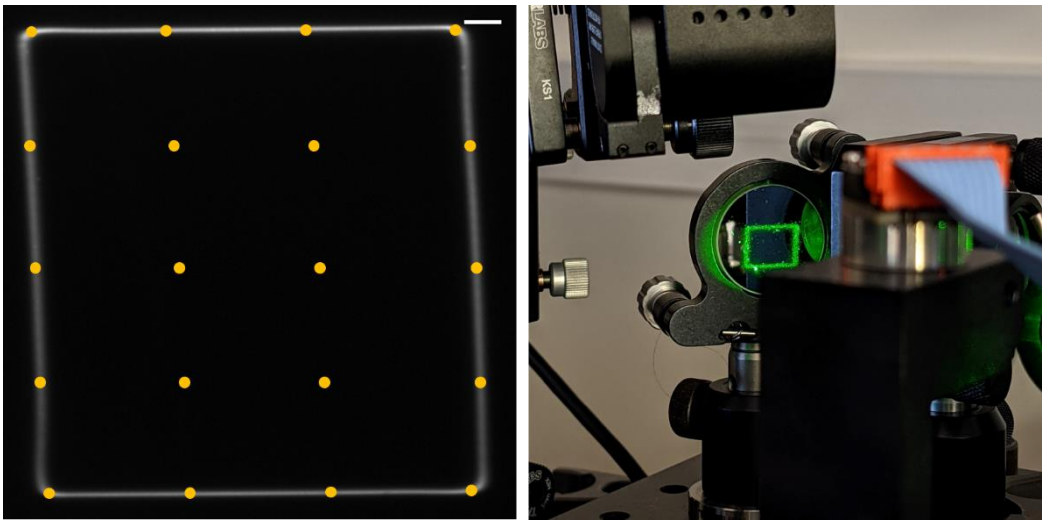

FIG. 40 – Calibration of soSPIM architecture. *The left panel shows the field of view when the rectangular calibration pattern is produced by scanning the beam through the galvo-mirrors. The yellow dots represent the focused beam being scanned over the rectangular pattern. Scale bar 10 μm. The right panel shows how the beam is steered to produce a rectangle with dimensions smaller than the optics of the soSPIM architecture.*

3.3 Automated tunable telescope for the tuning of the excitation volume

Our method has been developed with the idea of providing a modular system able to produce a confined, tunable excitation light-sheet to match the acquisition volume defined by multifocus grating installed on the detection path. For this we designed an automated tunable telescope to be installed on the illumination path, that regulates the dimension of the excitation beam. In the configuration in which

the light-sheet is originated by steering a focused Gaussian beam, the tunable telescope sets the size of the excitation laser before it enters the soSPIM architecture. The excitation volume is defined by the waist of the Gaussian beam. The waist of the focused beam can be regulated by changing the dimension of the collimated laser at the back pupil of the illumination objective (FIG. 41). We designed a tunable telescope that, ideally, introduces a range of demagnification factors for which the size of the beam waist varies between 1 µm and 10 µm.

Moreover, in our method, the excitation beam can be deviated to a different beam shaping module (see paragraph 3.4.4 and FIG. 33) before going through the soSPIM architecture. In this configuration, the automated tunable telescope is used to optimize the dimension of the beam in order to reduce the light losses caused by the shaping.

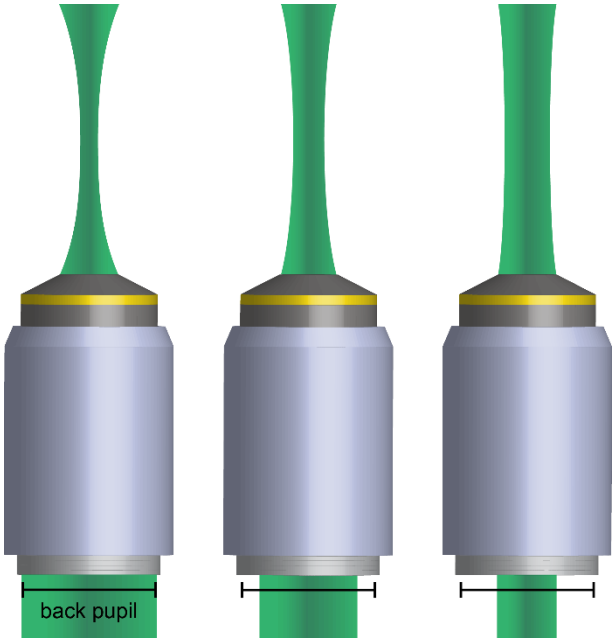

FIG. 41 – Working principle of the tunable beam expander. *The excitation volume can be tune by regulating the thickness of the light-sheet. By changing the size of the collimated excitation beam at the back pupil of the objective, the waist of the focus beam can be varied, and thus the excitation volume. Specifically, the minimum waist is obtained when the beam overfills the back pupil of the objective, and it increases when the size of the collimated excitation beam is reduced.*

3.3.1 Modeling the automated tunable telescope

To tune the excitation volume, we designed the beam expander module to regulate the dimension of the excitation beam at the back pupil of the illumination objective, typically a water-immersion, 60X, 1.27 NA. In this paragraph, first, the modeling of the automated tunable telescope will be described with reference to FIG. 42. Later, the calibration procedure will be presented in details. The complete procedure for precise alignment can be found in A1.2.

In our setup, a laser combiner (L6Cc, wavelengths: 405 nm, 488 nm, 561 nm, 640 nm, by Oxxius) is coupled with an optical fiber $NA_{fiber} = 0.12$. At the output of

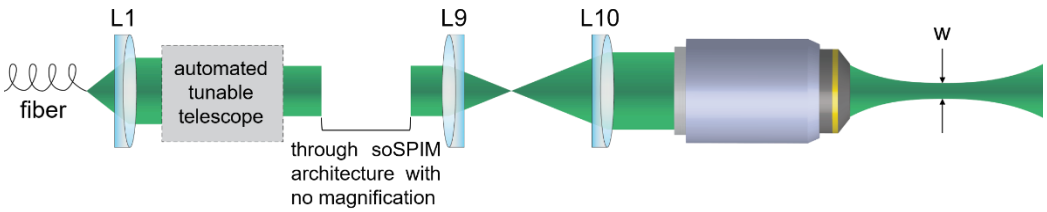

FIG. 42 – Beam expander function. *The beam expander is designed to tune the excitation beam size before it enters the soSPIM module. The design of the beam expander unit takes in account the magnification introduced by the beam steering module.*

the fiber, the laser beam is collimated by a collimator $L1$ (F950FC-A, by Thorlabs) with focal length $f_1 = 10$ mm. The size of the collimated beam is $D_0 = 2f_1 NA_{fiber} = 2.4$ mm. Considering the collimated laser entering the back pupil of the illumination objective, the waist of the excitation beam of wavelength λ can be estimated as

$$w = 0.61 \frac{\lambda}{NA_{eff}}, \tag{3.6}$$

in which the effective numerical aperture

$$NA_{eff} = n \sin\left(\arctan\left(\frac{D_{obj}}{2f_{obj}}\right)\right) \tag{3.7}$$

depends on the refractive index of the objective immersion medium n of, the diameter of the collimated beam at the BFP of the objective D_{obj} and its focal length f_{obj}. By construction

$$f_{obj} = f_{TL}/M, \tag{3.8}$$

where M is the magnification introduced by the combination of the objective and the tube lens TL of f_{TL} focal length.

Considering (3.6) and (3.7), in order to tune the waist w of the excitation beam, we designed a tunable telescope that introduces the optimal range of magnification to control the dimension of the beam at the back pupil of the objective D_{obj}. For that, we took in consideration that the soSPIM architecture introduces another magnification factor f_{10}/f_9 given by the lenses $L10$ and $L9$. Therefore, from (3.6), (3.7) and (3.8), the magnification factor that the automated tunable telescope is designed to introduce in order to obtain a certain thickness of the light-sheet w is

$$M_{tel} = \frac{1}{NA_{fiber} M} \frac{f_{TL} f_9}{f_0 f_{10}} \tan\left(\arcsin\left(\frac{0.61\lambda}{wn}\right)\right). \tag{3.9}$$

In a standard, two-lenses, telescope, the two optics are placed at a distance that equals the sum of their focal lengths. The magnification factor of the telescope is given by the ratio between the focal lengths of the two optics, that constitute the two degrees of freedom describing the system. To be able to tune the magnification, the two degrees of freedom must be variable. For that, our automated tunable telescope has been designed as a compact, three-lenses compound system, in which the first lens is a tunable electrical lens EL (EL-16-40-TC-VIS-20D, controlled by a lens driver 4i, by Optotune) and the second lens $L2$, with fixed focal length, is placed on a translation stage (LNR502/M, TravelMax by Thorlabs), controlled by a stepper-motor (BSC201, by Thorlabs). The third lens, $L3$, has fixed focal length and it collimates the output beam (**FIG. 43**). Moving the translation stage results in varying the distance between L2 and L3 and thus the effective focal length of their combination, as well as the distance to the EL. The focal lens of the electric lens is adjusted accordingly in order to collimate the output beam. Our module is designed to output a collimated beam with a magnification equal to the desired one, given by equation (3.9). These conditions impose the definite geometry of our module. We define f_{EL}, f_2 and f_3 the focal lengths of EL, $L2$ and $L3$, respectively. We call d_2 the distance between EL and $L2$ and d_3 the interspace between $L2$ and $L3$. The front focal length of the three-lenses compound system is

$$F = \frac{f_3(d_3 - \Phi)}{d_3 - (\Phi + f_3)}, \tag{3.10}$$

where

$$\Phi = \frac{f_{EL}(d_2 - f_2)}{d_2 - (f_1 + f_2)} \tag{3.11}$$

is the back focal length of the module.

The magnified excitation beam exiting the automated tunable telescope is collimated if $F \to \infty$, which is obtained from (3.10) and (3.11) when

$$[d_2 - (f_{EL} + f_2)](d_3 - f_3) - f_{EL}(d_2 - f_2) = 0\,. \tag{3.12}$$

The design of our module imposes that, at every displacement s of the translator, $d_2 = D_2 + s$ and $d_3 = D_3 - 3s$, where D_2 and D_3 are the initial distances between EL and $L2$ and $L2$ and $L3$, respectively. Moreover, the translator can produce a maximum displacement of 50 mm, while the optical power range of EL is -10 dpt to 10 dpt. Imposing these boundary conditions in the solution of (3.12) gives the combination of displacement s and focal length f_{EL} for all the magnification values M_{tel} that the module is required to produce. For that, $L2$ and $L3$ has been chosen so that $f_2 = f_3 = 50$ mm (AC254-050-A, by Thorlabs) and placed in a way that

$D_2 = \overline{\text{ELM5}} + \overline{M5\text{M6}} + \overline{\text{M6M7}} + \overline{\text{M7M8}} = 500$ mm and $D_3 = \overline{\text{L2L3}} = 100$ mm. For these values of D_2 and D_3, the EL is kept flat, and $M_{tel} = 1$.

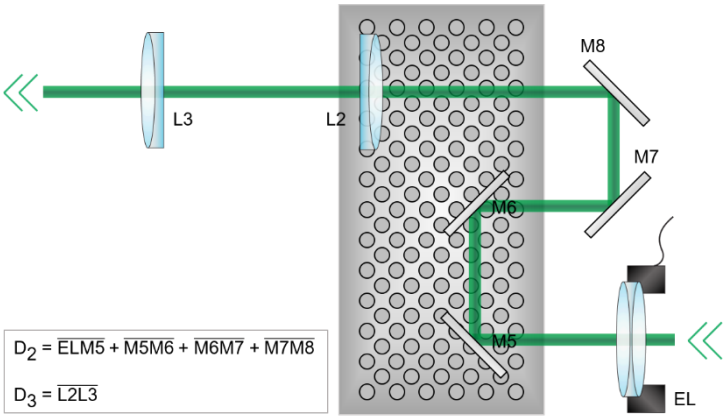

FIG. 43 – Optical scheme of the tunable beam expander. *The displacement of the translation stage changes the distances between EL and L2 and between L2 and L3. The focal length of EL is varied according to the displacement of the translation stage.*

3.3.2 Calibration and automatization of the tunable beam expander

As described by (3.9) and (3.12), to obtain a light-sheet with a certain thickness w, the tunable telescope has to introduce a certain demagnification factor that depends on the focal length of the electrical lens f_{EL} and the displacement of the translator s. An accurate calibration of the tunable beam expander module has been performed to determine the values of f_{EL} and s needed to regulate precisely the thickness of excitation light-sheet.

To calibrate the relationship between the displacement s and the focal length f_{EL}, we measured the optical power of EL that produces a collimated beam at the output of the tunable telescope for different positions of the translator s, checking the collimation with a shear plate. The measurement was repeated for all the combination predicted by the theoretical model to generate the span of magnification M_{tel}. The collimation becomes more sensitive to the optical power of EL when short focal length f_{EL} are required. In fact, the collimation of the beam at long f_{EL} could be found in an optical power range wider than the sensitivity of the lens driver, but limited to up to 4 digits. In this case, averaging the values for which the beam appears to be collimated gives the required optical power of EL. We decided to evaluate the uncertainty as the maximum distance from the average value because of the limited range of variability of the measurement. For short f_{EL} the uncertainty is given by the sensitivity of the lens driver. The calibration curve describing the relationship between the displacement s and optical power of EL shows a different behavior from the predicted curve. First, an offset of the optical power appears when the current that controls the shape of EL is set to 0 and the

lens is supposed to be flat. This means that the electrical lens has and offset focal length $f_{EL}^{offset} \sim 1200$ mm. Second, for short f_{EL} the calibration curve steps away from the predicted curve. This is due to a non-perfectly linear response of the EL. Also, although we placed the EL horizontally to moderate the gravity effect, the lens introduces some aberration in the wave-front of the beam that might affect the reading of the collimation (FIG. 44).

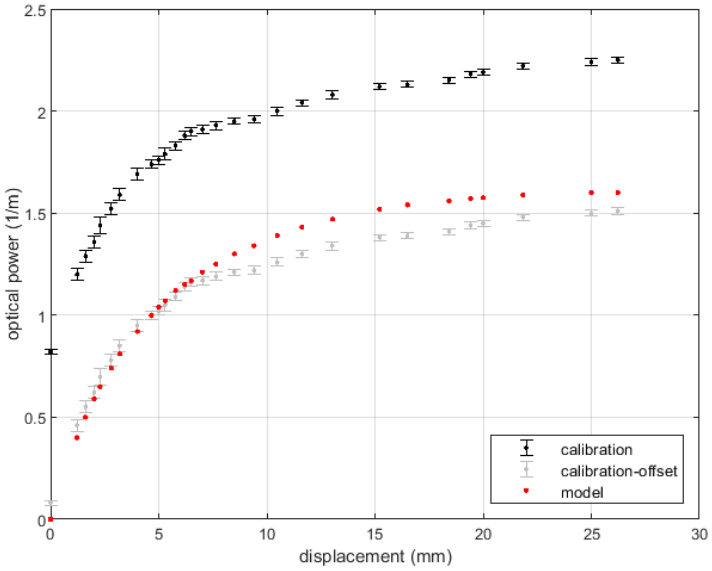

FIG. 44 – Calibration curve of EL optical power as a function of the translator displacement. *The curve describes the collection of values of EL optical power and translator displacemen that are needed to produce the span of magnification factors (black). The optical power of EL presents an offset that appears when the lens is supposed to be flat, inducing an offset focal length f_{offset}. Taking in consideration the offset value the calibration curve (grey) and the model (red) still differs because the EL introduces aberration of the beam front-wave.*

The displacement s and the focal length f_{EL}(or the optical power of EL) are the parameters that control the demagnification factor introduced by the tunable telescope M_{tel}. To completely characterize the performance of the system, we measured the demagnification factors introduced by the calibrated combinations (s, f_{EL}). Using a CMOS camera, we imagined the collimated beam profile for each calibrated set of values $(s, f_{EL})_i$. The beam size D_i has been determined by fitting the normal distribution of the beam to a Gaussian curve. For each combination $(s, f_{EL})_i$, the demagnification factor $M_{tel,i}$ is determined as the ratio D_i/D_0, where D_0 is the beam size measured for $(s, f_{EL}) = (0, f_{EL}^{offset})$. The uncertainty on the quantification of the beam size is obtained as the standard deviation calculated over multiple measurements of D_0. As shown in FIG. 45, the telescope introduces the expected demagnification factors for optical powers below 1.5 m^{-1} (corresponding to $f_{EL} \sim 670$ mm). Above this value the measured demagnification factors depart from the predicted values. This region corresponds to strong demagnification factor M_{tel}. To obtain such results the beam must be highly focused along the optical path by EL, and the short focal length introduce astigmatism [108]. Also, although we placed the EL horizontally to reduce the gravity effect, aberrations and distortions of the beam wavefront are still introduced, compromising the performance of the

beam expander module. However, the range of magnification introduced by the tunable telescope over which the measurements behave as predicted allows to regulate the thickness of the light-sheet between 1μm and 4 μm. This range matches the span of acquisition volumes defined by the different multifocus gratings placed on the detection path (see paragraph 3.1.3).

To automatize the tunable telescope, we have developed a LabVIEW [109] program, based on the calibration curves that relate the magnification M_{tel} with the displacement s and the optical power of the EL (or its focal length f_{EL}). The code integrates the drivers that control the translator stage (APT software, by Thorlabs) and the tunable lens (Lens Driver Controller, by Optotune). The interface allows to introduce the desired excitation volume, while the program automatically operates the displacement of the translator stage and the regulation of the EL optical power to obtain the correspondent M_{tel}.

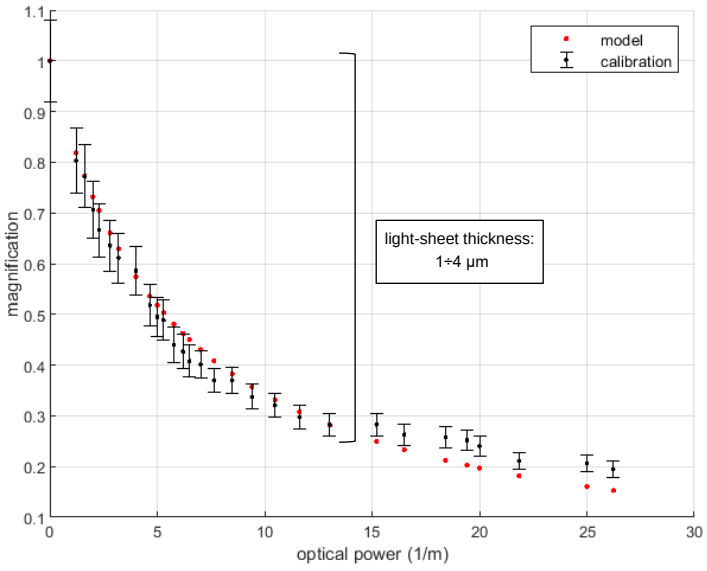

FIG. 45 - Calibration curve of the magnification factors. *The graph shows the magnification M_{tel} introduced by the beam expander as a function of the displacement of the translation stage. For any displacement, the optical power of EL must be adjusted according to the previous calibration. The calibration follows completely the model for all the magnification factors for which a light-sheet with thickness between 1 μm and 4 μm is produced.*

3.4 Homogeneous excitation by beam shaping and beam steering

The single-molecule detection and localization precision strictly depend on the number of photons that the single emitter produces (see equation (1.15) in paragraph 1.5). In our method, we confine the excitation to a selected volume of the sample to produce instantaneous 3D imaging. Therefore, it is crucial to produce homogeneous illumination over the volume of interest in order to set identical excitation and detection conditions.

To produce homogeneous excitation, two different methods for producing have

been explored in this project. The first strategy is based on the 2D scan of a focused Gaussian beam, and it has been implemented by modifying the Metamorph plugin that controls the beam steering module. The second strategy is based on producing homogenous excitation by shaping the beam wavefront. For that, we designed a beam shaping module, engineered to work for multiple wavelengths. The modulation of the beam wavefront is performed by a digital micromirror device (DMD). A removable mirror, mounted on a magnetic base, controls the optical path of the excitation beam path following the tunable beam expander. The beam can be directed first to the beam shaping module or to the steering module directly (see FIG. 33). In the following paragraphs, the details of the design and implementation of the module will be described, together with an introduction to the optics of DMD and coherent light. The paragraph will conclude presenting the results obtained for the homogeneous illumination.

3.4.1 Homogeneous excitation through two-dimensional scanning of a focused Gaussian beam

The first strategy that we explored to produce volumetric homogenous excitation is based on scanning a diffraction limited focused Gaussian beam in two dimensions, one being the width of the light-sheet and one being its height. In this configuration, the size of the excitation beam to be focused and scanned is regulated by the automated tunable telescope, and then sent directly towards the beam steering module. To be able to produce the two-dimensional steering of the beam, the team of Jean-Baptiste Sibarita at IINS, Bordeaux developed a dedicated scanning mode in the Metamorph plugin that controls the soSPIM architecture. The module performs a two-dimensional scan of the excitation reflected beam in the $x-z$ plane (FIG. 46). To create a thick light-sheet, the beam is steered on multiple lines along x, separated by a defined interline distance along z. To note here that in reality the beam is scanned laterally in $x-y$. The reflection on the side micromirror transforms it to a $y-z$ scan. To regulate this excitation, in addition to the width of light-sheet and its position compared to the well in the “Control” tab, two more parameters for the beam steering have been added in the “Setup” tab to regulate the thickness of the light-sheet and the interline distance along z. The shorter the interline distance is, the more homogeneous the light-sheet becomes. Also, the thickness parameter must be adjusted to be a multiple of the interline value. The thickness and the interline parameters determine the duration of the light-sheet scan. The latter must be a sub-multiple of the exposure time of the camera to reach a homogeneous excitation in each acquired frame.

However, this method did not provide the desired results in terms of homogeneity and tunability of the excitation (see paragraph 3.4.5 for the details of

the analysis). Also, we noticed that the synchronization of the scan of the beam with the exposure time of the camera was not optimal. These issues motivated us to develop an alternative strategy for producing homogeneous volumetric excitation based on the modulation of the illumination wavefront. Detailed description of the modeling and development of the beam shaping module, the optimization needed for performing with multiple wavelengths and the comparison of the performances of the two methods are given in the next paragraphs.

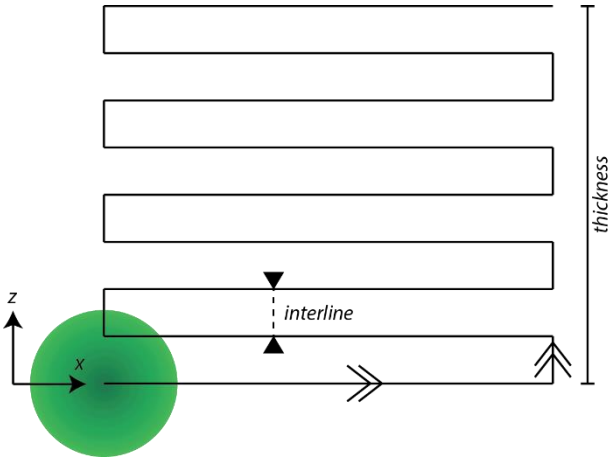

FIG. 46 – Homogeneous illumination by 2D scan of a Gaussian beam. *A dedicated function in the soSPIM Metamorph plugin has been developed for producing a thick selective excitation. The thickness and interline parameters that regulate such light-sheet can be adjusted to synchronize the scan with the exposure time of the camera.*

3.4.2 Design and optimization of DMD-based beam shaping for homogeneous excitation

A strategy for shaping a beam profile is based on liquid crystal spatial light modulators. Each pixel in such device controls the phase and amplitude of the part of the beam that it transmits. Other approaches for beam shaping rely on magneto-optic or acousto-optic devices and deformable mirrors. These technologies have been widely used for multiple fluorescence microscopy and adaptive optics applications [110], [111]. For the development of our beam shaping unit, we adopted a digital micro-mirror device (DMD) approach for shaping the intensity profile of the excitation laser beam. Such devices are cheap, can handle high light intensities and are not sensitive to light polarization.

The first step of the development has been the optimization of the pattern to be created by the DMD. We derived the ideal DMD pattern by simulating the intensity of a light-sheet produced by scanning an intensity-shaped Gaussian beam at the sample plane. We optimized the pattern to be produced by the DMD mirrors in order to obtain a light-sheet that could excite an extended sample volume with homogeneous intensity. We developed a MATLAB code for generating the modulation pattern and simulating the result of the beam steering (see A2.2). In the

code, the DMD is simulated as a matrix in which each element represents a miniaturized mirror that can be tilted by $\pm t$. To simulate the spatial modulation, the code superimposes the original Gaussian beam and the DMD pattern by matrices multiplication. The physical size of the mirrors D, as well as the grating pitch d, have been taken in consideration for evaluating the diffraction pattern. The obtained beam at the focal plane of the objective takes in account the diffraction limit imposed by the optics on the excitation path.

To derive the optimum modulation that produces homogenous excitation intensity, we initially considered the intensity profile obtained by scanning laterally a Gaussian beam (see equation (2.1) in paragraph (2.1)). The size of such beam can be controlled thanks to the automated tunable telescope that has been described in paragraph 3.3. The light-sheet produced by scanning such beam will generate a Gaussian excitation profile along z axis over the range of the different MFM imaging planes. The main issue with such profile is the high peak intensity in the center of the Gaussian profile when scanned along one dimension. A uniform light distribution requires the deletion of specific parts of the Gaussian beam and keeping only the uniform-intensity parts. Here we exploited the radial symmetry of a Gaussian beam: the intensity is distributed in concentric rings around the central peak. Our approach was thus to produce a central dark area in the middle of the beam and keeping a ring of light. A beam modulated with such pattern shows a reduced intensity in the central part, as well as the deletion of the outer tails of the typical Gaussian distribution when scanned. To find a more homogeneous intensity distribution we produced a double arch pattern by truncating the doughnut. Such modulated beam is composed by two arched parts that are steered horizontally to produce the light-sheet. The intensity profile of the excitation presents steep tails, while the central part can be further optimized. For that, we modified the double arch pattern such that the internal borders of the arches follow an elliptical curve proportional to $3y^2 + z^2$. The modulated beam with the elliptical double arch pattern is steered laterally (y dimension) to produce the light-sheet with a homogenous intensity distribution (**FIG. 47**). It is important to note that, due to diffraction effects, it is impossible to completely remove the tails of the average intensity distribution outside of the desired excitation volume. To regulate the excitation volume, the dimensions of the double arch pattern are adjusted. In the same time, and in order to minimize the light-loss, the automated beam expander regulates the dimension of the excitation beam to match the desired DMD pattern.

In practice, the DMD can be approximated to a 2D blazed grating. The excitation light being coherent, additional optical effects must be taken into considerations. To completely understand the design of the beam shaping module, an introduction to the DMD devices is given in the next paragraph, with a focus of the performance of such device when used in combination with coherent light.

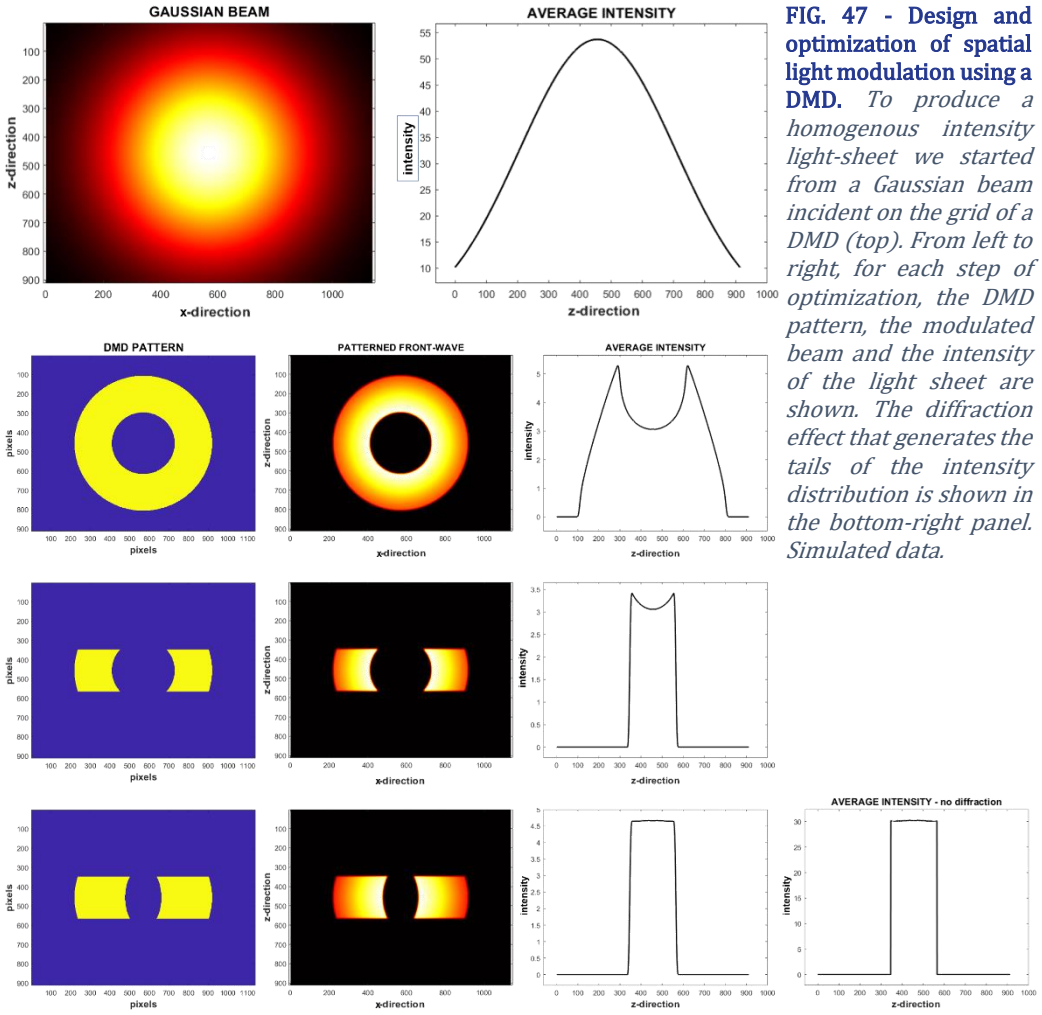

FIG. 47 - Design and optimization of spatial light modulation using a DMD. *To produce a homogenous intensity light-sheet we started from a Gaussian beam incident on the grid of a DMD (top). From left to right, for each step of optimization, the DMD pattern, the modulated beam and the intensity of the light sheet are shown. The diffraction effect that generates the tails of the intensity distribution is shown in the bottom-right panel. Simulated data.*

3.4.3 Digital micromirror device (DMD) and coherent light

A digital micromirror device represents the core of the digital light processing (DLP™) technology for the spatial modulation of light, developed and trademarked by Texas Instrument [112]. A DMD is a micro-optoelectrical system composed by a matrix of electro-mechanical miniaturized mirrors, each can be independently rotated by a tilt angle $\pm t$. The reflected light is thus modulated according to the orientation of the different mirrors.

Although the technology was originally developed for video projection, the wide availability, low cost and high speed of DMD, attracted many optical microscopy applications such as optical sectioning and super-resolution imaging [113], [114], SIM microscopy [115]–[117] or confocal microscopy [118]. However, using DMD in combination with coherent light sources originates non-trivial problems for the design of the microscope system, especially for multiwavelength applications. The

DMD is to be considered as a reflective blazed grating, and diffraction effects must be taken in account for the optimal design of the setup.

To introduce the elements of the optical theory that describes the functioning of a DMD in combination with coherent light, the diffraction effect introduced by the micromirrors that constitute the unit elements of the DMD must be considered. First, introducing the diffraction of light through a single slit will represent an approximation of the diffraction of a single mirror in 1D. Then the problem will be extended to multiple slits, before introducing the reflection effects. Finally, the DMD will be described as a two-dimensional reflective blazed grating. theoretical basis can be found in [5], [119].

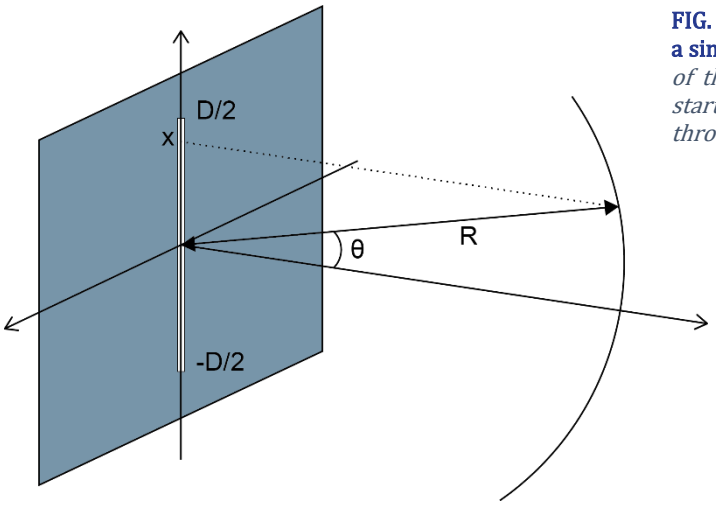

FIG. 48 – Plane wave-front through a single slit. *For modeling the effect of the DMD on coherent light, we start from the diffraction of light through a 1D slit.*

Let us consider a plane wave-front, incoming on a one-dimensional slit of width D. Light going through the slit and projected on a curved screen of radius $R \gg D$ will show interfering pattern (FIG. 48). It is possible to show that, for the angle θ, the intensity distribution of the diffracted light is

$$I(\theta) \propto \left(\frac{\sin\beta}{\beta}\right)^2 := \operatorname{sinc}^2\beta\,, \tag{3.13}$$

where $\beta = \pi D/\lambda \sin\alpha$. For a varying angle of incidence on the slit α_i, the peak of the $\operatorname{sinc}^2\beta$ will be centered on $\theta = -\theta_i$ and the (3.13) becomes

$$I(\theta) \propto \operatorname{sinc}^2\left[\frac{\pi D}{\lambda}(\sin\theta - \sin\theta_i)\right]. \tag{3.14}$$

Considering that $-\pi/2 < \alpha < \pi/2$, the total intensity in the far-field results

$$I \propto \int_{-\pi/2}^{\pi/2} \operatorname{sinc}^2\left[\frac{\pi D}{\lambda}(\sin\theta - \sin\theta_i)\right]. \tag{3.15}$$

If now we consider multiple identical slits so that the distance between the centers of two consecutive apertures is d, the phase relationship between the slits produces constructive and destructive interference effects that define the diffraction pattern of the slits. For normal incidence of light, it is possible to demonstrate that, for N slits

$$I(\theta) \propto \left(\frac{\sin\beta}{\beta}\right)^2 \left(\frac{\sin(N\alpha)}{\sin\alpha}\right)^2 , \tag{3.16}$$

where $\alpha = \pi d/\lambda \sin\theta$. Therefore, the local maxima of the light intensity distribution define the different diffraction orders. For normal incidence of light, the m^{th} diffraction order is located at $\sin\theta_m = m\lambda/d$, which becomes

$$\sin\theta_m = \frac{m\lambda}{d} - \sin\theta_i , \tag{3.17}$$

when the light incomes onto the slits with an incident angle θ_i. Also, the slit intensity profile constitutes an envelope function for the light intensity distribution in the different diffraction orders. Since the orders and the envelope move together with changing θ_i, the 0^{th} order and the envelope function are locked together (FIG. 49).

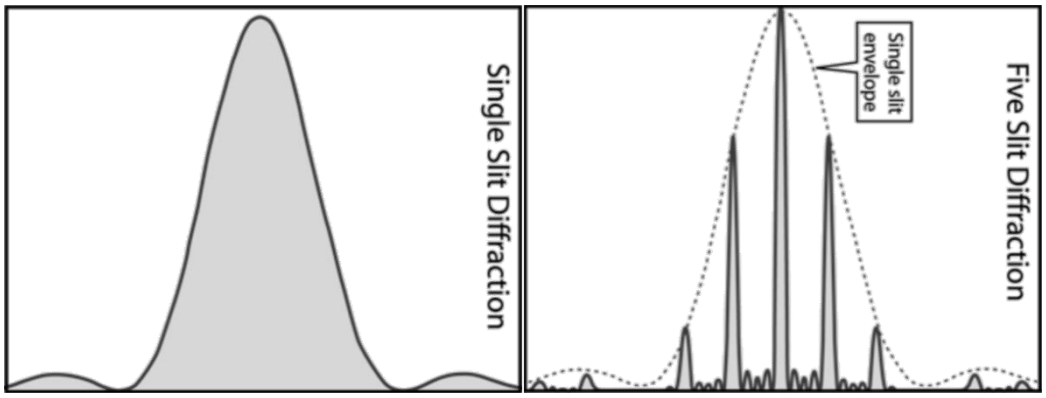

FIG. 49 – Light distributes in diffraction orders after going through five slits. *The amplitude of each diffraction order is given by the envelope function corresponding to the single slit intensity profile. Adapted from* [145].

Let us consider now a reflective grating so that the mirrored surfaces replace the slits. The orders location will be determined by the grating pitch d, the wavelength λ and the incident angle θ_i, the 0^{th} order being located at $\theta_0 = -\theta_i$ (incident and reflected light are on the same side with respect to the grating). The peak of the envelope function is at the specular reflection position. It depends only on the grating tilt angle t, according to

$$\theta_E = 2t - \theta_i , \tag{3.18}$$

and for that, is decoupled from the 0^{th} order. The m^{th} diffraction order is said to be blazed when θ_i and the tilt angle t of the groove faces are arranged such that the envelope peak in centered on it. In this case that is also known as the blazing condition, the majority of the light intensity is directed to the m^{th} diffraction order. If the envelope function falls in between orders, the light is distributed over several of them, describing the off-blaze condition. To conclude, it is fundamental to note that the different diffraction orders location depends on the grating pitch d, the wavelength λ and the incident angle θ_i while the position of the envelope peak depends on incident angle θ_i and the tilt angle t. Here, the zero-intensity of the envelope function depend on the width of the slit D and the wavelength λ. As a consequence, for all $m \neq 0$ only a given order is blazed for a certain wavelength (**FIG. 50**).

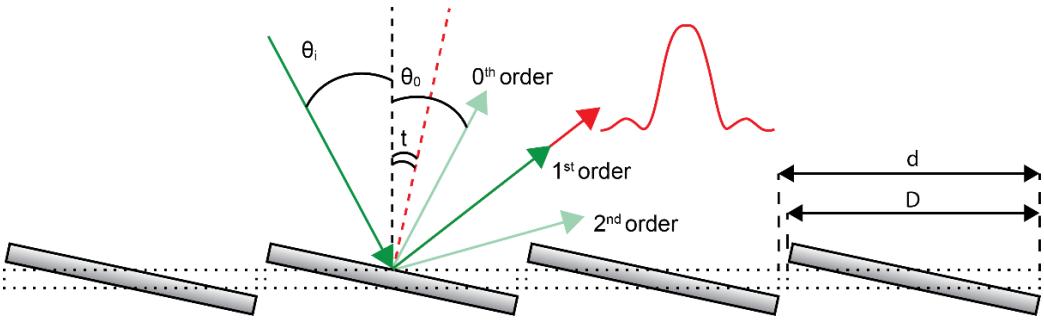

FIG. 50 - DMD as a reflective grating. *The light incomes on the grating with an incident angle θ_i respect to the grating normal (dashed line in black). The 0^{th} order is always located at an angle $\theta_0 = -\theta_i$. The tilt angle t defines the position of the envelope function (red arrow). The figure represents the 1^{st} diffraction order in the blazing condition. In this condition, the envelope function is located at the 1^{st} diffraction order, which contains most of the intensity of light. The dotted lines represent the miniaturized mirrors of the DMD in the parked (flat) position.*

Let us now consider the case of a two-dimensional reflective blazed grating, D_x and D_y describing the dimensions of the reflective surfaces and d_x and d_y being the grating pitches. The diffraction orders are constrained in two dimensions and appears like high-intensity peaks located at $(m\lambda/d_x, m\lambda/d_y)$. Here the (0, 0) order is located at the specular grating reflection. A DMD can be described as a two-dimensional reflective blazed grating, composed of miniaturized squared mirrors of size $D_x = D_y = D$. The DMD pitch is equal to d in both directions, and each mirror can be independently tilted by an angle $\pm t$ in respect to its diagonal. As a result [105], according to the incident angle of light θ_i, only the $m = n$ diffraction orders can verify the blazing condition when centered with the envelope function

$$F_E = \mathrm{sinc}^4\left[\frac{\pi D}{\lambda}(\sin\theta - \sin\theta_i)\right]. \tag{3.19}$$

In a recent work, Lachetta *et al.* proposed a detailed theoretical model that

describes the functioning of DMD with coherent laser light [120] (**FIG. 51**). The model takes in account all the possible incident directions $\vec{a}$ and all the possible refractive directions $\vec{b}$. For each mirror in the DMD matrix, any point on the surface is identified by $\vec{c} = (l, h)$, where $0 < l, h < D$, D being the width of the squared mirror. Each mirror can rotate by the angle t around the normalized diagonal axis $\vec{n} = 1/\sqrt{2}(1,1)$ via the rotation matrix $R_n(t)$. Each mirror in the $N_x \times N_y$ DMD matrix is defined by the vector $\vec{m} = d(q_x, q_y)$, where $d = D + g$ is the DMD pitch, g being the interspace between two mirrors and $0 < q_{x,y} \leq N_{x,y}$. The DMD can spatially modulate the light intensity by rotating each mirror by an angle equal to $\pm t$. The equation $\vec{d}_{q_x,q_y}(t, l, h, d) = R\left(t_{q_x,q_y}\right)\vec{c}(l, h) + d(m_x, m_y, 0)$ describes the rotation of a single mirror. The monochromatic coherent light incoming onto the DMD is described by the electromagnetic field $E = E_0(\vec{a}, \vec{d})e^{i\phi}$, in which the phase $\phi = \vec{d} \cdot (\vec{a} - \vec{b})2\pi/\lambda$ depends on the optical path length $\vec{d} \cdot \vec{a} - \vec{d} \cdot \vec{b}$. As a result of this model, the electromagnetic field diffracted at a specific point on the DMD is

$$E_{one\ point} = E_0\left(\vec{a}, t_{m_x,m_y}, l, h\right)\exp\left(\frac{2\pi}{\lambda}\vec{d}_{m_x,m_y} \cdot (\vec{a} - \vec{b})\right). \tag{3.20}$$

By integrating over each single mirror and summing over the entire DMD the diffracted field distribution can be written

$$E = \sum_{m_x,m_y} \iint_0^D dldh\, E_0\left(\vec{a}, t_{m_x,m_y}, l, h\right)\exp\left(\frac{2\pi}{\lambda}\vec{d}_{m_x,m_y} \cdot (\vec{a} - \vec{b})\right). \tag{3.21}$$

The authors proposed several methods to approximate equation (3.21), but in following part of this paragraph the focus is on the so-called analytic phase shifting approach. In this method, each mirrors can only be in the $+t$ or $-t$ tilt state and the field amplitude is assumed to be constant over a single mirror, that implies $E_0\left(\vec{a}, t_{m_x,m_y}, l, h\right) \rightarrow E_0\left(\vec{a}, t_{m_x,m_y}\right)$ in the (3.21). The pixelated incident Gaussian beam is simulated by varying the electromagnetic field intensity over an opportunely sized arrays of mirrors. For coherent light, the different tilt of a mirror $\pm t$ induces a phase shift $E_{shift}(\vec{a}, \vec{b}, d, \lambda)$ between the reflected wave-fronts. With this approach the total diffracted shaped beam is obtained by summing the contribution from each pixel $E_{mirror}(\vec{a}, \vec{b}, t_{m_x,m_y}, D, \lambda)$ after taking in account the different phase shifts. In this approximation the diffracted field results

$$E = \sum_{m_x,m_y} E_0\left(\vec{a}, t_{m_x,m_y}\right)E_{mirror}(\vec{a}, \vec{b}, t_{m_x,m_y}, D, \lambda)E_{shift}(\vec{a}, \vec{b}, d, \lambda). \tag{3.22}$$

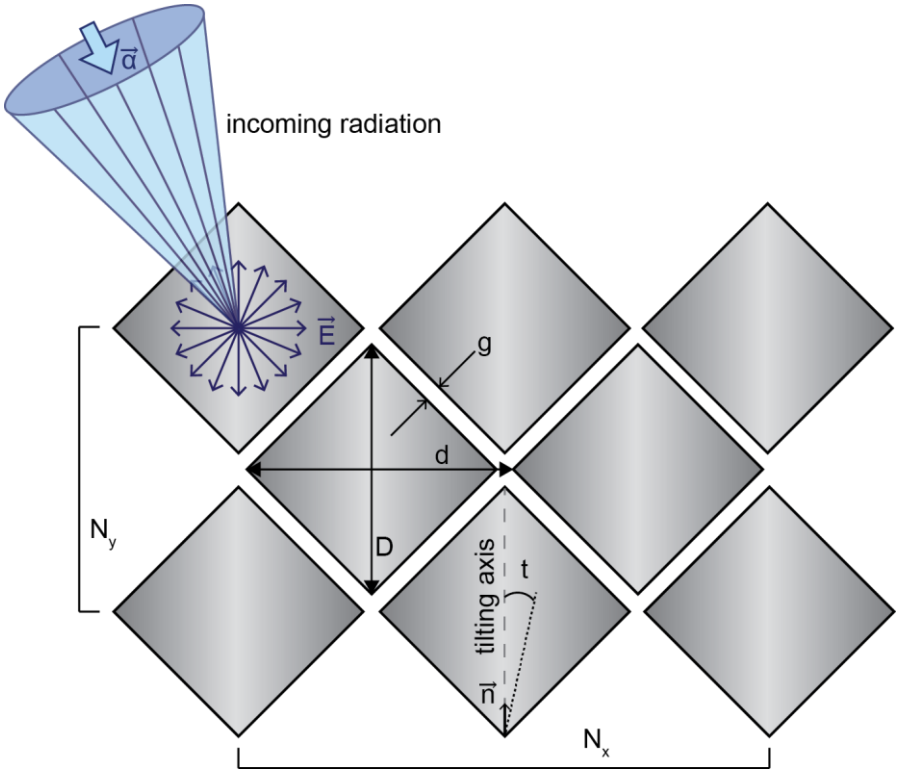

FIG. 51 – Diamond arrangement of $N_x \times N_y$ miniaturized mirrors. *D, d and g represent the size of a mirror, the DMD pitch and the interspace between mirrors. Each mirror rotates around its diagonal axis by a tilt angle t, defined by $\vec{n}$. The incoming radiation is defined by $\vec{\alpha}$. On each point of each mirror, the electromagnetic field component is $\vec{E}$. Integrating all the components give the total diffracted field.*

Thanks to this modelization, in [120], the authors proposed a configuration in which the blazed condition was obtained simultanesouly for several wavelengths that are typically used in a fluorescent microscope. The same configuration could fit our setup that is equipped with similar DMD pixel size and excitation wavelegnths. We explored the proposed solution, however the results obtained did not satisfy our expectations. For this reason, we optimized a different design for performing multiwavelength beam shaping by DMD devices as described in the next paragraph.

3.4.4 Design, optimization and precise alignment of the beam shaping module for multi-wavelengths applications

To produce selective and homogenous volumetric excitation, we designed the beam shaping module around a DLP LightCrafter 4500 (DLPLCR4500EVM, by Texas Instruments). It contains a 0.45-inch DMD (DLP4500) with 1140×912 mirrors, arranged in diamond geometry. The width of each mirror is $D = 7.637$ µm, the grating pitch is $d = 10.8$ µm (**FIG. 51**).

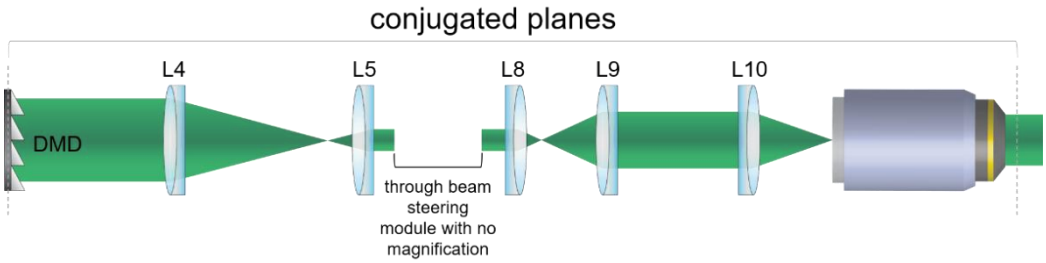

FIG. 52 – Beam shaping module positioning. *The beam shaping module is designed in a way that the DMD is conjugated to the sample plane. In this way, the image of the modulated beam is reproduced at the specimen.*

The simulation described in paragraph 3.4.2 suggests that a light-sheet produced by steering a beam modulated with an elliptical double arch pattern provides homogenous excitation intensity. To excite the sample with such modulated beam, the DMD has to be placed on a plane conjugated with the sample plane. In this way, the image of the beam, modulated by the DMD, is reproduced on the specimen plane. Moreover, for a correct display of the beam modulated with the DMD pattern, the arrangement of the mirrors in a diamond geometry and the tilt axis on their diagonal must be taken in account. Consequently, the distance between two consecutive mirrors is not the same along the two dimensions of the DMD matrix. The code for generating the modulation pattern (see A2.2) was thus adjusted, such as the number of mirrors along the direction perpendicular to the tilt axis is divided by a factor 2.

To optically conjugate the DMD with the sample plane, we introduced an achromatic relay lens $L4$ with focal length $f_4 = 400$ mm (AC254-400-A, by Thorlabs) on the optical path, placing it precisely at a distance f_4 from the DMD and $f_4 + f_5$ from the lens $L5$ of the beam steering module (FIG. 52).

To create a modulation with high resolution, a high number of mirrors is necessary. The choice of the relay lens is crucial as it sets the total magnification introduced along the illumination optical path. When using the 60X, water-immersion, objective, this is $60 \times f_8/f_9 \times f_4/f_5 = 160$. This means that,

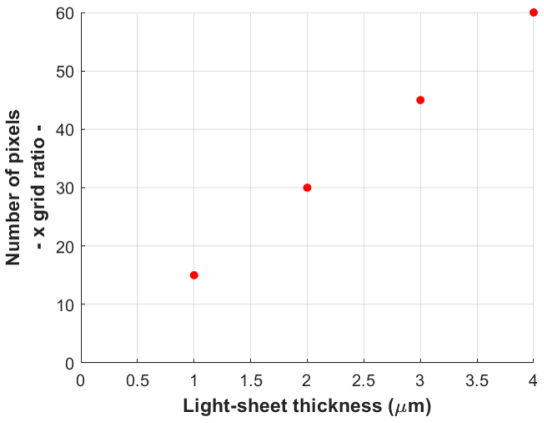

FIG. 53 - Number of mirrors as a function of the illumination thickness. *The resolution of the modulation is determined by the number of mirrors used to shape the illumination. With the choice of L4, and considering that the DMD grid is composed by* 1140 × 912 *mirrors, it is possible to estimate that* 60 × 74 *mirrors are used to create a light-sheet 4 μm thick. Similarly, for 3 μm, 2 μm and 1 μm thickness, we estimate that* 45 × 56, 30 × 37 *and* 15 × 19 *mirrors are necessary*

considering the DMD pitch $d = 10.8$ µm, each mirror corresponds to ~68 nm at the sample plane. This value being below the diffraction limit, the pixelization effects doesn't affect the pattern of the beam at the sample plane. With this choice, it is possible to estimate the number of mirrors that modulate the illumination (**FIG. 53**). The choice of $L4$ is important in order to keep the module relatively compact while producing precise beam shaping.

Alignment of multiwavelength coherent light modulated by the DMD

As presented in paragraph (3.4.3), a DMD can be described as a two-dimensional reflective blazed grating when used in combination with coherent light. The intensity modulation of a coherent light at different wavelengths is a non-trivial problem. The main challenge originates from the wavelength-dependent diffraction pattern. Here, it is reported the procedure that we established to design the beam shaping module, referring to the DMD as a one-dimensional reflective blazed grating for simplicity.

A diffraction order is in the blazing condition if it overlaps with the peak of the envelope function of the grating. When the excitation beam is incident on the DMD with an angle $\theta_i \neq 0$, and considering equation (3.17) and (3.18), the m^{th} diffraction order satisfies the blazing condition if

$$m = 2\frac{d}{\lambda}[\sin(t)\cos(\theta_i - t)] \tag{3.23}$$

is an integer number, t being the tilt angle of the mirrors.

In our case, $d = 10.8$ µm, $t^{\pm} = \pm 12°$ and the excitation wavelengths are $\lambda_1 = 405$ nm, $\lambda_2 = 488$ nm, $\lambda_3 = 561$ nm, $\lambda_4 = 640$ nm. According to (3.23), for $\theta_i \sim 20°$, it is possible to determine the blazed diffraction orders for each wavelength, that are $m_1 = 11, m_2 = 9, m_3 = 8, m_4 = 7$, respectively. In reality, the two-dimensional diamond geometry of the grid and the rotational axis built on the diagonal of each miniaturized mirror results in a different, more complex, prediction of the DMD blazing conditions. In fact, we observed that if all the wavelengths λ_1, λ_2, λ_3 and λ_4 are incident on the DMD with the same incident angle θ_i, the respective refractive angles $\theta_{m1}, \theta_{m2}, \theta_{m3}$ and θ_{m4} are different. Moreover, we observed that, at a given θ_i for which λ_1, λ_2 and λ_4 satisfy the blazing condition, λ_3 is off-blazed (**FIG. 54**). Specifically, for $\theta_i \sim 20°$, the observed blazed order for λ_1, λ_2 and λ_4 are $m_1^{ob} = (10, 10)$, $m_2^{ob} = (8,8), m_4^{ob} = (6,6)$, while for λ_3, the light is mostly distributed in the orders (6,6), (6,7), (7,6) and (8,8). Therefore, for the design and optimization of the beam shaping module we had to face two issues. First, we wanted the shaped beams at different wavelengths to be refracted with the same angle, so that they would propagate on the same optical path. Second, we wanted to optimize the energy distribution in the diffraction orders to excite the sample with

high illumination intensity for performing efficient single-molecule imaging. As anticipated at the end of paragraph 3.4.3, a solution for which wavelengths $\lambda_2, \lambda_3, \lambda_4$ are diffracted at the same angle, all in blazing conditions, is proposed in [120]. In the proposed solution, the wavelengths $\lambda_2 = 488$ nm and $\lambda_4 = 640$ nm are incident with a negative angle $\theta_i^{2,4} = -40.6°$ on the DMD, the mirrors being tilted at the angle $t^- = -12°$. If wavelength $\lambda_3 = 561$ nm is incident on the DMD with a positive angle $\theta_i^3 = 16.6°$, the mirrors will be seen by λ_3 tilted with an angle $t^+ = +12°$.

Although we explored this option, this geometry does not provide an efficient solution for the design of our beam shaping module because of two main issues. First, the geometry was too sensitive to the different incident angles. Second, in our case the different wavelengths must be incident on the same area of the DMD in order to produce the same modulation on all the beams. This limitation factor is not taken in account for the solution proposed in [120].

In the following section I describe the final design of the beam shaping module that produces overlapping high intensity diffraction orders for $\lambda_1, \lambda_2, \lambda_3$ and λ_4. A precise alignment protocol can be found in A1.2.

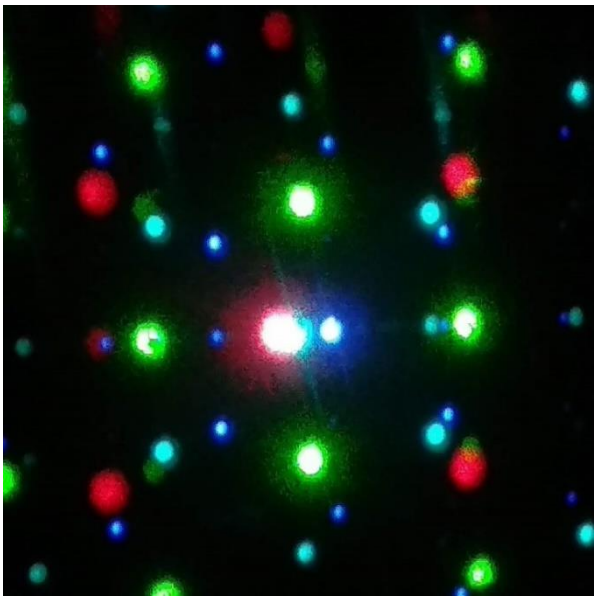

FIG. 54 – Diffraction orders of a DLP4500 DMD for multiple wavelengths. *When all the miniaturized mirrors are tilted to t^+, for an incident angle $\theta_i = 20°$, the wavelengths $\lambda_1 = 405$ nm, $\lambda_2 = 488$ nm, $\lambda_3 = 561$ nm and $\lambda_4 = 640$ nm distribute as shown in the picture. This geometry produces blazed orders for λ_1, λ_2 and λ_4 while λ_3 is off-blazed. For different geometry it is possible to obtain the blazing condition for λ_3, but in this case for λ_1, λ_2 and λ_4 are off-blazed. The picture also shows that the diffraction orders of the different wavelengths are diffracted by the DMD with different angles.*

<u>Optimized configuration of the beam shaping module</u>

The physical properties of the DLP4500 DMD and the optical limitation previously discussed in this paragraph limit its multi-wavelength application. Imposing the blazing condition for certain wavelengths produces off-blazed orders for some others. For this reason, and to mitigate this effect, we found a compromise between the blazing conditions and the efficiency of diffraction for the different excitation wavelengths. With this in mind, we used specific dichroic mirrors to

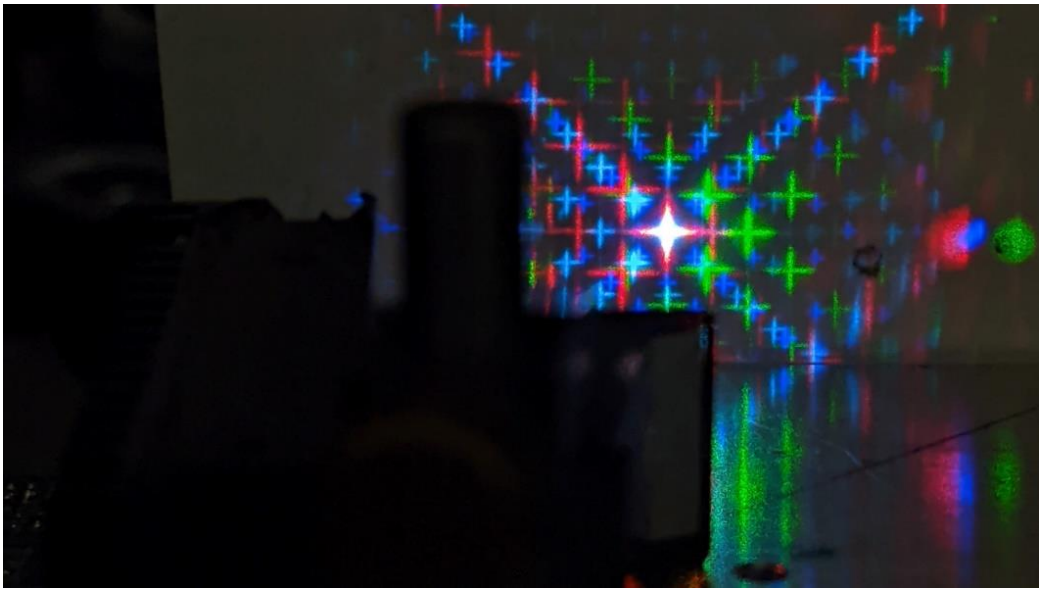

FIG. 55 - High intensity diffraction orders of λ_1, λ_2, λ_3 and λ_4 overlap after beam modulation by the DMD. *To obtain this effect the incident angle and the incident position of each wavelength was optimally regulated using dedicated dichroic beamsplitters and mirrors.*

separate the optical path of $\lambda_1, \lambda_2, \lambda_3$ and λ_4 before the DMD. In this way it is possible to change specifically the incident angle of each wavelength so that the optical paths of the modulated beams overlap (FIG. 55).

For the final design of the beam shaping module we used a total internal reflection (TIR) prism that was included in the original DLP LightCrafter 4500 spatial light modulator. When placed correctly in front of the DMD grid, the effect of the TIR-prism is to overlap the diffracted orders containing the maximum energy of the wavelengths λ_2 and λ_4 (this has inspired alternative designs of the beam shaping module that we explored - see Annex 3). The same optical path was thus possible for λ_2 and λ_4. In practice the dichroic beamsplitter $D1$ (ZT405rdc UF2, by Chroma) reflects λ_1 and transmits λ_2, λ_3 and λ_4. The multiband dichroic beamsplitter $D3$ (ZT488/640dcrb UF2, by Chroma) reflects λ_2 and λ_4 and transmits λ_3. In this way, the incident angle θ_i^1 and position of λ_1 in respect to the DMD grid can be regulated by $D1$ and a second identical beamsplitter $D2$. In the same way, the incidence of λ_2 and λ_4 can be regulated by $D3$ and a second equal multiband dichroic beamsplitter $D4$. The regulation of the incidence of λ_3 is done using the mirrors $M9$ and $M10$ (FIG. 33).

3.4.5 Selective, homogenous illumination: comparison between beam shaping and 2D scan methods

In the previous paragraphs, the two methods for producing a selective and

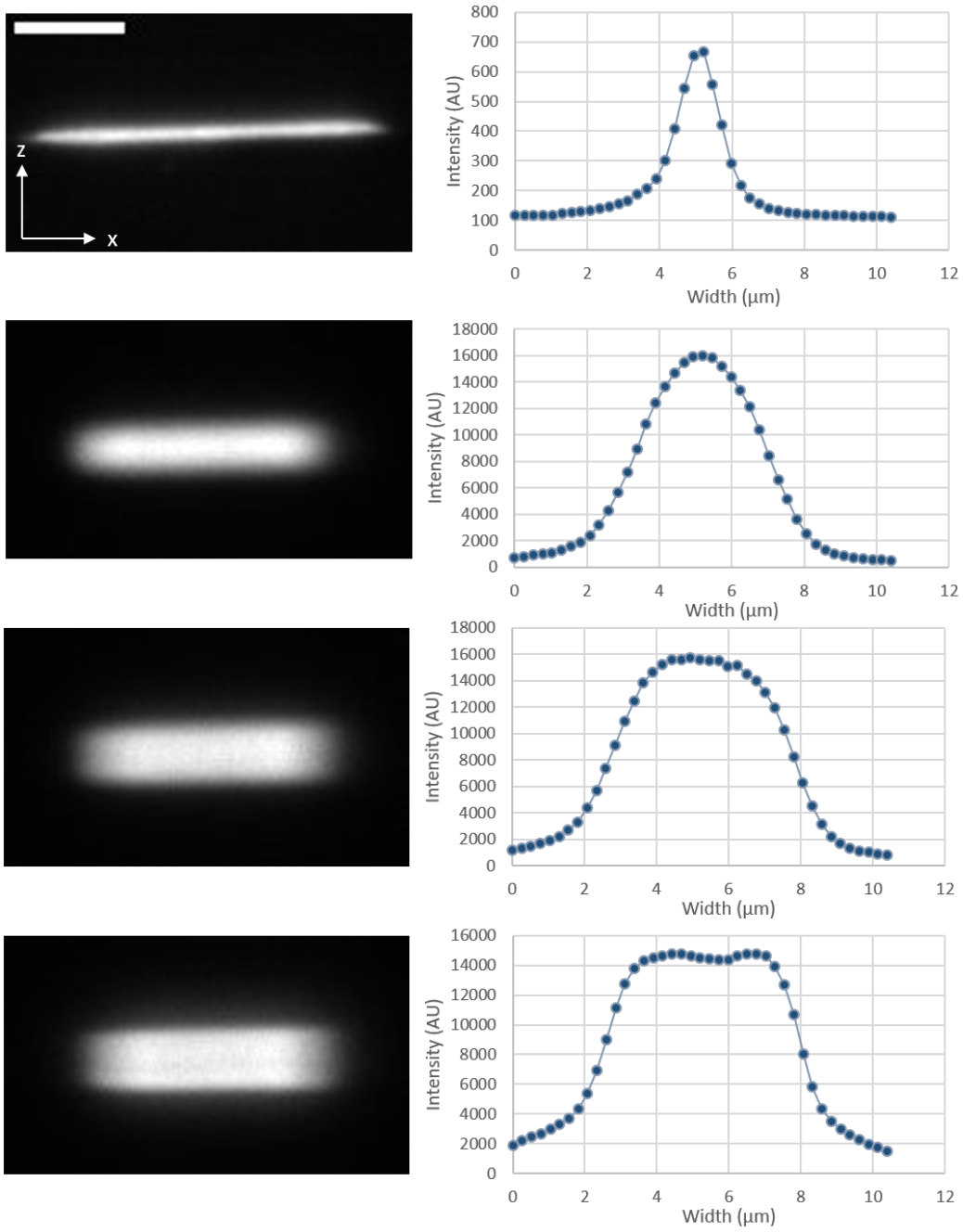

FIG. 56 - Homogeneous excitation of extended volumes through the 2D scan of a Gaussian beam. *The top pictures shows the thin light-sheet produced by scanning a Gaussian beam along the x direction. Selected excitation volumes can be produced by scan the Gaussian beam in the x and z direction. This approach efficiently produces homogeneous excitation volumes > 3 µm height. Scale bar 10 µm.*

homogeneous excitation of the sample have been presented. This paragraph contains the comparison of the performances of the two methods in producing a homogenous excitation. To evaluate the illumination uniformity and size produced by modulating the excitation light-sheet or by steering a Gaussian beam in two dimensions, we fabricated a homogenous fluorescent layer. For that, we mixed a fluorescent pigment, extracted from a marker, in a 5% polyvinyl alcohol (PVA)

solution. With this fluorescent solution, we spin-coated the surface of a coverglass.

First, we evaluated the homogeneity of the volumetric excitation that we can produce by the 2D scan of a Gaussian beam (FIG. 56). We observed that the performances of the 2D scan methods in producing small homogeneous excitation volumes are poor, while this method is highly efficient for producing extended excitation volumes. In particular, the homogeneity of a 4 μm thick illumination light-sheet produced with the 2D scan method is 85%, while the homogeneity of a 3 μm thick light-sheet produced is limited to 74%, and the intensity starts to show a Gaussian-like profile. This is even more evident for smaller excitation volume. On the other hand, with the 2D scan method we were able to produce thick light-sheets with homogeneous intensity. The homogeneity of the excitation intensity of light-sheet covering volumes of 5 μm and 5.5 μm has been evaluated to be 80% and 83%, respectively (FIG. 57). This is an interesting feature for possible future developments, however, at the moment, such extended volumes are outside of the range that we want to observe by MFM.

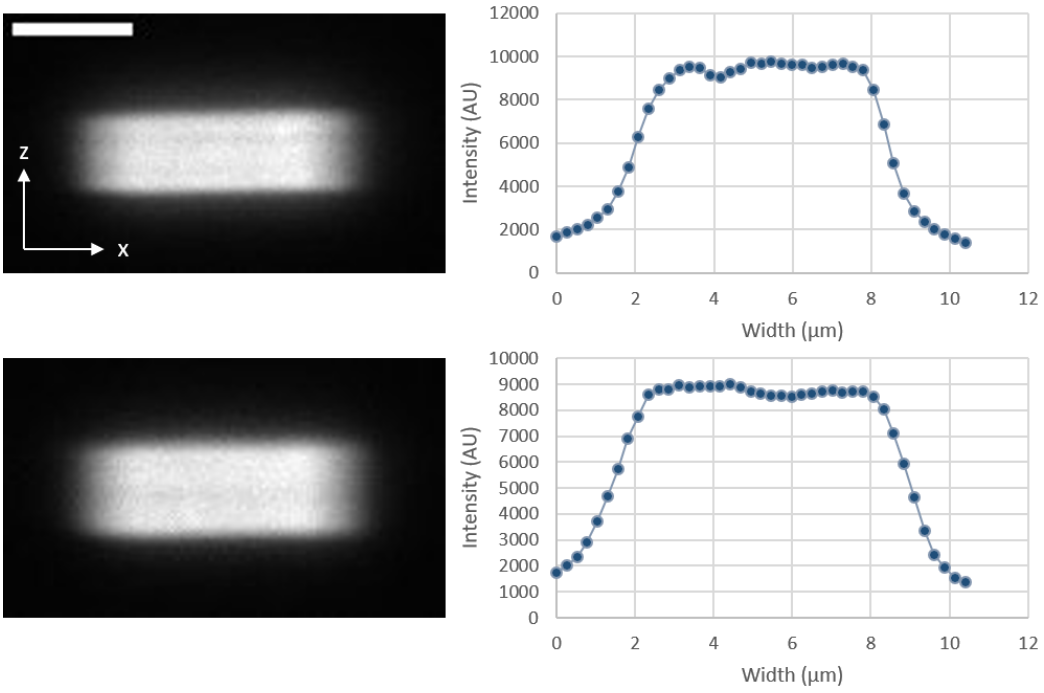

FIG. 57 – 2D scan methods for wide excitation volume. *This method produces high performances if used to create homogeneous excitation of wide volumes. Although at the moment these volumes are outside of the observable range of MFM, this is an important feature for future developments.*

To improve the homogeneity of excitation over a wider range of volumes we developed the beam shaping approach. To evaluate the performances of this configuration, we developed multiple elliptical double arch DMD patterns to produce light-sheets with different thickness. By steering the modulated beam along the x direction, we acquire the images of different excitation volumes, ranging

between 2 µm and 5 µm height. We imaged and measured their cross-sectional intensity using ImageJ software, evaluating the homogeneity as the standard deviation of the intensity values in the flat portion of the illumination profile (FIG. 58). The homogeneity of the 2 µm excitation volume is 83%. Equivalently, the

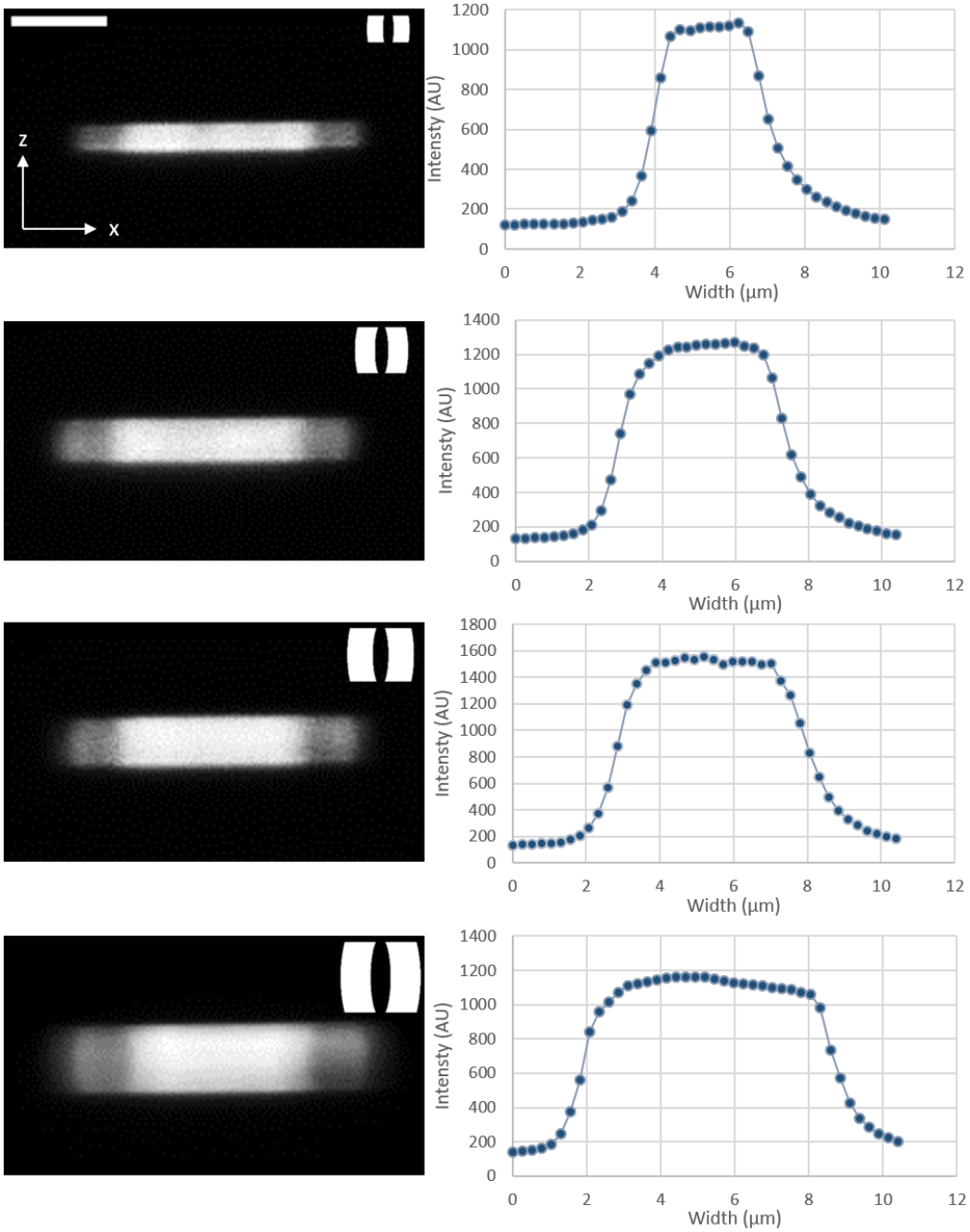

FIG. 58 – Homogeneous selective illumination through DMD-based beam shaping. *By steering a beam modulated with elliptical double arch patterns of different size, we can produce the homogeneous excitation of volumes with different heights. On the left side, the different homogeneous light-sheet are shown together with the relative DMD pattern. On the right side, the intensity profiles are shown. The illumination is homogeneous over different excitation volume. The tails of the distribution are due to the convolution of the DMD pattern with the excitation PSF and the fluorescence PSF.*

excitation homogeneity of volumes with thicknesses of 3 μm, 4 μm and 5 μm are 80%, 84% and 74%, respectively. We can observe that the excitation is less homogeneous over the 5 μm excitation volume, but since our observation volume is limited to up to 4 μm by the 9-planes MFG_9, we can consider the performance to be satisfying. To note here that the acquired images are the convolution of the DMD modulation with the PSF of the excitation and the PSF of the emission. For this reason, we can observe the pronounced tails that characterize the intensity profile of the different excitation volumes. Independently from the width of the excitation, the intensity drops to 50% within ~600 nm distance. In reality, the illumination profile at the sample is slightly different and we can expect less pronounced tails.

To conclude, this analysis has evaluated the performances of the two methods for producing homogeneous excitation over volumes of different heights. From the comparison of the two methods we can conclude that the beam shaping approach performs sensibly better than the 2D scan method when we are interested in producing homogenous excitation of volumes in the observable range of MFM.

3.4.6 Double arch-modulated beam propagation

According to the design and development of the beam shaping module, the DMD is placed on a plane that is optically conjugated to the sample plane. This configuration results in a collimated intensity-shaped beam at the output of the microscope objective. In practice, the propagation of the excitation beam maintains the properties of a Gaussian beam (see paragraph 3.4.1) and the propagation profile needs to be quantified.

To characterize the propagation of the modulated double-arc beam after the objective, we imaged the beam profile at increasing distances from the focal plane of the objective using a fluorescent layer mounted on a coverglass. For that, we displaced the EMCCD camera by Δ, according to

$$\Delta = M^2 \delta \,, \tag{3.24}$$

where δ is the displacement of the fluorescent layer from the focal plane and M is the magnification of the objective. The objective remained fixed and the sample was shifted axially thanks to a piezo stage. We evaluated the propagation of the patterned beam over 20 μm, acquiring images for $\delta = -10$ μm, -5 μm, -4 μm, -3μm, -2 μm, -1 μm, 1 μm, 2 μm, 3 μm, 4 μm, 5 μm and 10 μm focal shifts (**FIG. 59**). By looking at the resolution of the elliptical double arch pattern and at the average intensity of the modulation at different position, we can evaluate that the modulated beam has a Rayleigh length of ~5 μm, which establish that the

homogeneous excitation has a length of ~10 µm. This measurement was performed with a simple coverslip colored with a marker. Considering that and the fact that the modulated beam was not scanned laterally, we expected to have less precise average intensity profile than the ones show in FIG. 58.

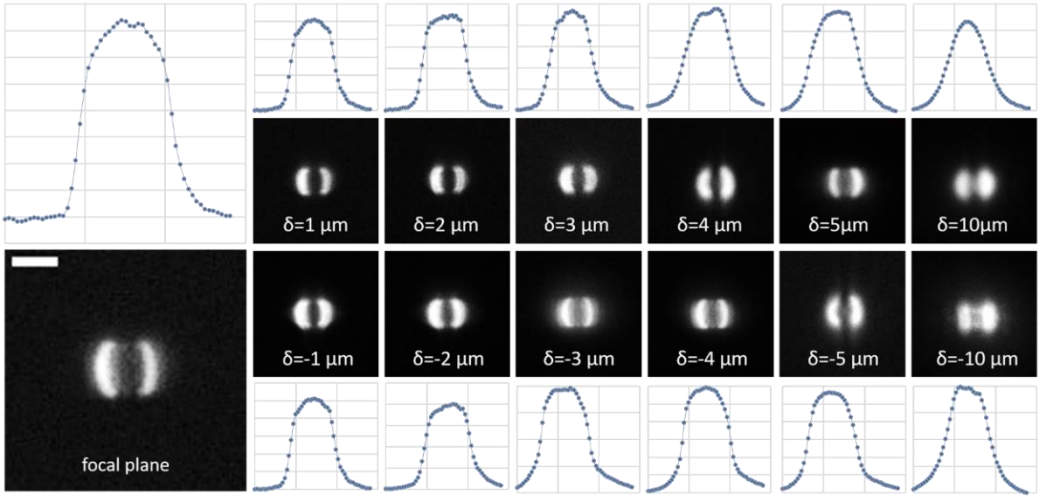

FIG. 59 - Propagation of the modulated beam. *Images are acquired at a distance δ from the focal plane. The Rayleigh length of the modulated beam is ~5 µm and the length over which the excitation intensity is homogenous is ~10 µm. Scale bar 5 µm.*

We also evaluated the propagation of the modulated beam inside the dedicated soSPIM chamber. After the reflection on the mirror we observed that the elliptical double arch modulation is visible at the waist of the excitation beam (FIG. 60).

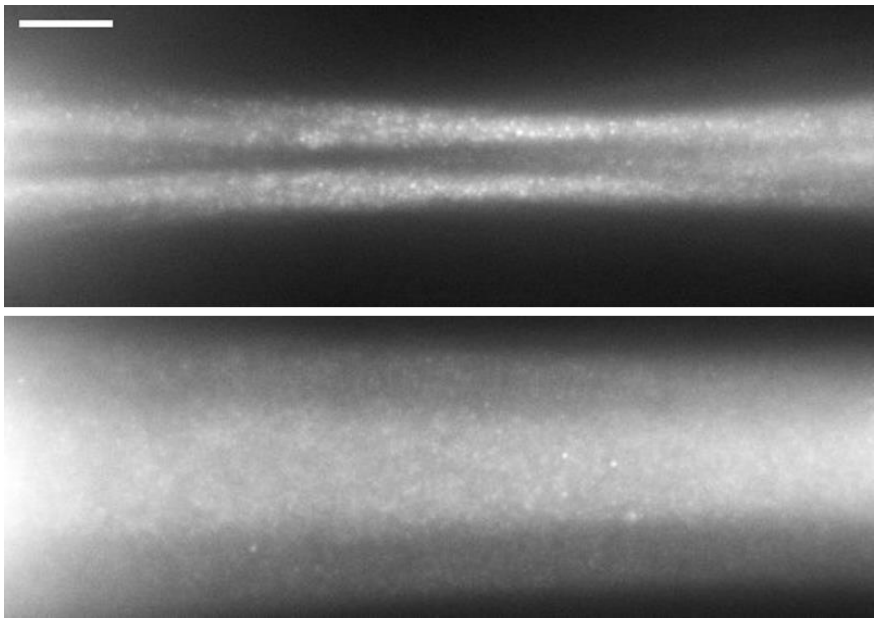

FIG. 60 - Modulated beam propagating inside a soSPIM chamber. *The modulation appears at the waist of the beam (top). The steering of the modulated beam produces a light-sheet with homogeneous intensity (bottom). Scale bar 10 µm.*

3.4.7 Evaluation of light-loss along the optical path

The shaping of the excitation beam intensity profile has an inherent drawback of reducing the excitation power on the sample. In fact, the energy incident on the DMD is distributed over multiple diffraction orders. The off-blazed condition that allowed us to implement a multi-wavelength system, results in an excitation intensity distributed over multiple diffraction orders. In single-molecule imaging, the excitation intensity impacts directly the obtainable signal-to-noise ratio (see paragraph 0). For this reason, it has been crucial to evaluate the light loss along the optical path for the three excitation wavelengths $\lambda_2 = 488$ nm, $\lambda_3 = 561$ nm and $\lambda_4 = 640$ nm (the activation wavelength $\lambda_1 = 405$nm has not been evaluated). First, we measured the Gaussian beam intensity at the source. We then compared it to the intensity of the refracted beam with and without the application of the double arc pattern. In the latter, all the mirrors of the DMD were tilted by $t^+ = 12°$ to produce a reflected Gaussian beam. Finally, for the two kinds of modulation, we measured the intensity at the output of the 60X, 1.27 NA, water-immersion objective. The measurements are reported in (FIG. 61). Estimating the exact amount of light on the sample is more complicated, the reflection efficiency of the mirror inside soSPIM chamber can't be measured.

Super-resolution imaging based on single-molecule localization has been performed using excitation light-sheet with elliptical double arch modulation (see paragraph 4.5.3), demonstrating that our approach provides sufficient energy for efficient single-molecule imaging.

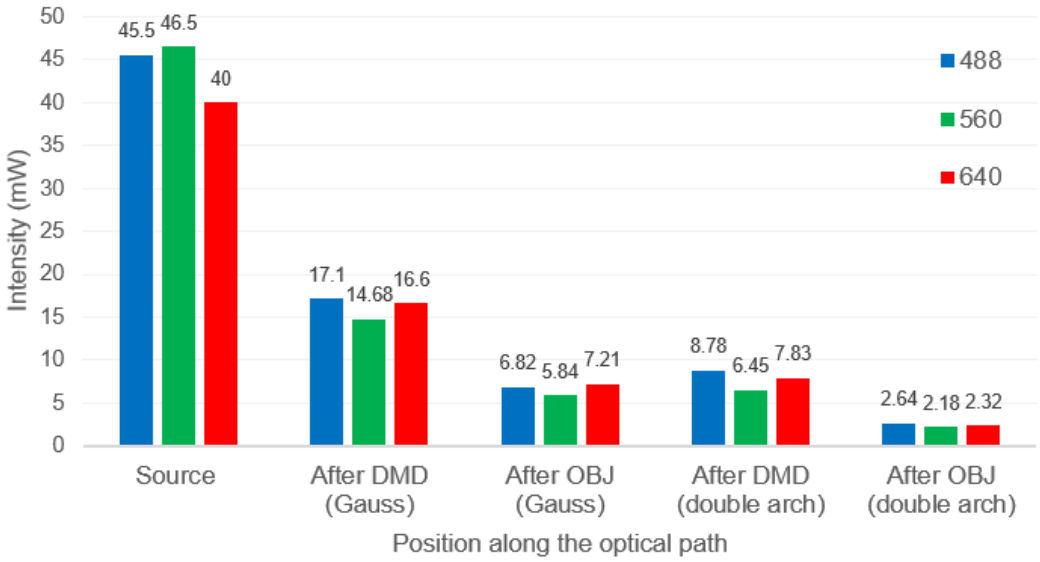

FIG. 61 – Excitation intensity along the optical path. *To evaluate the light loss caused by the modulation of the excitation beam through the DMD, we measured the intensity at several position along the optical path. Considering also the light loss caused by the off-blazed working condition of the DMD, we estimated the final excitation intensity.*

To summarize, in this chapter I presented the modular system that we developed in my PhD project. It aims at providing a cutting-edge imaging method that overcomes the multiple obstacles for efficient single-molecule microscopy in biological samples. By providing instantaneous volumetric imaging thanks to MFM, our method promises high time resolutions, which is fundamental to investigate 3D samples. The detection module can be tuned to adjust the observation volume to the sample of interest. Moreover, the tunable beam expander, the beam shaping and the beam steering modules provide selective, tunable and homogenous excitation that can be adapted to the observation volume.

The modular imaging system that we developed allowed us to perform single-molecule experiments, in both living and fixed samples. Studies of single-molecule 3D dynamics in the nucleus of living cells and super-resolution imaging results will be described in the following chapter.

Chapter 4

Selective and volumetric imaging at the single-molecule level: analysis and results

In this PhD project, we developed an innovative method for single-molecule fluorescence microscopy. The design, optimization and characterization of all the components of the newly developed microscope has been presented in Chapter 3. By producing selective and homogeneous volumetric excitation in combination with instantaneous 3D imaging, we believe that our system offers a tool for fast, volumetric fluorescence microscopy in dense and complex environments at the molecular scale. Being able to detect and localize single fluorescent molecules over the volume of the sample and further away from the coverslip surface, our method overcomes the challenges that we encounter for imaging realistic *in vivo* microenvironments. To prove the efficiency of our newly developed method, we focused our interest on the two main applications of single-molecule fluorescence microscopy, that are single-particle tracking and super-resolution microscopy. The results are described in this chapter.

The first part of this chapter shows the benefits provided by selective illumination of the sample over non-specific widefield illumination. We demonstrated that light-sheet excitation increases dramatically the efficiency of an imaging system for the observation of dense and 3D extended samples.

In the second part of the chapter, we demonstrate the importance of performing efficient 3D imaging and the key-role provided by the modules that we developed for producing volumetric and homogeneous excitation. Also, we show the tunability of both the excitation and acquisition volumes offered by our modular system. For that, we analyzed the dynamics of single fluorescent beads of variable size diffusing at different concentration in different solutions with distinct viscosities. Using this ideal environment, we could mimic densely labeled samples and proof that, in such

environments, our microscope can analyze the fast, volumetric dynamics of isolated emitters.

The third part of the chapter contains the demonstration of the performances of our method for 3D single-particle tracking experiments and the observation of the dynamics of multiple biomolecules in living samples. In our group, the interest is mainly focused on the nucleus of the cell. This is a very dense environment in three dimensions. These factors constitute the main challenges to face for detecting single, nuclear biomolecules using fluorescence microscopy. Focusing on the nucleus of cells, we demonstrated that our microscope can detect and localize single, fluorescent molecules in volumetric biological samples, and we use this information for the analysis of biomolecules dynamics. Willing to explore different ranges of dynamics, first we observe the 3D motion of H2B histones in living human osteosarcoma cells (U2OS). After that, we observed the volumetric dynamics of Cohesin and CTCF nuclear factors in mouse embryonic stem (mES) cells. The interest toward CTCF and Cohesin rises from a work previously conducted in our lab by Laura Caccianini [121], in which the two nuclear factors have been deeply studied as crucial players in genome organization and chromatin folding. The observation made with our system and reported in this chapter do not aim to answer biological questions, but show the possibility of extending such investigations from 2D to volumetric samples.

Finally, we wanted to demonstrate that, by performing single-molecule detection and localization, the microscope developed in this PhD project can perform super-resolution imaging. For that, by using DNA-PAINT technique (see paragraph 1.7.2), we produced super-resolution images of the Lamin B1 protein of the nuclear membrane of genetically modified human osteosarcoma cells (U2OS-NUP96EGFP).

Protocols for the culture of the cells used for the experiments described in this chapter, as well as the details regarding the preparation of the multiple kind of samples are contained in Annex 4

The 3D localization of single fluorescent molecules has been performed for all the acquisitions using a radial symmetry algorithm [122]. This algorithm was previously developed in our lab by Yasmina Fedala, and the details will not be presented in this manuscript (Fedala *et al.* – in preparation).

4.1 Illuminating the sample with a thin light-sheet

The main obstacle for reaching the single-molecule regime while imaging a 3D and dense specimen is the fluorescence of out-of-focus emitters that produces high background noise. For this reason, in our method we implemented selective excitation by exploiting soSPIM technique (see paragraph 3.2). Thanks to soSPIM,

we combine the advantage of sample optical sectioning with the use of high-NA objective for the fluorescence collection.

In our method, the different modules developed for tailoring the illumination produce tunable, selective and volumetric excitation. From the preliminary experiments that we performed, a selective illumination shows a clear improvement in comparison to non-specific widefield excitation. As shown in this paragraph, confining the excitation in a thin light-sheet placed at the focal plane of the objective produce a dramatic signal-to-noise ratio increase. Also, the effect of the specimen optical sectioning is shown through 4-planes MFM acquisitions.

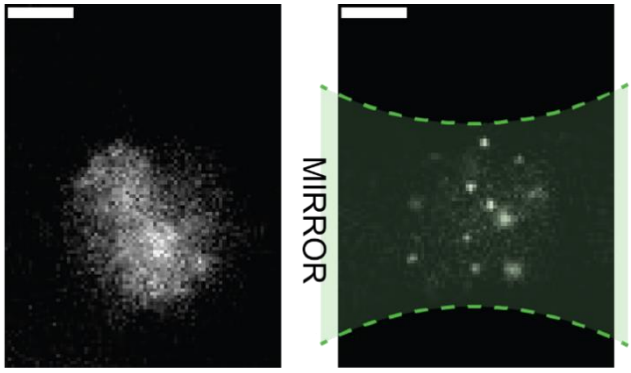

FIG. 62 – 2D imaging of H2B histones dynamics in the nucleus of living cell. *The two images show the same nucleus excited with widefield (left) and light-sheet (right) illuminations, demonstrating that confining the excitation reduces the background noise. With the light-sheet mode, individual molecules are immediately detectable, while, for widefield excitation, long photobleaching is required to reach the single-molecule regime. Scale bar 5 µm.*

First, the reduction of the background noise obtained with selective excitation has been crucial to perform imaging of single histones diffusing in the nucleus of living cells (see paragraph 4.3 for the analysis of histones volumetric dynamics). While the background noise was too high in the case of widefield illumination, the confinement of the light in a thin light-sheet allowed to isolate single diffusing proteins (**FIG. 62**).

For the quantitative evaluation of the signal-to-noise ratio, 2D imaging of HaloTag H2B histones in living human osteosarcoma (U2OS) has been performed using Halo-conjugated Alexa Fluor 647 dyes at 5 nM concentration, using both non-specific widefield illumination and light-sheet excitation. We compared the signal-to-noise ratio (SNR) of raw 2D acquisitions obtained with unspecific widefield excitation and with light-sheet excitation using FIJI analysis software [123]. The signal-to-noise ratio is defined by

$$SNR = \frac{I}{\sigma_{noise}}, \tag{4.1}$$

where I is the signal from the single emitter and σ_{noise} is the standard deviation of the background noise. We measured the intensity profile over a 2 pixels width band, centered on the detectable histone. To determine the signal I emitted from the molecule, the average background was subtracted from the intensity peak. To

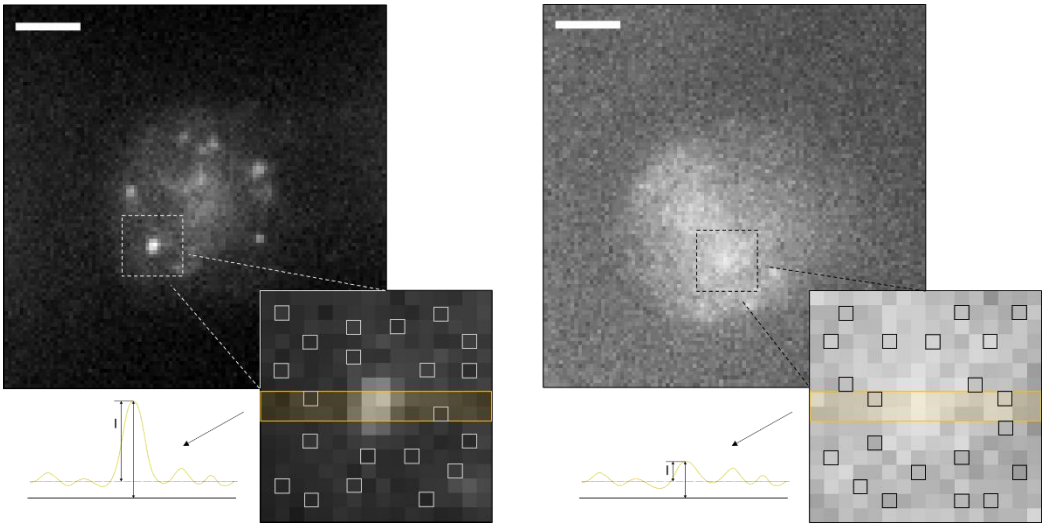

FIG. 63 - Signal-to-noise ratio in single-molecule imaging with light-sheet (left) and widefield (right) excitation. *Raw 2D images of single H2B histones labeled with Alexa Fluor 647 dye, diffusing in the nucleus of living cells have been analyzed to estimate the different signal-to-noise ratio achievable in the two different excitation mode. The signal has been measured as the difference between the maximum intensity and the average background measured over a 2-pixels width band (yellow) centered on the single emitters. The noise has been evaluated has the standard deviation of the intensity measured over 40 pixels far away from the fluorescent molecule. Scale bar 5 µm.*

determine the noise, the standard deviation of the background intensity was evaluated over 40 single pixels, far from the emitter. By reducing the excitation of out-of-focus emitters, light-sheet illumination provides a signal-to-noise ratio $SNR_{LS} = 8.26$, while the high background noise that we obtain with unspecific widefield excitation limits the signal-to-noise ratio to $SNR_{WF} = 2.35$ (**FIG. 63**).

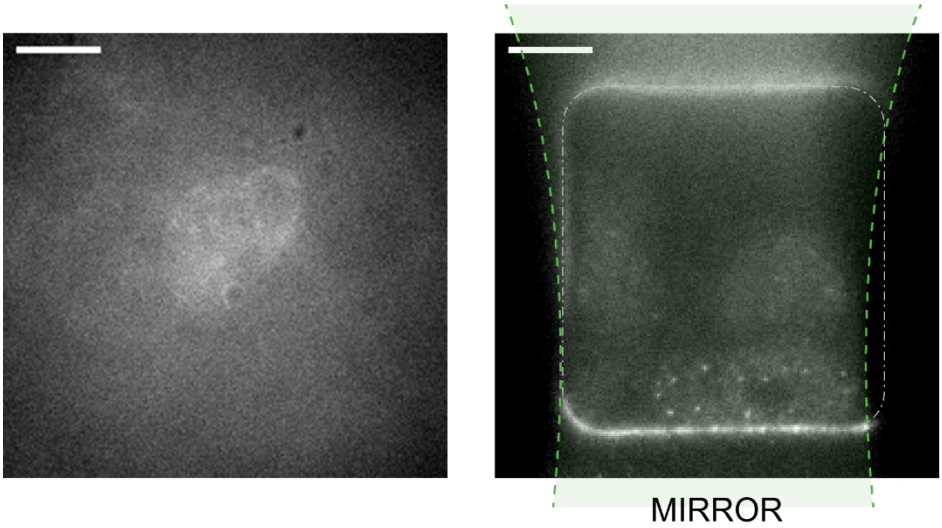

FIG. 64 – DNA-PAINT imaging requires a good optical sectioning of the sample. *Raw acquisitions of Lamin-B protein targeted by CY3 dyes, performed with widefield (left) and light-sheet (right) excitation. With widefield excitation, the high background noise coming from the diffusing imager strands covers the signal form single emitters. The right image shows the cell in the soSPIM well when excited with a light-sheet. The optical sectioning of the light-sheet increases the signal-to-noise ratio and allow the detection of single fluorescent dyes. Scale bar* 10 µm.

Also, reaching the single-molecule regime using widefield excitation requires long preliminary exposures to produce the photobleaching of the sample. This condition is not optimum to perform efficient single-molecule imaging in living sample because the photon-budget is not optimized, the phototoxicity is high, and the probability of acquiring long trajectories reduced.

The optical sectioning power of light-sheet microscopy has been crucial to perform super-resolution imaging of the nuclear membrane of fixed U2OS cells using DNA-PAINT techniques (see paragraph 4.5 for the details about super-resolution imaging results). In DNA-PAINT, the numerous imager strands present in solution produce a high back-ground noise if excited with unspecific widefield illumination, avoiding the detection of single emitters bounded to the nuclear membrane (**FIG. 64**).

To show the optical sectioning power of soSPIM, a thin light sheet was produced and scanned along the optical axis of the objective without moving the sample. The sample was fixed U2OS cells stably expressing fluorescent Nup96 nuclear pores. Producing instantaneous volumetric acquisition by MFM, MFG_4 being on the optical path, the different sections of the nucleus appear sequentially in the planes while scanning the light-sheet through the sample (**FIG. 65**).

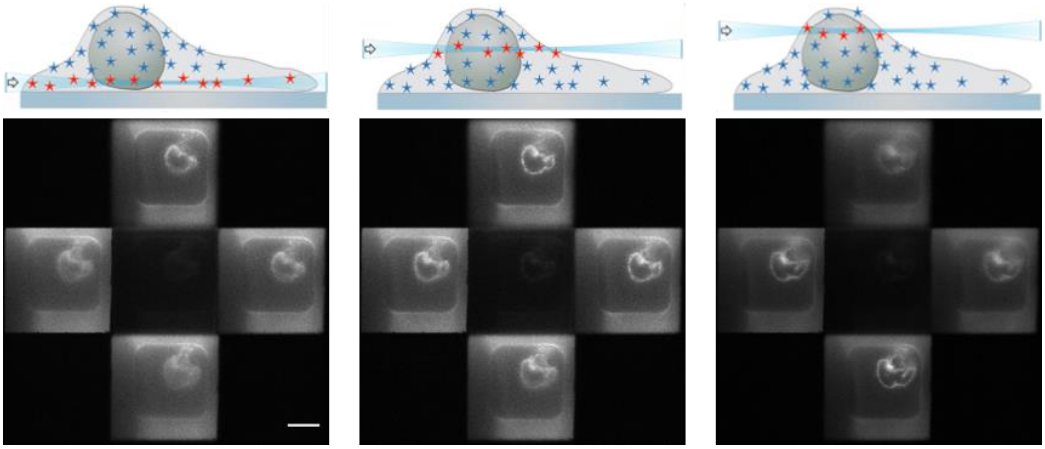

FIG. 65 – Raw MFM images of Nup96 nuclear pores labeled with EGFP produced by z −scanning a thin light-sheet. *The different sections of the sample appear sequentially in the 4 planes. The interspace between consecutive planes is* ~500 *nm, demonstrating the optical sectioning of soSPIM. Scale bar* 10 *μm.*

4.2 Dynamics of fluorescent beads in viscous media as representation of densely labeled samples

Experiments on 2D cell cultures give only a partial view of the mechanisms that regulate the complex *in vivo* microenvironment of the specimen. The first challenge to face when imaging complex systems is represented by the high density of

emitters, that hinders the capability of the microscope to detect single fluorescent molecules over the volume of the specimen. However, we believe that the combination of selective, volumetric and homogeneous excitation with instantaneous 3D imaging capabilities that our newly developed method provides, overcomes this challenge.

To represent such challenging condition, we used fluorescent beads in solution in a viscous medium. Using beads of different sizes and media of various viscosity, we could demonstrate the importance of combining volumetric imaging with 3D selective excitation for detecting and tracking fast single fluorescent emitters in volumetric and dense environments.

We started by exploring ranges of slow dynamics by imaging 200 nm beads (T7280, by Invitrogen) suspended in a solution 1:1 PBS-Glycerole + 4% BSA (A9418, by Sigma-Aldrich), at a concentration of 20 μM. This solution is incubated under vacuum in the soSPIM chip for the beads to enter inside the microwells. BSA is used to passivate the walls of the microwells and, thus, to avoid nonspecific interaction and binding of the beads. To explore several ranges of volumetric dynamics, and different densities we prepared two different solutions. First, we made a solution of 200 nm beads in PBS and 4% BSA at 1:100 volume/volume concentration. After, we suspended beads of 15 nm radius (redF-NH2, by Micromer) in a solution of 1:1 PBS+Glycerole + 4% BSA, at a final concentration of 100ng/ml.

To demonstrate the crucial role played by the combination of selective volumetric excitation and instantaneous 3D imaging, we explored different combination of the excitation and acquisition volumes for all the different conditions. Specifically, using the MFM detection module, we varied the detection volumes by using MFG_9 and MFG_4 to acquire instantaneously 9 planes and 4 planes, respectively. Using the beam shaping module, we produced homogeneous illumination of different thicknesses, ranging from 2 μm to 5 μm, by laterally scanning the excitation beam modulated with the elliptical double arch pattern. For all the acquisitions presented in this paragraph, we inserted an addition 1.5X magnification on the detection path to assure a correct sampling in xy and z directions. In this way, the pixel size was ~133 nm while the interplane distance given by the calibration of MFM (see paragraph 3.1.2) was ~480 nm and ~250 nm when using MFG_9 and MFG_4, respectively. In the two combinations, by setting an exposure time of 20 ms/frame, we could acquire 50 volumes with size of 22 μm × 22 μm × 4μm and 22 μm × 22 μm × 2μm per second, respectively.

4.2.1 The importance of MFM: 2D vs 3D beads dynamics

As seen in paragraph 1.2, the depth of field of a standard microscope is limited to ~600 nm. This imposes a critical limitation for performing single-particle

tracking experiments and study the dynamics of individual biomolecules diffusing in the volume of the sample. In fact, molecules that moves in the specimen can exit the observable depth of field, resulting in short reconstructed trajectories. Consequently, the final analysis of the dynamics can be biased, giving an incorrect representation of the biomolecules motions and interactions.

This paragraph contains the demonstration of the crucial role played by MFM for performing efficient 3D single-particle tracking experiments. We compared the case of 200 nm beads diffusing in more viscous (PBS+Glycerol+BSA) and less viscous (PBS+BSA) medium. During the acquisition of the data, we produced a 4 µm thick light-sheet with homogenous intensity using the beam shaping module and we tuned the acquisition volume by inserting MFG_9 in the MFM detection module to acquire simultaneously 9 planes.

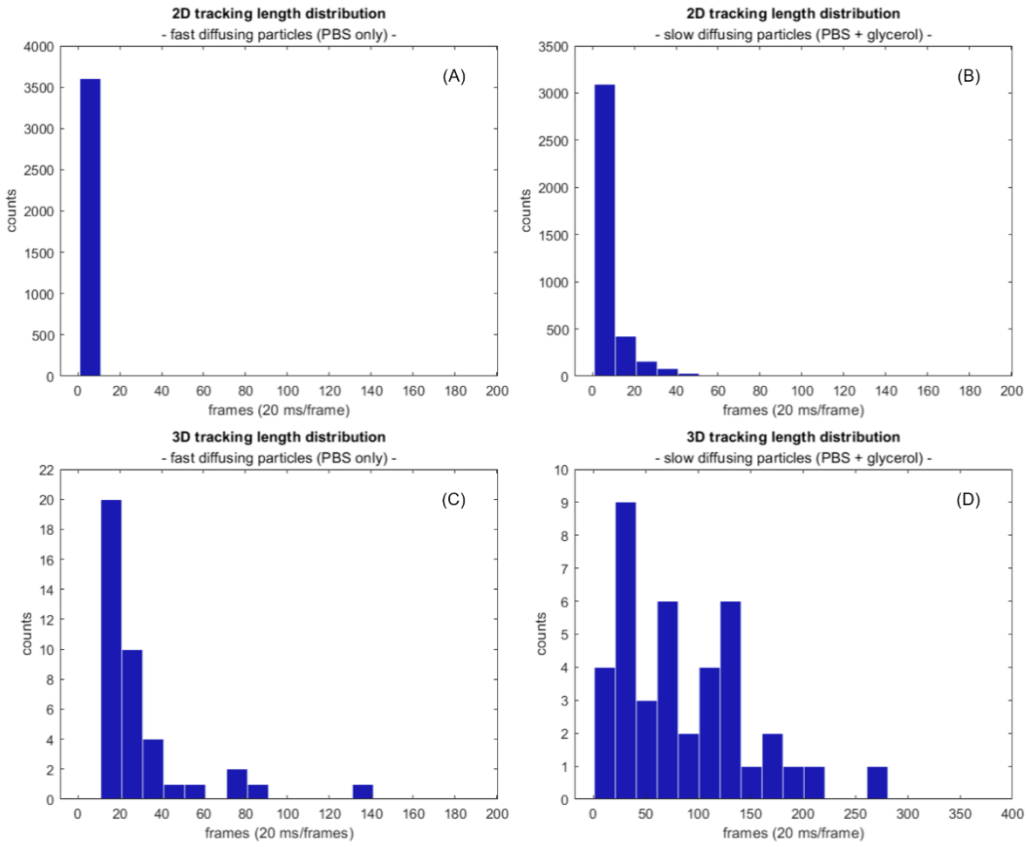

FIG. 66 – 2D vs 3D tracking of single fluorescent beads. *(A) 2D tracking of fast diffusing beads shows very short trajectories. (B) For slow diffusing beads, 2D tracking experiments are able to generate slightly longer trajectories. The real game changer in performing single-particle tracking is to perform 3D imaging. (C) and (D) show that using MFM detection unit, we are able to track single beads more efficiently, generating much longer trajectories.*

By analyzing the trajectories that we can reconstruct using 2D and 3D acquisitions, we demonstrated that the MFM detection module allow us to reconstruct longer trajectories for both samples (FIG. 66). The length of tracks that

we could obtain from 2D acquisitions of slow diffusing particles (more viscous medium) is ≤ 50 frames, with most of the tracks being ≤ 20 frames long. From 3D acquisition, we could generate a big collection of tracks ≤ 150 frames long, and it was possible to track beads for up to ~280 frames. For fast diffusing (less viscous medium) particles, 2D acquisition allowed us to generated only very short tracks, with length ≤ 10 frames, while 3D acquisition show tracks ≤ 40 frames and reaching up to ~140 frames.

To be noted that every single plane of an MFM acquisition gave us a 2D acquisition of the same sample. Also, in a 2D acquisition, a single bead can easily exit from the observable depth of field and then can enter it again after some frames. Several, separated, short trajectories are those generated. These two reasons explain the difference in the number of 2D and 3D trajectories in FIG. 66.

4.2.2 The importance of matching the excitation and acquisition volumes

To completely exploit the advantage of instantaneous volumetric imaging provided by the MFM detection module, it is crucial that the selective excitation is confined in a volume of the same size. The perfect adjustment of the excitation volume cancels the emission of molecules present outside of the observable volume and that could originate high background noises.

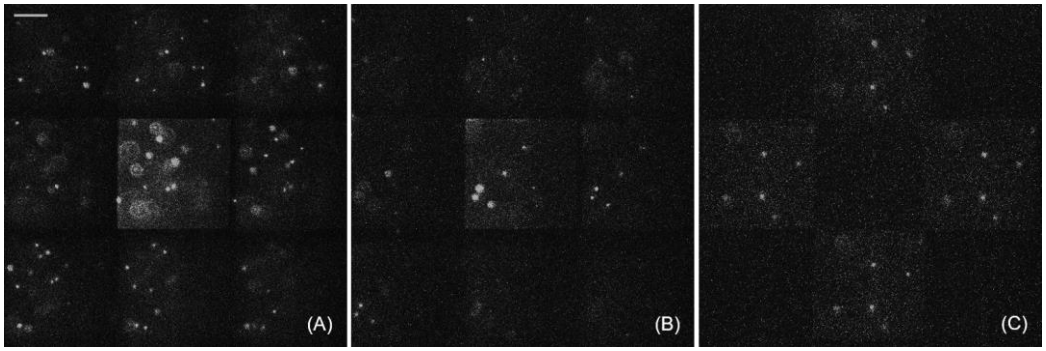

FIG. 67 – Matching the thickness of the light-sheet with the acquisition volume. *(A) When MFG_9 is in the MFM detection module, a ~4 µm thick volume is instantaneously acquired. In this case we produced a 4 µm thick light-sheet to match the acquired volume. (B) Combining MFG_9 with a 2 µm thick light-sheet do not match the excitation and observation volumes. Beads are detectable only in some of the acquired planes despite the tails of the excitation produced by modulating the beam with an elliptical double arch pattern. In this case, the fluorescence directed in the outer planes is wasted. (C) By introducing MFG_4 instead of MFG_9 in the MFM detection module, we can tune the acquisition volume. In this case, the photon budget is optimized for all the acquired planes. Scale bar 10 µm.*

To demonstrate the importance of matching the two volumes, we imaged 200 nm fluorescent beads diffusing in PBS+glycerol while tuning the light-sheet thickness and the observation volume. By tailoring the illumination

using the beam expander and beam shaping units, we produced homogeneous excitation light-sheet with thickness of 2 μm and 4 μm that match respectively the observable volume set by diffraction gratings MFG_4 and MFG_9 in the MFM detection module (FIG. 67).

We compared the acquisitions performed combining a light-sheet of 4 μm thickness with MFG_9 and a 2 μm thick light-sheet with MFG_4. In this way we evaluated the effects of tuning the excitation and acquisition volumes on single-particle tracking experiments. The perfect match of selective illumination and observed volume size allows to detect and track individual beads diffusing in volumes of different extension. Long trajectories can be reconstructed in both the cases, specifically up to ~110 frames over a 2 μm thick volume and ~140 frames over a 4 μm thick volume (FIG. 68).

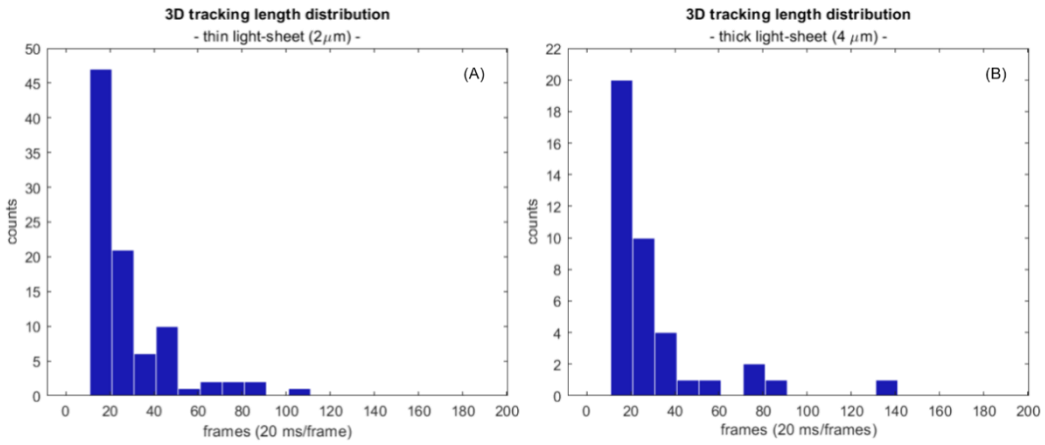

FIG. 68 – Histograms of the length of diffusing beads trajectories reconstructed after 3D single-particle tracking experiments. *Two light-sheet of thickness 2 μm (A) and 4 μm (B) are produced to match with MFG_4 and MFG_9 respectively. These combinations permitted to reconstruct long trajectories of fluorescent beads diffusing in volumes of different size.*

4.2.3 Exploring various ranges of dynamics in high- and low-density environments

Thanks to the MFM detection module we are able to produce volumetric imaging at a rate that is limited only by the acquisition speed of the camera and the brightness of the fluorescent molecules. As a consequence, MFM gives the possibility to explore also fast dynamic ranges of biomolecules.

We preliminarily demonstrated this by comparing the dynamics of 15 nm beads and 200 nm beads suspended in PBS+glycerol+BSA medium, respectively at 1:1 (high density) and 1:100 (low density) volume/volume concentration. For these acquisitions we placed MFG_9 in the MFM detection module to acquire

simultaneously a volume of ~4 μm and we produced a homogenous, 4 μm thick light-sheet thanks to the beam shaping module.

According to equation (1.18) in paragraph 1.6 considering the 3D case and the frame rate of the camera $\tau = 20$ ms, we derived the diffusion coefficient and the mean square displacement from the reconstructed trajectories of the diffusing beads (FIG. 69). As expected, smaller beads show a wider range of dynamics.

The analysis performed on fluorescent beads at different density, diffusing in media with various viscosity constituted an ideal sample that allowed us to demonstrate the fundamental characteristics of our imaging method. The encouraging results provided a safe base to tackle more realistic biological conditions. The following paragraphs contain the results obtained for the observation of the dynamics of various nuclear biomolecules, whereas the last section of this chapter contains the results of super-resolution imaging of the nuclear membrane.

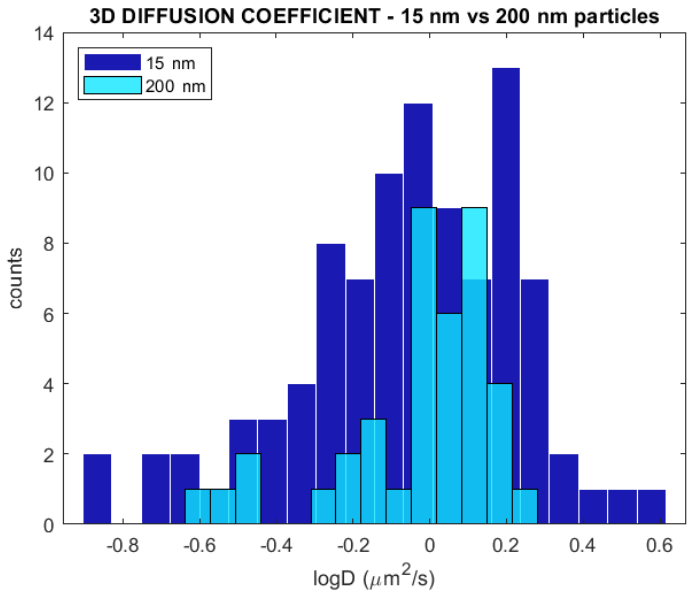

FIG. 69 – Fast and slow dynamics of fluorescent beads. *The histogram of the diffusion coefficient calculated for 15 nm and 200 nm radius beads and reported in logarithmic scale shows that the smaller particles have a faster range of dynamics.*

4.3 Imaging the dynamics of single H2B histones in the nucleus of living cells

To demonstrate the efficiency of our microscopy method in biological samples, we used it to observe the volumetric dynamics of H2B histones in the nucleus of living human osteosarcoma (U2OS) cells.

Histones are basic proteins that are the structural components of the chromatin. DNA fold around histones to create small structural units called nucleosomes. There

are five families of histones: H1-H5 (linker histones) and H2, H3, H4 (core histones). H2A-H2B and H3-H4 form the core of nucleosomes and are fundamental to the compaction of chromatin in the nucleus (**FIG. 70**). Thus, histone variants contribute to the spatial organization of the genome, participating to the regulation of gene expression and chromatin maintenance. They have been deeply investigated with several different approach. Ensemble dynamics of histones variants has been studied in living cells with photobleaching techniques [124], [125], while single-molecule imaging has been used to investigate single histones dynamics, but performed mostly close to the surface of the coverslip using TIRF microscopy [126]. Volumetric single-molecule fluorescence microscopy has been performed on fixed cells to produce the STORM super-resolution description of 3D organization of histones variants during S-phase of the nucleus [127]. However, techniques that allow the 3D detection and tracking in living cells of densely labeled histones are still missing. We demonstrated that with our newly developed microscope we were able to detect and localize in 3D single H2B histones in the nucleus of living U2OS cells, far away from the coverslip. These observations do not aim at providing a quantitative description of the 3D dynamics of single H2B histones, but open the way for future investigations on the role of these proteins in regulating the chromatin organization and dynamics.

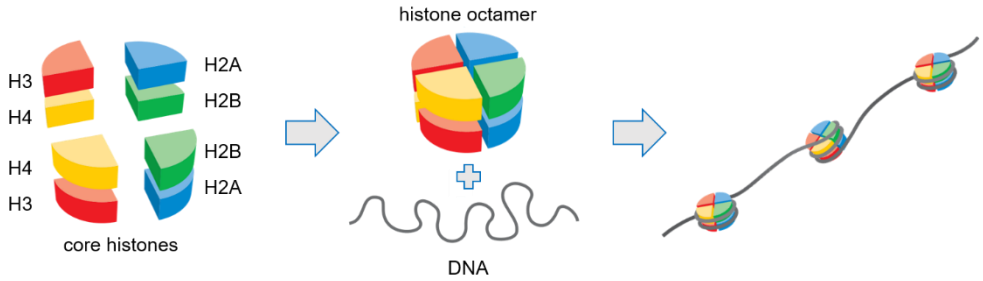

FIG. 70 - Histones constitute a structural component of the chromatin. *DNA folds around the histone octamer to form the DNA structural unit called nucleosome.*

Tracking single histones in dense environments, far from the coverslip surface.

To observe the 3D dynamics of single H2B histones we used human osteosarcoma (U2OS) cells from a stable cell line. Cells were transfected to express HaloTag-H2B and labeled with HaloTag-AlexaFluor 647 at a concentration of 5nM (see paragraph A4.2). To perform imaging of living cells in physiological conditions, we kept them in enriched DMEM at 37° and 5% CO2 with a heating system (INUBG2E-PPZI, by Tokai Hit) during the observation.

Placing MFG_4 in the MFM detection module, we performed 3D instantaneous imaging of the nucleus at a frame rate of 30 ms/frame, thus acquiring ~30 volumes of 22 µm × 22 µm × 2µm size per second. Despite the high density labeling, and

thanks to the volumetric selective excitation, we were able to reach the single-molecule regime by illuminating the nucleus for about ten seconds with < 1 mW on-sample intensity. In this way, we limited the photodamage of the living sample.

When living cells are placed in the soSPIM chip, they can crawl along the walls of the cavities and find themselves far away from the coverslip surface. By regulating the height of the light-sheet compare to the mirror of the soSPIM chip, we could image portion of the nucleus of cells that were up to 20 µm above the coverslip surface. Thus, these observations demonstrated that our method allow the observation of dense microenvironments at their molecular scale, far away from the coverslip surface.

As already described in paragraph 4.2.3, we performed analysis of single-particle trajectories considering the 3D case and the frame rate of the camera $\tau = 30$ ms. We derived the apparent diffusion coefficient of H2B histones moving in the nucleus of living cells (**FIG. 71**). Histones range of dynamics was found to be quite restricted, as confirmed by the distribution of apparent diffusion coefficient which spans the interval of values $0.001\ \mu m^2/s \leq D < 1\ \mu m^2/s$ and shows a peak for $\log D = -1.75\ \mu m^2/s$. This is an expected result considering the structural role that they play in the chromatin folding and for the formation of nucleosome structures. Later, we decided to explore faster dynamics ranges that could emphasize the strengths of our newly developed imaging system. In the next paragraph, the experiments conducted on mES cells are presented together with the analysis of trajectories of single CTCF and Cohesin nuclear factors.

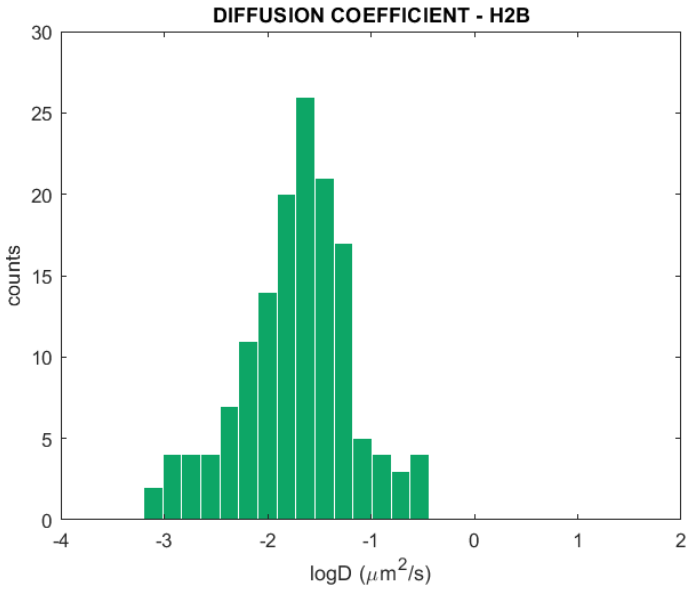

FIG. 71 – Distribution of apparent diffusion coefficient of single H2B. *Reported in a logarithmic scale, the apparent diffusion coefficient distribution confirms the limited diffusion of histones due to the role that they play for the structural organization of the chromatin in the nucleus of living cells*

4.4 Observation of CTCF and Cohesin nuclear factors in living stem cells

Chromatin architecture and cellular functions are tightly related. In the last decades, DNA folding have been proven to be a fundamental regulatory mechanism, thanks to significant technological advancements in biochemistry, molecular biology and imaging [128]. In mammals, chromatin is organized in different three-dimensional domains that span over a wide genomic and spatial scales, from the smallest nucleosomes formed by ~100 base-pairs (bp)/10 nm to the biggest chromosomes made of $\sim 10^6$ bp/μm. In this paragraph, I will focus on nuclear factors that are responsible for the regulation of a particular class of chromatin domains called topologically associating domains (TADs, $10^5 \div 10^6$ bp/10^2 nm) [129], [130].

TAD formation in mammals relies on DNA loop extrusion by Cohesin and their boundaries are defined by convergent CTCF binding sites [129], [131]. These two nuclear factors are remarkably different: while Cohesin is a multiprotein complex (> 300 kDa) with no preferential binding sequence, CTCF is a reasonably small DNA-binding protein (75 kDa) with specific target sites on the genome (**FIG. 72**). Previous work in the lab has shown the dynamic heterogeneity of these two factors, investigating their coupled behavior via single molecule tracking in 2D [132].

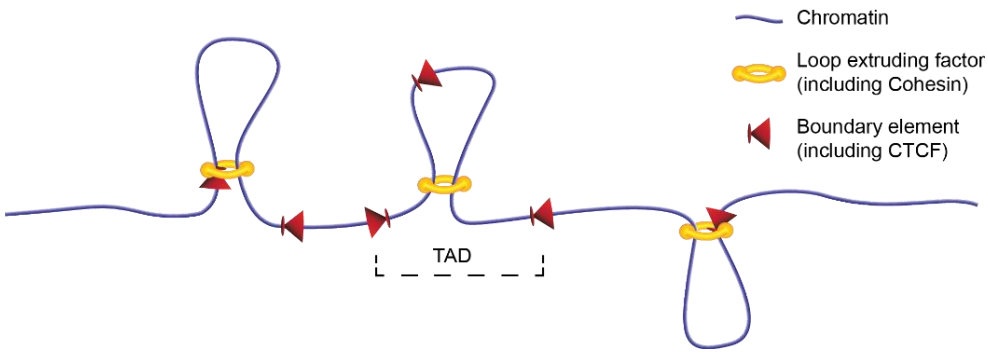

FIG. 72 - Loop extrusion as a model for chromatin organization in topological associating domains (TADs). *CTCF and Cohesin are nuclear factors that contribute to the formation of chromatin loops.*

Willing to explore different ranges of dynamics in biological samples, we decided to observe CTCF and Cohesin in the nucleus of living mouse embryonic stem cells. The use of stem cells for our experiments has required a specific training. In fact, they are more delicate than the U2OS cells that we used for the observation of H2B histones dynamics (see paragraph 4.3) and super-resolution imaging (see paragraph 4.5). By reducing the background noise, the selective illumination of our method provided single-molecule sensitivity with low excitation intensity, resulting in the limitation of photobleaching and phototoxicity. Therefore, our method resulted to be an optimal tool for low-intrusive observation of delicate sample such

as stem cells. Another factor of interest for our project is that stem cells have the tendency of growing in colonies, even when placed inside a well of the soSPIM chip. In this way, we were able to perform volumetric single-molecule imaging in depth, at a distance of ~20 μm from the coverslip surface (FIG. 73).

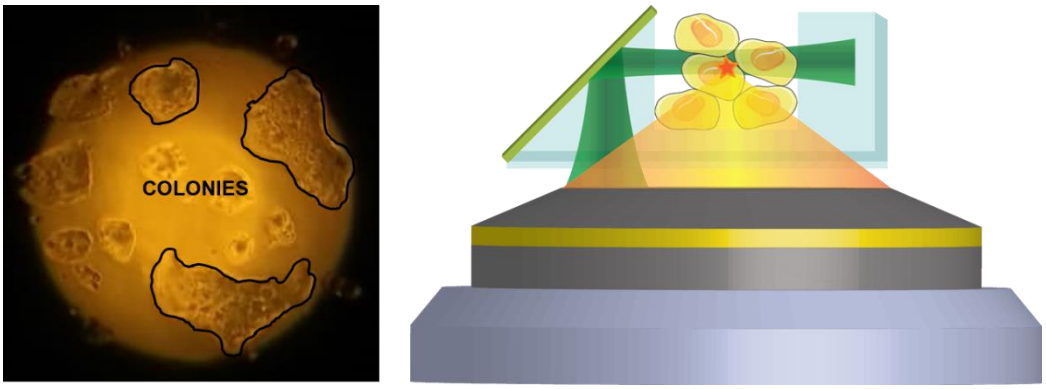

FIG. 73 – Stem cells tend to grow in colonies. *The image on the left, acquired with a transmission light microscope, shows how cultured stem cells tend to form colonies. We exploited this tendency of stem cells to create aggregates of cells in the cavities of the soSPIM chip. This permitted us to image cells that were far from the coverslip surface.*

Exploring the volumetric dynamics of CTCF and Cohesin

To observe the 3D dynamics of single CTCF and Cohesin nuclear factors we used two kinds of mouse embryonic stem (mES) cells, edited and provided by Elphège Nora. A HaloTag was encoded in the CTCF and Cohesin subunit Rad21 proteins sequence of the mES cells. This HaloTag allowed us to label the nuclear factors with Halo-JF549 dyes, provided by Luke Levis at Janelia Research Center. We used labeling concentration of 0.5 nM – 2nM. To maintain physiological conditions during the imaging, the sample was mounted with the required culture media (Fluorobrite DMEM) in a heated stage on the microscope, maintaining thus 37° incubation temperature and 5% CO2 environment.

For the observation of volumetric dynamics of CTCF and Cohesin, we placed MFG_4 in the MFM detection module to acquire 4 different planes simultaneously. With a fine tune of the excitation intensity, we could reach the single-molecule regime after short photobleaching of the sample. By using the beam expander module, we produced a 2 μm thick light-sheet to selectively excite the specimen. Thanks to the selective illumination and the high brightness of JF549 dyes, instantaneous volumetric imaging was performed with a time resolution of 20 ms, being able to detect individual fluorescent molecules over > 10000 frames. By using a limited excitation intensity, we minimized any sample photodamage.

Taking advantage of the tendency of stem cells to form colonies, we could detect

and track individual CTCF and Cohesin nuclear factors diffusing in the nucleus of living mES cells up to 30 μm far from the surface of the coverslip. For both CTCF and Cohesin we could reconstruct long trajectories up to 40 frames. As already described for the case of fluorescent beads (see paragraph 4.2) and H2B histones (see paragraph 4.3), we derived the distribution of apparent diffusion coefficient of CTCF (**FIG. 74**) and Cohesin (**FIG. 75**).

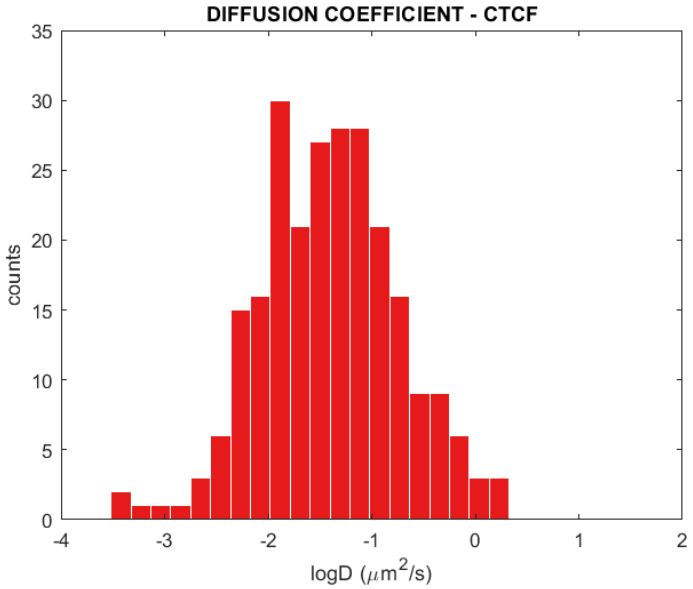

FIG. 74 – Distribution of apparent diffusion coefficient of individual CTCF diffusing in the nucleus of living stem cells. *Reported in logarithmic scale, the distribution shows that CTCF has a wider range of dynamics in comparison with H2B, including also ranges of faster dynamics.*

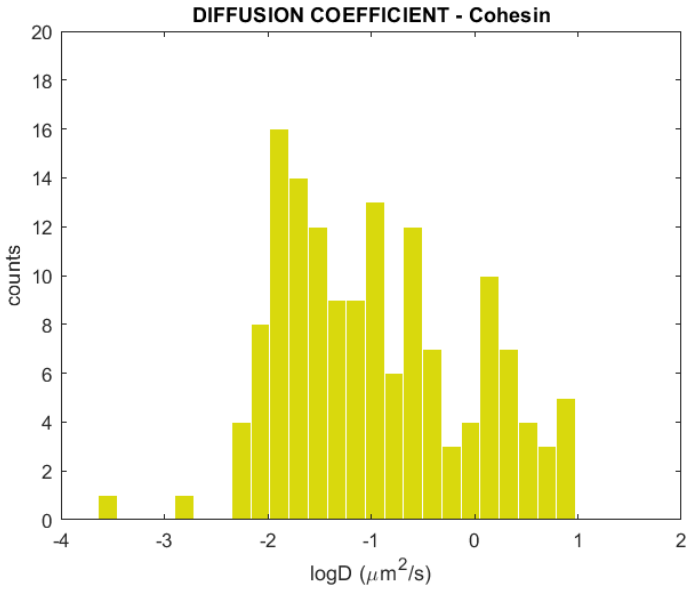

FIG. 75 – Distribution of apparent diffusion coefficient of single Cohesin diffusion in the nucleus of living stem cells. *Reported in logarithmic scale, the distribution of apparent diffusion coefficient shows that Cohesin present the widest range of dynamics in comparison with H2B and CTCF. The several peaks confirm the variability of Cohesin motion and the presence of several subpopulations.*

The distribution of apparent diffusion coefficient of CTCF DNA-binding protein spans from high motility ($D > 1\ \mu m^2/s$), to histones-like low motility ($D \leq 0.01\ \mu m^2/s$). The distribution peak $0.01\ \mu m^2/s < D < 0.1\ \mu m^2/s$ describes the subpopulation of molecules that are bound to DNA. The distribution of apparent diffusion coefficient of Cohesin shows the high variability of this nuclear factor motion. The wide distribution reaches extreme values of $D \sim 10\ \mu m^2/s$ on one side, that characterize the dynamics of high motile molecules, and $D < 0.01\ \mu m^2/s$ on the other side, related to bound molecules. The high variability of Cohesin dynamics was confirmed visually at each step by the reconstruction of 3D trajectories overlaid with the raw data (FIG. 76).

It must be recall that these observations did not aim at providing a complete description of the dynamics and interactions of the two nuclear factors. For a thorough characterization of the mechanisms that drive the dynamics of CTCF and Cohesin, more statistics would be necessary. Our preliminary results are in good agreement with the results of the work of Laura Caccianini [121] and other related projects [133], [134]. However, all these works are based on 2D single-molecule imaging and tracking. This demonstrates that our method opens the way for expanding the study of regulatory mechanism of chromatin organization from observing a 2D section to a thick volume of the nucleus through single-molecule fluorescence microscopy.

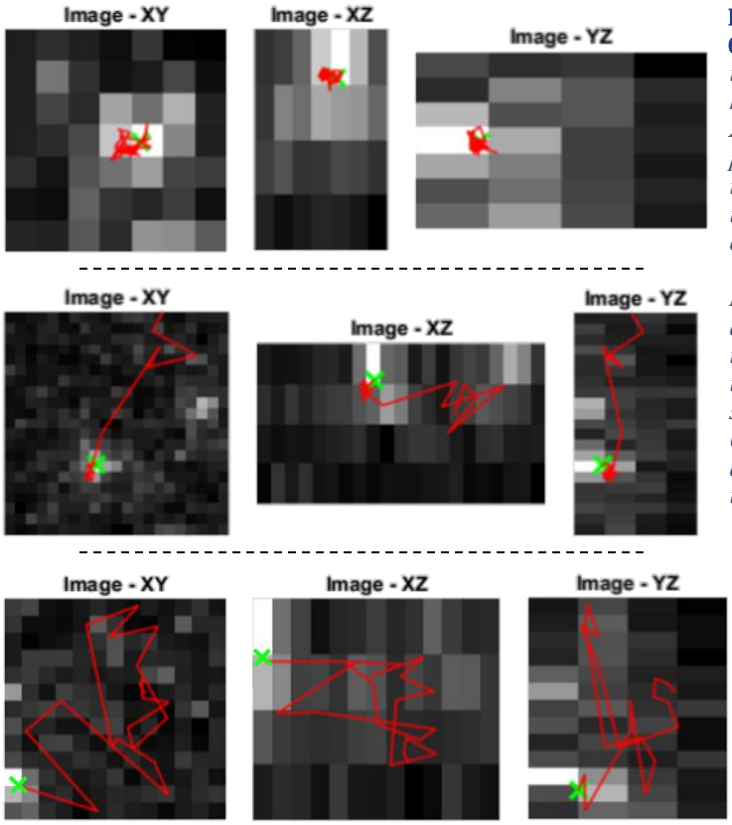

FIG. 76 – High variability of Cohesin 3D dynamics. *The three panels (top, center, bottom) show the XY (left), XZ (center) and YZ (right) projections of the volumetric trajectories of Cohesin. The top panel shows an example of a bound Cohesin molecule. The central panel show a molecule that is highly diffusive initially and binds to chromatin at the end of its trajectory. The bottom panel shows a high motility Cohesin nuclear factor that diffuse for the entire trajectory.*

4.5 Super-resolution imaging of the nuclear membrane through DNA-PAINT

After demonstrating the efficiency of our method at performing 3D tracking experiments for the observation of the dynamics of individual biomolecules, we performed also super-resolution imaging. In fact, this is the other main application of single-molecule fluorescence microscopy. Detection and precise localization of single emitters is at the base of super-resolution methods such as (F)PALM/(d)STORM (see paragraph 1.7.1), but also DNA-PAINT (see paragraph 1.7.2). We decided to use this latter approach to demonstrate the super-resolution imaging capabilities of our system. In fact, as anticipated in paragraph 4.1, moving from unspecific widefield illumination to selective excitation is required to detect single imager strands in DNA-PAINT super-resolution. Also, the optical sectioning of the light-sheet excitation allows to increase the concentration of the imager strands. For all these reasons, we believed that the combination of DNA-PAINT technique with the selective volumetric excitation and instantaneous 3D imaging of our newly developed method could efficiently produce volumetric super-resolution images, while reducing the experimental time and the amount of collected data. This paragraph contains the results obtained with such combination, preceded by the optimization of the sample preparation and the imaging parameters.

4.5.1 Unspecific targeting as an obstacle to overcome

Focusing our interest on the structure of the nucleus of cells, we decided to perform super-resolution imaging through DNA-PAINT technique of the nuclear membrane, looking specifically at the Lamin B1 protein. For super-resolution imaging, we used human osteosarcoma cells from a stable cell line, carrying a modified gene for the expression of EGFP-labeled NUP96 nuclear pore complex protein (U2OS-NUP96EGFP).

As seen in paragraph 1.7.2, in DNA-PAINT experiments, the structure of interest is marked with DNA docker strands. The binding rate determines how fast the DNA imager strands carrying the fluorescent dye bind to and unbind from the docker strands. In our case, to specifically label the Lamin B1 protein with the docker strands we used an immunofluorescence protocol: a primary antibody targets the Lamin B1 at the nuclear membrane, and the complementary secondary antibody carries the DNA docker strands (see appendix A4.3). However, unspecific targeting affected critically our first experiments, in which fluorescent dyes were detected and localized not only on the nuclear membrane but also inside the nucleus and in the cytoplasm (**FIG. 77**).

An extensive optimization of the sample preparation and the imaging parameters was necessary to reduce dramatically the unspecific targeting of the sample. For that, the composition of the blocking buffer, with the addition of salmon sperm DNA and dextran sulfate was a game changer (see paragraph A4.3). We also optimized the incubation time and the concentration of the primary antibody.

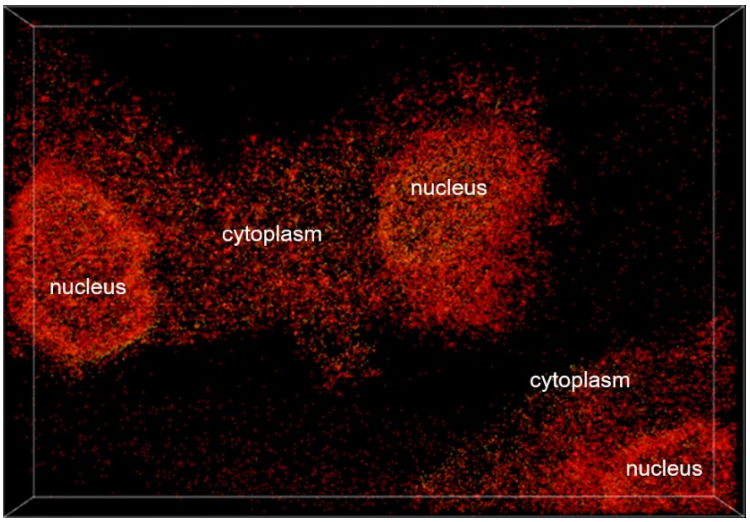

FIG. 77 – Unspecific targeting in DNA-PAINT super-resolution imaging. *An extensive optimization of the sample preparation protocol has been necessary to reduce the unspecific labeling of the cytoplasm and the internal part of the nucleus.*

4.5.2 Drift correction

Single-molecule localization-based super-resolution images are obtained as the pointillistic reconstruction of the map of individual chromophores, each one that appears in the final image as a point of width given by the localization precision. To obtain high quality super-resolution images, high molecular density is required, which implies acquiring tens of thousands of images during very long time. To note here that the acquisition duration of the time series increases even more for volumetric super-resolution imaging (except when acquired with MFM) since most of the techniques are based on the scan of the sample.

During the acquisition time, the sample undergoes mechanical drift, which affects the final reconstruction if not corrected. Common strategies for the drift correction can be divided in three categories. Methods in the first category use stably fluorescent fiducial marker fixed on the coverslip surface to track the drift movements [35], [37], [135], [136]. However, inserting fiducial markers in the sample can increase the experimental complexity. Methods in the second category correct the drift by calculating the cross-correlation between fluorescent or reconstructed super-resolution images of the sample [137]–[140]. Methods in the third category corrects the drift by using transmission images of the sample [104], [141]. The drift correction can be in real-time using a piezoelectric sample stage or

in post-processing.

A central component of our imaging system is the soSPIM chip that permits to use the same high-NA objective to produce the selective excitation of the sample and collect the fluorescence. Mechanical drifts during soSPIM imaging introduce an additional issue. In fact, as seen in paragraph 3.2.2, any lateral displacement of the soSPIM chip results in a displacement of the excitation beam on the mirror. As a consequence, in soSPIM, the lateral drift of the sample is associated with the axial displacement of the light-sheet. For this reason, it would be necessary to correct the drift in real-time. For that, the team of Jean-Baptiste Sibarita and Rémi Galland fabricates soSPIM chips with nanodiamonds embedded in the polymer. These are used as fiducial markers for real-time lateral drift correction based on a feedback loop algorithm, that controls the piezoelectric stage of the microscope.

For the moment, we have not implemented a real-time drift correction mechanism on our system. Nevertheless, by acquiring multiple planes at every frame, MFM helps to mitigate the problem associated with the axial displacement of the light-sheet after soSPIM chip lateral drift. For super-resolution imaging, we corrected the focus drift using the *perfect focus system* by Nikon microscopes, and we adopted two strategies for correcting the lateral drift in post processing. First, in the acquisitions in which a nanodiamond was in the MFM field of view, its localization served as a reference for correcting the lateral displacement of the soSPIM chip. Second, in the absence of such fiducial marker in the MFM field of view, the lateral drift was corrected by the cross-correlation method.

For this method we made the following three assumptions. First, we assumed that the blinking of the molecules that label the biological structure of interest is random. Second, we assumed that the localizations accumulated over a hundred of frames are sufficient to recognize biological structure of interest, which implies having abundant detections per frame. Third, we hypothesized that the drift is not significant during a hundred of frames.

To correct the drift, we divided the acquisition in group of a hundred of frames, the localizations of each being convolved with a sub-diffraction Gaussian profile to reconstruct an image. Each image formed in this way is cross-correlated to another image formed by the localizations accumulated over the following hundred frames. The cross-correlation maximum is related to the lateral drift of the sample. The calculated drift is later used to correct the real localizations in each frame.

4.5.3 Reconstructed super-resolution images

We performed super-resolution imaging of the Lamin B1, a protein present on the nuclear membrane of the cells. We adopted U2OS-NUP96EGFP cells from a stable cell line. The nuclear pores of these cells are stably labeled with EGFP dye. We

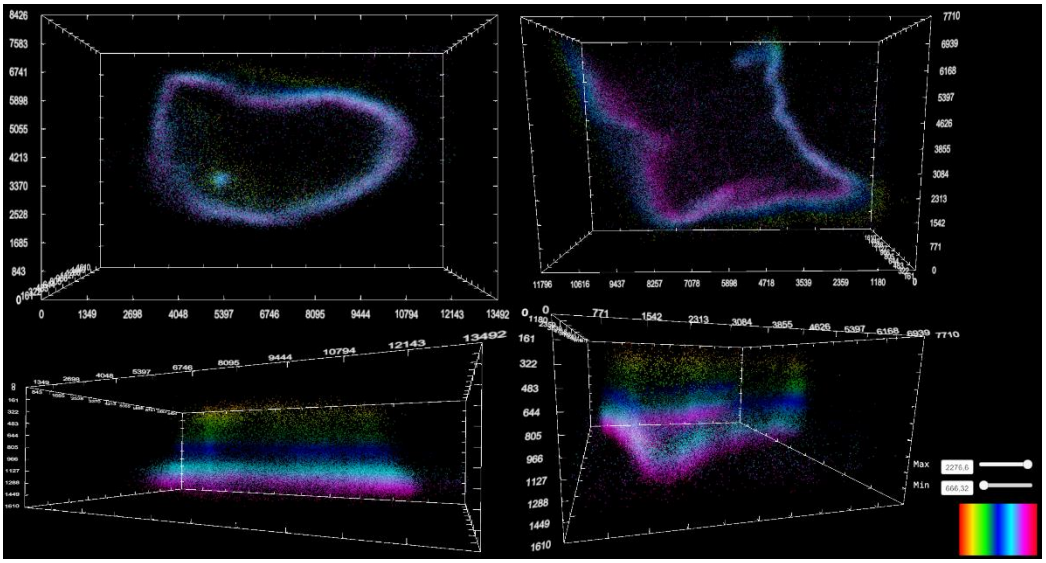

FIG. 78 – Super-resolution imaging of Lamin B1 through DNA-PAINT. *Observed volume* 22 $\mu m \times$ 22 $\mu m \times$ 2 μm. *Lateral drift corrected by cross-correlation method. Color-code for z.*

prepared the cells according to the optimized immunofluorescence sample preparation protocol presented in A4.3. For the imaging, we used DNA imager strands, carrying Cy3B dyes, at a concentration of 2.5 nM. The fluorescence channels of EGFP and Cy3B were completely separated and we could use the fluorescent nuclear pores of the cells as a reference for the nuclear membrane.

To be able to reconstruct super-resolution images, we acquired 25000 to 50000 frames per sample. We found that, according to the binding rate of the imager strands, the best results were obtained for an exposure time of 200 ms. Although single emitters were clearly detectable also at faster frame rate, the number of unspecific detections was higher for shorter exposure times. We configured the MFM detection module with MFG_4. All the images contained in this paragraph have been produced with Genuage, an open-source platform for the visualization of multidimensional point clouds developed recently in our lab [142].

For the first examples here showed, we used the 60X, 1.27 NA, water-immersion objective. The interplane separation was 570 nm and the lateral pixel size was 200 nm. With such imaging parameters, we acquired 5 volumes with dimension of 22 µm × 22 µm × 2 µm every second. We selectively excited this volume with a homogenous intensity light-sheet of 2 µm thickness, produced using the beam shaping module of our system. The final images are reconstructed as a pointillistic map of 110000 localizations of single emitters. The drift was corrected with the cross-correlation method. From the reconstructions, we can observe the volumetric extension of the nucleus and the curvature of its membrane (FIG. 78). However, the imaging parameters did not provide a perfect sampling of the 3D PSF of a single emitter, affecting the localization precision.

To sample the PSF in $x - y$ and z correctly, we inserted ad additional 1.5X

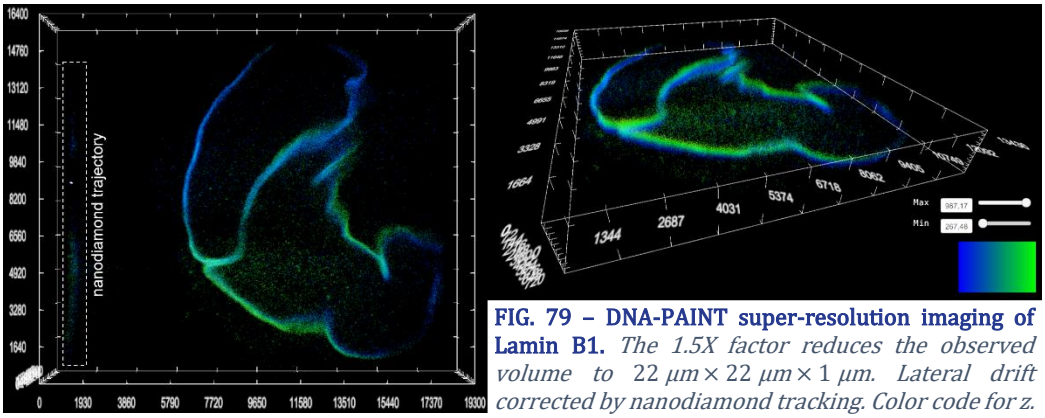

FIG. 79 – DNA-PAINT super-resolution imaging of Lamin B1. *The 1.5X factor reduces the observed volume to 22 μm × 22 μm × 1 μm. Lateral drift corrected by nanodiamond tracking. Color code for z.*

magnification factor on the detection path. In this way we obtained a pixel size of 133 nm and an interplane distance of 250 nm. Thus, the good sampling came at the cost of smaller observation volume of 22 μm × 22 μm × 1 μm size. In the first reconstruction (FIG. 79), obtained from 188000 localizations, we can observe two nuclei at different heights. Cells were 14 μm above the coverslip surface. In this acquisition the drift has been corrected by tracking a nanodiamond that was in the MFM field of view.

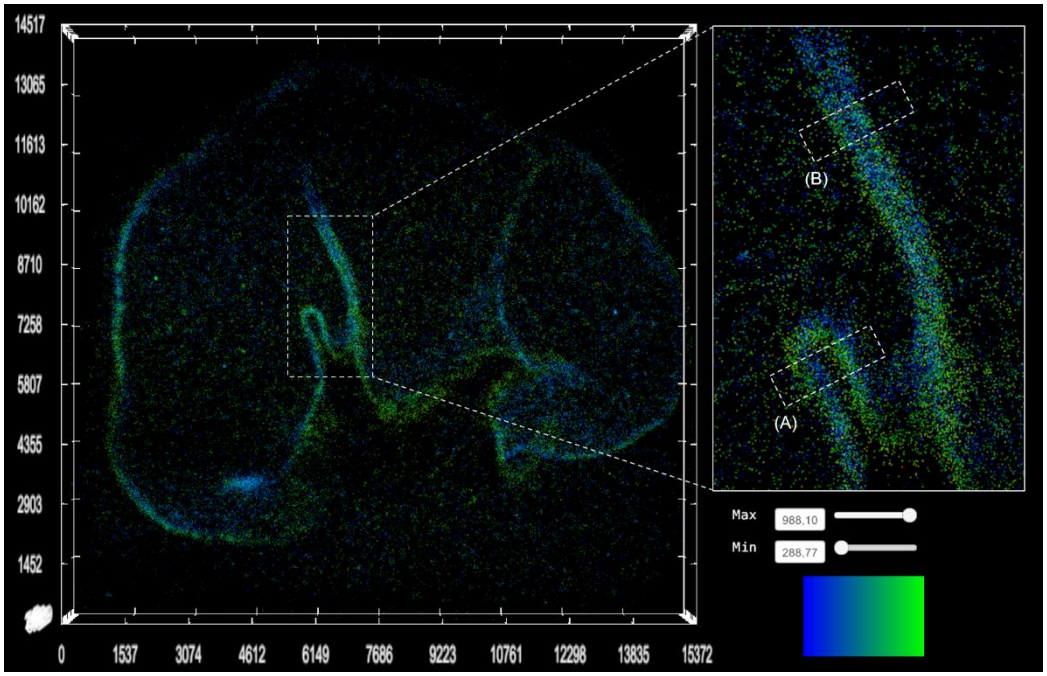

FIG. 80 – DNA-PAINT super-resolution imaging of Lamin B1 protein. *The reconstructed nucleus presents several invaginations of the membrane. Region (A) and (B) are used to evaluate the resolving power of the imaging system.*

Using this configuration, we also reconstructed super-resolution images correcting the drift with the cross-correlation method (FIG. 80). This example is

obtained from 96000 localizations and shows the nucleus of a cell that was 16 µm far from the coverslip surface. The nuclear membrane shows several invaginations. A preliminary quantification of the achievable lateral resolution was performed. Two areas (A) and (B) were identified in the reconstruction in which the walls of the invaginated nuclear membrane were in close proximity. Here, the histograms of the (x, y) localizations along a crossing segment identifies clear peaks for both regions. The distance between the peaks in the histogram relative to the area (A) is 250 nm, while for the region (B), the two peaks are separated by 160 nm, a value beyond the resolution limit (FIG. 81).

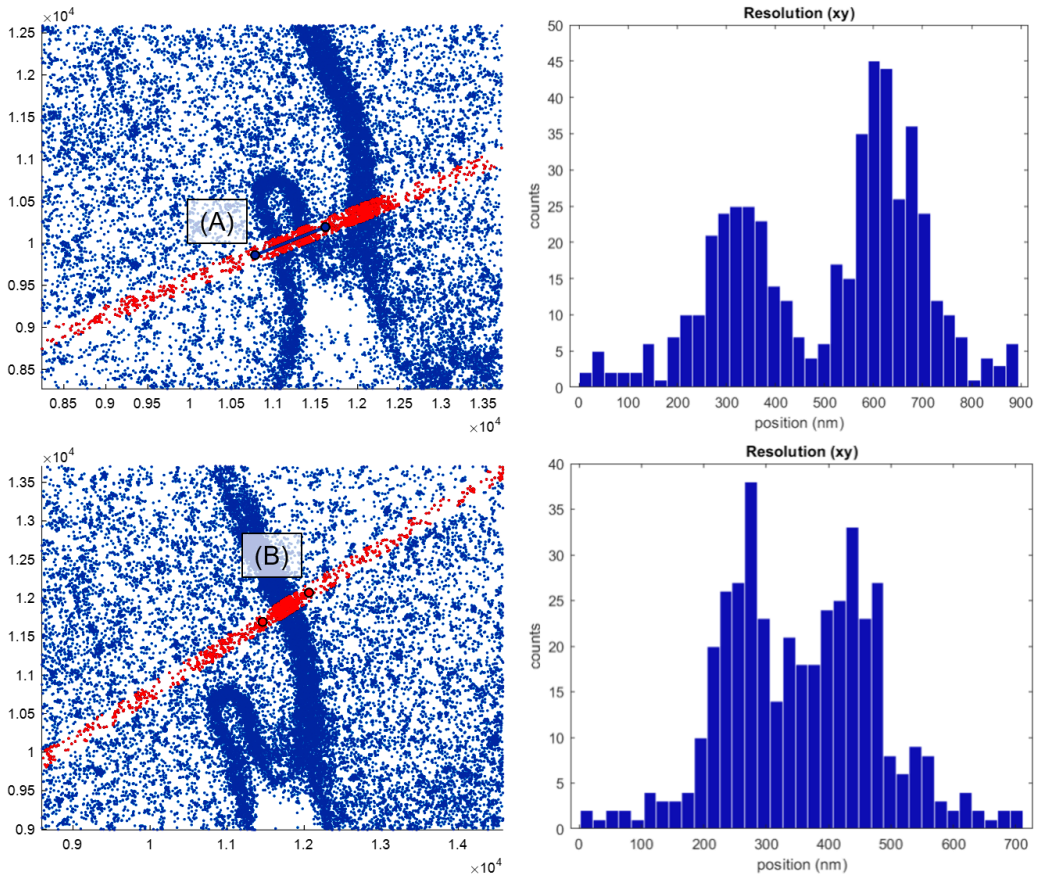

FIG. 81 – Measuring the resolving power of the imaging system. *The histograms of localizations of the region (A, top) and (B, bottom) show two clear peaks describing the walls of the nuclear membrane.*

We also evaluated the 3D localization precision of our method. For that, we took in consideration single emitters that appeared on at least 5, consecutive frames within a 300nm radius. We repeated the measurement of the same molecule position and calculated the standard deviation s of the (x, y, z) localization. The measured values are reported as histograms for x, y and z localization precision. The peaks of the distribution suggest that our method achieves localization precision $\sigma_x = \sigma_y = 20$ nm in $x - y$ and $\sigma_z = 50$ nm (FIG. 82).

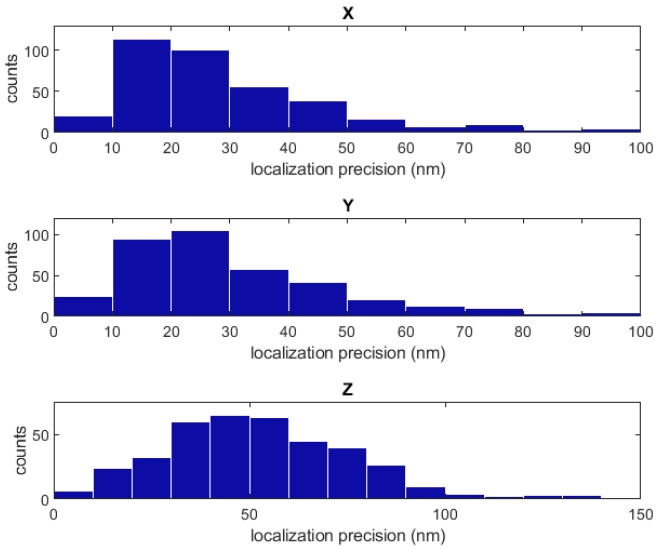

FIG. 82 – 3D localization precision. *The histograms show the distribution of x, y, and z localization precision of single emitters. To build the histograms, we took in consideration the emitters that were localized at least 5 times during the acquisition. We calculated the standard deviation on the coordinates (x, y, z). The localization precision for a single emitter is evaluated as the ratio between the standard deviation on the coordinates and its intensity.*

In conclusion, this chapter contains the results that we obtained using our newly developed imaging system for applications of single-particle tracking and super-resolution imaging. We demonstrated the capabilities of our method of performing selective, volumetric and homogenous excitation of the sample, and we showed the benefits it can bring for imaging complex and dense environments at the single-molecule level, far from the coverslip surface. The next steps and the future perspectives of this project will be discussed in the next chapter.

Chapter 5

Conclusion and perspectives

Complex, volumetric biological samples, such as cells colonies, cells spheroids and organoids, impose challenging conditions for performing efficient 3D imaging at the single-molecule level. In fact, high signal-to-noise ratio, high temporal resolution and the capability of detecting single emitters far from the coverslip surface are required. In this project we developed a novel method for single-molecule fluorescence microscopy that provides selective volumetric and homogeneous excitation to performs real-time 3D imaging in dense environments. I presented the details of the optical system that is based on separated functional units. The design has been guided by the idea of creating a system in which the different modules can be independently adjusted, but work together to produce the perfect match between the selective, volumetric and homogenous excitation on one side and the observation volume on the other side.

We demonstrated the performances of our system by analyzing the volumetric dynamics of single fluorescent beads of different sizes diffusing in media of various viscosities. Such analysis shows that, thanks to our method, it is now possible to explore efficiently different ranges of fast dynamics in 3D with single-molecule tracking approach. This kind of sample provided a representation of challenging imaging condition that we find in complex biological samples. Later, we demonstrated the 3D single-molecule imaging capabilities of our method by observing multiple biological samples.

The observation of volumetric dynamics of single, H2B histones, deep in the nucleus of living U2OS cells has been a first demonstration of potential applications that can be performed using our method. As expected, this observation confirmed the low motility of histones. The observation of the 3D dynamics of nuclear factors such as CTCF and Cohesin in the nucleus of living stem cells demonstrated the compatibility of our system with samples that require low excitation intensity. The analytical results of this observations provide only a partial view of the dynamics of

CTCF and Cohesin. For a complete study of the mechanisms more experiments would be required. I would like to emphasize the potential benefits that, in my view, our system could bring to an extensive study of these or similar mechanisms. In fact, I believe that our method excels in applications that require a compromise between time resolution and single-molecule detection efficiency, and in which the imaging method is required to be non-invasive. Expanding the knowledge of chromatin dynamics and organization is a fascinating and continuously evolving research line. I am convinced that our method will contribute to this field by offering a performant imaging tool for the investigation of many regulatory mechanisms, such as, for example, the loop extrusion model or the mobility of genomic loci.

Also, we demonstrated that our method is compatible with super-resolution imaging such as DNA-PAINT technique. It is noteworthy to mention that, by providing instantaneous volumetric imaging, our method dramatically decreases the experimental time that is necessary to acquire enough data for super-resolution images reconstruction. The results obtained until now can be further improved. For that, the very next step in the optimization of our system is the upgrade of the drift correction. In fact, it is crucial to adjust the displacement of the sample in a real-time when using soSPIM (see paragraph 3.2.2). A possible strategy for real-time drift correction that we could adopt for our system is based on the use of adaptive optics [143]. Using adaptive optics would also bring benefits for the correction of aberrations that can appear when imaging far from the coverglass or deep in scattering samples. We note here, that the aberration correction produced by MFM, in combination with the use of water-immersion objective, already limits the insurgence of spherical aberrations originating from imaging deep in the sample.

A game changer for improving the performance of our method would be the possibility of using the 100X, 1.4 NA, oil-immersion objective, or even a silicon-immersion objective (to match the refractive index of the sample), with similar NA and magnification. As a consequence, we will improve the photon collection efficiency, and thus will be able to split the fluorescence over the 9 planes of MFG_9. In this way, we will be able to acquire instantaneously thick volumes, and we will improve the sampling of the PSF in the three dimensions. To use such objectives, the design of the soSPIM chip needs to be optimized, especially the distance between the well and the mirrors. A light-sheet produced with such objectives has in fact a shorter Rayleigh length.

Our method is compatible with any super-resolution imaging technique based on the localization of single emitters, and I believe that it can be easily combined with other approaches that has been described in this manuscript. For example, the combination of our method with PSF engineering or SELFI promises to give fascinating results. With the development of multifocus grating that acquire the

images of planes with a higher interplane distance, these PSF engineering or SELFI can provide the right sampling between consecutive planes. As a result, instantaneous 3D imaging of big volumes can be produced with high temporal and spatial resolution.

Altogether, the continuous development of new techniques and methods makes the single-molecule fluorescence microscopy a quickly evolving field that, with time, is destined to reveal complicated biological mechanisms in many different kinds of samples. I hope that, with the realization of this project, I gave my contribution to make a step forward in this direction.

Annex 1

Alignment procedures

This annex contains the detailed procedure for the alignment of the automated tunable beam expander module and the multiwavelength beam shaping module.

A1.1 Alignment of the tunable beam expander module

The correct functioning of the module requires an optimal alignment of the lenses in order to displace the optics precisely along the optical path. The pointing direction of the excitation beam is supposed to remain aligned to the optical axis of the system. Also, to minimize the effect of gravity on the electrical lens we placed it horizontally. For that we installed a vertical breadboard on the optical table.

The collimated beam is reflected in the vertical direction by the mirror $M1$, A mirror $M2$ is installed in a mount for cage system (KCB1/M, by Thorlabs). Using a couple of pinholes installed on the cage system, the tilting of $M1$ is optimized to keep the laser parallel to the breadboard ($z-$ direction) and at a constant height ($y-$ direction). Using $M3$ and $M4$, the beam is brought back to propagate horizontally. The tilting of the two mirrors is adjusted so that the height of the beam is constant over the optical table ($z-$ direction) and the propagation direction of the is parallel to the displacement of the translator ($x-$ direction), which is fixed directly on the optical table. Specifically, to align the beam with the displacement direction, target at the same height are mounted on the same line on top of a removable carrier. The carrier is fixed on the translator aligning the tip of the first column with the beam. The tilting of $M3$ and $M4$ is adjusted until the shadows produced by the two columns overlap (**FIG. 83A**). After removing the carrier, a target is placed on the translator, centered with the beam to double-check the alignment of the displacement with the propagation direction. The beam must stay centered on the target while displacing the translator. $M5$, installed in a second mount for cage system, placed on a two-axis tilting support, is fixed on the translator

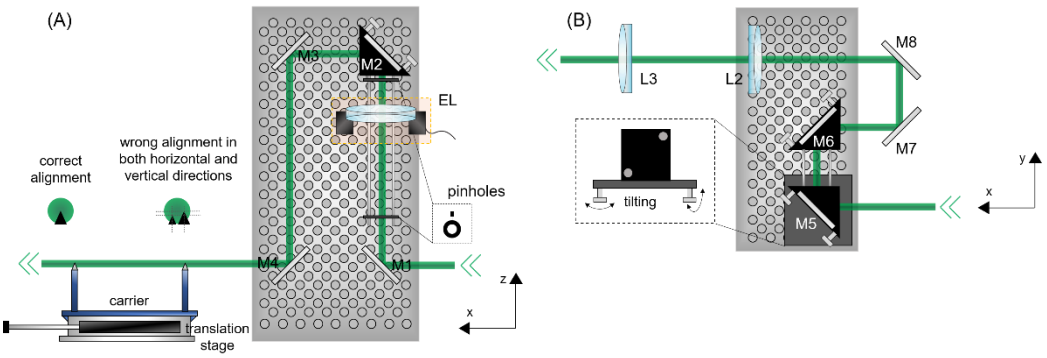

FIG. 83 – Scheme of the optical alignment of the tunable telescope. (*A) The optical path has been deviated on a vertical breadboard so that the electrical lens EL can be placed horizontally to reduce the gravity effect. A removable carrier with two parallel targets on top can be mounted on the translation stage to align the excitation beam with the displacement direction. The alignment is verified when the shadow of the two targets overlap at the center of the beam. (B) M5, M6 and L2 are mounted on the translation stage. In this way, for any displacement s of the stage, the distance between EL and L2 varied by 3s and the distance between L2 and L3 by s.*

to be centered with the beam. A flat mirror is screwed on the first surface of the cage system mount. The back reflection is adjusted by operating on one of the tilting axes of the support. Then the flat mirror is screwed on the second surface and the back reflection is corrected by adjusting the tilting of the mirror $M5$. Mirror $M6$ is also placed in a cage system mount and connected to $M5$ with short cage bars. The flat mirror is screwed on the second surface of the $M6$ mount to back reflect the beam. The tilting of $M6$ is adjusted to correct the back reflection. $M7$ and $M8$ are placed outside of the translator and tilted so that the beam propagates along the $x-$ direction and with a constant height. At this stage, it is fundamental to find the optimum alignment of the system, with small adjustment of mirrors $M5$ and $M6$. For that, some additional mirrors are inserted on the optical path to reflect the beam several times. A target is placed at a long distance, centered with the beam. The translator is moved at the final position. The beam will slightly move from the target and it must be realigned using $M6$. Then the translator is moved again to the initial position and the beam will appear de-centered in some directions. Acting on $M5$, the beam must be slightly displaced in the same directions of the decentering and realigned with the target using the additional mirrors. Then the translator is displaced to the final position again and the same procedure repeated to minimize the decentering of the beam at the displacement of the translator. Remove the additional mirrors and place a target centered with the beam. Lens $L2$ is aligned checking the centering on the target and the back reflection from the lens. If $L2$ is well positioned, no displacement of the beam on the target are visible while moving the translator. Align lens $L3$ with the same procedure. With no electrical lens on the optical path $L2$ and $L3$ constitute a 1X telescope. Therefore, the position of $L3$ is established using a shear plate to check the collimation of the output beam (**FIG. 83B**). Finally, the electrical lens EL is placed on the breadboard at the design

distance from $L2$. The centering and the back reflection of EL are optimized by sending a sinusoidal current to vary the focal length.

A1.2 Alignment of the beam shaping module

With reference to **FIG. 84**, the first, crucial, step in the configuration of the beam shaping module is the alignment of the relay lens $L4$. This lens conjugates the DMD plane to the sample plane and the quality of the modulated illumination is sensitive to its positioning. For a correct alignment a laser pointer that can be placed on the objective wheel of the microscope has been used. With no $EL2$, CYL and MM on the optical path, the laser has been sent through the beam steering module in the opposite direction of the excitation. A target has been fixed far from $L5$ so that $L4$ could be placed in between this and the lens $L5$. To find the exact position of $L4$, a collimated beam has been sent in the opposite direction of the excitation from a position in between of $L5$ and $L6$. In this way, using a shear plate, the position of $L4$ that gives a collimated beam at the output has been determined. For the correct centering of $L4$, the pointer and the target previously placed has been used as references, adjusting the tilt of the lens looking at the back-reflection.

For an optimum alignment of the optical paths of the different wavelengths, using our MATLAB code for the design of the DMD pattern (see A2.2), the intensity of the beam has been modulated to form a cross shape. The high intensity diffraction order of λ_1, λ_2, λ_3 and λ_4 could be overlapped precisely by adjusting the tilting of the corresponding dichroic beamsplitters. Considering that a tilting of any dichroic beamsplitter modifies the optical path of the reflected and transmitted wavelengths, the alignment procedure has been done in the following order. First, using dichroic beamsplitters $D1$ and $D2$, the incident angle θ_i^1 of λ_1 has been adjusted to produce a diffracted beam such as the modulated light evenly distributes over both the arms of the cross profile. After, considering that the TIR-prism overlaps the optical path of the high intensity diffraction order of wavelengths λ_2 and λ_4, the dichroic beamsplitters $D3$ and $D4$ have been tilted to align the diffracted patterns with the high intensity order of λ_1, making sure that the two arms of the cross patterns were well centered. Finally, the same procedure has been repeated for wavelength λ_3 using the two mirrors $M9$ and $M10$.

To finalize the alignment of the beam shaping module, the overlapped diffraction orders must be aligned with the optical path of the beam steering module. For that, the mirrors $M11$ and $M12$ must be placed on the optical path. The positioning of the two optics is crucial because they determine the distance between the DMD and the relay lens $L4$. For the DMD to be optically conjugated to the sample plane, this distance must be equal to the focal length $f_4 = 400$ mm of $L4$. To determine the position of $M11$ and $M12$ a collimated beam, propagating in the opposite direction

of the modulated excitation has been used. In this configuration, the beam is focused by $L4$ and the position of $M11$ and $M12$ can be adjusted to make the focus coincides with the DMD plane. To align the high intensity diffraction orders with the optical path of the beam steering module we used the laser pointer, placed on the objective wheel. The orientation of $M11$ and $M12$ has been adjusted to overlap the optical path of the excitation beams with the optical path of the laser pointer through all the optical system.

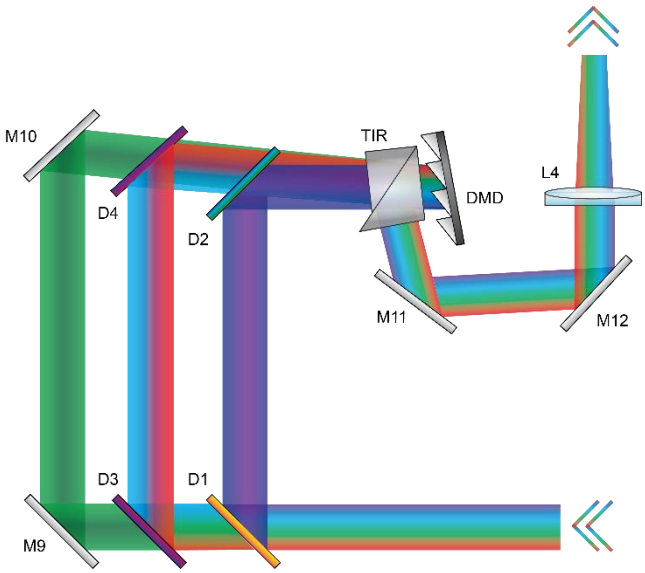

FIG. 84 – Beam shaping module optical scheme. *Two couple of dichroic beamsplitters, a couple of mirrors and a TIR-prism permits to regulate the incidence of $\lambda_1, \lambda_2, \lambda_3$ and λ_4 on the DMD so that the optical path of high intensity diffraction orders overlap.*

Annex 2

MATLAB programs for DMD-based beam modulation

This Annex contains the program developed in MATLAB for the simulation of the average excitation intensity produced by steering a beam modulated by a DMD. Also, it includes the program that has been developed in MATLAB for the design of the DMD patterns.

A2.1 Simulating the steering of a beam modulated with a DMD

The code simulates the intensity profile that we obtain at the sample plane by steering the excitation beam modulated by the DMD, the device being placed on a Fourier plane of the objective. Considering the DMD as a grating, the code takes in account the diffraction effect.

```
clear all
close all

%% Generate DMD and PSF

% microscope total magnification
Mag=160;

% DMD size
m=912;
n=1140;
ps=10.8*10^3; %nm -micromirror dimension-

x=(1:n)-n/2;
y=(1:m)-m/2;
[X,Y]=meshgrid(x,y);

%StandardDeviation PSF
NA=1.27;
lambda=600; %nm
SD=0.61*lambda/NA; % @ the image plane
```

```
psS=ps/Mag; %nm -micromirror dimension @ the image plane-

%PSF
a=(-10:10)*psS;
b=(-10:10)*psS;
[A,B]=meshgrid(a,b);
PSF=1/(SD*sqrt(2*pi))*exp(-(A.^2 + B.^2)/(2*SD^2));

%% Select DMD pattern

% %DMD pattern - all ON = Gaussian beam
% DMD=ones(m,n);


% %DMD pattern - Gaussian beam without center
% rmax=350;
% rmin=160;
%
% DMD=zeros(m,n);
% for i=1:m
%     for j=1:n
%         if ((X(i,j)^2 + Y(i,j)^2) <=rmax^2)&((X(i,j)^2 + Y(i,j)^2) >=
rmin^2)%&(abs(Y(i,j))<110)
%             DMD(i,j)= 1;
%         end
%     end
% end

% %DMD pattern - double arch
% rmax=350;
% rmin=160;
%
% DMD=zeros(m,n);
% for i=1:m
%     for j=1:n
%         if ((X(i,j)^2 + Y(i,j)^2) <=rmax^2)&((X(i,j)^2 + Y(i,j)^2) >=
rmin^2)&(abs(Y(i,j))<110)
%             DMD(i,j)= 1;
%         end
%     end
% end

% DMD pattern - double arch with elipticticity 3
rmax=350;
rmin=160;

DMD=zeros(m,n);
for i=1:m
    for j=1:n
        if ((X(i,j)^2 + Y(i,j)^2) <=rmax^2)&((3*X(i,j)^2 + Y(i,j)^2) >=
rmin^2)&(abs(Y(i,j))<110)
            DMD(i,j)= 1;
        end
    end
end

%% FIGURES

% DMD profile
figure
imagesc(DMD)
title ('DMD PATTERN', 'FontSize', 16, 'FontWeight', 'bold')
xlabel ('pixels', 'FontSize', 14, 'FontWeight', 'bold')
ylabel ('pixels', 'FontSize', 14, 'FontWeight', 'bold')

% DMD profile WITH diffraction effect - convolution PSF&DMD
C=conv2(DMD,PSF,'same');
% figure
% imagesc(C)
% title ('DMD PATTERN WITH DIFFRACTION EFFECT', 'FontSize', 16, 'FontWeight',
'bold')
% xlabel ('pixels', 'FontSize', 14, 'FontWeight', 'bold')
% ylabel ('pixels', 'FontSize', 14, 'FontWeight', 'bold')
```

```
I0= 100*exp(-(X.^2 + Y.^2)/(2*(250)^2)); %Gaussian beam
% figure
% imagesc(I0)
% axis equal
% colormap hot
% lim = caxis;

% Patterned profile WITHOUT diffraction effect
I1=I0.*DMD;

% Patterned profile WITH diffraction effect
I2=I0.*C;

figure
imagesc(I2)
axis equal
colormap hot
title ('PATTERNED FRONT-WAVE', 'FontSize', 14, 'FontWeight', 'bold')
xlabel ('z-direction', 'FontSize', 14, 'FontWeight', 'bold')
ylabel ('intensity', 'FontSize', 14, 'FontWeight', 'bold')

% % Average intensity WITHOUT diffraction effect
% r1=mean(I1,2);
% figure
% plot(r1, 'LineWidth', 1.5, 'Color', 'k')
% axis padded
% title('AVERAGE INTENSITY - no diffraction', 'FontSize', 14, 'FontWeight',
'bold')
% xlabel ('z-direction', 'FontSize', 14, 'FontWeight', 'bold')
% ylabel ('intensity', 'FontSize', 14, 'FontWeight', 'bold')


% Average intensity WITH diffraction effect
r2=mean(I2,2);
figure
plot(r2, 'LineWidth', 1.5, 'Color', 'k')
axis padded
title('AVERAGE INTENSITY', 'FontSize', 14, 'FontWeight', 'bold')
xlabel ('z-direction', 'FontSize', 14, 'FontWeight', 'bold')
ylabel ('intensity', 'FontSize', 14, 'FontWeight', 'bold')

display('DONE')
```

A2.2 Generation of DMD pattern

The code generates the pattern to be displayed on the DMD grid, telling which miniaturized mirrors to rotate to the tilt states $\pm t$. The diamond geometry and the rotational axis on the diagonal of each mirror impose a rescale of the DMD grid. The code includes the instruction to generate the elliptical double arch pattern and the cross target for the alignment of the beam shaping module. At the end, it saves the generated pattern in a format that can be uploaded to the software that control the DMD.

```
clear all
close all

m=1140/2;
n=912;

% size of the ring
rmax=150;
rmin=110;

% % size of the cross
```

```
% a=10
% b=100

x=(1:n)-n/2;
y=(1:m)-m/2;
[X,Y]=meshgrid(x,y);

A=zeros(m,n);

% double arch

for i=1:m
    for j=1:n
        if ((X(i,j)^2 + Y(i,j)^2) <=rmax^2)&((3*X(i,j)^2 + Y(i,j)^2) >=
rmin^2)&(abs(Y(i,j))<80)
            A(i,j)= 1;
        end
    end
 end

% % cross
% for i=(m/2-a/2):(m/2+a/2)
%     for j=1:n
%         A(i,j)= 0;
%     end
% end
%
% for j=(n/2-a/2):(n/2+a/2)
%     for i=1:m
%         A(i,j)= 0;
%     end
% end

figure
imagesc(A)
axis equal

B=((-1+2^8)*(round(imresize(A,[m*2,n]))));

figure
imagesc(B);
axis equal
imwrite(B,'H:\Softwars and drivers\DMD_Soft\matrix.bmp')

display('DONE')
```

Annex 3

Exploring a prism-based strategy for the alignment of DMD-modulated light at different wavelength

Observing that the TIR-prism overlap the high intensity diffraction orders of the modulated wavelengths $\lambda_2 = 488$ nm and $\lambda_4 = 640$ nm inspired us to evaluate if we could fabricate a prism that could overlap also λ_1 and λ_4. With this code, we simulate the optical path of $\lambda_1, \lambda_2, \lambda_3, \lambda_4$ being incident on the DMD with the same incident angle. The diffraction effect of the DMD is described by the grating equation (3.23). The Snell's law describes the refraction of light at the surfaces of the prism. For the design of the prism, we could tune the refractive index of the material and the prism angle. The code takes in account for the orientation of the prism compare to the DMD.

```
clear all
close all

control=0;

%% prism parameters

alpha=20; % prism angle in degrees
alpha=alpha*pi/180; % prism angle in radiants

AB=20; %hypotenuse prism
AC=AB*sin(alpha); %short cathetus prism

p=1.5; %rotation of the prism in degrees
p=p*pi/180; %rotation of the prism in radiants

%n=[1.4696,1.4630,1.4595,1.4568]; % index of refraction of fused silica
%n=[1.4962,1.4905,1.4874,1.4852]; % index of refraction of FK51A
n=[1.5302,1.5222,1.518,1.5148]; % index of refraction of BK7
%n=[1.5894,1.5793,1.5740,1.5701]; % index of refraction of BAK1
%n=[1.6947,1.6798,1.6722,1.6667]; % index of refraction of BAF10
%n=[1.7109,1.6871,1.6758,1.6679]; % index of refraction of SF5
%n=[1.7756,1.7460,1.7321,1.7224]; % index of refraction of SF10
%n=[1.8421,1.8060,1.7893,1.7778]; % index of refraction of FK51A
%n=[1.8983,1.8685,1.8542,1.8441]; % index of refraction of LASF9
```

```
%% optical path

lambda=[0.405,0.488,0.560,0.640]; % wavelength in micron

d=10.8; %DMD pitch in micron

%m=7; % DMD diffraction order
m=[11 9 8 7]; % DMD diffraction order for different colors

teta_i_deg=20; % incident angle on DMD in degrees
teta_i=teta_i_deg*pi/180; % incident angle on DMD in radians

teta_m=asin((m.*lambda/d)-sin(teta_i)); % DMD output angle of the m order in
radians
teta_m_deg=teta_m*180/pi; % DMD output angle of the m order in degrees

phi_i=teta_m+p; % incident angle on first prism surface in radians
phi_i_deg=phi_i*180/pi; % incident angle on first prism surface in degrees

%phi_r=[asin((1/n(1)*sin(phi_i(1)))), asin((1/n(2)*sin(phi_i(2)))),
asin((1/n(3)*sin(phi_i(3)))), asin((1/n(4)*sin(phi_i(4))))]; % output angle at
the first prism surface in radiants
phi_r=asin((1./n.*sin(phi_i)));
phi_r_deg=phi_r*180/pi; % output angle at the first prism surface in degrees

%% plot prism and spatial definition

A=[4 7];
B=[];
C=[];

if (p>=0) && (p<=alpha)

    B=[A(1)+AB*cos(p) A(2)+AB*sin(p)];

    C=[A(1)+AC*cos(pi/2+p-alpha) A(2)+AC*sin(pi/2+p-alpha)];

elseif (p>alpha) && (p<=pi/2)

    B=[A(1)+AB*cos(p) A(2)+AB*sin(p)];

    C=[A(1)-AC*cos(pi/2-p+alpha) A(2)+AC*sin(pi/2-p+alpha)];

elseif (p<=0) && (abs(p)<(pi/2-alpha))

    B=[A(1)+AB*sin(pi/2-abs(p)) A(2)-AB*cos(pi/2-abs(p))];

    C=[A(1)+AC*cos(pi/2-alpha-abs(p)) A(2)+AC*sin(pi/2-alpha-abs(p))];

elseif (p<0) && (abs(p)>=(pi/2-alpha))

    B=[A(1)+AB*sin(pi/2-abs(p)) A(2)-AB*cos(pi/2-abs(p))];

    C=[A(1)+AC*cos(abs(p)-pi/2+alpha) A(2)-AC*sin(abs(p)-pi/2+alpha)];

else

    disp('check the value of p')

end

figure

plot ([A(1),B(1)],[A(2),B(2)],'k','LineWidth',1);
hold on
text (A(1)-1, A(2)-1, 'A');

plot ([A(1),C(1)],[A(2),C(2)],'k','LineWidth',1);
text (C(1)-1, C(2)+1, 'C');

plot ([B(1),C(1)],[B(2),C(2)],'k','LineWidth',1);
```

```
text (B(1)+1, B(2), 'B');

% xlim([-5,50])
% ylim([-10,40])

%fit to determine the geometrical defintion

AB = polyfit([A(1) B(1)], [A(2) B(2)],1); %line through AB
AC = polyfit([A(1) C(1)], [A(2) C(2)],1); %line through AC
BC = polyfit([B(1) C(1)], [B(2) C(2)],1); %line through BC

%% first surface

r=15;

x_DMD=5; %x DMD
y_DMD=0; %y DMD

g=15; % guess incidence on prism surfaces

% ---------- to the first surface of the prism -----------

scatter (x_DMD-r*sin(teta_i), y_DMD+r*cos(teta_i),'k','LineWidth',1);
plot ([x_DMD-r*sin(teta_i), x_DMD],[y_DMD+r*cos(teta_i),y_DMD], 'k');

% calculate intersections first surface (fs)

x_fs=[0 0 0 0];
y_fs=[0 0 0 0];

for i=1:4

    P = polyfit([x_DMD x_DMD+g*sin(teta_m(i))], [y_DMD
y_DMD+g*cos(teta_m(i))],1);

    x_fs(i)= fzero(@(x) polyval(P-AB,x),3);
    y_fs(i) = polyval(P,x_fs(i));

end

scatter (x_fs(1), y_fs(1),'*c','LineWidth',1);
scatter (x_fs(2),y_fs(2),'*b','LineWidth',1);
scatter (x_fs(3),y_fs(3),'*g','LineWidth',1);
scatter (x_fs(4),y_fs(4),'*r','LineWidth',1);

plot ([x_DMD,x_fs(1)],[y_DMD,y_fs(1)],'c');
plot ([x_DMD,x_fs(2)],[y_DMD,y_fs(2)],'b');
plot ([x_DMD,x_fs(3)],[y_DMD,y_fs(3)],'g');
plot ([x_DMD,x_fs(4)],[y_DMD,y_fs(4)],'r');

%% second surface

omega_i=[0 0 0 0]; %initialization omega_i
omega_r=[0 0 0 0]; %initialization omega_r

x_ss = [0 0 0 0]; %initialization x_ss - second surface
y_ss = [0 0 0 0]; %initialization y_ss - second surface

x_w = [0 0 0 0]; %initialization x_w - wall
y_w = [0 0 0 0]; %initialization y_w - wall

gamma_i = [0 0 0 0]; %initialization gamma_i
gamma_r = [0 0 0 0]; %initialization gamma_r

x_ts = [0 0 0 0]; %initialization x_ts
y_ts = [0 0 0 0]; %initialization y_ts

w = 5; %distance of the wall

if (p>=0) && (p<=alpha)

    % choose the good prism surface
```

```
    plot1 = plot ([x_fs(1) x_fs(1)+g*sin(phi_r(1)-p)], [y_fs(1)
y_fs(1)+g*cos(phi_r(1)-p)],'k','LineWidth',1); %to see where the 405 goes
    plot2 = plot ([x_fs(2) x_fs(2)+g*sin(phi_r(2)-p)], [y_fs(2)
y_fs(2)+g*cos(phi_r(2)-p)],'k','LineWidth',1); %to see where the 488 goes
    plot3 = plot ([x_fs(3) x_fs(3)+g*sin(phi_r(3)-p)], [y_fs(3)
y_fs(3)+g*cos(phi_r(3)-p)],'k','LineWidth',1); %to see where the 560 goes
    plot4 = plot ([x_fs(4) x_fs(4)+g*sin(phi_r(4)-p)], [y_fs(4)
y_fs(4)+g*cos(phi_r(4)-p)],'k','LineWidth',1); %to see where the 640 goes

    q=0;

% calculate intersections second surface (ss) and wall (w)

    while q==0
        surface =  input ('\n Do you want to use AC or BC? ', 's')

        if strcmp(surface, 'AC')
            q=AC;

            for i=1:4

                P = polyfit([x_fs(i) x_fs(i)+g*sin(phi_r(i)-p)], [y_fs(i)
y_fs(i)+g*cos(phi_r(i)-p)],1);

                x_ss(i) = fzero(@(x) polyval(P-q,x),3);
                y_ss(i) = polyval(P,x_ss(i));

                omega_i(i)=pi/2+phi_r(i)-alpha; %incident angle in radiants

                if abs(n(i)*sin(omega_i(i)))<=1

                    omega_r(i)=asin(n(i)*sin(omega_i(i))); %output angle in
radians

                    x_w(i) = x_ss(i)+w*tan(omega_r(i)+alpha-p-pi/2);
                    y_w(i) = y_ss(i)+(y_ss(1)-y_ss(1))+w;

                else %total internal reflection on AC

                    P = polyfit([x_ss(i) x_ss(i)+g*cos(omega_i(i)-alpha+p)],
[y_ss(i) y_ss(i)+g*sin(omega_i(i)-alpha+p)],1);

                    x_ts(i) = fzero(@(x) polyval(P-BC,x),3);
                    y_ts(i) = polyval(P,x_ts(i));

                    gamma_i(i) = pi/2-omega_i(i);
                    gamma_r(i) = asin(n(i)*sin(gamma_i(i))); %output angle in
radians

                    x_w(i) = x_ts(i)+w*cot(pi/2-gamma_r(i)-alpha+p);
                    y_w(i) = y_ts(i)+w;

                end

            end %for cycle

        elseif strcmp(surface, 'BC')
            q=BC;

            for i=1:4

                if (phi_r(i)<alpha)

                    P = polyfit([x_fs(i) x_fs(i)+g*sin(phi_r(i)-p)], [y_fs(i)
y_fs(i)+g*cos(phi_r(i)-p)],1);

                    x_ss(i) = fzero(@(x) polyval(P-q,x),3);
                    y_ss(i) = polyval(P,x_ss(i),1);

                    omega_i(i)=alpha-phi_r(i); %incident angle in radians
                    omega_r(i)=asin(n(i)*sin(omega_i(i)));% output angle surface
in radians
```

```
                    x_w(i) = x_ss(i)-w*cot(pi/2-omega_r(i)+alpha-p);
                    y_w(i) = y_ss(i)+w;

                elseif (phi_r(i)>=alpha)

                    P = polyfit([x_fs(i) x_fs(i)+g*sin(phi_r(i)-p)], [y_fs(i)
y_fs(i)+g*cos(phi_r(i)-p)],1); %intersections second surface (ss)

                    x_ss(i) = fzero(@(x) polyval(P-q,x),3);
                    y_ss(i) = polyval(P,x_ss(i),1);

                    omega_i(i)=phi_r(i)-alpha; %incident angle in radiants
                    omega_r(i)=asin(n(i)*sin(omega_i(i))); % output angle surface
in radians

                    x_w(i)=x_ss(i)+w*cot(pi/2-omega_r(i)-alpha+p);
                    y_w = y_ss+w;

                else
                    q=0;
                end %if cycle
            end %for cycle
        end %if cycle
    end %while cycle


elseif (p>alpha) && (p<=pi/2)
    q=BC;

    for i=1:4

        if (phi_r(i)<alpha)

% calculate intersections second surface (ss) and wall (w)

            P = polyfit([x_fs(i) x_fs(i)-g*cos(pi/2+phi_r(i)-p)], [y_fs(i)
y_fs(i)+g*sin(pi/2+phi_r(i)-p)],1);

            x_ss(i) = fzero(@(x) polyval(P-q,x),3);
            y_ss(i) = polyval(P,x_ss(i));

            omega_i=alpha-phi_r; %incident angle in radians
            omega_r(i)=asin(n(i)*sin(omega_i(i)));% output angle surface in
radians

            x_w(i) = x_ss(i)-w*cot(pi/2-omega_r(i)+alpha-p);
            y_w(i) = y_ss(i)+w;


        elseif (phi_r(i)>=alpha)

            P = polyfit([x_fs(i) x_fs(i)+g*cos(pi/2-phi_r(i)+p)], [y_fs(i)
y_fs(i)+g*sin(pi/2-phi_r(i)+p)],1);

            x_ss(i) = fzero(@(x) polyval(P-q,x),3);
            y_ss(i) = polyval(P,x_ss(i));

            omega_i(i)=phi_r(i)-alpha; %incident angle in radians
            omega_r(i)=asin(n(i)*sin(omega_i(i))); % output angle surface in
radians

            x_w(i) = x_ss(i)+w*tan(omega_r(i)+alpha-p);
            y_w(i) = y_ss(i)+w;

        end %if elseif cycle
    end %for cycle
end


omega_i_deg = omega_i*180/pi; %incident angle in radians
omega_r_deg = omega_r*180/pi; % output angle surface in radians
```

```
%% PLOT

delete ([plot1, plot2, plot3, plot4]);

scatter(x_ss(1),y_ss(1),'*c','LineWidth',1);
scatter(x_ss(2),y_ss(2),'*b','LineWidth',1);
scatter(x_ss(3),y_ss(3),'*g','LineWidth',1);
scatter(x_ss(4),y_ss(4),'*r','LineWidth',1);

plot([x_fs(1),x_ss(1)],[y_fs(1),y_ss(1)],'c');
plot([x_fs(2),x_ss(2)],[y_fs(2),y_ss(2)],'b');
plot([x_fs(3),x_ss(3)],[y_fs(3),y_ss(3)],'g');
plot([x_fs(4),x_ss(4)],[y_fs(4),y_ss(4)],'r');

if gamma_i==0

    plot([x_ss(1),x_w(1)],[y_ss(1),y_w(1)],'c');
    plot([x_ss(2),x_w(2)],[y_ss(2),y_w(2)],'b');
    plot([x_ss(3),x_w(3)],[y_ss(3),y_w(3)],'g');
    plot([x_ss(4),x_w(4)],[y_ss(4),y_w(4)],'r');

    scatter(x_w(1),y_w(1),'*c','LineWidth',1);
    scatter(x_w(2),y_w(2),'*b','LineWidth',1);
    scatter(x_w(3),y_w(3),'*g','LineWidth',1);
    scatter(x_w(4),y_w(4),'*r','LineWidth',1);

else

    scatter(x_ts(1),y_ts(1),'*c','LineWidth',1);
    scatter(x_ts(2),y_ts(2),'*b','LineWidth',1);
    scatter(x_ts(3),y_ts(3),'*g','LineWidth',1);
    scatter(x_ts(4),y_ts(4),'*r','LineWidth',1);

    plot([x_ss(1),x_ts(1)],[y_ss(1),y_ts(1)],'c');
    plot([x_ss(2),x_ts(2)],[y_ss(2),y_ts(2)],'b');
    plot([x_ss(3),x_ts(3)],[y_ss(3),y_ts(3)],'g');
    plot([x_ss(4),x_ts(4)],[y_ss(4),y_ts(4)],'r');

    scatter(x_w(1),y_w(1),'*c','LineWidth',1);
    scatter(x_w(2),y_w(2),'*b','LineWidth',1);
    scatter(x_w(3),y_w(3),'*g','LineWidth',1);
    scatter(x_w(4),y_w(4),'*r','LineWidth',1);

    plot([x_ts(1),x_w(1)],[y_ts(1),y_w(1)],'c');
    plot([x_ts(2),x_w(2)],[y_ts(2),y_w(2)],'b');
    plot([x_ts(3),x_w(3)],[y_ts(3),y_w(3)],'g');
    plot([x_ts(4),x_w(4)],[y_ts(4),y_w(4)],'r');

end
```

However, this simulation showed that we could only produce parallel but not overlapping optical paths for $\lambda_1, \lambda_2, \lambda_3, \lambda_4$ after being reflected by the DMD (**FIG. 85**).

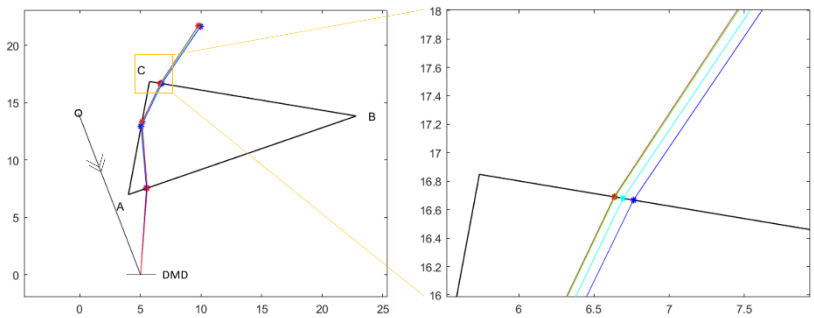

FIG. 85 – Multi-wavelength alignment of DMD-modulated light. *Simulations only showed parallel $\lambda_1, \lambda_2, \lambda_3, \lambda_4$, but not overlaping.*

Annex 4

Cell culture and samples preparation

This annex contains the information regarding the culturing of the cell types used for the experiments presented in this manuscript. Also, it includes the instructions for the preparation of the various biological samples

A4.1 U2OS, U2OS-Nup96 and mES cell culture

For the imaging of H2B histones 3D dynamics we used human osteosarcoma (U2OS) cells from a stable cell line. For the super-resolution experiments, we used a similar cell line, the cells of which carrying a modified NUP96 gene. As a result, the cells from this cell line expressed fluorescent nuclear pore complex protein NUP96, labeled with EGFP (U2OS-NUP96EGFP).

The cell culture protocol is the same for U2OS and U2OS-NUP96EGFP. We used DMEM (11880, by Thermo Fisher Scientific) + 1% Glutamax + 1% Penicillin-Streptavidin supplemented with 10% fetal bovine serum (26140079, by Thermo Fisher Scientific). Cells were maintained at a density of $0.2 - 1.5\ 10^5$ cells/cm^2 by passaging using TrypLE (12563011, by Thermo Fisher Scientific) at 37° and 5% CO2. Cells were checked for mycoplasma infection every 3-4 months and tested negative.

For the observation of the 3D dynamics of CTCF and Cohesin we used mouse embryonic stem (mES) cells. In general, stem cells are more delicate then cells from stable lines, and require dedicate protocols for cell culture. The cells used for the experiments reported in this manuscript were cultured in DMEM+Glutamax (10566-016, by Thermo Fisher Scientific) supplemented with 15% fetal bovine serum (S1810-050, Lot S15642S1810, by DUTSCHER), 550mM b-mercaptoethanol (21985-023, by Thermo Fisher Scientific), 1mM sodium pyruvate (11360-070, by Thermo Fisher Scientific) and 104U of leukemia inhibitory factor (ESG1107, by Millipore). Cells were maintained at a density of $0.2 - 1.5\ 10^5$ cells/cm^2 by

passaging using TrypLE (12563011, by Thermo Fisher Scientific) every 24h − 48h on 0.1% gelatin-coated dishes (ES-006-B, by Millipore) at 37° and 5% CO2. Medium was changed daily when cells were not passaged. Cells were checked for mycoplasma infection every 3-4 months and tested negative. The day before experiment, cells were seeded at a density of $3 \cdot 10^5/\text{cm}^2$ the day before the experiments in Fluorobrite DMEM (A1896701, by Life Technologies SAS-Thermo Fisher Scientific).

A4.2 Cell transfection and labeling

To observe the dynamics of H2B histones, confluent U2OS cells seeded in a Petri dish were transfected to express protein carrying a Halo-tag. To transfect the cells, we prepared a solution of 100 µL of DMEM + 3% X-tremeGENE HP DNA transfection reagent (6366236001, by SigmaAldrich). This solution was incubated 5 minutes at room temperature to form vesicles that will carry DNA material into the cell. After that we added 1 µg of H2B-Halo plasmid to the solution, incubating for 45 minutes at room temperature. This mixture was added to the Petri dish and incubate 24 hours before imaging.

For these experiments, we labeled the transfected cells with fluorescent dyes. For that, we incubated them for 15 minutes in 1 mL solution of enriched DMEM and 5 nM Halo-conjugated AlexaFluor 647 dyes. Cells were washed with enriched DMEM before being seeded in a soSPIM chip, in which, previously, enriched DMEM was incubated for 30 minutes under vacuum.

To observe the dynamics of CTCF and Cohesin in the nucleus of stem cells, confluent mES cells in a Petri dish, cultured in Fluorobrite DMEM, were labeled with Halo-conjugated JF549 by incubating them for 15 minutes in 1 mL solution of Fluorobrite DMEM and dyes at different concentration. After washing the cells with Fluorobrite DMEM, they were seeded in a soSPIM chip, in which, previously, Fluorobrite DMEM was incubated for 30 minutes under vacuum.

A4.3 Immunofluorescence labeling protocol for super-resolution imaging of Lamin B1 protein through DNA-PAINT

To produce super-resolution images of the nuclear membrane through DNA-PAINT technique we used U2OS-NUP96 fixed cells, optimizing a protocol for immunostaining of the Lamin B1 protein.

First, cells were transferred from the culturing flask into a soSPIM chip, in which,

previously, enriched DMEM was incubated for 30 minutes under vacuum. After 15 minutes cells were precipitated in the cavities and could be fixed. For the fixation, cells were incubated in a solution of PBS + 4% PFA (weight/volume) for 10 minutes at room temperature. After being washed with PBS, cells were incubated for 10 minutes in a solution of PBS + 150 mM glycin (26-128-6405-C, by EUROMEDEX) to quench the autofluorescence of the PFA. After being washed, cells were incubated for 10 minutes in a solution of PBS + Triton™ X-100 at a concentration of 2% (volume/volume) to be permeabilized. Cell were washed and then incubated in the blocking buffer for 90 minutes. The optimal composition of the blocking buffer is PBS + 3% BSA (A9418, by Sigma-Aldrich) + 0.1 mg/mL of sheared salmon sperm DNA (AM9680, by Thermo Fischer Scientific) + 1% dextran sulfate sodium (D4911, by Sigma). After the blocking buffer being removed, cells were incubated in a solution of blocking buffer and recombinant anti-Lamin B1 primary antibody (ab229025, by abcam). The optimal concentration of the solution is 1:1/250 (volume/volume). After being washed with the blocking buffer, cells were incubated for 60 minutes in a solution of blocking buffer and secondary antibody (included in MASSIVE-SDAB 1-PLEX by Massive photonics) at a concentration of 1:1/500 (volume/volume). In DNA-PAINT experiments, the secondary antibody carries the DNA docker strands. After washing the sample with blocking buffer and imaging buffer (included in MASSIVE-SDAB 1-PLEX by Massive photonics), the solution with the DNA imager strands were added to cells. The optimized imaging solution was prepared with imaging buffer and imager strands complementary to the secondary antibody (included in MASSIVE-SDAB 1-PLEX by Massive photonics) at a concentration of 2.5 nM. After imaging, cells can be stored in blocking buffer at 4°C.

Bibliography

[1] J. W. Lichtman and J. A. Conchello, "Fluorescence microscopy," *Nat. Methods*, vol. 2, no. 12, pp. 910–919, 2005, doi: 10.1038/nmeth817.

[2] Q. Zheng, S. Jockusch, Z. Zhou, and S. C. Blanchard, "The Contribution of Reactive Oxygen Species to the Photobleaching of Organic Fluorophores," *Photochem. Photobiol.*, vol. 90, no. 2, pp. 448–454, Mar. 2014, doi: 10.1111/php.12204.

[3] G. B. Airy, *On the Diffraction of an Object-glass with Circular Aperture: From the Transactions of the Cambridge Philosophical Society, Vol. V, Part III*. Printed at the Pitt Press by John Smith, 1835.

[4] M. Born *et al.*, *Principles of Optics*. Cambridge University Press, 1999.

[5] E. Hecht, *Optics, 4th Edition*, 4th ed. Pearson, Addison-Wesley, 2002.

[6] B. Richards and E.Wolf, "Electromagnetic diffraction in optical systems, II. Structure of the image field in an aplanatic system," *Proc. R. Soc. London. Ser. A. Math. Phys. Sci.*, vol. 253, no. 1274, pp. 358–379, Dec. 1959, doi: 10.1098/rspa.1959.0200.

[7] S. F. Gibson and F. Lanni, "Experimental test of an analytical model of aberration in an oil-immersion objective lens used in three-dimensional light microscopy," *J. Opt. Soc. Am. A*, vol. 9, no. 1, p. 154, Jan. 1992, doi: 10.1364/JOSAA.9.000154.

[8] E. Abbe, "Beiträge zur Theorie des Mikroskops und der mikroskopischen Wahrnehmung," *Arch. für Mikroskopische Anat.*, vol. 9, no. 1, pp. 413–468, Dec. 1873, doi: 10.1007/BF02956173.

[9] Rayleigh, "XXXI. Investigations in optics, with special reference to the spectroscope," *London, Edinburgh, Dublin Philos. Mag. J. Sci.*, vol. 8, no. 49, pp. 261–274, Oct. 1879, doi: 10.1080/14786447908639684.

[10] T. Dertinger, R. Colyer, G. Iyer, S. Weiss, and J. Enderlein, "Fast, background-free, 3D super-resolution optical fluctuation imaging (SOFI)," *Proc. Natl. Acad. Sci.*, vol. 106, no. 52, pp. 22287–22292, Dec. 2009, doi: 10.1073/pnas.0907866106.

[11] H. Deschout *et al.*, "Complementarity of PALM and SOFI for super-resolution live-cell imaging of focal adhesions," *Nat. Commun.*, vol. 7, no. 1, p. 13693, Dec. 2016, doi: 10.1038/ncomms13693.

[12] N. Gustafsson, S. Culley, G. Ashdown, D. M. Owen, P. M. Pereira, and R. Henriques, "Fast live-cell conventional fluorophore nanoscopy with ImageJ through super-resolution radial fluctuations," *Nat. Commun.*, vol. 7, no. 1, p. 12471, Nov. 2016, doi: 10.1038/ncomms12471.

[13] M. G. L. Gustafsson, "Surpassing the lateral resolution limit by a factor of two using structured illumination microscopy," *J. Microsc.*, vol. 198, no. 2, pp. 82–

87, 2000, doi: 10.1046/j.1365-2818.2000.00710.x.
[14] M. G. L. Gustafsson, "Nonlinear structured-illumination microscopy: Wide-field fluorescence imaging with theoretically unlimited resolution," *Proc. Natl. Acad. Sci. U. S. A.*, vol. 102, no. 37, pp. 13081–13086, 2005, doi: 10.1073/pnas.0406877102.
[15] L. Shao, P. Kner, E. H. Rego, and M. G. L. Gustafsson, "Super-resolution 3D microscopy of live whole cells using structured illumination," *Nat. Methods*, vol. 8, no. 12, pp. 1044–1046, Dec. 2011, doi: 10.1038/nmeth.1734.
[16] S. W. Hell and J. Wichmann, "Breaking the diffraction resolution limit by stimulated emission: stimulated-emission-depletion fluorescence microscopy," *Opt. Lett.*, vol. 19, no. 11, p. 780, 1994, doi: 10.1364/ol.19.000780.
[17] N. Kilian *et al.*, "Assessing photodamage in live-cell STED microscopy," *Nat. Methods*, vol. 15, no. 10, pp. 755–756, Oct. 2018, doi: 10.1038/s41592-018-0145-5.
[18] R. Schmidt, C. A. Wurm, S. Jakobs, J. Engelhardt, A. Egner, and S. W. Hell, "Spherical nanosized focal spot unravels the interior of cells," *Nat. Methods*, vol. 5, no. 6, pp. 539–544, Jun. 2008, doi: 10.1038/nmeth.1214.
[19] S. Li, C. Kuang, X. Hao, Z. Gu, and X. Liu, "Generation of a 3D isotropic hollow focal spot for single-objective stimulated emission depletion microscopy," *J. Opt.*, vol. 14, no. 8, p. 085704, Aug. 2012, doi: 10.1088/2040-8978/14/8/085704.
[20] M. Hofmann, C. Eggeling, S. Jakobs, and S. W. Hell, "Breaking the diffraction barrier in fluorescence microscopy at low light intensities by using reversibly photoswitchable proteins," *Proc. Natl. Acad. Sci.*, vol. 102, no. 49, pp. 17565–17569, Dec. 2005, doi: 10.1073/pnas.0506010102.
[21] E. Betzig and R. J. Chichester, "Single Molecules Observed by Near-Field Scanning Optical Microscopy," *Science (80-.).*, vol. 262, no. 5138, pp. 1422–1425, Nov. 1993, doi: 10.1126/science.262.5138.1422.
[22] T. Funatsu, Y. Harada, M. Tokunaga, K. Saito, and T. Yanagida, "Imaging of single fluorescent molecules and individual ATP turnovers by single myosin molecules in aqueous solution," *Nature*, vol. 374, no. 6522, pp. 555–559, Apr. 1995, doi: 10.1038/374555a0.
[23] Y. Sako, S. Minoghchi, and T. Yanagida, "Single-molecule imaging of EGFR signalling on the surface of living cells," *Nat. Cell Biol.*, vol. 2, no. 3, pp. 168–172, Mar. 2000, doi: 10.1038/35004044.
[24] G. J. Schütz, G. Kada, V. P. Pastushenko, and H. Schindler, "Properties of lipid microdomains in a muscle cell membrane visualized by single molecule microscopy," *EMBO J.*, vol. 19, no. 5, pp. 892–901, Mar. 2000, doi: 10.1093/emboj/19.5.892.
[25] M. K. Cheezum, W. F. Walker, and W. H. Guilford, "Quantitative Comparison of Algorithms for Tracking Single Fluorescent Particles," *Biophys. J.*, vol. 81, no. 4, pp. 2378–2388, Oct. 2001, doi: 10.1016/S0006-3495(01)75884-5.
[26] R. E. Thompson, D. R. Larson, and W. W. Webb, "Precise nanometer localization analysis for individual fluorescent probes," *Biophys. J.*, vol. 82, no. 5, pp. 2775–2783, 2002, doi: 10.1016/S0006-3495(02)75618-X.
[27] K. I. Mortensen, L. S. Churchman, J. A. Spudich, and H. Flyvbjerg, "Optimized localization analysis for single-molecule tracking and super- resolution microscopy," no. April, 2010, doi: 10.1038/nmeth.1447.
[28] H. Deschout *et al.*, "Precisely and accurately localizing single emitters in

fluorescence microscopy," *Nat. Methods*, vol. 11, no. 3, pp. 253–266, 2014, doi: 10.1038/nmeth.2843.

[29] A. Small and S. Stahlheber, "Fluorophore localization algorithms for super-resolution microscopy," *Nat. Methods*, vol. 11, no. 3, pp. 267–279, 2014, doi: 10.1038/nmeth.2844.

[30] A. Yildiz, "Myosin V Walks Hand-Over-Hand: Single Fluorophore Imaging with 1.5-nm Localization," *Science (80-.).*, vol. 300, no. 5628, pp. 2061–2065, Jun. 2003, doi: 10.1126/science.1084398.

[31] M. J. Saxton, "Single-particle tracking: the distribution of diffusion coefficients," *Biophys. J.*, vol. 72, no. 4, pp. 1744–1753, Apr. 1997, doi: 10.1016/S0006-3495(97)78820-9.

[32] G. J. Kremers, S. G. Gilbert, P. J. Cranfill, M. W. Davidson, and D. W. Piston, "Fluorescent proteins at a glance," *J. Cell Sci.*, vol. 124, no. 15, p. 2676, 2011, doi: 10.1242/jcs.095059.

[33] G. V. Los *et al.*, "HaloTag: A Novel Protein Labeling Technology for Cell Imaging and Protein Analysis," *ACS Chem. Biol.*, vol. 3, no. 6, pp. 373–382, Jun. 2008, doi: 10.1021/cb800025k.

[34] K. Kolberg, C. Puettmann, A. Pardo, J. Fitting, and S. Barth, "SNAP-Tag Technology: A General Introduction," *Curr. Pharm. Des.*, vol. 19, no. 30, pp. 5406–5413, Jul. 2013, doi: 10.2174/13816128113199990514.

[35] M. J. Rust, M. Bates, and X. Zhuang, "Sub-diffraction-limit imaging by stochastic optical reconstruction microscopy (STORM)," *Nat. Methods*, vol. 3, no. 10, pp. 793–795, 2006, doi: 10.1038/nmeth929.

[36] S. van de Linde *et al.*, "Direct stochastic optical reconstruction microscopy with standard fluorescent probes," *Nat. Protoc.*, vol. 6, no. 7, pp. 991–1009, Jul. 2011, doi: 10.1038/nprot.2011.336.

[37] E. Betzig *et al.*, "Imaging intracellular fluorescent proteins at nanometer resolution," *Science (80-.).*, vol. 313, no. 5793, pp. 1642–1645, 2006, doi: 10.1126/science.1127344.

[38] S. T. Hess, T. P. K. Girirajan, and M. D. Mason, "Ultra-High Resolution Imaging by Fluorescence Photoactivation Localization Microscopy," *Biophys. J.*, vol. 91, no. 11, pp. 4258–4272, Dec. 2006, doi: 10.1529/biophysj.106.091116.

[39] A. Sharonov and R. M. Hochstrasser, "Wide-field subdiffraction imaging by accumulated binding of diffusing probes," *Proc. Natl. Acad. Sci.*, vol. 103, no. 50, pp. 18911–18916, Dec. 2006, doi: 10.1073/pnas.0609643104.

[40] J. Schnitzbauer, M. T. Strauss, T. Schlichthaerle, F. Schueder, and R. Jungmann, "Super-resolution microscopy with DNA-PAINT," *Nat. Protoc.*, vol. 12, no. 6, pp. 1198–1228, 2017, doi: 10.1038/nprot.2017.024.

[41] F. Balzarotti *et al.*, "Nanometer resolution imaging and tracking of fluorescent molecules with minimal photon fluxes," *Science (80-.).*, vol. 355, no. 6325, pp. 606–612, 2017, doi: 10.1126/science.aak9913.

[42] Y. Eilers, H. Ta, K. C. Gwosch, F. Balzarotti, and S. W. Hell, "MINFLUX monitors rapid molecular jumps with superior spatiotemporal resolution," *Proc. Natl. Acad. Sci.*, vol. 115, no. 24, pp. 6117–6122, Jun. 2018, doi: 10.1073/pnas.1801672115.

[43] K. C. Gwosch *et al.*, "MINFLUX nanoscopy delivers 3D multicolor nanometer resolution in cells," *Nat. Methods*, vol. 17, no. 2, pp. 217–224, Feb. 2020, doi: 10.1038/s41592-019-0688-0.

[44] R. S. Fischer, Y. Wu, P. Kanchanawong, H. Shroff, and C. M. Waterman, "Microscopy in 3D: a biologist's toolbox," *Trends Cell Biol.*, vol. 21, no. 12, pp.

682–691, Dec. 2011, doi: 10.1016/j.tcb.2011.09.008.

[45] A. Von Diezmann, Y. Shechtman, and W. E. Moerner, "Three-Dimensional Localization of Single Molecules for Super-Resolution Imaging and Single-Particle Tracking," *Chem. Rev.*, vol. 117, no. 11, pp. 7244–7275, 2017, doi: 10.1021/acs.chemrev.6b00629.

[46] B. Hajj, M. El Beheiry, I. Izeddin, X. Darzacq, and M. Dahan, "Accessing the third dimension in localization-based super-resolution microscopy," *Phys. Chem. Chem. Phys.*, vol. 16, no. 31, pp. 16340–16348, 2014, doi: 10.1039/c4cp01380h.

[47] P. Prabhat, S. Ram, E. S. Ward, and R. J. Ober, "Simultaneous Imaging of Different Focal Planes in Fluorescence Microscopy for the Study of Cellular Dynamics in Three Dimensions," *IEEE Trans. Nanobioscience*, vol. 3, no. 4, pp. 237–242, Dec. 2004, doi: 10.1109/TNB.2004.837899.

[48] E. Toprak, H. Balci, B. H. Blehm, and P. R. Selvin, "Three-Dimensional Particle Tracking via Bifocal Imaging," *Nano Lett.*, vol. 7, no. 7, pp. 2043–2045, Jul. 2007, doi: 10.1021/nl0709120.

[49] A. Descloux *et al.*, "Combined multi-plane phase retrieval and super-resolution optical fluctuation imaging for 4D cell microscopy," *Nat. Photonics*, vol. 12, no. 3, pp. 165–172, Mar. 2018, doi: 10.1038/s41566-018-0109-4.

[50] M. F. Juette *et al.*, "Three-dimensional sub-100 nm resolution fluorescence microscopy of thick samples," *Nat. Methods*, vol. 5, no. 6, pp. 527–529, 2008, doi: 10.1038/nmeth.1211.

[51] S. Abrahamsson *et al.*, "Fast multicolor 3D imaging using aberration-corrected multifocus microscopy," *Nat. Methods*, vol. 10, no. 1, pp. 60–63, 2013, doi: 10.1038/NMETH.2277.

[52] H. P. Kao and A. S. Verkman, "Tracking of single fluorescent particles in three dimensions: use of cylindrical optics to encode particle position," *Biophys. J.*, vol. 67, no. 3, pp. 1291–1300, Sep. 1994, doi: 10.1016/S0006-3495(94)80601-0.

[53] L. Holtzer, T. Meckel, and T. Schmidt, "Nanometric three-dimensional tracking of individual quantum dots in cells," *Appl. Phys. Lett.*, vol. 90, no. 5, p. 053902, Jan. 2007, doi: 10.1063/1.2437066.

[54] B. Huang, W. Wang, M. Bates, and X. Zhuang, "Three-dimensional super-resolution imaging by stochastic optical reconstruction microscopy," *Science (80-.).*, vol. 319, no. 5864, pp. 810–813, 2008, doi: 10.1126/science.1153529.

[55] R. Piestun, Y. Y. Schechner, and J. Shamir, "Propagation-invariant wave fields with finite energy," *J. Opt. Soc. Am. A*, vol. 17, no. 2, p. 294, Feb. 2000, doi: 10.1364/JOSAA.17.000294.

[56] S. R. P. Pavani *et al.*, "Three-dimensional, single-molecule fluorescence imaging beyond the diffraction limit by using a double-helix point spread function," *Proc. Natl. Acad. Sci. U. S. A.*, vol. 106, no. 9, pp. 2995–2999, 2009, doi: 10.1073/pnas.0900245106.

[57] M. D. Lew, S. F. Lee, M. Badieirostami, and W. E. Moerner, "Corkscrew point spread function for far-field three-dimensional nanoscale localization of pointlike objects," *Opt. Lett.*, vol. 36, no. 2, p. 202, Jan. 2011, doi: 10.1364/OL.36.000202.

[58] D. Baddeley, M. B. Cannell, and C. Soeller, "Three-dimensional sub-100 nm super-resolution imaging of biological samples using a phase ramp in the objective pupil," *Nano Res.*, vol. 4, no. 6, pp. 589–598, Jun. 2011, doi: 10.1007/s12274-011-0115-z.

[59] S. Jia, J. C. Vaughan, and X. Zhuang, "Isotropic three-dimensional super-resolution imaging with a self-bending point spread function," *Nat. Photonics*, vol. 8, no. 4, pp. 302–306, Apr. 2014, doi: 10.1038/nphoton.2014.13.

[60] Y. Shechtman, S. J. Sahl, A. S. Backer, and W. E. Moerner, "Optimal point spread function design for 3D imaging," *Phys. Rev. Lett.*, vol. 113, no. 3, pp. 1–5, 2014, doi: 10.1103/PhysRevLett.113.133902.

[61] Y. Shechtman, L. E. Weiss, A. S. Backer, S. J. Sahl, and W. E. Moerner, "Precise Three-Dimensional Scan-Free Multiple-Particle Tracking over Large Axial Ranges with Tetrapod Point Spread Functions," *Nano Lett.*, vol. 15, no. 6, pp. 4194–4199, Jun. 2015, doi: 10.1021/acs.nanolett.5b01396.

[62] I. Izeddin, M. El Beheiry, J. Andilla, D. Ciepielewski, X. Darzacq, and M. Dahan, "PSF shaping using adaptive optics for three-dimensional single-molecule super-resolution imaging and tracking," *Opt. Express*, vol. 20, no. 5, p. 4957, Feb. 2012, doi: 10.1364/OE.20.004957.

[63] M. Badieirostami, M. D. Lew, M. A. Thompson, and W. E. Moerner, "Three-dimensional localization precision of the double-helix point spread function versus astigmatism and biplane," *Appl. Phys. Lett.*, vol. 97, no. 16, p. 161103, Oct. 2010, doi: 10.1063/1.3499652.

[64] R. M. Dickson, D. J. Norris, Y.-L. Tzeng, and W. E. Moerner, "Three-Dimensional Imaging of Single Molecules Solvated in Pores of Poly(acrylamide) Gels," *Science (80-.).*, vol. 274, no. 5289, pp. 966–968, Nov. 1996, doi: 10.1126/science.274.5289.966.

[65] H. Cang, C. M. Wong, C. S. Xu, A. H. Rizvi, and H. Yang, "Confocal three dimensional tracking of a single nanoparticle with concurrent spectroscopic readouts," *Appl. Phys. Lett.*, vol. 88, no. 22, p. 223901, May 2006, doi: 10.1063/1.2204652.

[66] N. P. Wells *et al.*, "Time-Resolved Three-Dimensional Molecular Tracking in Live Cells," *Nano Lett.*, vol. 10, no. 11, pp. 4732–4737, Nov. 2010, doi: 10.1021/nl103247v.

[67] P. Jouchet *et al.*, "Nanometric axial localization of single fluorescent molecules with modulated excitation," *Nat. Photonics*, vol. 15, no. 4, pp. 297–304, Apr. 2021, doi: 10.1038/s41566-020-00749-9.

[68] T. Ruckstuhl and D. Verdes, "Supercritical angle fluorescence (SAF) microscopy," *Opt. Express*, vol. 12, no. 18, p. 4246, 2004, doi: 10.1364/OPEX.12.004246.

[69] N. Bourg *et al.*, "Direct optical nanoscopy with axially localized detection," *Nat. Photonics*, vol. 9, no. 9, pp. 587–593, 2015, doi: 10.1038/nphoton.2015.132.

[70] J. Deschamps, M. Mund, and J. Ries, "3D superresolution microscopy by supercritical angle detection," *Opt. Express*, vol. 22, no. 23, p. 29081, 2014, doi: 10.1364/oe.22.029081.

[71] S. Sivankutty, I. Coto Hernández, N. Bourg, G. Dupuis, and S. Lévêque-Fort, "Supercritical angle fluorescence for enhanced axial sectioning in STED microscopy," *Methods*, vol. 174, pp. 20–26, Mar. 2020, doi: 10.1016/j.ymeth.2019.03.027.

[72] C. v. Middendorff, A. Egner, C. Geisler, S. W. Hell, and A. Schönle, "Isotropic 3D Nanoscopy based on single emitter switching," *Opt. Express*, vol. 16, no. 25, p. 20774, Dec. 2008, doi: 10.1364/OE.16.020774.

[73] G. Shtengel *et al.*, "Interferometric fluorescent super-resolution microscopy

resolves 3D cellular ultrastructure," *Proc. Natl. Acad. Sci.*, vol. 106, no. 9, pp. 3125–3130, 2009.

[74] P. Bon *et al.*, "Self-interference 3D super-resolution microscopy for deep tissue investigations," *Nat. Methods*, vol. 15, no. 6, pp. 449–454, Jun. 2018, doi: 10.1038/s41592-018-0005-3.

[75] H. Shroff, C. G. Galbraith, J. A. Galbraith, and E. Betzig, "Live-cell photoactivated localization microscopy of nanoscale adhesion dynamics," *Nat. Methods*, vol. 5, no. 5, pp. 417–423, 2008, doi: 10.1038/nmeth.1202.

[76] M. Tokunaga, N. Imamoto, and K. Sakata-Sogawa, "Highly inclined thin illumination enables clear single-molecule imaging in cells," *Nat. Methods*, vol. 5, no. 2, pp. 159–161, Feb. 2008, doi: 10.1038/nmeth1171.

[77] V. M. Serdyuk and J. A. Titovitsky, "A Simple Analytic Approximation for the Refracted Field at Gaussian Beam Incidence upon a Boundary of Absorbing Medium," *J. Electromagn. Anal. Appl.*, vol. 02, no. 11, pp. 640–648, 2010, doi: 10.4236/jemaa.2010.211084.

[78] D. Axelrod, "Cell-substrate contacts illuminated by total internal reflection fluorescence.," *J. Cell Biol.*, vol. 89, no. 1, pp. 141–145, Apr. 1981, doi: 10.1083/jcb.89.1.141.

[79] J. Huisken, J. Swoger, F. Del Bene, J. Wittbrodt, and E. H. K. Stelzer, "Optical sectioning deep inside live embryos by selective plane illumination microscopy," *Science (80-.).*, vol. 305, no. 5686, pp. 1007–1009, 2004, doi: 10.1126/science.1100035.

[80] P. J. Keller *et al.*, "Fast, high-contrast imaging of animal development with scanned light sheet-based structured-illumination microscopy," *Nat. Methods*, vol. 7, no. 8, pp. 637–642, 2010, doi: 10.1038/nmeth.1476.

[81] A.-K. Gustavsson, P. N. Petrov, and W. E. Moerner, "Light sheet approaches for improved precision in 3D localization-based super-resolution imaging in mammalian cells [Invited]," *Opt. Express*, vol. 26, no. 10, p. 13122, 2018, doi: 10.1364/oe.26.013122.

[82] Y. S. Hu, M. Zimmerley, Y. Li, R. Watters, and H. Cang, "Single-molecule super-resolution light-sheet microscopy.," *Chemphyschem*, vol. 15, no. 4, pp. 577–586, Mar. 2014, doi: 10.1002/cphc.201300732.

[83] F. Cella Zanacchi *et al.*, "Live-cell 3D super-resolution imaging in thick biological samples," *Nat. Methods*, vol. 8, no. 12, pp. 1047–1050, 2011, doi: 10.1038/nmeth.1744.

[84] J. G. Ritter, R. Veith, A. Veenendaal, J. P. Siebrasse, and U. Kubitscheck, "Light sheet microscopy for single molecule tracking in living tissue," *PLoS One*, vol. 5, no. 7, pp. 1–9, 2010, doi: 10.1371/journal.pone.0011639.

[85] J. C. M. Gebhardt *et al.*, "Single-molecule imaging of transcription factor binding to DNA in live mammalian cells," *Nat. Methods*, vol. 10, no. 5, pp. 421–426, 2013, doi: 10.1038/nmeth.2411.

[86] Y. S. Hu *et al.*, "Light-sheet Bayesian microscopy enables deepcell super-resolution imaging of heterochromatin in live human embryonic stem cells," *Opt. Nanoscopy*, vol. 2, no. 1, pp. 1–12, 2013, doi: 10.1186/2192-2853-2-7.

[87] S. Cox *et al.*, "Bayesian localization microscopy reveals nanoscale podosome dynamics," *Nat. Methods*, vol. 9, no. 2, pp. 195–200, Feb. 2012, doi: 10.1038/nmeth.1812.

[88] A. K. Gustavsson, P. N. Petrov, M. Y. Lee, Y. Shechtman, and W. E. Moerner, "3D single-molecule super-resolution microscopy with a tilted light sheet," *Nat. Commun.*, vol. 9, no. 1, pp. 1–8, 2018, doi: 10.1038/s41467-017-02563-4.

[89] T. A. Planchon *et al.*, "Rapid three-dimensional isotropic imaging of living cells using Bessel beam plane illumination," *Nat. Methods*, vol. 8, no. 5, pp. 417–423, 2011, doi: 10.1038/nmeth.1586.

[90] L. Gao, L. Shao, B. C. Chen, and E. Betzig, "3D live fluorescence imaging of cellular dynamics using Bessel beam plane illumination microscopy," *Nat. Protoc.*, vol. 9, no. 5, pp. 1083–1101, 2014, doi: 10.1038/nprot.2014.087.

[91] L. Gao *et al.*, "Noninvasive imaging beyond the diffraction limit of 3D dynamics in thickly fluorescent specimens.," *Cell*, vol. 151, no. 6, pp. 1370–85, Dec. 2012, doi: 10.1016/j.cell.2012.10.008.

[92] B. C. Chen *et al.*, "Lattice light-sheet microscopy: Imaging molecules to embryos at high spatiotemporal resolution," *Science (80-.).*, vol. 346, no. 6208, 2014, doi: 10.1126/science.1257998.

[93] C. Dunsby, "Optically sectioned imaging by oblique plane microscopy.," *Opt. Express*, vol. 16, no. 25, pp. 20306–16, Dec. 2008, doi: 10.1364/oe.16.020306.

[94] M. B. Bouchard *et al.*, "Swept confocally-aligned planar excitation (SCAPE) microscopy for high speed volumetric imaging of behaving organisms.," *Nat. Photonics*, vol. 9, no. 2, pp. 113–119, Feb. 2015, doi: 10.1038/nphoton.2014.323.

[95] T. Li *et al.*, "Axial plane optical microscopy," *Sci. Rep.*, vol. 4, pp. 1–6, 2014, doi: 10.1038/srep07253.

[96] B. Yang *et al.*, "Epi-illumination SPIM for volumetric imaging with high spatial-temporal resolution.," *Nat. Methods*, vol. 16, no. 6, pp. 501–504, 2019, doi: 10.1038/s41592-019-0401-3.

[97] E. Sapoznik *et al.*, "A Single-Objective Light-Sheet Microscope with 200 nm-Scale Resolution," *bioRxiv*, pp. 1–40, 2020, doi: https://doi.org/10.1101/2020.04.07.030569.

[98] A. G. Z. Millett-Sikking, A. York, "High NA single-objective light-sheet." https://andrewgyork.github.io/high_na_single_objective_lightsheet/. doi.org/10.5281/ zenodo.3244420.

[99] J. Kim *et al.*, "Oblique-plane single-molecule localization microscopy for tissues and small intact animals," *Nat. Methods*, vol. 16, no. 9, pp. 853–857, Sep. 2019, doi: 10.1038/s41592-019-0510-z.

[100] S. An *et al.*, "Axial plane single-molecule super-resolution microscopy of whole cells," *Biomed. Opt. Express*, vol. 11, no. 1, p. 461, 2020, doi: 10.1364/boe.377890.

[101] M. B. M. Meddens, S. Liu, P. S. Finnegan, T. L. Edwards, C. D. James, and K. A. Lidke, "Single objective light-sheet microscopy for high-speed whole-cell 3D super-resolution," *Biomed. Opt. Express*, vol. 7, no. 6, p. 2219, 2016, doi: 10.1364/boe.7.002219.

[102] R. Galland, G. Grenci, A. Aravind, V. Viasnoff, V. Studer, and J. B. Sibarita, "3D high-and super-resolution imaging using single-objective SPIM," *Nat. Methods*, vol. 12, no. 7, pp. 641–644, 2015, doi: 10.1038/nmeth.3402.

[103] R. Edmondson, J. J. Broglie, A. F. Adcock, and L. Yang, "Three-Dimensional Cell Culture Systems and Their Applications in Drug Discovery and Cell-Based Biosensors," *Assay Drug Dev. Technol.*, vol. 12, no. 4, pp. 207–218, May 2014, doi: 10.1089/adt.2014.573.

[104] B. Hajj *et al.*, "Whole-cell, multicolor superresolution imaging using volumetric multifocus microscopy," *Proc. Natl. Acad. Sci. U. S. A.*, vol. 111, no. 49, pp. 17480–17485, 2014, doi: 10.1073/pnas.1412396111.

[105] B. Hajj, L. Oudjedi, J. B. Fiche, M. Dahan, and M. Nollmann, "Highly efficient multicolor multifocus microscopy by optimal design of diffraction binary gratings," *Sci. Rep.*, vol. 7, no. 1, pp. 1–9, 2017, doi: 10.1038/s41598-017-05531-6.
[106] S. Abrahamsson *et al.*, "Multifocus microscopy with precise color multi-phase diffractive optics applied in functional neuronal imaging," *Biomed. Opt. Express*, vol. 7, no. 3, p. 855, 2016, doi: 10.1364/boe.7.000855.
[107] "MetaMorph Microscopy Automation and Image Analysis Software (RRID:SCR_002368)."
[108] K. Lou, S. Granick, and F. Amblard, "How to better focus waves by considering symmetry and information loss," *Proc. Natl. Acad. Sci.*, vol. 115, no. 26, pp. 6554–6559, Jun. 2018, doi: 10.1073/pnas.1803652115.
[109] C. Elliott, V. Vijayakumar, W. Zink, and R. Hansen, "National Instruments LabVIEW: A Programming Environment for Laboratory Automation and Measurement," *JALA J. Assoc. Lab. Autom.*, vol. 12, no. 1, pp. 17–24, Feb. 2007, doi: 10.1016/j.jala.2006.07.012.
[110] C. Maurer, A. Jesacher, S. Bernet, and M. Ritsch-Marte, "What spatial light modulators can do for optical microscopy," *Laser Photon. Rev.*, vol. 5, no. 1, pp. 81–101, Jan. 2011, doi: 10.1002/lpor.200900047.
[111] N. Ji, "Adaptive optical fluorescence microscopy," *Nat. Methods*, vol. 14, no. 4, pp. 374–380, Apr. 2017, doi: 10.1038/nmeth.4218.
[112] T. Instruments, "DLP ™ System Optics," *Prod. Appl. Rep.*, no. July, pp. 1–26, 2010.
[113] N. Chakrova, B. Rieger, and S. Stallinga, "Development of a DMD-based fluorescence microscope," Mar. 2015, p. 933008, doi: 10.1117/12.2077677.
[114] D. Dan *et al.*, "DMD-based LED-illumination Super-resolution and optical sectioning microscopy," *Sci. Rep.*, vol. 3, pp. 1–7, 2013, doi: 10.1038/srep01116.
[115] D. Dan, B. Yao, and M. Lei, "Structured illumination microscopy for super-resolution and optical sectioning," *Chinese Sci. Bull.*, vol. 59, no. 12, pp. 1291–1307, 2014, doi: 10.1007/s11434-014-0181-1.
[116] A. Sandmeyer, M. Lachetta, H. Sandmeyer, W. Hübner, T. Huser, and M. Müller, "DMD-based super-resolution structured illumination microscopy visualizes live cell dynamics at high speed and low cost." bioRxiv, 2019, doi: 10.1101/797670.
[117] A. Descloux *et al.*, "High-speed multiplane structured illumination microscopy of living cells using an image-splitting prism," *Nanophotonics*, vol. 9, no. 1, pp. 143–148, Dec. 2019, doi: 10.1515/nanoph-2019-0346.
[118] F. P. Martial and N. A. Hartell, "Programmable illumination and high-speed, multi-wavelength, confocal microscopy using a digital micromirror," *PLoS One*, vol. 7, no. 8, 2012, doi: 10.1371/journal.pone.0043942.
[119] TI Instruments, "Using Lasers with DLP ® DMD technology," 2008.
[120] M. Lachetta, H. Sandmeyer, A. Sandmeyer, J. S. am Esch, T. Huser, and M. Müller, "Simulating digital micromirror devices for patterning coherent excitation light in structured illumination microscopy," *Philos. Trans. R. Soc. A Math. Phys. Eng. Sci.*, vol. 379, no. 2199, p. rsta.2020.0147, Jun. 2021, doi: 10.1098/rsta.2020.0147.
[121] L. Caccianini, "Imagerie de l'architecture dynamique de la chromatine dans la cellule unique," 2019.
[122] H. Ma, F. Long, S. Zeng, and Z.-L. Huang, "Fast and precise algorithm based on

maximum radial symmetry for single molecule localization," *Opt. Lett.*, vol. 37, no. 13, p. 2481, 2012, doi: 10.1364/ol.37.002481.

[123] J. Schindelin *et al.*, "Fiji: an open-source platform for biological-image analysis," *Nat. Methods*, vol. 9, no. 7, pp. 676–682, Jul. 2012, doi: 10.1038/nmeth.2019.

[124] H. Kimura, "Histone dynamics in living cells revealed by photobleaching," *DNA Repair (Amst).*, vol. 4, no. 8, pp. 939–950, Jul. 2005, doi: 10.1016/j.dnarep.2005.04.012.

[125] A. Kitamura and M. Kinjo, "Determination of diffusion coefficients in live cells using fluorescence recovery after photobleaching with wide-field fluorescence microscopy," *Biophys. Physicobiology*, vol. 15, pp. 1–7, 2018, doi: 10.2142/biophysico.15.0_1.

[126] D. T. Gruszka, S. Xie, H. Kimura, and H. Yardimci, "Single-molecule imaging reveals control of parental histone recycling by free histones during DNA replication," *Sci. Adv.*, vol. 6, no. 38, p. eabc0330, Sep. 2020, doi: 10.1126/sciadv.abc0330.

[127] C. Clément *et al.*, "High-resolution visualization of H3 variants during replication reveals their controlled recycling," *Nat. Commun.*, vol. 9, no. 1, p. 3181, Dec. 2018, doi: 10.1038/s41467-018-05697-1.

[128] J. Dekker and L. Mirny, "The 3D Genome as Moderator of Chromosomal Communication," *Cell*, vol. 164, no. 6, pp. 1110–1121, Mar. 2016, doi: 10.1016/j.cell.2016.02.007.

[129] M. Merkenschlager and E. P. Nora, "CTCF and Cohesin in Genome Folding and Transcriptional Gene Regulation," *Annu. Rev. Genomics Hum. Genet.*, vol. 17, no. 1, pp. 17–43, Aug. 2016, doi: 10.1146/annurev-genom-083115-022339.

[130] B. Bintu *et al.*, "Super-resolution chromatin tracing reveals domains and cooperative interactions in single cells," *Science (80-.).*, vol. 362, no. 6413, p. eaau1783, Oct. 2018, doi: 10.1126/science.aau1783.

[131] A. S. Hansen, "CTCF as a boundary factor for cohesin-mediated loop extrusion: evidence for a multi-step mechanism," *Nucleus*, vol. 11, no. 1, pp. 132–148, Jan. 2020, doi: 10.1080/19491034.2020.1782024.

[132] E. P. Nora *et al.*, "Molecular basis of CTCF binding polarity in genome folding," *Nat. Commun.*, vol. 11, no. 1, p. 5612, Dec. 2020, doi: 10.1038/s41467-020-19283-x.

[133] A. S. Hansen, I. Pustova, C. Cattoglio, R. Tjian, and X. Darzacq, "CTCF and cohesin regulate chromatin loop stability with distinct dynamics," *Elife*, vol. 6, p. e25776, 2017.

[134] H. Agarwal, M. Reisser, C. Wortmann, and J. C. M. Gebhardt, "Direct Observation of Cell-Cycle-Dependent Interactions between CTCF and Chromatin," *Biophys. J.*, vol. 112, no. 10, pp. 2051–2055, May 2017, doi: 10.1016/j.bpj.2017.04.018.

[135] S. H. Lee *et al.*, "Using fixed fiduciary markers for stage drift correction," *Opt. Express*, vol. 20, no. 11, p. 12177, May 2012, doi: 10.1364/OE.20.012177.

[136] C. Geisler, T. Hotz, A. Schönle, S. W. Hell, A. Munk, and A. Egner, "Drift estimation for single marker switching based imaging schemes," *Opt. Express*, vol. 20, no. 7, p. 7274, Mar. 2012, doi: 10.1364/OE.20.007274.

[137] A. Wade and F. Fitzke, "A fast, robust pattern recognition asystem for low light level image registration and its application to retinal imaging," *Opt. Express*, vol. 3, no. 5, p. 190, Aug. 1998, doi: 10.1364/OE.3.000190.

[138] M. Guizar-Sicairos, S. T. Thurman, and J. R. Fienup, "Efficient subpixel image

registration algorithms," *Opt. Lett.*, vol. 33, no. 2, p. 156, Jan. 2008, doi: 10.1364/OL.33.000156.

[139] Y. Wang *et al.*, "Localization events-based sample drift correction for localization microscopy with redundant cross-correlation algorithm," *Opt. Express*, vol. 22, no. 13, p. 15982, Jun. 2014, doi: 10.1364/OE.22.015982.

[140] M. J. Mlodzianoski *et al.*, "Sample drift correction in 3D fluorescence photoactivation localization microscopy," *Opt. Express*, vol. 19, no. 16, p. 15009, Aug. 2011, doi: 10.1364/OE.19.015009.

[141] R. McGorty, D. Kamiyama, and B. Huang, "Active microscope stabilization in three dimensions using image correlation," *Opt. Nanoscopy*, vol. 2, no. 1, p. 3, 2013, doi: 10.1186/2192-2853-2-3.

[142] T. Blanc, M. El Beheiry, C. Caporal, J.-B. Masson, and B. Hajj, "Genuage: visualize and analyze multidimensional single-molecule point cloud data in virtual reality," *Nat. Methods*, vol. 17, no. 11, pp. 1100–1102, Nov. 2020, doi: 10.1038/s41592-020-0946-1.

[143] G. Grover, W. Mohrman, and R. Piestun, "Real-time adaptive drift correction for super-resolution localization microscopy," *Opt. Express*, vol. 23, no. 18, p. 23887, Sep. 2015, doi: 10.1364/OE.23.023887.

[144] M. Sergides, L. Perego, T. Galgani, C. Arbore, F. S. Pavone, and M. Capitanio, "Probing mechanotransduction in living cells by optical tweezers and FRET-based molecular force microscopy," *Eur. Phys. J. Plus*, vol. 136, no. 3, p. 316, Mar. 2021, doi: 10.1140/epjp/s13360-021-01273-7.

[145] C. R. Nave, "Hyperphysics." http://hyperphysics.phy-astr.gsu.edu/hbase/phyopt/mulslid.html.

RÉSUMÉ

L'imagerie de la molécule unique (SM) offre un moyen d'étudier l'organisation et la dynamique des biomolécules avec une haute résolution temporelle et spatiale. Cependant, l'imagerie avec une faible profondeur de champ d'un microscope standard ne reflète pas l'organisation volumétrique internes des cellules et limite la gamme des dynamiques qui peuvent être observées en 3D. La réalisation d'une imagerie SM efficace et précise dans un échantillon biologique volumétrique est confrontée à deux défis principaux. Premièrement, les molécules excitées hors foyer produisent un bruit de fond élevé qui affecte la précision de localisation. Deuxièmement, les molécules qui diffusent rapidement ont tendance à s'échapper à la profondeur de champ d'imagerie. Pour relever ces défis, nous proposons une nouvelle méthode d'imagerie volumétrique sélective et instantanée avec une sensibilité SM. Dans le cadre de mon projet de doctorat, nous avons développé un système modulaire inspiré de deux techniques de pointe : la microscopie multifocale (MFM) et la microscopie sélective à feuille de lumière et à objectif unique (soSPIM). Grâce au MFM, notre système est capable d'imager instantanément un volume avec une haute résolution temporelle et une sensibilité SM. Nous avons l'architecture du soSPIM afin de créer une excitation en nappe de lumière uniforme et accordable qui s'adapte à la profondeur d'imagerie du MFM. Nous avons illustré l'avantage de notre méthode par l'imagerie de la dynamique des facteurs nucléaires tels que H2B, CTCF et Cohesin à plusieurs microns de profondeur dans des cellules U2OS et cellules souches embryonnaires de souris avec une haute résolution temporelle et spatiale. Nous avons pu imager la dynamique des SM jusqu'à 50 volumes de 35×35×4 μm^3 par seconde. Enfin, nous avons reconstruit des images volumétriques en super-résolution de Lamine-b, une protéine de la membrane nucléaire, par DNA-PAINT. Cette thèse ouvre la voie à l'observation de l'organisation et de la dynamique moléculaires à haute résolution temporelle et spatiale dans des organismes multicellulaires et des tissus.

MOTS CLÉS

Feuille de lumière, Molécule unique, Imagerie 3D, Super-résolution, Dynamique, Noyau

ABSTRACT

Single-molecule (SM) imaging offer a mean to investigate the nanoscale organization and dynamics of biomolecules with high temporal and spatial resolution. However, the limited imaging depth of a standard SM microscope does not reflect the inherent volumetric organization of the inner organelles of cells and limits the range of SM dynamics that can be observed in 3D. Performing efficient SM imaging with high localization precision in a volumetric biological sample faces two main challenges. First, excited out-of-focus molecules produce high background noise that affect the localization precision. Second, fast diffusing molecules tend to escape the limited depth of field of the imaging microscope objective. To address these challenges, we propose a new method for selective and true instantaneous volumetric imaging with SM sensitivity. In my PhD project, we developed a modular system, with, at the core, two cutting-edge techniques: multifocus microscopy (MFM) and single-objective selective plane illumination microscopy (soSPIM). Thanks to the MFM, our system is able to image a volume instantaneously with high temporal resolution and SM sensitivity. We remodeled the soSPIM architecture in order to create a tunable and uniform light sheet excitation that matches the desired range of MFM detection. We illustrated the advantage our method by imaging the dynamics of nuclear factors such as H2B, CTCF and Cohesin at several microns deep in U2OS and mouse embryonic stem cells with high temporal and spatial resolution. We were able to image SM dynamics up to 50 volumes of 35×35×4 μm^3 size per second. Finally, we reconstructed volumetric super-resolution images of the nuclear, performing DNA-PAINT on the Lamin-b protein. This thesis paves the way for exploring the molecular organization and dynamics at high temporal and spatial resolution in multicellular organisms and tissues.

KEYWORDS

Light-sheet, Single-molecule, 3D imaging, Super-resolution, Dynamics, Nucleus